PHOTOELECTRON TRANSPORT AND ENERGY BALANCE IN THE LOW-LATITUDE IONOSPHERE

A Dissertation

Presented to the Faculty of the Graduate School

of Cornell University

in Partial Fulfillment of the Requirements for the Degree of

Doctor of Philosophy

by

Roger Hale Varney

August 2012

PHOTOELECTRON TRANSPORT AND ENERGY BALANCE IN THE LOW-LATITUDE IONOSPHERE

Roger Hale Varney, Ph.D.

Cornell University 2012

Theoretical studies of ionospheric structure and dynamics require knowledge of the underlying thermal structure of the ionosphere since it affects the chemical reaction rates, recombination rates, and pressure gradients. Measurements of ionospheric temperatures have been made for decades with a variety of ground- and space-based techniques. This thesis is motivated in particular by the recent improvements in the temperature measurements made by the Jicamarca Radio Observatory (JRO) using the incoherent scatter radar (ISR) technique. Modern ionospheric models all have widely different treatments of ionospheric energetics, and none can produce satisfactory quantitative agreement with the JRO measurements even in quiet conditions. This thesis explores the energy balance calculations in the widely used, open source SAMI2 model in detail, and shows that it is the oversimplification of the treatment of nonlocal heating by photoelectrons in particular which is preventing this model from predicting JRO measurements. This thesis presents an extended version of the SAMI2 model, called SAMI2-PE, which includes a newly developed photoelectron transport model. The model uses finite volume methods which guarantee conservation of particles and energy, incorporates the magnetic field geometry and magnetic mirroring effects, and can be extended to any spatial, energy, and pitch-angle resolution. The new model shows promising agreement with the JRO measurements.

BIOGRAPHICAL SKETCH

Roger Hale Varney was born on March 29, 1987 in Chester, Pennsylvania. He graduated from Strath Haven High School in 2005. His first introduction to plasma physics came from a summer job in 2004 as a laboratory assistant for the Swarthmore Spheromak eXperiment (SSX) lab run by Prof. Michael Brown at Swarthmore College. He graduated from Cornell University in January 2009 with a B.S. in electrical and computer engineering (ECE). As an undergraduate he participated in research under the direction of Prof. Michael Kelley from June 2006 onwards, was a visiting research fellow at SRI International in Menlo Park, California during the summer of 2007, and studied at the Jicamarca Radio Observatory outside of Lima, Peru during the summer of 2008 as part of the Jicamarca International Research Experience Program. He joined Eta Kappa Nu and the American Geophysical Union. In January 2009 he entered the M.S./Ph.D. program in ECE at Cornell University. In June 2009 he was awarded a Graduate Research Fellowship by the National Science Foundation. From June 2010 to June 2012 he served as a student representative to the Coupling, Energetics, and Dynamics of Atmospheric Regions (CEDAR) Science Steering Committee (CSSC). In March 2012 it was announced that he was awarded a Jack Eddy Postdoctoral Fellowship for 2012-2014 from the NASA Living With a Star (LWS) Program.

This thesis is dedicated to my loving and supportive parents, Earl and Mina Varney.

ACKNOWLEDGEMENTS

This thesis work was primarily motivated by recent observations from the Jicamarca Radio Observatory, which is a facility of the Instituto Geofisíco del Perú operated with support from NSF cooperative agreement AGS-0905448 through Cornell University. Thanks to all of the Jicamarca staff for operating a world class observatory. The material in this thesis was developed while I was supported by a National Science Foundation Graduate Research Fellowship under Grant No. DGE-0707428 (June 2009 - May 2012). During June and July 2012 I was supported through the Jicamarca award directly while I finished this thesis. This thesis makes extensive use of and improvements to the SAMI2 ionosphere model written and developed by the Naval Research Laboratory (NRL).

Several other people need to be thanked for their contributions to this thesis. Firstly I need to acknowledge my advisor, Prof. Kelley, who gave me amazing research opportunities as an undergraduate and convinced me to stay at Cornell for the M.S./Ph.D. program. I doubt I ever would have found my way into the field of aeronomy had it not been for Prof. Kelley's influence. Under Prof. Kelley's direction I worked on a variety of different projects throughout my time at Cornell, most of which are not discussed in this thesis.

The idea to reexamine the energy balance calculations in SAMI2 to allow for more detailed comparisons with Jicamarca data originally came from Prof. Hysell. Prof. Hysell pitched this idea to me midway through graduate school when I was greatly in need of direction, and encouraged me to take left turn away from radar experiments into the realm of ionospheric modeling. This change has transformed the way I conduct and approach research. Prof. Hysell has been closely involved with every part of this thesis, and has also been a huge part of the rest of my experience in graduate school.

Another vital contributor to this thesis was Dr. Swartz. Having been both a student and TA in his undergrad classes I already had a significant relationship with him by the time I entered graduate school, but once I became interested in photoelectrons Dr. Swartz became invaluable to my research. Dr. Swartz's own dissertation was about photoelectron transport, and thus he was intimately involved with this thesis work.

I also want to thank Dr. Huba at the NRL for all of his help with the SAMI2 code. The SAMI2 source code is intuitive to work with and served as an excellent starting point for this thesis work. Finally I want to thank Prof. Seyler for serving as the final professor on my thesis committee and for having many stimulating discussions on plasma physics and numerical computation in general with me.

TABLE OF CONTENTS

LIST OF TABLES

LIST OF FIGURES

CHAPTER 1

INTRODUCTION

The goal of aeronomy is to observationally and theoretically specify the structure and composition of the Earth's upper atmosphere and ionosphere. This area of basic research is a prerequisite for studies of space weather and its impact on society. A component aeronomy is the study of ionospheric energetics, i.e. the ways energy is produced, transported, and transformed in the ionospheric plasma. This thesis was inspired to revisit this old problem by recently improved measurements of plasma temperatures in the ionosphere and inner plasmasphere made at the Jicamarca Radio Observatory, an equatorial incoherent scatter radar [*Hysell et al.*, 2008, 2009]. These measurements cover the F-region ionosphere, the topside ionosphere, and inner plasmasphere up to $\sim$1500 km altitude. Our objective is to create a theoretical model which can reproduce these Jicamarca temperature measurements both in a quantitative and qualitative sense. Such a model can be used to gain insight as to which physical processes influence the measured temperatures in different regimes, why the measured temperatures display day-to-day variability, and what we could potentially learn about the larger ionosphere-thermosphere-plasmasphere system from these observations.

In this thesis we have not created an entire ionospheric model from scratch. Our development has been based on the widely used open source SAMI2 model [*Huba et al.*, 2000a]. Ch. 3 reviews the physics and numerics in this model, with a particular emphasis on the energy balance calculations, and compares SAMI2 results with Jicamarca data. We argue that the phenomenological treatment of photoelectron transport in particular is the most significant aspect of SAMI2 which is preventing it from satisfactorily reproducing Jicamarca data. SAMI2 is not the

only model which suffers from this limitation; as Sec. 2.3 explains, few existing ionospheric models have physical treatments of photoelectrons.

The remainder of this thesis is devoted to the description and use of an extended version of SAMI2 which includes a physical treatment of photoelectrons called SAMI2-PE. Ch. 4 explains the physics added in SAMI2-PE and derives all the pertinent equations. Numerous authors have derived variations of the photoelectron transport equations before, and the equations used by previous authors are either equivalent to, or limiting cases of, the equations used in SAMI2-PE (see Sec. 2.4). Nonetheless we chose to go through all the derivations in Ch. 4 in order to discuss every approximation involved. These approximations determine the limits of applicability of the final equations. Ch. 4 also shows many of the intermediate steps needed in the derivations which do not appear in journal articles.

Ch. 5 describes the specific numerical algorithms used in SAMI2-PE. The energy reapportionment calculations are performed using an algorithm which is equivalent to that originally described by *Swartz* [1985], but implemented in a different way. In particular, our implementation allows for ionizing collisions to be treated in a single step instead of having to loop over all possible secondary energies (see Sec. 5.2). The steady state transport solver described in Sec. 5.1 is an original algorithm developed for SAMI2-PE. It uses finite volume ideas to guarantee conservation of particles and energy. A variation of this algorithm which uses flux limiters to eliminate some numerical pitch-angle diffusion is described in Sec. 5.1.1, although the tests shown in Sec. 6.3.1 suggest that these higher order corrections are unnecessary in the region of interest in this thesis (i.e. the low-latitude ionosphere at altitudes up to 1500 km).

Ch. 6 discusses example SAMI2-PE results in detail and compares them to Jicamarca data. Example runs with a variety of different inputs are compared to elucidate the effects of various physical drivers. These tests suggest possible sources of the day-to-day variability observed in high-altitude electron temperature measurements from Jicamarca. The thermospheric winds in particular are shown to have important effects on the electron densities and temperatures at high altitudes (600-1500 km). Despite the small neutral densities at these altitudes, the motions of the neutral thermosphere are still coupled to the high-altitude plasma through larger system processes. Finally, Ch. 7 contains concluding remarks discussing what this thesis has accomplished and gives recommendations for future work.

CHAPTER 2

BACKGROUND

This thesis builds on an old field, and thus a substantial amount of background information must be reviewed. First, Sec. 2.1 gives a brief introduction to incoherent scatter radar and showcases the measurements which motivated this thesis. Sec. 2.2 provides history and a top level overview of the theory of ionospheric energetics. Then Sec. 2.3 describes how many existing ionospheric models treat ionospheric energetics. Like SAMI2, most modern ionospheric models do not have a physical treatment of photoelectrons with the notable exceptions of FLIP and SUPIM. Finally, Sec. 2.4 gives a history of photoelectron transport modeling. The various different forms of the photoelectron transport equation solved by other models are shown to be either equivalent to, or limiting cases of, the equation solved in SAMI2-PE.

2.1 Ionospheric temperature measurements using incoherent scatter radar

Gordon [1958] was the first to theorize that Thompson scatter from electrons in the ionosphere could be detected with a sufficiently large radar. He believed that the scattered waves from the individual electrons would add with random phases and hence be a type of incoherent scattering. Under this assumption the Doppler width of the received signal would be determined by the electron thermal speed. Shortly after the publication of this original theory, *Bowles* [1958] made the first detection of Thompson scatter from ionospheric electrons and showed that the Doppler width was much narrower than expected based on the electron thermal speeds. This

observations prompted numerous theorists to derive expressions for the spectrum of electron density fluctuations in a warm plasma [e.g. *Dougherty and Farley*, 1960; *Farley et al.*, 1961; *Dougherty and Farley*, 1963; *Farley*, 1966; *Swartz and Farley*, 1979; *Fejer*, 1960a, b, 1961; *Salpeter*, 1960, 1961; *Hagfors*, 1961; *Rosenbluth and Rostoker*, 1962; *Woodman*, 1967]. These theories used very different reasonings, yet all derived equivalent expressions. Sec. 2.1.1 presents a quick derivation of the basic theory based on the approach of *Swartz and Farley* [1979] and gives additional references for more advanced treatments. For radar wavelengths much longer than the electron Debye length collective effects are important and the spectral width is related to the ion thermal speed, even though the scatter comes from the electrons. Hence the phenomenon is not strictly a form of incoherent scattering, but the name incoherent scatter radar (ISR) has stuck.

The ISR data presented in this thesis all come from the Jicamarca Radio Observatory (JRO), which is located outside of Lima, Peru on the magnetic equator. This observatory opened in 1962 and recently celebrated 50 years of operations. Despite its age, the quality of Jicamarca ISR data has improved throughout its history as a result of upgrades to the hardware, refinements to ISR theory, advances in signal processing techniques, and more sophisticated inverse methods. Sec. 2.1.2 reviews the major components of an ISR experiment with an emphasis on the methods used at Jicamarca today. Sec. 2.1.3 then shows examples of some of the recent Jicamarca observations which motivated this thesis.

2.1.1 Basic theory of incoherent scattering

Linear media with stochastic index of refraction fluctuations scatter electromagnetic waves. The radar reflectivity (i.e. the radar scattering cross section per unit

volume) in the radian Doppler frequency interval between ω and $\omega + d\omega$ above the transmitted frequency ω_0 is related to the power spectral density of index of refraction fluctuations, $\langle|n(\mathbf{k},\omega)|^2\rangle$, by [e.g. *Booker*, 1956; *Tatarski*, 1961; *Hocking*, 1985]

$$\sigma(\omega_0 + \omega)d\omega = \frac{k^4}{32\pi^3}\sin^2\delta\langle|n(\mathbf{k},\omega)|^2\rangle d\omega, \tag{2.1}$$

where δ is the angle between the wavevectors of the incident and the scattered waves, and $\mathbf{k}$ is the Bragg scattering wavenumber. For a monostatic radar $\delta = \pi$ and $k = 4\pi/\lambda_R$, where λ_R is the radar wavelength. In the ionosphere for frequencies which are much greater than the electron gyrofrequency the index of refraction squared is

$$n^2 = 1 - \frac{\omega_{pe}^2}{\omega^2} \tag{2.2}$$

$$\tag{2.3}$$

where the plasma frequency is a function of the electron density,

$$\omega_{pe}^2 = \frac{e^2 N_e}{\epsilon_0 m_e}. \tag{2.4}$$

Hence the radar reflectivity for a monostatic radar can be rewritten as a function of the power spectral density of electron density fluctuations, $\langle|n_e(\mathbf{k},\omega)|^2\rangle$, [e.g. *Hocking*, 1985]

$$\sigma(\omega_0 + \omega)d\omega = \sigma_e\langle|n_e(\mathbf{k},\omega)|^2\rangle\frac{d\omega}{2\pi}, \tag{2.5}$$

where

$$\sigma_e = 4\pi r_e^2 = \frac{1}{4\pi\epsilon_0^2}\frac{e^4}{m_e^2 c^4} \approx 10^{-28}\ \mathrm{m}^2 \tag{2.6}$$

is the Thompson scattering cross section of a single electron [e.g. *Jackson*, 1999]. (Note this formula differs from that in *Jackson* [1999] by a factor of 3/2 because it

is a radar scattering cross section instead of an extinction cross section. The extra factor of 3/2 is the directivity of a Herztian dipole antenna in the backscattered direction). When unstable plasma waves and/or plasma turbulence are present $\langle|n_e(\mathbf{k},\omega)|^2\rangle$ can be a significant fraction of N_e^2 and large amounts of backscattered power can be received from the ionosphere. This is called coherent scattering in the ionospheric community [e.g. *Woodman and La Hoz*, 1976]. In a stable plasma $\langle|n_e(\mathbf{k},\omega)|^2\rangle$ will never be exactly zero, however, because the electrons themselves are points in space. In the simple case where the electrons are randomly distributed throughout the scattering volume with a uniform distribution in space and a distribution $\hat{f}(v)$ in line of sight velocities, $\langle|n_e(\mathbf{k},\omega)|^2\rangle = \frac{2\pi}{k}N_e\hat{f}(\omega/k)$. Inserting this into Eq. 2.5 and integrating over all Doppler shifts gives a total reflectivity of $\eta = \int \sigma(\omega_0+\omega)\,d\omega = \sigma_e N_e$, which is what *Gordon* [1958] expected.

For radar wavelengths longer than the electron Debye length the electrons cannot be assumed to be uniformly distributed in space because of collective effects. In this case $\langle|n_e(\mathbf{k},\omega)|^2\rangle$ must be determined using statistical mechanics and plasma kinetic theory. In this endeavor the Generalized Nyquist Theorem (a.k.a. the Fluctuation-Dissipation Theorem), is a useful tool from statistical mechanics [*Callen and Welton*, 1951]. Consider a linear system in which the Laplace transform of the response function $I(s)$ is related to the Laplace transform of a generalized forcing function $V(s)$ through an an admittance function $Y(s)$ i.e.

$$I(s) = Y(s)V(s). \tag{2.7}$$

When in thermodynamic equilibrium at temperature T and not driven by any forces random thermal motions will cause this system to emit a stochastic response with power spectral density [*Callen and Welton*, 1951].

$$\langle|I(s)|^2\rangle = 2k_BT\Re\{Y(s)\} \tag{2.8}$$

This response can be thought of as originating from a stochastic force with power spectral density

$$\langle |V(s)|^2 \rangle = \frac{2k_B T}{|Y(s)|^2} \Re\{Y(s)\}. \tag{2.9}$$

The original development of ISR theory by *Dougherty and Farley* [1960] applied the Generalized Nyquist Theorem by deriving a single admittance for the entire plasma. *Swartz and Farley* [1979] generalized this approach to plasmas which were not in perfect thermodynamic equilibrium (e.g. $T_e \neq T_i$). In the *Swartz and Farley* [1979] method an admittance relating the velocity fluctuations to the forces applied is defined for each plasma species. Let the electron density be $N_e + n_e$ and the electron flux be $N_e \mathbf{U}_e + n_e \mathbf{U}_e + N_e \mathbf{u}_e$ where N_e and $\mathbf{U}_e$ are the background electron density and electron velocity and n_e and $\mathbf{u}_e$ are small perturbations which are proportional to $\exp[i(\mathbf{k} \cdot \mathbf{r} - \omega t)]$. The electron admittance, $Y_e(\mathbf{k}, \omega)$ is defined such that

$$N_e \mathbf{u}_e = Y_e \mathbf{F}, \tag{2.10}$$

where $\mathbf{F}$ is any force applied to the electron gas. Analogous quantities are defined for the ions. In a warm plasma the electron and ion flux fluctuations are driven both by stochastic forces which capture the effects of random thermal motions, $\mathbf{F}_e$ and $\mathbf{F}_i$, and by the self consistent electric field in the plasma, i.e.

$$N_e \mathbf{u}_e = Y_e \left(\mathbf{F}_e - e\mathbf{E} \right) \tag{2.11}$$

$$N_e \mathbf{u}_i = Y_i \left(\mathbf{F}_i + e\mathbf{E} \right), \tag{2.12}$$

where a quasineutral background is assumed ($N_e = N_i$). The electric field obeys Gauss' Law

$$i\mathbf{k} \cdot \mathbf{E} = \frac{e}{\epsilon_0} \left(n_i - n_e \right). \tag{2.13}$$

Finally, the density fluctuations can be related to the velocity fluctuations through the linearized continuity equations

$$-i\omega n_e + i\mathbf{k}\cdot(n_e\mathbf{U}_e + N_e\mathbf{u}_e) = 0 \tag{2.14}$$

$$-i\omega n_i + i\mathbf{k}\cdot(n_i\mathbf{U}_i + N_e\mathbf{u}_i) = 0. \tag{2.15}$$

This system of five equations can be solved for the electron density fluctuations

$$n_e = \frac{kY_e}{\omega_e}\frac{[Y_i/\omega_i - i\epsilon_0/e^2]\,F_e + [Y_i/\omega_i]\,F_i}{Y_i/\omega_i + Y_e/\omega_e - i\epsilon_0/e^2}, \tag{2.16}$$

where for notational convenience the Doppler shifted frequencies are defined as

$$\omega_e = \omega - \mathbf{k}\cdot\mathbf{U}_e \tag{2.17}$$

$$\omega_i = \omega - \mathbf{k}\cdot\mathbf{U}_i. \tag{2.18}$$

The stochastic forces $\mathbf{F}_e$ and $\mathbf{F}_i$ are uncorrelated and have power spectral densities related to the admittances and temperatures of the electron and ion respectively through the Generalized Nyquist Theorem. Squaring and averaging Eq. 2.16 gives

$$\langle|n_e(\mathbf{k},\omega)|^2\rangle = 2k^2\frac{|Y_i/\omega_i - i\epsilon_0/e^2|^2 T_e\Re\{Y_e\}/\omega_e^2 + |Y_e/\omega_e|^2 T_i\Re\{Y_i\}/\omega_i^2}{|Y_i/\omega_i + Y_e/\omega_e - i\epsilon_0/e^2|^2}. \tag{2.19}$$

A more elegant expression results by defining normalized admittances for each species

$$y_\alpha = \frac{k^2 T_\alpha}{N_\alpha\omega_\alpha}, \tag{2.20}$$

and dimensionless susceptibilities

$$\chi_\alpha = \frac{iy_\alpha}{k^2\lambda_{D\alpha}^2}, \tag{2.21}$$

where the Debye lengths are [e.g. *Bellan*, 2006]

$$\lambda_{D\alpha} = \sqrt{\frac{\epsilon_0 k_B T_\alpha}{Z_\alpha^2 e^2 N_\alpha}}. \tag{2.22}$$

The spectrum of electron density fluctuations can then be written as

$$\langle |n_e(\mathbf{k},\omega)|^2 \rangle = 2k^2 N_e \frac{|1+\chi_i|^2 \lambda_{De}^2 \Im\{\chi_e\}/\omega_e + |\chi_e|^2 \lambda_{Di}^2 \Im\{\chi_i\}/\omega_i}{|1+\chi_e+\chi_i|^2} \tag{2.23}$$

The generalization of this formula to an arbitrary number of ion species is [*Swartz and Farley*, 1979]

$$\langle |n_e(\mathbf{k},\omega)|^2 \rangle = 2k^2 N_e \frac{|1+\sum_j \chi_j|^2 \lambda_{De}^2 \Im\{\chi_e\}/\omega_e + |\chi_e|^2 \sum_j Z_j \frac{N_j}{N_e} \lambda_{Dj}^2 \Im\{\chi_j\}/\omega_j}{|1+\chi_e+\sum_j \chi_j|^2}, \tag{2.24}$$

where the sums over j refer to sums over all ion species.

The susceptibilities themselves are determined by solving the linearized Vlasov-Poisson system of equations [see *Bellan*, 2006; *Ichimaru*, 2004]. For a simple collisionless, unmagnetized, Maxwellian plasma species the susceptibility is [e.g. *Bellan*, 2006]

$$\chi_\alpha(\mathbf{k},\omega) = \frac{1}{k^2 \lambda_\alpha} \left[1 + \theta_\alpha Z(\theta_\alpha)\right] \tag{2.25}$$

where the normalized frequency defined as

$$\theta_\alpha \equiv \frac{\omega_\alpha}{\sqrt{2}k} \sqrt{\frac{m_\alpha}{k_B T_\alpha}}, \tag{2.26}$$

and $Z(\theta_\alpha)$ is the plasma dispersion function [*Fried and Conte*, 1961].

The dispersion relation for electrostatic waves in a plasma is [e.g *Bellan*, 2006; *Ichimaru*, 2004]

$$1 + \chi_e + \sum_j \chi_j = 0. \tag{2.27}$$

Thus the denominator of Eq. 2.24 goes to 0 at $(\mathbf{k},\omega)$ values which correspond to electrostatic normal modes. The denominator will never go precisely to 0 for real ω values, however, since all electrostatic waves experience some kind of damping.

The ISR spectrum has several peaks where the Doppler shifts of the peaks match the phase velocities of electrostatic waves and the widths of the peaks are related to the damping rates of those electrostatic waves. In the case of an unmagnetized plasma there is a broad peak near the ion acoustic resonance, known as the ion line, and a narrow peak at the Langmuir wave resonance, known as the plasma line. Most of the power is in the ion line. Fig. 2.1 shows examples of ion line spectra for an O^+ plasma for different values of T_e/T_i. The two peaks correspond to the phase velocities of ion acoustic waves traveling towards and away from the radar. The locations of these peaks gives a measure of T_i and the area under the curve is related to N_e. If the plasma is moving along the radar's line of sight the entire spectrum will be Doppler shifted. The widths of the peaks are related to the Landau damping rate of the ion acoustic waves and are thus related to T_e/T_i. Thus ion line spectra contain unambiguous information about electron densities, both electron and ion temperatures, and line of sight plasma velocities. When multiple ions are present composition information can also be determined if the masses of the ions are sufficiently different. Fig. 2.2 compares ion line spectra for plasmas containing both O^+ and H^+. A pure H^+ plasma has a spectrum which is four times wider than an O^+ plasma. The spectra for mixtures are not simple superpositions of the single ion spectra, but nonetheless both narrow and wide spectral features are present so the H^+ fraction can be determined.

Eq. 2.24 applies to any stable plasma [*Swartz and Farley*, 1979], but for different types of background conditions the susceptibilities will change. Expressions for magnetized plasmas have been derived [e.g. *Farley et al.*, 1961; *Fejer*, 1961; *Hagfors*, 1961; *Salpeter*, 1961] (see also section 4.4 of *Ichimaru* [2004] for an excellent discussion of electrostatic waves in magnetized plasmas). For aspect angles away from perpendicular to $\mathbf{B}$ the ISR spectrum will have three lines: an ion line

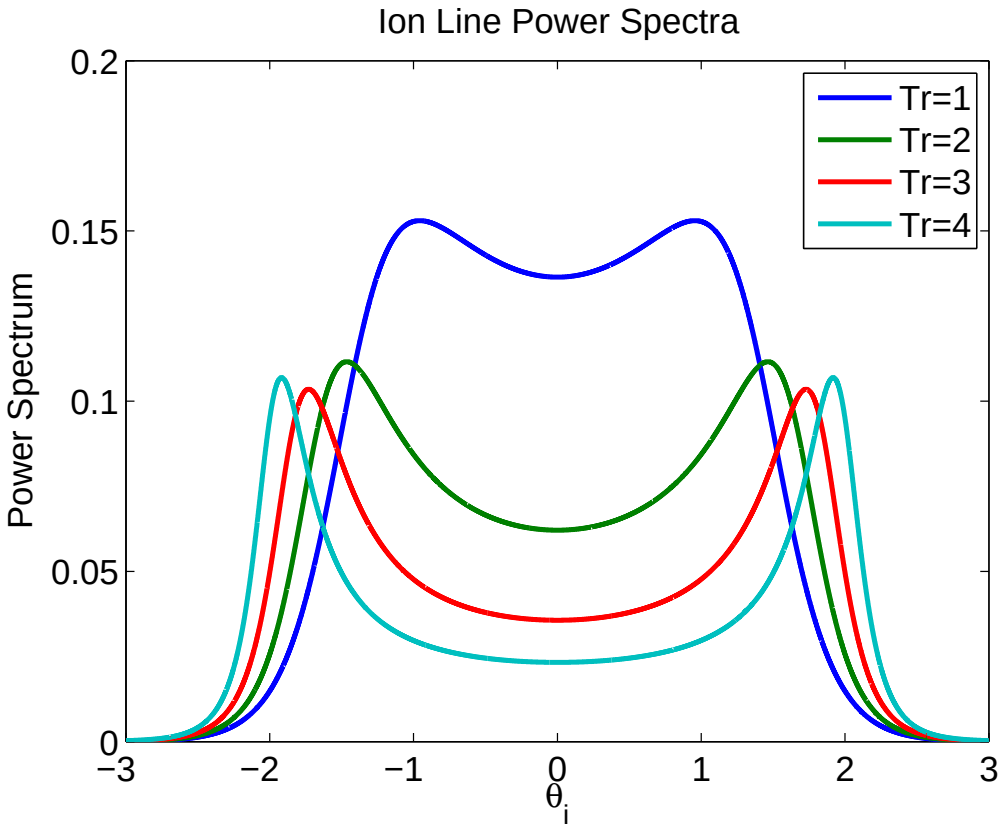

Figure 2.1: Normalized incoherent scatter spectra for various different temperature ratios, T_e/T_i. The vertical axis is in arbitrary units and the horizontal axis is the ion normalized frequency. The plasma is assumed to be unmagnetized, pure O^+, at rest, and $k\lambda_{De} = 0.2$.

which is similar to the ion line from the unmagnetized case, a plasma line which moves between the Langmuir wave and upper hybrid wave resonance as the aspect angle moves closer to perpendicular to **B**, and a gyro line near the electrostatic electron cyclotron wave resonance. Perpendicular to **B** the ion line collapses into a narrow spike at low frequencies [*Woodman and Hagfors*, 1969; *Kudeki et al.*, 1999]. Collisions with neutrals have been incorporated into the theory in a variety of different ways [*Dougherty and Farley*, 1963; *Tanenbaum*, 1968; *Hagfors and Brockelman*, 1971]. All of these theories predict that the spectrum will converge to a narrow Lorentzian shape at *D*-region altitudes, but that ion-neutral

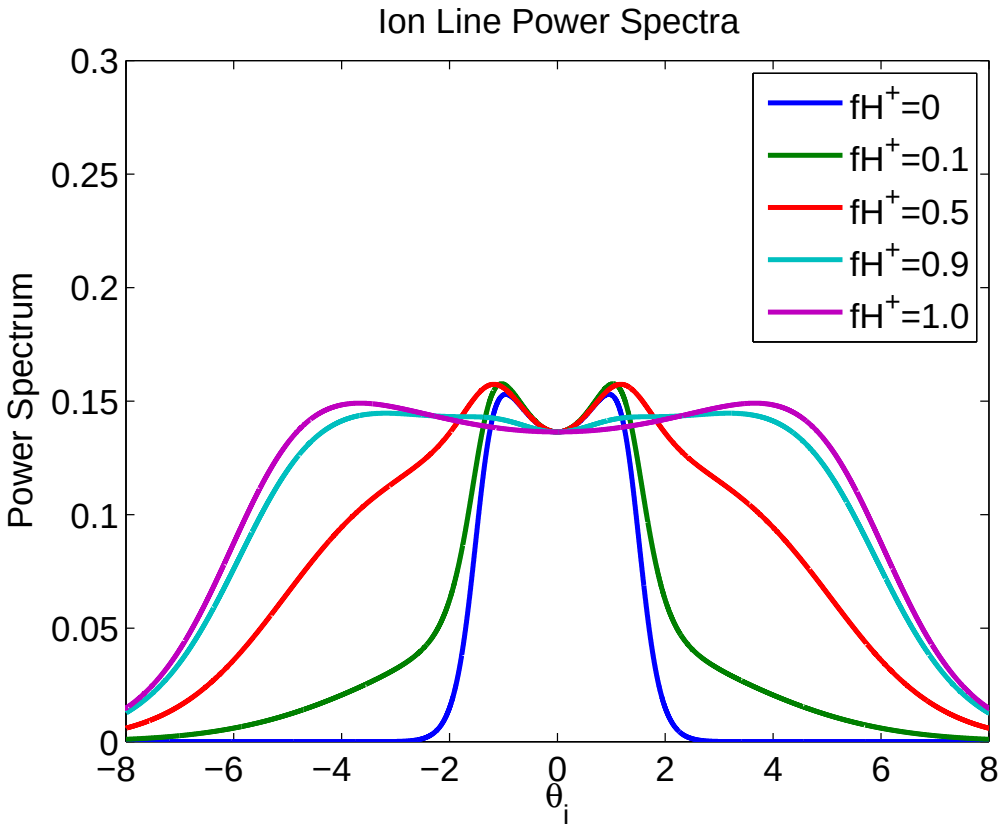

Figure 2.2: Normalized incoherent scatter spectra for various mixtures of O^+ and H^+. The vertical axis is in arbitrary units and the horizontal axis is the normalized frequency for O^+. The temperatures of all three species are assumed to be equal and all other parameters are the same as in Fig. 2.1

collisions have a minor effect at F-region altitudes and above. The presence of suprathermal electrons can greatly enhance the power in the plasma lines, but has a negligible effect on the ion line spectra [*Perkins and Salpeter*, 1965; *Yngvesson and Perkins*, 1968]. Recently, substantial efforts have been spent to incorporate magnetoionic effects and Coulomb collisions between the charged species into ISR theory because these effects have detectable effects on spectra obtained looking nearly perpendicular to **B** [*Sulzer and Gonzalez*, 1999; *Aponte et al.*, 2001; *Woodman*, 2004; *Kudeki and Milla*, 2006; *Milla and Kudeki*, 2006; *Kudeki and Milla*, 2011; *Milla and Kudeki*, 2011]. The Coulomb collision problem was solved analyt-

ically by *Woodman* [2004] for the case where $T_e = T_i$, but no analytic solution is known for the more general case. The approaches of *Sulzer and Gonzalez* [1999] for small magnetic aspect angles and *Milla and Kudeki* [2011] for aspect angles going all the way to perpendicular to **B** required running computer simulations of test particles traveling through plasmas and interpolating the tabulated results. The incorporation of Coulomb collision effects has corrected a historical problem with T_e/T_i measurements made at Jicamarca first noted by *Pingree* [1990].

2.1.2 Experimental considerations

Usually ISR signals are sufficiently broadband that they constitute overspread targets and thus conventional pulse-to-pulse radar analysis methods cannot be used. Notable exceptions are the ISR spectra perpendicular to **B** [*Woodman and Hagfors*, 1969; *Kudeki et al.*, 1999] and in the highly collisional D-region [for recent examples see *Chau and Kudeki*, 2006a; *Raizada et al.*, 2008; *Nicolls et al.*, 2010]. The spectra of overspread targets are difficult to measure because real radars transmit pulses of finite length and receive signals in a limited band. Let $s(t)$ be the transmitted waveform in baseband and $h(t)$ be the impulse response of the receiver. The baseband voltage received at sample time t_s is (in arbitrary units)

$$y(t_s) = \int dt d^3\mathbf{r} e^{i\mathbf{k}\cdot\mathbf{r}} s(t - 2r/c)\Delta N_e(\mathbf{r}, t - r/c)h^*(t_s - t) + n(t_s), \tag{2.28}$$

where $n(t_s)$ is white Gaussian noise with power N, $\Delta N_e(\mathbf{r}, t)$ is the deviation of the electron density from the background density at a given location and time, and the asterisk denotes complex conjugation [*Hysell et al.*, 2008]. These voltages will be zero mean Gaussian random variables, and thus all the information is contained in their second moments. The lag product between voltages received at times t_{s1}

and t_{s2} is

$$\begin{aligned}\langle y(t_{s2})y^*(t_{s1})\rangle =& N\delta(t_{s2}-t_{s1})+ \\ & \int dt_1 dt_2 d^3\mathbf{r} d^3\mathbf{r}' e^{i\mathbf{k}\cdot\mathbf{r}'}\langle \Delta N_e(\mathbf{r}+\mathbf{r}',t_2)\Delta N_e^*(\mathbf{r}+\mathbf{r}',t_2)\rangle \\ & s(t_2-2r/c)h^*(t_{s2}-t_2)s^*(t_1-2r/c)h(t_{s1}-t_1),\end{aligned} \tag{2.29}$$

where it is assumed that $\mathbf{r}'$ is a displacement from the center of the scattering volume which is small compared to the correlation length in the plasma [*Hysell et al.*, 2008]. With the definition $\tau = t_2 - t_1$ this expression can be written in a form which is similar to a convolution [*Hysell et al.*, 2008]

$$\langle y(t_{s2})y^*(t_{s1})\rangle = N\delta(t_{s2}-t_{s1}) + \int d\tau d^3\mathbf{r}\rho(\mathbf{k},\tau;\mathbf{r})W_{t_{s2},t_{s1}}(\tau,r), \tag{2.30}$$

where the plasma autocorrelation function is

$$\rho(\mathbf{k},\tau;\mathbf{r}) \equiv \int d^3\mathbf{r}'\langle \Delta N_e(\mathbf{r}+\mathbf{r}',t+\tau)\Delta N_e(\mathbf{r},t)\rangle \tag{2.31}$$

$$= \frac{1}{2\pi}\int \langle |n_e(\mathbf{k},\omega)|^2\rangle e^{i\omega\tau}\, d\omega, \tag{2.32}$$

and the radar ambiguity function is [*Lehtinen*, 1986; *Lehtinen et al.*, 1996; *Nygrén*, 1996]

$$W_{t_{s2},t_{s1}}(\tau,r) = \int dt\, s(t+\tau-2r/c)h^*(t_{s2}-t-\tau)s^*(t-2r/c)h(t_{s1}-t). \tag{2.33}$$

The ambiguity function is like an instrument response function characterizing a particular radar experiment.

The ambiguity function is entirely determined by the design of a radar experiment. If a radar experiment can be constructed such that the ambiguity function is nearly a delta function then each lag product corresponds to the plasma autocorrelation function at a single range and lag time. A classic radar experiment which nearly accomplishes this, and has been used extensively at Jicamarca, is the

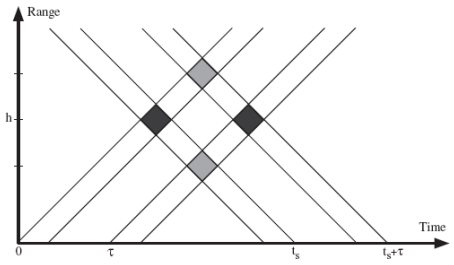

Figure 2.3: Range-Time diagram for a double pulse experiment (figure courtesy of D. T. Farley).

double pulse experiment [*Farley*, 1969b; *Pingree*, 1990]. The transmitted pulse is a pair of pulses each of length T spaced a time $\tau \geq T$ apart, i.e.

$$s(t) = u(t)u(T-t) + u(t-\tau)u(T-t+\tau), \tag{2.34}$$

where $u(t)$ is the unit step function. The receiver uses a filter matched to a single response, i.e.

$$h(t) = u(t)u(T-t). \tag{2.35}$$

The ambiguity function is localized between lags of $\tau - T$ and $\tau + T$ and a span of ranges which is only cT wide. Fig. 2.3 illustrates this experiment with a range-time diagram. The shaded regions indicate volumes which are responsible for the scattering sampled at times t_s and $t_s + \tau$. Only returns from the same altitude will be correlated, thus only the darkly shaded volumes contribute to the averaged lag product. The lightly shaded regions do not contribute to the expected values of the lag product, but they will contribute to the mean. This extra "self-clutter" can be completely eliminated in the double pulse experiment by using two orthogonal polarizations for the two pulses [*Farley*, 1969b].

The double pulse experiment only gives information about the autocorrelation function at a single lag. One must cycle through many different pulse spacings, τ, to construct the entire autocorrelation function [*Farley*, 1969b]. Thus double

pulse experiments take a long time to build up sufficient statistics. Many other ISR experiments have been designed with highly localized ambiguity functions which can build up statistics faster than the double pulse including multi-pulses [*Farley*, 1972; *Nygrén*, 1996], random codes [*Sulzer*, 1986], and alternating codes [*Lehtinen and Häggström*, 1987; *Lehtinen et al.*, 1997; *Hysell*, 2000].

The experiments described above are designed such that the plasma autocorrelation function at individual ranges can be constructed. Once this is accomplished these autocorrelation functions can be fit one at a time for the plasma parameters at each range. An alternative is to fit for the plasma parameters at all ranges and include the radar ambiguity function in the inverse problem [*Lehtinen*, 1986; *Holt et al.*, 1992; *Lehtinen et al.*, 1996; *Hysell et al.*, 2008]. In principle, this type of "full profile analysis" can be used with any type of radar experiment, not just those with carefully contrived pulsing schemes. Fitting for the parameters at all altitudes also allows for the inclusion of extra regularization which encourages solutions which are smoothly varying in altitude [*Hysell et al.*, 2008].

Radars typically record voltages in arbitrarily sized analog-to-digital converter counts. The received powers must be calibrated by comparing to an independent measurement of electron density. Faraday rotation measurements are the method of choice for calibration at Jicamarca [*Farley*, 1969a; *Pingree*, 1990]. Different polarizations travel at slightly different phase velocities in magnetized plasmas. Thus when the radar transmits and receives on two different orthogonal polarizations, the phase difference between the two channels gives a measurement of the absolute electron density integrated from the radar to the scattering volume and back.

2.1.3 Recent Jicamarca observations

The Jicamarca antenna is a phased array which can be configured to point in different directions by changing lengths of waveguides. Incoherent scatter experiments are divided into perpendicular experiments, where the beam is pointed exactly perpendicular to **B**, and oblique experiments, where the beam is pointed a few degrees away from perpendicular. The perpendicular experiments can be used to make highly accurate plasma drift measurements (1 m/s or better), but cannot be used to derive plasma temperatures or composition [*Woodman and Hagfors*, 1969; *Kudeki et al.*, 1999]. The oblique experiments can be used to derive plasma temperatures and composition, but cannot be used for drift measurements. As this thesis is concerned with temperature measurements, all the Jicamarca data shown will be from oblique experiments.

Fig. 2.4 shows data from an oblique experiment on April 19, 1999. The experiment was a standard double pulse experiment with calibration by Faraday rotation [*Pingree*, 1990]. The fitted parameters shown are electron density, electron temperature and ion temperature. No fitting for composition was attempted. The double pulse mode produces reliable temperature measurements throughout the F-region, but in the topside where the densities (and thus signal strengths) decrease fits are difficult to obtain.

One method for gaining topside data in an oblique experiment is to interleave long pulses coded with alternating codes with the double pulses [*Hysell*, 2000]. Fig. 2.5 shows data from such an experiment performed on December 4, 2002. The data below 450 km come from the double pulses and the data above 450 km come from the alternating coded pulses. The long pulses are unusable below 450 km because of ground clutter. The alternating coded data can be fitted for H^+

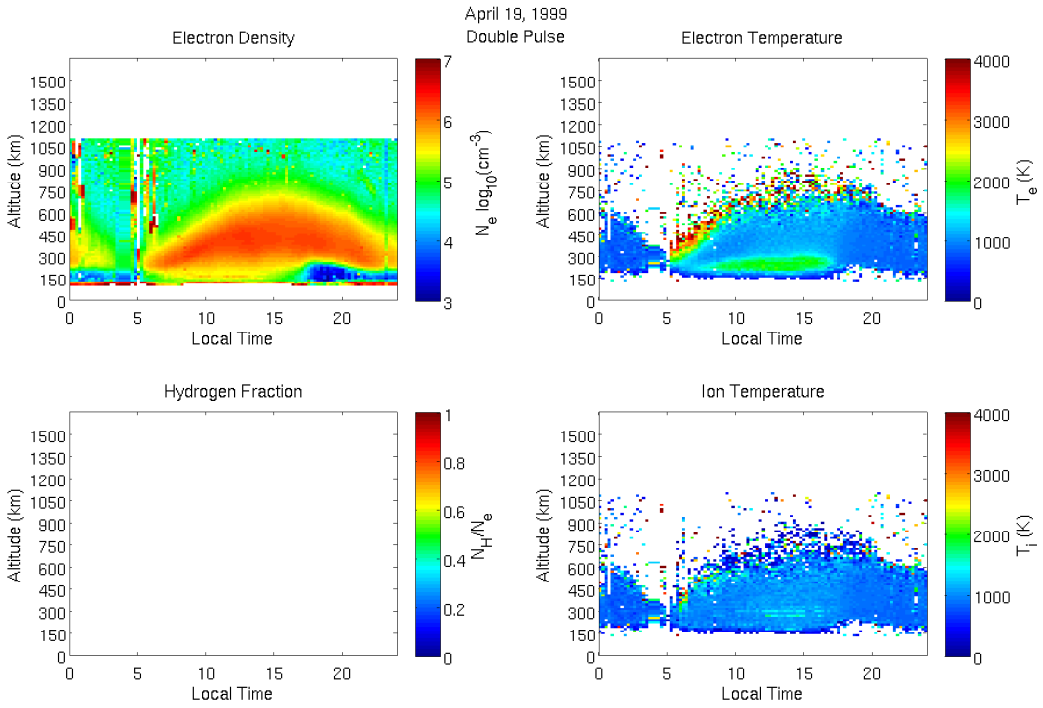

Figure 2.4: Fitted parameters from an oblique experiment on April 19, 1999 using double pulses. White regions indicate missing data.

fractions or T_e/T_i, but not both. The double pulse data is always fitted for T_e/T_i but never for H^+ fraction. In Fig. 2.5 the alternating code data is fit for T_e/T_i in the morning, assuming the H^+ fraction is zero, and fit for H^+ fraction during the rest of the day assuming $T_e/T_i = 1$. On this particular day an unphysical discontinuity is apparent in the T_i data when the fitting for T_e/T_i is disabled.

An even better method for extending oblique experiments into the topside is the mode described by *Hysell et al.* [2008], which shall henceforth be referred to as the full profile mode. Uncoded long pulses are interleaved with double pulses. The long pulse data is unusable below 450 km due to ground clutter, but above 450 km it is fit with a full profile algorithm. The long pulse has excellent sensitivity, but has an ambiguity function which extends over a wide span of ranges. A full

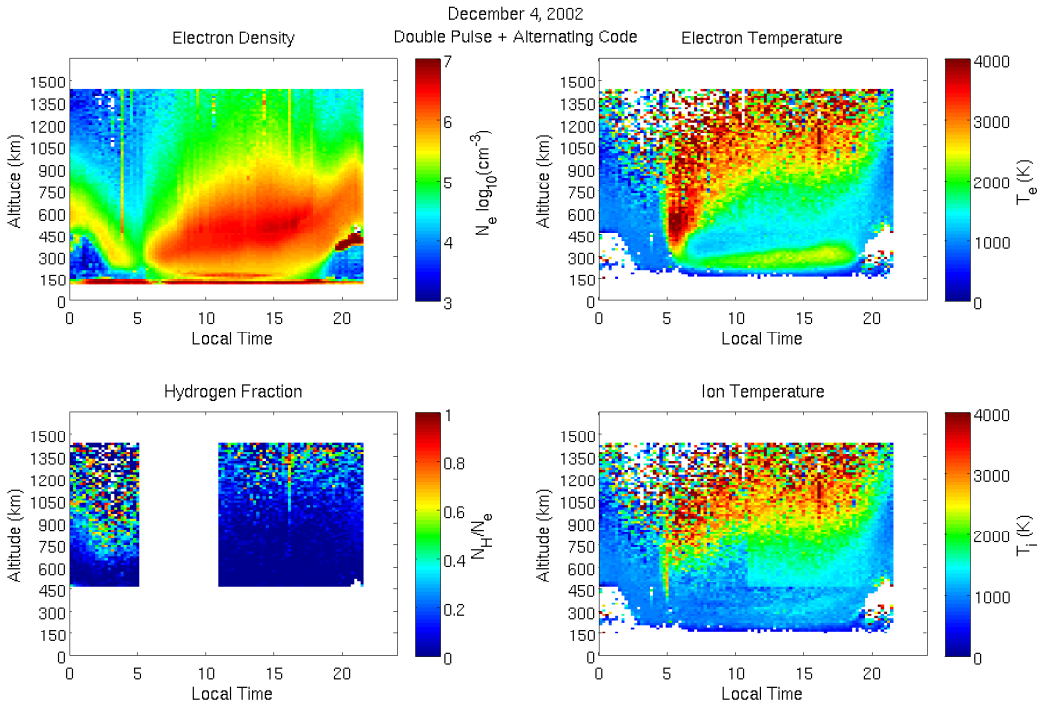

Figure 2.5: Fitted parameters from an oblique experiment on December 4, 2002. Data above 450 km use alternating codes while data below 450 km use double pulses. White regions indicate missing data.

profile analysis is necessary to properly cope with such an ambiguity function. Six additional regularization conditions are added to the cost function minimized in the inverse problem. The first three minimize the magnitudes of the second derivatives of the electron temperatures, ion temperatures, and H^+ fractions with altitude. Two others ensure $T_e > T_i$ and the H^+ and He^+ fractions added together do not exceed 1. The final regularization condition minimizes the He^+ fraction since it is expected to be small and it is the most difficult parameter to fit for, and thus the most sensitive to noise. The full profile mode is the only oblique experiment at Jicamarca which can be fit for He^+ fraction. Fig. 2.6 shows data from an oblique experiment on March 25, 2009 which uses this mode. The increased sensitivity of the long pulse combined and the extra smoothness conditions imposed by the

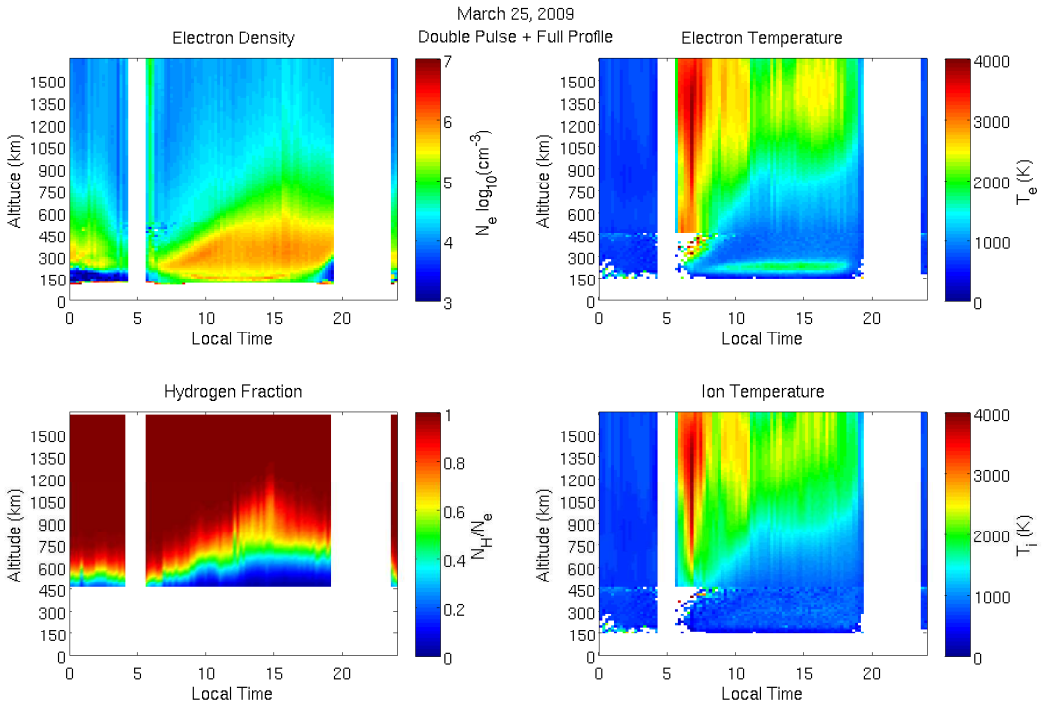

Figure 2.6: Fitted parameters from an oblique experiment on March 25, 2009. Data above 450 km use uncoded long pulses fit with a full profile algorithm while data below 450 km use double pulses. White regions indicate missing data.

additional regularization produce much cleaner temperature measurements at high altitudes. It is worth noting that the electron densities in Fig. 2.5 are much higher than those in Fig. 2.6 since 2002 was near solar max, whereas 2009 was in the deepest solar minimum since the dawn of the space age. Thus the full profile mode can produce cleaner data at altitudes extending up to ∼1500 km even with weaker signals. The low solar activity in 2009 is also why the transition from O^+ to H^+ is so low.

Ch. 6 shows additional examples of full profile data from Jicamarca. The topside temperatures exhibit large amounts of day-to-day variability. The primary purpose of this thesis is to compare these new topside temperature measurements

with current theories and to explore possible sources of this variability. This task demands an in depth reexamination of ionospheric energetics.

2.2 History and overview of ionospheric energetics

Schunk and Nagy [1978] provide a detailed review of the early history of ionospheric energetics. *Maris and Hulburt* [1928] were the first to suggest that the upper atmosphere should be hot ($\sim$ 1000 K) as a result of the absorption of ionizing radiation. Early estimates of upper atmospheric temperatures from the disappearance of meteor trails indicated temperatures of only 300-350 K [*Lindemann and Dobson*, 1923], but estimates based on the absorption of radio waves indicated much higher temperatures [*Martyn and Pulley*, 1936; *Appleton*, 1937]. The conclusion of a hot upper atmosphere was ultimately correct, even though the logic used in these early radio wave experiments was flawed [*Schunk and Nagy*, 1978].

The availability of V-2 rockets shortly after World War II made it possible to attempt *in situ* measurements of upper atmospheric parameters. The feasibility of flying a Langmuir probe on a rocket was first demonstrated by *Reifman and Dow* [1949], but technical issues rendered the data from this rocket, and many subsequent attempts, useless [*Schunk and Nagy*, 1978]. *Boggess et al.* [1959] made the first successful *in situ* electron temperatures measurements on a rocket launched in 1958. These measurements, and numerous other successful *in situ* measurements made shortly afterwards, indicated that the electron temperatures exceeded the ion and neutral temperatures [*Schunk and Nagy*, 1978]. This controversial result was confirmed in the 1960s after the advent of incoherent scatter radar [see *Evans*, 1969; *Farley*, 1991, for reviews of the early days of ISR]. ISR observations of en-

hanced plasma lines further confirmed the presence of suprathermal electrons in the ionosphere [*Yngvesson and Perkins*, 1968; *Evans and Gastman*, 1970].

Prior to the 1960s the dominant opinion was that all of the components of the upper atmosphere should be in thermodynamic equilibrium, i.e. $T_e = T_i = T_n$ [*Schunk and Nagy*, 1978]. In a largely ignored paper, *Drukarev* [1946] suggested that the plasma and the neutrals should have different temperatures and derived an expression for the temperature difference based on the average photoelectron energies. A few others began to speculate about the possibility of a lack of thermodynamic equilibrium in the 1950s [e.g. *Mitra*, 1952; *Rawer*, 1957]. In the early 1960s, *Hanson and Johnson* [1961], *Hanson* [1963], and *Dalgarno et al.* [1963] calculated T_e, T_i, and T_n theoretically in a local approximation where the heating rates balanced the cooling rates. This studies corroborated the experimental picture which was beginning to emerge at the same time; the electron temperatures substantially exceed the ion temperatures, especially in the lower F-region.

Conceptually Fig. 2.7 summarizes the modern picture of the important pathways through which energy flows in the low latitude ionosphere (c.f. Fig.2 in *Schunk and Nagy* [1978] and Fig. 9.1 in *Schunk and Nagy* [2009]). Chapter 9 of *Schunk and Nagy* [2009] gives a basic introduction to these various processes. The primary source of input energy is solar extreme ultraviolet (EUV) and soft X-ray radiation. When these photons ionize the neutral atmospheric species nearly all of the excess energy is given to the ejected photoelectron. These photoelectrons lose their energy through a variety of different types of collisions. Collisions with thermal electrons will efficiently heat the ambient electron gas. Elastic collisions with ions and neutrals, however, will not transfer appreciable amounts of energy due to the extreme mass difference. The ion and neutral gases are heated by

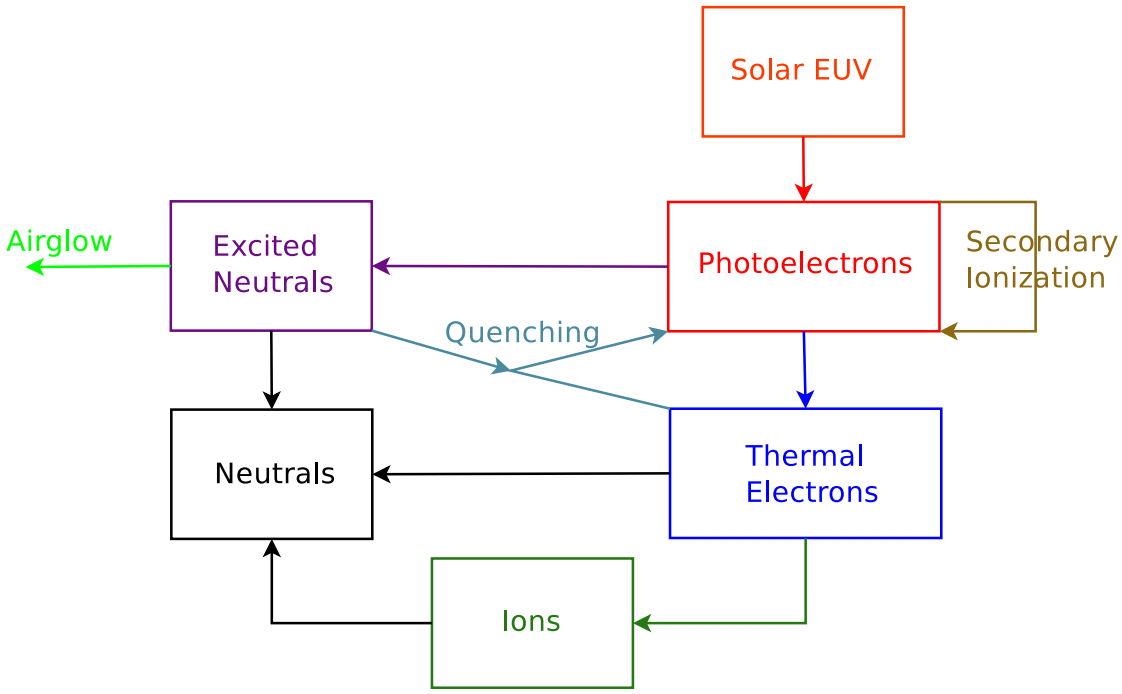

Figure 2.7: Conceptual diagram of major pathways of energy flow in the low latitude ionosphere.

collisions with the ambient electron gas. Electron-ion collisions do not transfer energy efficiently due to the disparate mass ratios, but electron-neutral collisions can transfer energy well through inelastic collision processes. The ion and neutral gases are strongly coupled to each other since they have similar masses. Photoelectrons with sufficiently high energies can produce secondary electrons through impact ionization of neutrals. These secondary electrons are usually suprathermal and thus behave like a part of the photoelectron spectrum. Inelastic collisions between suprathermal electrons and neutrals can also generated excited neutral species. Excited neutrals can also be produced as a result of direct photoabsorption or certain chemical reactions. The excited neutrals can relax by emitting photons in the visible spectrum, thus producing airglow. They can also relax through collisional quenching whereby the excess energy ends up as heat in the neutral gas. A few excited species can also be quenched by collisions with electrons. An important

example is N(^{2}D) which undergoes the reaction [*Richards*, 1986]

$$\mathrm{N}(^2\mathrm{D}) + e \rightarrow \mathrm{N}(^4\mathrm{S}) + e + 2.4 \text{ eV}. \tag{2.36}$$

This process will promote thermal electrons back up into the suprathermal population (see Sec. 4.2.5 for further details).

Variations of Fig. 2.7 have been understood for a long time, but the details of the individual pathways are complicated. Substantial efforts were exerted in the 1960s to compare *in situ* temperatures measurements, ISR temperatures measurements, and theoretical temperatures estimates to each other. The *in situ* measurements systematically exceeded the ISR measurements; this effect was ultimately attributed to surface impurity effects associated with Langmuir probes [*Schunk and Nagy*, 1978]. The theoretical models in use at the time all produced significantly different results because of the use of different cross sections and cooling rates. For example, *Dalgarno and Degges* [1968] showed that the addition of electron cooling by the excitations of the fine structures of atomic oxygen significantly lowered electron temperatures in the lower F-region and brought the theoretical values into closer agreement with measurements from Millstone Hill.

Fig. 2.7 also ignores transport. *Geisler and Bowhill* [1965a, b] and *da Rosa* [1966] were the first to add thermal conduction along the field lines to their theoretical calculations. Thermal conduction is important for explaining how the electrons temperatures in the upper F-region become elevated at mid-latitudes [*Geisler and Bowhill*, 1965a]. Thermal conduction down from the plasmasphere is also crucial to explaining raised electron temperatures at night at mid-latitudes [*Geisler and Bowhill*, 1965b]. *Nisbet* [1968] created the first detailed theoretical description of photoelectron transport. It was shown that some photoelectrons could escape from the ionosphere completely and travel all the way to conjugate

ionosphere. This provided an explanation for temperatures enhancements sometimes observed before dawn by ISRs [*Carlson*, 1966; *Carru et al.*, 1967; *Evans and Gastman*, 1970]. After *Nisbet* [1968] many other theoretical descriptions of photoelectron transport were created. Sec. 2.4 reviews the evolution of photoelectron transport models from *Nisbet* [1968] to the present in detail.

The first examinations of electron and ion temperature measurements obtained from the Jicamarca ISR were performed by *Hanson and Cohen* [1968] and *McClure* [1969]. *McClure* [1969] concluded that altitudinal and time of day variations in the Jicamarca electron and ion temperature measurements between 200 and 500 km were consistent with local theories like those developed by *Hanson* [1963] and *Dalgarno et al.* [1963]. During the day $T_e/T_i > 1$ at altitudes below 300-320 km and an isothermal region where $T_e/T_i \approx 1$ and the temperatures are constant with altitude appears between 300-500 km [*McClure*, 1969]. The use of local theories at altitudes as high as 500 km is only possible at Jicamarca because the horizontal magnetic field lines inhibit vertical photoelectron transport and vertical thermal diffusion [*Hanson and Cohen*, 1968; *McClure*, 1969]. Above 500 km both T_e and T_i begin to rapidly increase with altitude and this feature cannot reproduced with a local theory [*McClure*, 1969]. *Bailey et al.* [1975] created a steady state energy equation solver which used the *Swartz et al.* [1975] photoelectron transport model to derive nonlocal heating rates. The calculations performed by *Bailey et al.* [1975] for many field lines at a single time during the middle of the day (when a steady state assumption is appropriate for the energy equation) confirmed that the rapid temperature increase above 500 km routinely observed at Jicamarca was indeed due to nonlocal heating from photoelectrons.

2.3 Treatments of energy balance in modern ionospheric models

Many modern ionospheric models make major simplifications of processes involving photoelectrons because of the computational complexity of photoelectron transport routines. Two notable exceptions are FLIP [*Richards and Torr*, 1996] and SUPIM [*Bailey and Balan*, 1996], which both use the same photoelectron transport model (see Sec. 2.4.5). Photoelectrons are coupled to the ion continuity equations through the secondary production rates and to the electron energy equation through the electron heating rates. The latter connection can be completely removed by using an empirical temperature model instead of solving an energy equation. For example, PBMOD [*Retterer*, 2005] uses the model of *Brace and Theis* [1981] and IPM [*Schunk*, 2002] uses the model of *Titheridge* [1998] to set the temperatures. The original CTIP model [*Millward et al.*, 1996] had an energy equation solver, but this has been abandoned in the descendant models CTIPe [*Fuller-Rowell et al.*, 2002], GIP and IDEA [*Fuller-Rowell et al.*, 2008], in favor of the empirical *Titheridge* [1998] model.

Many models, including SAMI2, ignore secondary production entirely. A simple way to include secondaries is to multiply the primary photoproduction rates by $(1+p_e/p_i)$, where the secondary to primary production ratios, p_e/p_i, are computed using a detailed photoelectron transport model and tabulated as a function of photon wavelength and possibly optical depth [e.g. *Richards and Torr*, 1988; *Solomon and Qian*, 2005]. This formulation assumes secondary electrons are created by photoelectrons produced locally. At low altitudes these ratios are approximately constant, but at high altitude photoelectron transport effects become important. The p_e/p_i values can vary by as much as a factor of 2 above 250 km depending on

ionospheric conditions and the presence or absence of conjugate electrons [*Richards and Torr*, 1988]. The *Solomon and Qian* [2005] method, which is now a standard part of TIE-GCM [*Roble*, 1996], uses a single p_e/p_i value for each ion species and each wavelength computed at an optical depth of unity and ignores all variation with optical depth and/or altitude.

Electron heating rates can also be treated in a similar local empirical fashion. The TIGCM [*Roble et al.*, 1987, 1988], its descendants TIE-GCM and TIME-GCM [*Roble*, 1996], and GTIM [*Ridley et al.*, 2006] assume the electron heating rate equals the total local photoproduction rate times a photoelectron heating efficiency factor which is a function of the local electron and neutral densities. The concept of a photoelectron heating efficiency factor was originally introduced by *Hanson* [1963] and its altitude dependence was first investigated using Jicamarca temperature data by *Hanson and Cohen* [1968]. *Swartz and Nisbet* [1972] and more recently *Smithtro and Solomon* [2008] provide empirical expressions for the efficiency factor based on detailed photoelectron calculations. GAIT [*Smithtro and Sojka*, 2005] uses a similar local approximation for the heating rates, but instead of using an empirical efficiency factor it calculates the heating rates at low altitudes using a local equilibrium photoelectron model [*Richards and Torr*, 1983] and ignores electron heating at high altitudes.

None of the above approaches can incorporate the effects of photoelectron transport along the field lines. The electron heating model used in the original CTIP [*Millward et al.*, 1996], as well as the original SAMI2 [*Huba et al.*, 2000a] and its descendant SAMI3 [*Huba et al.*, 2009] attempts to account for photoelectron transport empirically. The *Swartz and Nisbet* [1972] efficiency factor is used below 300

km, and the heating rate above 300 km is set to

$$Q_{phe}(\ell) = \frac{N_e(\ell)B(\ell)}{N_e\left(\ell_{300N}\right)B\left(\ell_{300N}\right)} Q_{phe}\left(\ell_{300N}\right) \exp\left(-C_{qe}\int_{\ell}^{\ell_{300N}} N_e(\ell')d\ell'\right) \quad (2.37)$$
$$+ \frac{N_e(\ell)B(\ell)}{N_e\left(\ell_{300S}\right)B\left(\ell_{300S}\right)} Q_{phe}\left(\ell_{300S}\right) \exp\left(-C_{qe}\int_{\ell_{300S}}^{\ell} N_e(\ell')d\ell'\right),$$

where B is the magnetic field strength, and ℓ_{300N} and ℓ_{300S} are the points where the field line crosses 300 km in the northern and southern hemispheres respectively and the integrals are taken along the field line. The attenuation factor, C_{qe}, is a parameter which must be set a priori. The notion that electron heating rates decayed exponentially with the field line integrated electron density was first proposed by *Nisbet* [1968]. Using a modified diffusion photoelectron transport model and electron density profiles measured from Arecibo, *Nisbet* [1968] estimated values C_{qe} ranging from 6.95×10^{-14} to 9.58×10^{-14} cm^2 (see Table 2 of that paper). Ch. 3 of this thesis shows that changes to the free parameter, C_{qe}, have a large effect on the electron temperatures produced by SAMI2 at low latitudes and no one value produces satisfying agreement with Jicamarca data for all local times and altitudes.

2.4 History of theory and modeling of photoelectron transport

The problem of photoelectron transport and the closely related problem of energetic particle precipitation at high latitudes are two of the oldest in aeronomy. These problems are both special cases of electrons traveling through materials, a problem which has been studied in laboratory settings since the late 1930s [see *Spencer*, 1955, for a review]. A major application for this early research was char-

acterizing the harmful effects of β radiation on biological tissues [*Spencer*, 1955]. As will be shown below, the photoelectron transport equation is a type of radiative transfer equation. Similar equations appear in studies of the scattering of neutrons in nuclear reactors and the scattering of light in stellar and planetary atmospheres [e.g. *Chandrasekhar*, 1950]. Photoelectron models can be broadly classified by considering the treatment of the total electron distribution function, the treatment of transport, and the treatment of collisions.

A rigorous approach to a plasma containing suprathermal electrons is to directly solve the nonlinear Boltzmann-Fokker-Planck equation (i.e. a kinetic equation which uses a the Boltzmann collision integral for electron-neutral collisions and a Fokker-Planck operator for electron-electron collisions) for the total electron population [e.g. *Ashihara and Takayanagi*, 1974; *Jasperse*, 1976, 1977]. The computational complexity of this method makes it only practical when transport can be neglected. The more common approach is to divide the total electron distribution function into a thermal portion, which is presumed to be Maxwellian, and a suprathermal portion which is presumed to have a much smaller total density (see *Krinberg* [1973], *Hoegy* [1984], and Ch. 4 of this thesis for a more detailed discussion of this division). As is shown in Sec. 4.3, under these assumptions the nonlinear terms in the Boltzmann-Fokker-Planck equation for the suprathermal portion of the distribution function can be neglected, resulting in a tractable linear equation. Every other model mentioned in this thesis, including SAMI2-PE, divides the electron distribution function. With this division one can derive a simplified form of the Boltzmann-Fokker-Planck equation for the suprathermal populations [e.g. *Mantas*, 1975; *Strickland et al.*, 1976]. Ch. 4 derives the form of the simplified

Boltzmann-Fokker-Planck equation used in SAMI2-PE:

$$\mu\frac{\partial\Phi}{\partial\ell} - \delta B\frac{\partial}{\partial\mu}\left[\frac{1-\mu^2}{2}\Phi\right] = \mu\delta B\Phi + \hat{q} + \frac{\partial}{\partial\mathcal{E}}\left[L(\mathcal{E})\Phi\right] + D(\mathcal{E})\frac{\partial}{\partial\mu}\left[(1-\mu^2)\frac{\partial\Phi}{\partial\mu}\right] \tag{2.38}$$
$$- \sum_n(\bar{\sigma}_{an} + \bar{\sigma}_{en})N_n\Phi + \sum_n \bar{\sigma}_{en}N_n\frac{1}{2}\int_{-1}^{1} d\mu'\Phi(\ell,\mathcal{E},\mu')$$

where Φ is the photoelectron flux, ℓ is a spatial coordinate along the magnetic field line, μ is the cosine of the pitch angle, $\mathcal{E}$ is the kinetic energy of a photoelectron, $\delta B = \frac{1}{B}\frac{\partial B}{\partial\ell}$, $L(\mathcal{E})$ is the energy loss rate due to Coulomb collisions, $D(\mathcal{E})$ is the pitch angle diffusion rate due to Coulomb collisions, $\bar{\sigma}_{a(e)n}$ is the total inelastic (elastic) cross section for collisions with neutrals, and $\hat{q}$ is the total photoelectron production rate, including cascade production from higher energies and secondary production (see Ch. 4 for details).

Treatments of transport in suprathermal electron transport models can be divided into five broad classes: local approximations, renormalization of laboratory data, Monte Carlo techniques, transport techniques for the mid- and high-latitude ionosphere, and transport techniques for coupled ionosphere-plasmasphere models. SAMI2-PE belongs in the fifth class.

2.4.1 Local approximations

In the local approximation the transport of photoelectrons along the magnetic field lines is completely neglected. This assumption is justified if the distance a photoelectron travels away from the point where it is created before thermalizing is small compared to the length scales of the plasma and neutral densities. This approximation is better for lower energy electrons and for lower altitudes

where photoelectron-neutral collisions are frequent. A typical guideline is that local approximations can be used below ∼250 km [e.g. *Swartz et al.*, 1975]. If the photoelectron undergo so many collisions that transport can be neglected they will also be isotropically distributed, meaning the kinetic equations become a function of only speed, or equivalently energy [*Ashihara and Takayanagi*, 1974].

Despite the apparent simplicity of the local approximation, codes which use it can differ substantially depending on their treatments of collisions and the distribution function. *Jasperse* [1976, 1977] modeled collisions as continuous energy loss processes and iteratively solved nonlinear equations for the entire electron distribution function. *Ashihara and Takayanagi* [1974] further allowed for discrete loss processes associated with inelastic collisions. The most common approach is to divide the distribution function, use a linearized collision operator, but still allow for discrete energy loss processes [see *Swartz*, 1985, and references therein]. *Richards and Torr* [1983] introduced the concept of average energy losses to considerably simplify computations involving discrete loss processes. For calculations involving energy deposited by auroral secondary electrons, *Rees* [1989] says continuous loss approximations can be used if the primary electrons have energies of several hundreds of eV and the secondaries have energies less than 100 eV, but collisions must be treated as discrete loss processes if the primaries and secondaries are not well separated in energy. Sec. 4.3 derives an appropriate linearized collision operator. The production term $\hat{q}$ in Eq. 2.38 not only contains direct photoproduction, but also secondary production from ionizing collisions and cascade production from higher energies. If superelastic collisions which cause photoelectrons to gain energy are ignored then the secondary production and cascade production at a given energy level can be calculated if the flux at all higher energies is known. Thus the steady state equation can be solved one energy bin at a time working downwards in

energy. When using a discrete energy grid care must be taken to conserve energy when considering discrete energy losses. *Swartz* [1985] introduced an algorithm which will conserve energy perfectly on any energy grid (see Sec. 5.2 for details). This algorithm permits the use of non-uniformly spaced energy grids, which can greatly decrease the number of bins needed to adequately cover a given energy range.

2.4.2 Renormalization of laboratory data

For auroral calculations a common approach is to use empirical expressions derived from laboratory data instead of trying to compute the energetic electron distributions from first principles [see *Rees*, 1989, Sec. 3.3]. These type of calculations are only reasonable for high energy electrons [*Lummerzheim and Lilensten*, 1994], and thus have never been applied to photoelectrons. *Grün* [1957] and later *Barrett and Hays* [1976] performed experiments where monoenergetic beams of electrons with energies in the keV range were fired into chambers filled with air or pure N_2 gas. The resulting 391.4 nm emissions were recorded as a proxy for the ionization rates. Photons at this wavelength result from the following sequence of interactions [*Rees*, 1989]

$$N_2 + e^* \rightarrow N_2^+(B^2\Sigma) + e^* + e \tag{2.39}$$

$$N_2^+(B^2\Sigma, v' = 0) \rightarrow N_2^+(X^2\Sigma, v'' = 0) + h\nu(391.4 \text{ nm}). \tag{2.40}$$

This particular optical emission is used in laboratory experiments because its intensity is nearly independent of the primary electron energy, and thus it is a reliable measurement of the nitrogen ionization rate [see *Barrett and Hays*, 1976, and references therein]. The proportionality constant relating the optical emissions to

the energy deposition rate can be determined via conservation of energy (i.e. the integrated energy deposition rate must equal the power in the incident electron beam). An empirical expression for the energy deposition rate in eVcm^{-3}s^{-1} is [*Rees*, 1989]

$$\epsilon(z, E_p) = 10^{-3} F E_p \Lambda \left[\frac{s(z)}{R(E_p)}\right] \frac{\rho(z)}{R(E_p)} \tag{2.41}$$

where F is the incident electron flux in cm^{-2}s^{-1}, E_p is the energy of the electron beam in keV, ρ is the mass density of the gas in g cm^{-3}, $s(z)$ is the scattering depth in g cm^{-2} and $R(E_p)$ is the effective range in g cm^{-2}. The scattering depth is related to the mass density by

$$s(z) = \int_z^\infty \rho(z)\, dz, \tag{2.42}$$

and for energies in the range 0.2 keV $< E_p <$ 50 keV the effective range is approximately [*Rees*, 1989]

$$R(E_p) = 4.30 \times 10^{-7} + 5.36 \times 10^{-6} E_p^{1.67} \text{ g cm}^{-2}. \tag{2.43}$$

The empirical function Λ defines the distribution of the energy in space. It is normalized such that [*Grün*, 1957]

$$\int_{-\infty}^{\infty} \Lambda\left(\frac{s}{R}\right)\, d(s/R) = 1, \tag{2.44}$$

and must be determined from experiment for different energies. For keV electrons most of the energy deposition is in the form of secondary production, so the production rates are approximately [*Rees*, 1989]

$$q(z, E_p) = \frac{\epsilon(z, E_p)}{\Delta\epsilon_{ion}}, \tag{2.45}$$

where $\Delta\epsilon_{ion}$ is the average energy lost during an ionization in eV ($\sim$37 eV for N_2 and $\sim$33 eV for O_2) [*Rees*, 1989].

2.4.3 Monte Carlo techniques

Monte Carlo photoelectron models divide the total photoelectron population and use Monte Carlo techniques to compute the distribution function of the suprathermal portion. Random number generators are used to create a sample population of suprathermal electrons. The motions of these electrons are then computed using the equations of motion and randomly generated deflections to model collisions. The suprathermal electron distribution function as a function of position, energy, and pitch-angle is then generated by creating histograms of the sample population.

The first Monte Carlo code for photoelectron transport was created by *Cicerone and Bowhill* [1970, 1971]. Additionally *Berger et al.* [1970, 1974] created a Monte Carlo code for auroral electrons and *Porter and Green* [1975] created a Monte Carlo code for low energy auroral protons. Since then numerous other Monte Carlo codes have been created for photoelectrons, auroral electrons, auroral protons, and auroral atomic hydrogen [*Onda et al.*, 1992; *Kozelov and Ivanov*, 1992, 1994; *Kozelov*, 1993; *Synnes et al.*, 1998; *Solomon*, 1993, 2001]. *Solomon* [2001] also presented a hybrid model which uses Monte Carlo techniques for auroral protons and atomic hydrogen, but a two-stream transport technique for the resulting secondary electrons.

A great advantage of Monte Carlo codes is that the binning into discrete energy and pitch angle bins is done after the transport calculations for each electron have been performed when the histograms are formed. The individual electrons can take on any energy and pitch angle, experience angular deflections of any size, and lose energy through inelastic collisions in discrete steps of any size. Thus collisions in Monte Carlo codes can be described with very few approximations. However, Monte Carlo codes need integrable, analytic fit functions for quantities

like scattering phase angles and secondary energy distributions [*Solomon*, 2001]. The disadvantage of Monte Carlo codes is that a large number of particles are needed to generate sufficient statistics in the histograms, meaning these codes can be very computationally expensive. For this reason Monte Carlo techniques are often considered "brute force" methods which are used to validate other methods [*Solomon*, 2001].

2.4.4 Transport techniques for the mid- and high-latitude ionosphere

In the mid- and high-latitude ionosphere the magnetic field lines are approximately straight, meaning $\delta B = 0$. At ionospheric heights the pitch-angle diffusion due to Coulomb collisions can be neglected compared to elastic collisions with neutrals. Furthermore, when working on a discrete energy grid the continuous loss of energy to the thermal electrons can be treated like a discrete loss process having an effective cross section of σ_{th} (see Ch. 5 for details). These approximations result in a simpler photoelectron transport equation which is in the form of a radiative transfer equation:

$$\mu \frac{\partial \Phi}{\partial \ell} = \hat{q} - \sigma_{th} N_e \Phi - \sum_n (\bar{\sigma}_{an} + \bar{\sigma}_{en}) N_n \Phi + \sum_n \bar{\sigma}_{en} N_n \frac{1}{2} \int_{-1}^{1} d\mu' \Phi(\ell, \mathcal{E}, \mu') \quad (2.46)$$

The methods of *Chandrasekhar* [1950] developed for other radiative transfer problems can be used to make this integro-differential equation tractable. This equation must be solved one energy bin at a time, in descending order, and an energy reapportionment scheme like the *Swartz* [1985] algorithm must be used account for the cascade and secondary production.

A commonly used radiative transfer idea is the finite ordinate approximation

[*Chandrasekhar*, 1950]. The integral can be replaced with a sum using a quadrature rule

$$\int_{-1}^{1} \Phi(\mu')d\mu' \approx \sum_k g_k \Phi(\mu_k), \tag{2.47}$$

where the ordinates μ_k are a discrete set of size $2n$ and the g_k are an associated set of weights. The weights must satisfy $\sum_k g_k = 2$. *Chandrasekhar* [1950] recommends using Gauss-Legendre quadrature rules since these will be the most accurate for polynomial functions. The finite ordinate approximation transforms Eq. 2.46 into a set of $2n$ coupled ODEs where the $2n$ functions being differentiated are the flux evaluated at each of the ordinates. The finite ordinate approximation has been applied to photoelectrons by *Stolarski* [1972] and *Stamnes* [1977] and to auroral electrons by *Stamnes* [1980] and *Lummerzheim et al.* [1989].

An even simpler idea is the two-stream approximation, which was first applied to photoelectrons by *Banks and Nagy* [1970] and *Nagy and Banks* [1970] and later to auroral electrons by *Banks et al.* [1974]. Let the upwards and downward fluxes be defined by integrating over the upper and lower hemispheres, i.e.

$$\Phi^+(\ell, \mathcal{E}) = \pi \int_0^1 \Phi(\ell, \mathcal{E}, \mu)d\mu \tag{2.48}$$

$$\Phi^-(\ell, \mathcal{E}) = \pi \int_{-1}^0 \Phi(\ell, \mathcal{E}, \mu)d\mu. \tag{2.49}$$

Eq. 2.46 can then be written as a coupled pair of ordinary differential equations (ODEs)

$$\langle\mu\rangle^+ \frac{d\Phi^+}{d\ell} = \hat{q}^+ - \sigma_{th} N_e \Phi^+ - \sum_n (\bar{\sigma}_{an} + \bar{\sigma}_{en}) N_n \Phi^+ + \sum_n \bar{\sigma}_{en} N_n \frac{1}{2}\left(\Phi^+ + \Phi^-\right) \tag{2.50}$$

$$-\langle\mu\rangle^- \frac{d\Phi^-}{d\ell} = \hat{q}^- - \sigma_{th} N_e \Phi^- - \sum_n (\bar{\sigma}_{an} + \bar{\sigma}_{en}) N_n \Phi^- + \sum_n \bar{\sigma}_{en} N_n \frac{1}{2}\left(\Phi^+ + \Phi^-\right), \tag{2.51}$$

where the upwards and downwards productions are defined as

$$\hat{q}^{+}(\ell,\mathcal{E}) = \pi \int_{0}^{1} \hat{q}(\ell,\mathcal{E},\mu)d\mu \tag{2.52}$$

$$\hat{q}^{-}(\ell,\mathcal{E}) = \pi \int_{-1}^{0} \hat{q}(\ell,\mathcal{E},\mu)d\mu, \tag{2.53}$$

and the mean pitch angles are

$$\langle\mu\rangle^{+} = \frac{\int_{0}^{1} \mu\Phi(\ell,\mathcal{E},\mu)\,d\mu}{\int_{0}^{1} \Phi(\ell,\mathcal{E},\mu)\,d\mu} \tag{2.54}$$

$$\langle\mu\rangle^{-} = -\frac{\int_{-1}^{0} \mu\Phi(\ell,\mathcal{E},\mu)\,d\mu}{\int_{-1}^{0} \Phi(\ell,\mathcal{E},\mu)\,d\mu}. \tag{2.55}$$

This coupled pair of first order ODEs requires two boundary conditions. For photoelectrons in the ionosphere a simple choice is to set $\Phi^{+} = 0$ at the lowest altitudes and $\Phi^{-} = 0$ at the top of the atmosphere [*Banks and Nagy*, 1970]. In general Φ^{+} will not be 0 at the top boundary because photoelectrons can escape the ionosphere; this escape flux is determined as part of the solution to the two-stream equations [*Banks and Nagy*, 1970]. For auroral calculations Φ^{-} at the top of the atmosphere must be known a priori [*Banks et al.*, 1974]. Even if the auroral calculations are being conducted in darkness (i.e. without photoproduction) there will still be a non-zero escape flux because some fraction of the incident auroral electrons will backscatter out of the atmosphere [*Banks et al.*, 1974].

In the two-stream approximation the complete pitch-angle distribution is not computed, so these mean pitch angles must be specified a priori. In general $\langle\mu\rangle^{+}$ and $\langle\mu\rangle^{-}$ will not necessarily be equal and will be functions of position and energy. *Banks and Nagy* [1970], and most other two stream codes, simply assume $\langle\mu\rangle^{+}$ and $\langle\mu\rangle^{-}$ are equal and constant. For isotropic distributions $\langle\mu\rangle = 0.5$. The original work by *Banks and Nagy* [1970] used 0.375. The choice of $\langle\mu\rangle = 1/\sqrt{3} \approx 0.577$ will make the two-stream equations identical to a finite ordinate approximation using $n = 1$ and Gauss-Legendre quadrature, however the meanings of the two sets of

equations are subtly different. When using the finite ordinate approximation the functions are the fluxes evaluated at specific pitch-angles whereas in the two-stream approximation the functions are the integrals of the fluxes over specific ranges of pitch angles. Despite being the location of the ordinate for a 2-point Gaussian quadrature rule, an effective $\langle\mu\rangle$ of 0.577 is usually considered to be too large to be the average pitch angle [*Cicerone et al.*, 1973]. Lack of knowledge of $\langle\mu\rangle$ is a substantial source of uncertainty in two-stream models. Varying $\langle\mu\rangle$ in the *Banks and Nagy* [1970] code between 0.375 and 0.577 results in changes in the computed fluxes of as much as 50% [*Cicerone et al.*, 1973].

The above version of the two stream equation assumes isotropic collisions, however these equations are easily generalized to the case of anisotropic collisions by introducing backscatter probabilities, β_{en} [*Banks and Nagy*, 1970; *Stamnes*, 1981].

$$\langle\mu\rangle^{+}\frac{d\Phi^{+}}{d\ell} = \hat{q}^{+} - \sigma_{th}N_e\Phi^{+} - \sum_n(\bar{\sigma}_{an} + (1-\beta_{en})\bar{\sigma}_{en})N_n\Phi^{+} + \sum_n \bar{\sigma}_{en}N_n\beta_{en}\Phi^{-} \tag{2.56}$$

$$-\langle\mu\rangle^{-}\frac{d\Phi^{-}}{d\ell} = \hat{q}^{-} - \sigma_{th}N_e\Phi^{-} - \sum_n(\bar{\sigma}_{an} + (1-\beta_{en})\bar{\sigma}_{en})N_n\Phi^{-} + \sum_n \bar{\sigma}_{en}N_n\beta_{en}\Phi^{+}, \tag{2.57}$$

Stamnes [1981] has compared auroral calculations using these two-stream equations with $\langle\mu\rangle = 0.5$ and using the multi-stream finite ordinate approach of *Stamnes* [1980]. The two-stream results provide reasonable agreement with the multi-stream results as long as the backscatter probabilities are computed appropriately; the disagreements between the two models were most pronounced at the lowest altitudes (largest collision depths) [*Stamnes*, 1981].

Analysis of the average pitch angles produced by Monte Carlo codes shows the $\langle\mu\rangle$ usually will vary with position, especially at the highest altitudes. Particles

which are traveling nearly parallel to **B** will make fewer collisions on their journey up the field line and thus have a greater probability of escaping. As a result the mean pitch angle cosine of the upwards flux, $\langle\mu\rangle^+$, will be noticeably closer to 1 at high altitudes than at intermediate or low altitudes [*Cicerone et al.*, 1973]. For example, the effective $\langle\mu\rangle$ produced by the *Cicerone and Bowhill* [1971] Monte Carlo code at 500 km under the conditions tested by [*Cicerone et al.*, 1973] is 0.7. This effect is one of the primary reasons that the *Cicerone and Bowhill* [1971] Monte Carlo code produces different results from the *Banks and Nagy* [1970] two-stream code under identical conditions [*Cicerone et al.*, 1973].

The modified diffusion approach [*Nisbet*, 1968; *Swartz and Nisbet*, 1973] is an alternative to the two-stream equations which partially resolves this issue by explicitly incorporating the notion of an escape flux. Let the density of energetic electrons be defined as

$$n_E \equiv \frac{2\pi}{v} \int_{-1}^{1} \Phi \, d\mu, \tag{2.58}$$

and the total production rate be

$$\bar{q} \equiv 2\pi \int_{-1}^{1} \hat{q} \, d\mu. \tag{2.59}$$

Integrating Eq. 2.46 over all pitch angles produces

$$2\pi \int_{-1}^{1} \mu \frac{\partial \Phi}{\partial \ell} = \bar{q} - \sigma_{th} N_e v n_E - \sum_n \bar{\sigma}_{an} N_n v n_E. \tag{2.60}$$

The term on the left hand side is the net change in the photoelectron density caused by transport effects. The modified diffusion approach generates a tractable equation by making an assumption about the form of this term instead of making assumptions about the form of Φ itself. This term is assumed to be the sum of an escape term and a diffusion term. It can be written as

$$2\pi \int_{-1}^{1} \mu \frac{\partial \Phi}{\partial \ell} = F + \int_{-1}^{1} d\mu \, \mu \frac{\partial}{\partial \ell} \left(\phi_{md} \right), \tag{2.61}$$

where F is the rate at which photoelectrons are lost due to escape, and ϕ_{md} is a modified diffusion flux. The escape term can be expressed in terms of an escape probability, $\langle P_E \rangle$, as

$$F = \langle P_E \rangle \left[\bar{q} + v n_E \sum_n \bar{\sigma}_{en} N_n \right]. \tag{2.62}$$

For isotropically produced photoelectrons the position dependent escape probability is

$$\langle P_E \rangle = \frac{1}{2} \int_0^1 \exp\left[-\frac{\tau}{\mu} \right] d\mu, \tag{2.63}$$

where τ is the collision depth associated with that position [*Swartz and Nisbet*, 1973]. Neglecting collisions with ambient electrons, assuming an exponential neutral atmosphere with scale height H_n for neutral species n, and assuming the field line is straight with dip angle I the collision depth is [*Swartz and Nisbet*, 1973]

$$\tau = \frac{1}{\sin I} \sum_n N_n H_n \left[\bar{\sigma}_{an} + \bar{\sigma}_{en} \right]. \tag{2.64}$$

The diffusion component is derived by assuming that portion of the photoelectron population behaves like an isotropic distribution of particles diffusing in an ordinary gas. The modified diffusion flux is assumed to be [*Nisbet*, 1968]

$$\phi_{md} = \frac{1}{2} \beta \mu v \frac{\partial n_E}{\partial \ell}, \tag{2.65}$$

where the mean free path is [*Swartz and Nisbet*, 1973]

$$\beta = \left\{ \sum_n N_n \left[\bar{\sigma}_{an} + \bar{\sigma}_{en} \right] \right\}^{-1}. \tag{2.66}$$

This equation assumes the mean free path is shorter than characteristic scale lengths of the photoelectron density [*Nisbet*, 1968], i.e.

$$\frac{1}{\beta} \gg \frac{1}{n_E} \frac{\partial n_E}{\partial \ell}. \tag{2.67}$$

Using these various assumptions transforms Eq. 2.60 into a single second order ODE [*Swartz and Nisbet*, 1973, note Eq. 3 has sign error]

$$0 = \bar{q}\left[1 - \langle P_E \rangle\right] + v\left\{\frac{\partial}{\partial \ell}\left(\beta \frac{\partial n_E}{\partial \ell}\right) - n_E \sum_n N_n \left[\bar{\sigma}_{an} + \langle P_E \rangle \bar{\sigma}_{en}\right]\right\} \tag{2.68}$$

This second order ODE needs two boundary conditions. Obviously n_E should go to 0 at the lowest altitudes. Originally it was assumed that the divergence of the diffusive flux should go to 0 at the top boundary [*Nisbet*, 1968], i.e.

$$\frac{\partial}{\partial \ell}\left(\beta \frac{\partial n_E}{\partial \ell}\right) = 0. \tag{2.69}$$

However, all photoelectrons which cross the top boundary are escaping by definition. Thus the diffusive flux itself, ϕ_{md}, should be 0 at the top boundary. This in turn implies $\frac{\partial n_E}{\partial \ell} = 0$ at the top boundary. Applying this boundary condition instead noticeably decreases the high altitude fluxes produced by the modified diffusion method [see *Cicerone et al.*, 1973, Fig. 12]. Codes to solve this second order ODE and to solve the coupled pair of first order ODEs which make up the two-stream equations are of comparable complexity. Nonetheless, the high altitude fluxes produced by the modified diffusion method can exceed those produced by a two-stream method by as much as a factor of 2 depending on how the boundary conditions are set for the modified diffusion method, and on what $\langle \mu \rangle$ is chosen for the two-stream method [*Cicerone et al.*, 1973]. This discrepancy can be greatly reduced by setting the diffusive flux in the modified diffusion method equal to 0 at the top, and by using higher $\langle \mu \rangle$ values than the value 0.375 originally used by *Banks and Nagy* [1970]. The *Cicerone and Bowhill* [1971] Monte Carlo code produces results which are in between the other two models [*Cicerone et al.*, 1973].

Of the approaches discussed above the two-stream method has become the most popular. Since [*Banks and Nagy*, 1970], many other authors have written their own two-stream codes for a variety of applications using different energy grids,

collisions cross sections, backscatter coefficients, and computational methods. The GLOW code [*Solomon et al.*, 1988; *Solomon and Abreu*, 1989; *Bailey et al.*, 2002] predicts airglow emissions using a sophisticated photochemistry model and two-stream photoelectron transport equations. GLOW can be operated for ordinary photoelectrons as well as auroral electrons; the only change needed for auroral conditions is a specification of the downwards flux at the top boundary. *Link* [1992] created two-stream and multi-stream codes which use a method created by *Feautrier* [1964] for radiative transfer problems to improve the computational speed and accuracy on coarse spatial grids. As part of a procedure for inferring energetic electron spectra produced during HF heating experiments from artificially produced airglow, *Gustavsson and Eliasson* [2008] have created a two-stream model which includes an acceleration term to model the effects of HF waves on energetic electrons. This model uses an iterative solution method to cope with the fact that electrons will go both upwards and downwards in energy. *Hysell et al.* [2012] have written a different airglow inversion algorithm which incorporates results from SAMI2-PE. The photoelectron transport model inside of FLIP [*Richards and Torr*, 1996] is commonly called a two-stream model, although it contains several enhancements beyond the *Banks and Nagy* [1970] formulation which allow it to treat spatially varying magnetic fields. For this reason this code is discussed in more detail in the following subsection.

The numerical accuracy of the finite ordinate method for general radiative transfer problems has been studied by *Stamnes and Conklin* [1984], and this led to the creation of a general purpose finite ordinate code called DISORT [*Stamnes et al.*, 1988]. *Lummerzheim et al.* [1989], *Rees and Lummerzheim* [1989], and *Lummerzheim and Lilensten* [1994] describe a multi-stream auroral electron transport model based on DISORT. Despite being one of the oldest photoelectron transport

theories, the modified diffusion approach is no longer in widespread use.

2.4.5 Transport techniques for coupled ionosphere-plasmasphere models

When using a two-stream or modified diffusion model, setting $\Phi^- = 0$ or $\phi_{md} = 0$ at the top of the atmosphere ignores conjugate electrons. Issues with escape fluxes and boundary conditions at the top of the field line can be completely avoided if the computational domain is extended through the plasmasphere down to the bottom of the conjugate ionosphere. However, when considering an entire field line the variation of the magnetic field strength must be included. The changing magnetic field will alter the flux in two ways. First, the photoelectrons will change their pitch angles as they travel to preserve their 1^{st} adiabatic invariants. The final term on the left hand side of Eq. 2.38 causes this effect. This term is often called the magnetic mirror force term because it can also lead to trapping of particles in magnetic mirrors. Second, the flux will decrease as the magnetic field weakens (i.e. as the flux tube cross sectional area increases). The first term on the right hand side of Eq. 2.38 causes this effect. This term can be combined with the first term on the left hand side of Eq. 2.38 to create an alternate form of the photoelectron transport equation written in terms of Φ/B, which is independent of changes in

flux tube area.

$$\mu\frac{\partial}{\partial\ell}\left(\frac{\Phi}{B}\right)-\delta B\frac{\partial}{\partial\mu}\left[\frac{1-\mu^2}{2}\left(\frac{\Phi}{B}\right)\right]=\frac{\hat{q}}{B}+\frac{\partial}{\partial\mathcal{E}}\left[L(\mathcal{E})\left(\frac{\Phi}{B}\right)\right] + D(\mathcal{E})\frac{\partial}{\partial\mu}\left[(1-\mu^2)\frac{\partial}{\partial\mu}\left(\frac{\Phi}{B}\right)\right] - \sum_n(\bar{\sigma}_{an}+\bar{\sigma}_{en})N_n\left(\frac{\Phi}{B}\right) + \sum_n\bar{\sigma}_{en}N_n\frac{1}{2}\int_{-1}^{1}d\mu'\left(\frac{\Phi(\ell,\mathcal{E},\mu')}{B}\right) \tag{2.70}$$

Swartz et al. [1975] created one of the first photoelectron transport models which could include conjugate effects. The modified diffusion equations are solved in both hemispheres, but the boundary conditions at the top of each ionosphere are set by energy degraded versions of the escape fluxes from the conjugate ionosphere. *Lejeune* [1979] created a semi-analytic two-stream code which could use very large altitude step by assuming parameters varied exponentially with altitude within each altitude cell. This code could be configured as a two hemisphere code like the *Swartz et al.* [1975] code by treating the plasmasphere in between as one very large altitude step. Yet another approach to the coupled ionosphere-plasmasphere problem was introduced by *Mantas et al.* [1978], who solved multi-stream photoelectron transport equations in both ionosphere and in the plasmasphere in between simultaneously with carefully selected boundary conditions between the three domains. The ionospheric portions followed the development of *Mantas* [1975], whereas the plasmaspheric portion ignored collisions with neutrals, accounted for the changes in the flux tube volume, and incorporated the changes in the pitch angles due to the mirror force through a transformed distance coordinate. Pitch angle changes due to collisions were ignored in the plasmasphere, thus preventing any particles from becoming trapped in magnetic mirrors. Nonetheless, photoelectrons would still become quasi-trapped in the plasmasphere in this model by elastic backscat-

tering from the two ionospheres. *Mantas et al.* [1978] point out that fluxes at the top of an ionosphere are the rate of exchange between the ionosphere and plasmasphere, not "escape fluxes." The photoelectron flux in the plasmasphere which determines the plasmaspheric heating is not simply the sum of the "escape fluxes" from the two hemispheres.

All of the photoelectron transport models discussed so far have been used for calculations in a pre-specified background ionosphere and atmosphere. One of the first studies which coupled photoelectron calculations to fluid equations in a time dependent model was *Khazanov et al.* [1984], who created a single field line coupled ionosphere-plasmasphere model to study plasmaspheric refilling after geomagnetic storms. The electron heating in the ionosphere and plasmasphere in this model was computed using an simple embedded photoelectron transport model based on the approach of *Polyakov et al.* [1979]. Like *Mantas et al.* [1978], *Polyakov et al.* [1979] couples a plasmaspheric photoelectron transport code to two ionospheric photoelectron transport codes on either side. The solution methods used by *Polyakov et al.* [1979] are significantly different from those discussed above, however, but this article appears to have been largely ignored in the West because it was written in Russian. In the ionosphere *Polyakov et al.* [1979] write the flux as an infinite series

$$\Phi(\ell, \mathcal{E}, \mu) = \sum_{n=0}^{\infty} \Phi_n(\ell, \mathcal{E}) P_n(\mu), \tag{2.71}$$

where $P_n(\mu)$ is a Legendre polynomial of degree n. This series is truncated after 2 or 4 terms and substituted into an equation which is equivalent to Eq. 2.38 (i.e. it includes the mirror force and pitch-angle diffusion) to derive coupled equations for the coefficients $\Phi_n(\ell, \mathcal{E})$. Like the two-stream approximation or the finite ordinate approximation, this procedure leads to a system of 2 or 4 coupled linear ODEs which can be solved for each energy. *Polyakov et al.* [1979] treat the plasmasphere

like a leaking magnetic mirror trap using the same kinds of methods which are classically used to describe the radiation belts [e.g. *Roederer*, 1970]. Collisions with neutrals are ignored, and the photoelectron transport equation is averaged over all positions between the reflection points of the mirror trap. This results in a differential equation for the bounce-averaged distribution function in terms of the equatorial pitch angles of the particles which must be solved for each energy. The loss cone is coupled to the ionospheres on either side through boundary conditions. This type of bounce-averaged formalism is still used today in models of the ring current and inner magnetosphere [see *Fok et al.*, 2001, and references therein].

Two well known time dependent coupled ionosphere-plasmasphere models which include photoelectron transport are the Field Line Interhemispheric Plasma (FLIP) model [*Richards and Torr*, 1996] and the Sheffield University Plasmasphere-Ionosphere Model (SUPIM) [*Bailey and Balan*, 1996], which both use the same photoelectron transport code. This code is based on a two-stream approximation to Eq. 2.70 [*Young et al.*, 1980; *Torr et al.*, 1990; *Richards and Torr*, 1990]. Using the same definition of the up and down fluxes as above, the coupled pair of ODEs solved are

$$\begin{aligned}\langle\mu\rangle\frac{d}{d\ell}\left(\frac{\Phi^+}{B}\right) =& \frac{\hat{q}^+}{B} - \sigma_{th}N_e\left(\frac{\Phi^+}{B}\right) \\ &- \sum_n(\bar{\sigma}_{an} + (1-\beta_{en})\bar{\sigma}_{en})N_n\left(\frac{\Phi^+}{B}\right) + \sum_n \bar{\sigma}_{en}N_n\beta_{en}\left(\frac{\Phi^-}{B}\right) \qquad (2.72)\\ -\langle\mu\rangle\frac{d}{d\ell}\left(\frac{\Phi^-}{B}\right) =& \frac{\hat{q}^-}{B} - \sigma_{th}N_e\left(\frac{\Phi^-}{B}\right) \\ &- \sum_n(\bar{\sigma}_{an} + (1-\beta_{en})\bar{\sigma}_{en})N_n\left(\frac{\Phi^-}{B}\right) + \sum_n \bar{\sigma}_{en}N_n\beta_{en}\left(\frac{\Phi^+}{B}\right). \qquad (2.73)\end{aligned}$$

Pitch-angle diffusion due to Coulomb collisions is ignored. The effects of the magnetic mirror force are incorporated into these equations in an ad hoc manner [*Richards and Torr*, 1990]. At low altitudes $\langle\mu\rangle$ is fixed at 0.577, but above

a certain altitude $\langle\mu\rangle$ varies with the magnetic field strength the same way the pitch-angle cosine of a single collisionless electron would in the guiding center approximation. Furthermore, trapping of photoelectrons is included by specifying photoelectron trapping fractions a priori which determine the amount reflected from a nominal height of 1000 km [*Richards and Torr*, 1990].

The FLIP two-stream code has shown reasonable agreement with measurements of photoelectrons escaping from the high latitude ionosphere made by the FAST spacecraft [*Peterson et al.*, 2008; *Richards and Peterson*, 2008]. FLIP can adequately reproduce daytime F-region electron temperatures measurements from the Millstone Hill Observatory, however these comparisons are complicated by the lack of knowledge of the heat flux from the plasmasphere [*Richards and Khazanov*, 1997; *Buonsanto et al.*, 1997]. SUPIM can qualitatively reproduce features of the F-region electron temperatures measured by the Hintori satellite [*Balan et al.*, 1997] and the MU radar [*Otsuka et al.*, 1998]. Quantitatively, the plasmaspheric electron temperatures from SUPIM are as much as a factor of 2 too small compared to measurements from EXOS D (1000-8000 km), but they can be brought up to near agreement if the photoelectron trapping factor is raised and an extra high altitude heat source is added [*Balan et al.*, 1996a, b].

Predicting the heating rates in the plasmasphere requires a multi-stream model which can include magnetic mirror force effects in a rigorous way. The plasmasphere model presented by *Khazanov et al.* [1993] and later extended down to ionospheric heights by *Khazanov et al.* [1994] is such a model. These models write the photoelectron transport equation in yet another equivalent form by making a variable transformation from μ to [*Khazanov et al.*, 1979]

$$\mu_0(\ell,\mu) \equiv \frac{\mu}{|\mu|}\sqrt{1-\frac{B_0}{B(\ell)}\,(1-\mu^2)}, \tag{2.74}$$

where B_0 is the magnetic field strength at the apex of the field line. This variable is the pitch angle cosine a photoelectron will have when it crosses the equatorial plane. Like the 1st adiabatic invariant itself, μ_0 is a constant of motion for a collisionless electron. This attribute makes μ_0 a useful variable to use numerically in the collisionless or nearly collisionless regimes. The discrete equations in terms of μ_0 will keep trapped particles trapped between the same bounce points forever in the collisionless limit. However, the use of μ_0 substantially complicates the construction of the pitch angle grid and the boundary conditions in pitch angle space. The collision operators also need to be transformed as well. *Khazanov et al.* [1994] sidesteps this difficulty by treating all collision processes as continuous loss processes and small angle collision processes. Under these assumptions all collisions operators, not just the Coulomb collision operator, can be written as differential operators of the form

$$\frac{1}{v}\frac{\delta\Phi}{\delta t} = \frac{\partial}{\partial\mathcal{E}}\left[L(\mathcal{E})\Phi\right] + D(\mathcal{E})\frac{\partial}{\partial\mu}\left[(1-\mu^2)\frac{\partial\Phi}{\partial\mu}\right]. \tag{2.75}$$

These differential operators are much more straightforward to transform than the collision integrals themselves.

All of the aforementioned photoelectron transport models only consider steady state solutions. *Gefan and Khazanov* [1990] have argued that time dependent solutions are necessary during certain conditions when the photoelectron population is changing rapidly, such as plasmaspheric refilling events after geomagnetic storms. This argument motivated the extension of the *Khazanov et al.* [1994] model to a time-dependent photoelectron transport model which was coupled to high moment fluid equations [*Khazanov and Liemohn*, 1995; *Liemohn and Khazanov*, 1995]. This model has since been expanded to include parallel electric fields [*Liemohn et al.*, 1997], injections of plasma sheet electrons [*Khazanov et al.*, 2000], the drifts of photoelectrons around the planet into the nightside plasmasphere

[*Khazanov et al.*, 1996], and photoelectrons produced by starlight in the nightside plasmasphere [*Khazanov and Liemohn*, 2002]. All of these models use the same approximate treatment of collisions as *Khazanov et al.* [1994], and are primarily concerned with L-shells greater than L=2 (i.e. apex altitudes above 6371 km).

CHAPTER 3

ENERGY BALANCE IN THE SAMI2 MODEL

The models presented in this thesis are based on the SAMI2 model [*Huba et al.*, 2000a] because it is a widely used open source model which includes ion inertia and is thus capable of capturing a number of unique phenomena in the topside and plasmasphere [*Huba et al.*, 2000b, c; *Krall et al.*, 2008]. SAMI2 simulates a single magnetic longitude using a two-dimensional dipolar grid. This grid makes comparisons with a zenith pointing equatorial radar like Jicamarca straightforward; the radar's line of sight maps to a vertical line passing through the center of grid. This chapter will review the physics and numerical techniques included in the standard SAMI2 and discuss simulation results in the low-latitude ionosphere with a particular emphasis on the modeled temperatures. To facilitate sensitivity studies a steady state version of the temperature solver in SAMI2 has been written. This allows the energy balance calculations to be repeatedly performed for a single set of conditions in order to isolate the effects of individual physical processes. We will show that heating due to photoelectrons is the single most important process in the equatorial topside and the simplistic treatment of this term in SAMI2 is the most serious issue preventing SAMI2 from accurately reproducing Jicamarca data.

3.1 Fluid equations used in SAMI2

Fluid descriptions of plasmas can be derived from kinetic descriptions of plasmas by taking moments of the kinetic equations [see *Schunk and Nagy*, 2009, Chs. 3 and 5 for a detailed development]. The basic kinetic description of plasma species

α is the Boltzmann equation [e.g. *Bellan*, 2006; *Schunk and Nagy*, 2009];

$$\frac{\partial f_\alpha}{\partial t} + \mathbf{v} \cdot \frac{\partial f_\alpha}{\partial \mathbf{r}} + \left(\mathbf{g} + \frac{q_\alpha}{m_\alpha}\mathbf{E} + \frac{q_\alpha}{m_\alpha}\mathbf{v} \times \mathbf{B} \right) \cdot \frac{\partial f_\alpha}{\partial \mathbf{v}} = \frac{\delta f_\alpha}{\delta t}, \tag{3.1}$$

where the distribution function f_α is the expected number of particles of species α in a unit hypervolume of the six-dimensional position-velocity phase space $(\mathbf{r}, \mathbf{v})$, q_α and m_α are the charge and mass of the species, $\mathbf{g}$, $\mathbf{E}$ and $\mathbf{B}$ are the gravitational, electric and magnetic field strengths, and $\frac{\delta f_\alpha}{\delta t}$ is the rate of change of the distribution function due to the combined effects all types of interactions between multiple particles including collisions, chemical reactions, and photoionizations. The zeroth, first, and second moments of the Boltzmann equation give the equations of continuity, momentum, and energy respectively [e.g. *Schunk and Nagy*, 2009]:

$$\frac{\partial N_\alpha}{\partial t} + \nabla \cdot (N_\alpha \mathbf{u}_\alpha) = \frac{\delta N_\alpha}{\delta t} \tag{3.2}$$

$$N_\alpha m_\alpha \left(\frac{\partial \mathbf{u}_\alpha}{\partial t} + \mathbf{u}_\alpha \cdot \nabla \mathbf{u}_\alpha \right) + \nabla \cdot \mathbf{P}_\alpha - N_\alpha q_\alpha \left(\mathbf{E} + \mathbf{u}_\alpha \times \mathbf{B} \right) - N_\alpha m_\alpha \mathbf{g} = \frac{\delta M_\alpha}{\delta t} \tag{3.3}$$

$$\frac{\partial}{\partial t}\left(\frac{3}{2}p_\alpha\right) + \mathbf{u}_\alpha \cdot \nabla \left(\frac{3}{2}p_\alpha\right) + \frac{5}{2}p_\alpha \left(\nabla \cdot \mathbf{u}_\alpha\right) + \nabla \cdot \mathbf{q}_\alpha + \tau_\alpha : \nabla \mathbf{u}_\alpha = \frac{\delta E_\alpha}{\delta t}. \tag{3.4}$$

The above equations are expressed in terms of the moments [*Schunk and Nagy*, 2009]

$$\text{Density: } N_\alpha \equiv \int f_\alpha \, d\mathbf{v} \tag{3.5}$$

$$\text{Mean Velocity: } \mathbf{u}_\alpha \equiv \frac{1}{N_\alpha} \int \mathbf{v} f_\alpha \, d\mathbf{v} \tag{3.6}$$

$$\text{Scalar Pressure: } p_\alpha \equiv \frac{m_\alpha}{3} \int |\mathbf{v} - \mathbf{u}_\alpha|^2 \, f_\alpha \, d\mathbf{v} \tag{3.7}$$

$$\text{Pressure Tensor: } \mathbf{P}_\alpha \equiv m_\alpha \int (\mathbf{v} - \mathbf{u}_\alpha)(\mathbf{v} - \mathbf{u}_\alpha) \, f_\alpha \, d\mathbf{v} \tag{3.8}$$

$$\text{Stress Tensor: } \tau_\alpha \equiv \mathbf{P}_\alpha - p_\alpha \mathbf{I} \tag{3.9}$$

$$\text{Heat Flow Vector: } \mathbf{q}_\alpha \equiv \frac{m_\alpha}{2} \int |\mathbf{v} - \mathbf{u}_\alpha|^2 (\mathbf{v} - \mathbf{u}_\alpha) \, f_\alpha \, d\mathbf{v}. \tag{3.10}$$

The terms on the right hand sides of the fluid equations are defined in terms of moments of the collision term [*Schunk and Nagy*, 2009]

$$\frac{\delta N_\alpha}{\delta t} \equiv \int \frac{\delta f_\alpha}{\delta t}\, d\mathbf{v} \tag{3.11}$$

$$\frac{\delta M_\alpha}{\delta t} \equiv m_\alpha \int \mathbf{v} \frac{\delta f_\alpha}{\delta t}\, d\mathbf{v} \tag{3.12}$$

$$\frac{\delta E_\alpha}{\delta t} \equiv \frac{m_\alpha}{2} \int |\mathbf{v} - \mathbf{u}_\alpha|^2 \frac{\delta f_\alpha}{\delta t}\, d\mathbf{v}. \tag{3.13}$$

As presented, Eqs. 3.2, 3.3, and 3.4 cannot be used directly because the terms on the right hand sides cannot be evaluated without knowing the distribution function, and because the heat flow vector and stress tensor are not known. Moment equations for the heat flow vector and stress tensor will involve even higher moments of the distribution function, so the set of fluid equations can be extended indefinitely. The easiest solution is to assume collision dominance such that the distribution function is a drifting local Maxwellian [*Schunk and Nagy*, 2009]

$$f_\alpha(\mathbf{r}, \mathbf{v}, t) = N_\alpha(\mathbf{r}, t) \left(\frac{m_\alpha}{2\pi k_B T_\alpha(\mathbf{r}, t)} \right)^{3/2} \exp\left[-\frac{m_\alpha |\mathbf{v} - \mathbf{u}_\alpha(\mathbf{r}, t)|^2}{2 k_B T_\alpha(\mathbf{r}, t)} \right]. \tag{3.14}$$

In this case $\mathbf{q}_\alpha = 0$, $\tau_\alpha = 0$, $p_\alpha = N_\alpha k_B T_\alpha$, and the terms on the right hand side can be evaluated;

$$\frac{\delta N_\alpha}{\delta t} = P_\alpha - \sum_\beta R_\beta N_\alpha \tag{3.15}$$

$$\frac{\delta M_\alpha}{\delta t} = -\sum_\beta N_\alpha m_\alpha \nu_{\alpha\beta} (\mathbf{u}_\alpha - \mathbf{u}_\beta) \tag{3.16}$$

$$\frac{\delta E_\alpha}{\delta t} = Q_\alpha - \sum_\beta N_\alpha \frac{m_\alpha}{m_\alpha + m_\beta} \left[3 k_B \tilde{\nu}_{\alpha\beta} (T_\alpha - T_\beta) + m_\beta \nu_{\alpha\beta} |\mathbf{u}_\alpha - \mathbf{u}_\beta|^2 \right] \tag{3.17}$$

where P_α is the production rate (e.g. due to photoproduction or chemical reactions), R_β is the recombination rate for chemical reactions involving species β, $\nu_{\alpha\beta}$ is the momentum transfer collision frequency for collisions between α and β, $\tilde{\nu}_{\alpha\beta}$ is the energy transfer collision frequency for collisions between α and β, and Q_α

is an external heating rate. The two different types of collision frequencies can be written as

$$\nu_{\alpha\beta} = \frac{16}{3} N_\beta \frac{m_\beta}{m_\alpha + m_\beta} \Omega_{\alpha\beta}^{(1,1)} \Phi_{\alpha\beta} \tag{3.18}$$

$$\tilde{\nu}_{\alpha\beta} = \frac{16}{3} N_\beta \frac{m_\beta}{m_\alpha + m_\beta} \Omega_{\alpha\beta}^{(1,1)} \Psi_{\alpha\beta}, \tag{3.19}$$

where $\Omega_{\alpha\beta}^{(1,1)}$ is the Chapman-Cowling collision integral [*Chapman and Cowling*, 1970], and $\Phi_{\alpha\beta}$ and $\Psi_{\alpha\beta}$ are dimensionless velocity dependent correction factors which depend on the type of collision and are unity for Maxwell molecule collisions [see *Schunk and Nagy*, 2009, Ch. 4]. *Huba et al.* [2000a] list all of the chemical reactions considered in SAMI2 and give empirical expressions for the reaction rates, momentum transfer collision frequencies, and energy transfer collision frequencies.

Assuming a local Maxwellian forces the heat flow vectors to be 0. However, heat flow in the ionosphere is expected to be important since energy is absorbed nonuniformly by the upper atmosphere. A way to proceed is to retain the heat flow vector but perform a perturbation analysis where $\mathbf{q}_\alpha$ is presumed to be small. In this case the heat flow vectors can be approximately expressed in terms of lower moments of the distribution function [see *Schunk and Nagy*, 2009, section 5.12]. In a strongly magnetized plasma only the parallel component of the heat flow vector will be significant. For electron and ion gases the parallel components of the heat flow vectors are approximately [*Schunk and Nagy*, 2009; *Rees*, 1989]

$$\mathbf{q}_{e\parallel} = -\lambda_e \nabla_\parallel T_e - \beta_e \mathbf{J}_\parallel \tag{3.20}$$

$$\mathbf{q}_{i\parallel} = -\lambda_i \nabla_\parallel T_i, \tag{3.21}$$

where λ_e and λ_i are the electron and ion thermal conductivities, β_e is the thermoelectric coefficient, $\mathbf{J}_\parallel$ is the component of the current density parallel to the magnetic field, and $\nabla_\parallel$ denotes the derivative along a magnetic field line. In the

low latitude ionosphere there are no strong field aligned currents so we will ignore the thermoelectric term. Simple approximations for the thermal conductivities are [*Banks*, 1966; *Huba et al.*, 2000a; *Schunk and Nagy*, 2009]

$$\lambda_e = \frac{7.7 \times 10^5 T_e^{5/2}}{1 + 3.22 \times 10^4 T_e^2 N_q / n_e} \text{ eVcm}^{-1}\text{K}^{-1} \tag{3.22}$$

$$\lambda_i = \frac{1.24 \times 10^4 N T_i^{5/2}}{n_e} \text{ eVcm}^{-1}\text{K}^{-1}, \tag{3.23}$$

where,

$$N_q = n(O)q(O) + n(N_2)q(N_2) + n(O_2)q(O_2) \tag{3.24}$$

$$q(O) = 1.1 \times 10^{-16}(1 + 5.7 \times 10^{-4} T_e) \tag{3.25}$$

$$q(N_2) = 2.82 \times 10^{-17} T_e^{1/2}(1 - 1.21 \times 10^{-4} T_e) \tag{3.26}$$

$$q(O_2) = 2.2 \times 10^{-16}(1 + 3.6 \times 10^{-2} T_e^{1/2}) \tag{3.27}$$

$$N = n(O^+) + 2n(He^+) + 4n(H^+), \tag{3.28}$$

and all densities and temperatures are expressed in cm^{-3} and Kelvin, respectively.

Several additional assumptions are made in SAMI2 to simplify the fluid equations. First the quasineutrality condition, $N_e = \sum_j N_j$, is used instead of solving the electron continuity equation. Second the electron momentum equation is simplified by noting that $m_e/m_i \ll 1$ and $m_e/m_n \ll 1$;

$$0 = -\nabla p_e - N_e e \left(\mathbf{E} + \mathbf{u}_e \times \mathbf{B}\right). \tag{3.29}$$

The parallel component of this equation can be solved for the parallel ambipolar electric field,

$$E_\parallel = -\frac{1}{N_e e} \nabla_\parallel p_e. \tag{3.30}$$

This can then be substituted into the parallel component of the momentum equa-

tions for each ion,

$$N_j m_j \left(\frac{\partial u_{j\parallel}}{\partial t} + (\mathbf{u}_j \cdot \nabla) u_{j\parallel} \right) = -\nabla_\parallel p_j - \frac{N_j}{N_e} \nabla_\parallel p_e + N_j m_j g_\parallel - \sum_n \nu_{jn} \left(u_{j\parallel} - u_{n\parallel} \right) - \sum_{k \neq j} \nu_{jk} \left(u_{j\parallel} - u_{k\parallel} \right). \tag{3.31}$$

SAMI2 simplifies the perpendicular components of the electron and ion momentum equations by assuming the $\mathbf{E} \times \mathbf{B}$ drifts dominate the perpendicular motion such that $\mathbf{u}_{e\perp} = \mathbf{u}_{i\perp} = \mathbf{E} \times \mathbf{B}/B^2$. SAMI2 never solves for the perpendicular electric field and instead uses the empirical model of *Scherliess and Fejer* [1999] to specify it. A more complete approach, which is used in SAMI3[*Huba et al.*, 2008], is to retain the gravitational and diamagnetic drift terms and solve for the self consistent electric field which must form such that $\nabla \cdot \mathbf{J} = 0$ [e.g. *Kelley*, 2009].

Finally, the energy equations are expressed in a different form in SAMI2. Using the equation of state, $p_\alpha = N_\alpha k_B T_\alpha$, the source free continuity equation, $\partial N_\alpha / \partial t + \nabla \cdot (N_\alpha \mathbf{u}_\alpha) = 0$, and $\mathbf{q}_{\alpha\parallel} = -\lambda_\alpha \nabla_\parallel T_\alpha$, Eq. 3.4 can be rearranged as an equation for the temperature evolution [*Schunk and Nagy*, 2009];

$$\frac{3}{2} n_\alpha k_B \frac{\partial T_\alpha}{\partial t} = \underbrace{Q_\alpha}_{1} - \underbrace{L_\alpha}_{2} + \underbrace{\nabla_\parallel \cdot \lambda_\alpha \nabla_\parallel T_\alpha}_{3} - \underbrace{\frac{3}{2} n_\alpha k_B \mathbf{u}_\alpha \cdot \nabla T_\alpha}_{4} - \underbrace{n_\alpha k_B T_\alpha \nabla \cdot \mathbf{u}_\alpha}_{5}.$$

Physically the five terms on the right hand side represent local heating (1), local cooling (2), heat flow by thermal diffusion (3), heat advection (4), and heating/cooling by contraction/expansion (5). SAMI2 solves energy equations of this form for both the electrons and ions, although in the electron energy equation $\mathbf{u}_{e\parallel}$ is taken to be 0 such that terms 4 and 5 can be neglected [*Huba et al.*, 2000a]. Strictly speaking $\mathbf{u}_{e\parallel}$ should be determined from $\mathbf{J}_\parallel$, but $\mathbf{J}_\parallel$ is not known in SAMI2 because there is no self consistent electrodynamic solver. Nonetheless, electron temperature advection and heating due to expansion and contraction should be negligible compared to the other terms.

One of the heating terms in the electron energy equation represents the heating from photoelectrons. SAMI2 uses a simple phenomenological model of the photoelectron heating [*Millward et al.*, 1996; *Huba et al.*, 2000a]. Below 300 km the heating is assumed to be entirely local. Here the photoelectron heating rate is modeled as

$$Q_{phe} = \epsilon P_{photo}, \tag{3.32}$$

where P_{photo} is the photoproduction rate and the efficiency factor, ϵ, is given by the empirical expression [*Swartz and Nisbet*, 1972]

$$\epsilon = \exp\left[-\left(12.75 + 6.94x + 1.66x^2 + 0.08034x^3 + 0.001996x^4\right)\right] \text{ eV} \tag{3.33}$$

$$x = \ln\left(\frac{N_e}{N_{\mathrm{O}_2} + N_{\mathrm{N}_2} + 0.1N_{\mathrm{O}}}\right). \tag{3.34}$$

Above 300 km the nonlocal heating is at some point ℓ on a given field line is modeled as

$$\begin{aligned} Q_{phe}(\ell) =& \frac{N_e(\ell)B(\ell)}{N_e\left(\ell_{300N}\right)B\left(\ell_{300N}\right)} Q_{phe}\left(\ell_{300N}\right) \exp\left(-C_{qe}\int_{\ell}^{\ell_{300N}} N_e(\ell')d\ell'\right) \\ &+ \frac{N_e(\ell)B(\ell)}{N_e\left(\ell_{300S}\right)B\left(\ell_{300S}\right)} Q_{phe}\left(\ell_{300S}\right) \exp\left(-C_{qe}\int_{\ell_{300S}}^{\ell} N_e(\ell')d\ell'\right), \end{aligned} \tag{3.35}$$

where ℓ_{300N} and ℓ_{300S} are the points where the field line crosses 300 km in the northern and southern hemispheres respectively and the integrals are taken along the field line. The constant C_{qe} can be adjusted. Unless otherwise specified all of the examples presented below use $C_{qe} = 8 \times 10^{-14}$ cm^2. The effect of varying this parameter is discussed in Sec. 3.4.3.

3.2 Numerical Methods in SAMI2

Each time step in SAMI2 performs four tasks [*Huba et al.*, 2000a]. First the neutral atmospheric parameters are updated by calling NRLMSISE-00 [*Picone et al.*,

2002] for the densities and temperatures and HWM93 [*Hedin et al.*, 1991] for the winds. The fluid equations are then solved using a time splitting procedure. In the second step the parallel components of the ion momentum equations, ion continuity equations, electron temperature equation, and ion temperature equations are solved in that order. Photoproduction, chemical production and loss, and heating and cooling are all included in this parallel transport portion. Third the $\mathbf{E} \times \mathbf{B}$ drifts are computed from the model of *Scherliess and Fejer* [1999] and the state variables are updated with an explicit scheme for the perpendicular transport. Finally the Courant conditions are evaluated and the step size for the next time step is chosen. The nonlinear ion inertia term is treated explicitly so the Courant condition is set by the maximum ion velocity; the use of implicit methods for the parallel equations mean that the ion sound speeds have no effect on the time step size [*Huba et al.*, 2000a].

The position coordinates in SAMI2 are represented in an orthogonal dipole coordinate system, (q_d, p_d, ϕ_d) [*Huba et al.*, 2000a]. In terms of a spherical coordinate system centered on the offset and tilted magnetic dipole of the Earth, (r_e, θ_e, ϕ_e), and the radius of the Earth, R_E, these coordinates are defined as

$$q_d = \frac{R_E^2}{r_e^2} \cos\theta_e \tag{3.36}$$

$$p_d = \frac{r_e}{R_E} \frac{1}{\sin^2\theta_e} \tag{3.37}$$

$$\phi_d = \phi_e, \tag{3.38}$$

where a line of constant p_d and ϕ_d is a magnetic field line [see *Huba et al.*, 2000a, for a more detailed description of this coordinate system]. Following SAMI2 we will also define a coordinate $s = R_E q_d$ which has units of length and increases along a magnetic field line. This coordinate is related to the distance traveled along a

magnetic field line, ℓ, by

$$\frac{ds}{d\ell} = \frac{R_E^3}{r_e^3}(1 + 3\cos^2\theta_e)^{1/2} \equiv b_s. \tag{3.39}$$

This dimensionless curvilinear factor b_s is directly proportional to the magnetic field strength [*Huba et al.*, 2000a].

The original version of SAMI2 described by *Huba et al.* [2000a] used a Lagrangian grid where each field line moved with the $\mathbf{E}\times\mathbf{B}$ drift; however, subsequent revisions of the model have all been Eulerian. This entire thesis uses the Eulerian version of SAMI2. In the Eulerian version the perpendicular transport step advects the densities and temperatures in the perpendicular direction using a simple explicit donor cell upwinded method. The Eulerian SAMI2 grid is composed of a set of field lines which are all at the same magnetic longitude, ϕ_d. Each field line contains the same number of points along the field line and extends down to the same altitude (typically 85 km). This results in a slightly non-orthogonal grid; the normals to the cell faces between two grid cells on two different field lines do not exactly point in the direction of increasing p_d. Thus, perpendicular advection step includes a small amount of advection along the field line in addition to advection from one field line to the other.

3.3 A new steady state temperature model

Throughout most of the day the time derivative terms in the temperature equations are much smaller than all of the other terms. The typical thermal response times of the ionospheric plasma have been studied in detail by *Roble and Hastings* [1977]. Below 300 km the response times are less than 30 s, meaning that the steady state assumption is always valid. Between 300 and 600 km the temperatures

normally reach steady state within 200-1000 s. Above 600 km the electron and ion temperatures can display differing response times which vary depending on the densities, but are at most 2500 s. Thus the steady state assumption is valid in the topside when the heating is not varying significantly on time scales less than 2500 s, which is true during most of the day except at sunrise and sunset. When the time derivative terms are negligible the temperature equations become a boundary value problem in space. The final equations which we solve for each ion species and electrons are

$$0 = \underbrace{-\tilde{Q}_\alpha}_{1} + \underbrace{\tilde{L}_\alpha}_{2} + \underbrace{\frac{2}{3}\frac{1}{n_\alpha k_B}\nabla_\parallel \cdot \lambda_\alpha \nabla_\parallel T_\alpha}_{3} + \underbrace{\mathbf{u}_{\alpha\perp}\nabla_\perp T_\alpha}_{4a} + \underbrace{\mathbf{u}_{\alpha\parallel}\nabla_\parallel T_\alpha}_{4b} + \underbrace{\frac{2}{3}T_\alpha \nabla_\perp \cdot \mathbf{u}_{\alpha\perp}}_{5a} + \underbrace{\frac{2}{3}T_\alpha \nabla_\parallel \cdot \mathbf{u}_{\alpha\parallel}}_{5b}, \tag{3.40}$$

where $\tilde{Q}$ and $\tilde{L}$ are the local heating and cooling rates divided by $3/2N_\alpha k_B$. For boundary conditions the temperatures at the two ends of each field line and along the entire bottom field line are set equal to the neutral temperatures. Along the top field line the difference between the top field line and line immediately below is assumed to be 0. The details of the numerical techniques used to solve this equation are contained in Appendix A.

The model requires a number of other parameters to be specified. The densities and temperatures of all neutral species are specified by the NRLMSISE-00 model [*Hedin*, 1991; *Picone et al.*, 2002], the neutral winds are specified by the HWM93 [*Hedin et al.*, 1991], the $\mathbf{E} \times \mathbf{B}$ drifts are specified by the model of *Scherliess and Fejer* [1999], and the ion densities and parallel velocities must be fixed either by some other ionospheric model, such as SAMI2 or IRI, or using data. As a reference case we have run SAMI2 for 48 hours starting on May 8, 2008 with both the daily and average F10.7 flux set to 70 and an Ap of 4. These conditions correspond to

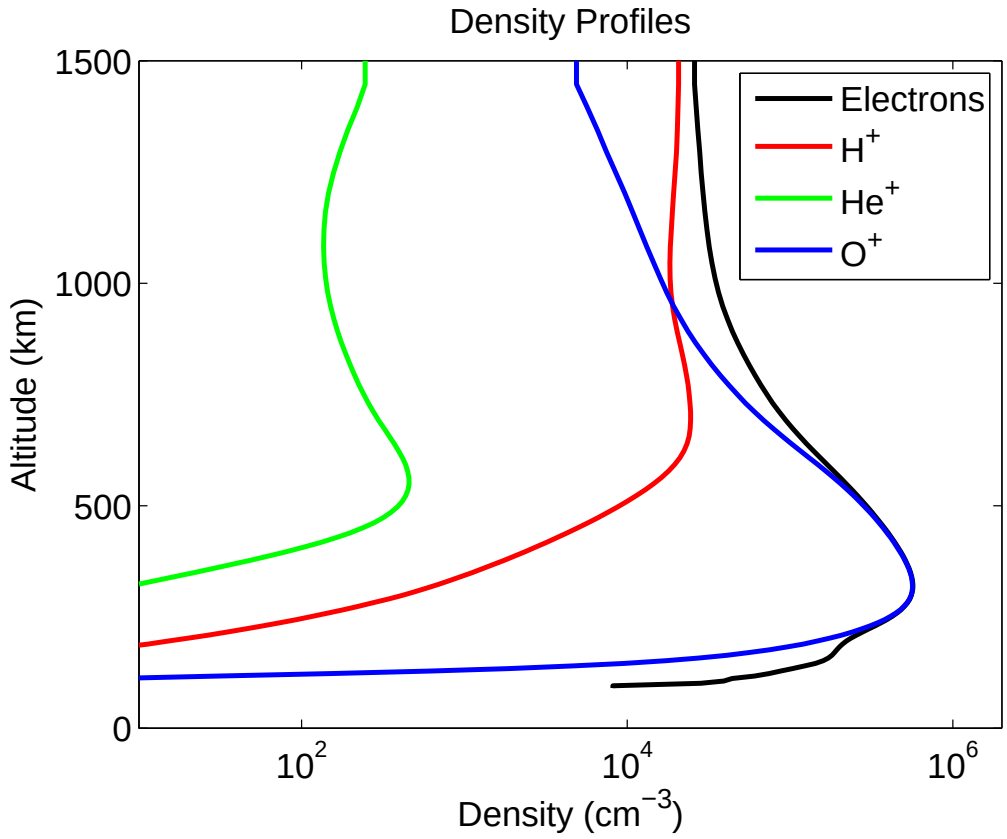

Figure 3.1: A vertical cut through the electron and ion density profiles above the magnetic equator at 14 LT for the reference case. Only three of the seven ion species used in SAMI2 are plotted. The electron density is higher than the O^+ density at low altitudes because the densities of the four additional ions (N^+, N_2^+, NO^+ and O_2^+) become significant at these low altitudes.

deep solar minimum. Running the model for two full days and ignoring the first 24 hours ensures that all transient behavior has ceased. Fig. 3.1 shows a cut through the density profiles at the magnetic equator at 14 LT on the second day for this reference case.

3.3.1 Results of Reference Case

Fig. 3.2 shows vertical profiles of the computed temperatures at 14 LT above Jicamarca for all four species for the reference case. Each plot shows the profile from SAMI2 and the solution obtained by the two-dimensional steady state model. The agreement between the model and SAMI2 is excellent at low altitude, but the steady state model predicts higher temperatures than SAMI2 in the 300-1000 km range. The discrepancy is most noticeable around 700 km because, in this case, those field lines connect to the equatorial arcs. As will be discussed in detail later, the nonlocal heating from the equatorial arcs has a large effect on the topside temperatures. The densities in the arcs are never in a steady state, but rather form throughout the afternoon. At any given time during the afternoon, the instantaneous nonlocal heating rate is higher than the average nonlocal heating rate over a typical response time of the temperatures. Thus the steady state solver consistently overestimates the temperature when nonlocal heating is important. Above 1000 km the steady state temperatures can be either higher or lower than the SAMI2 temperatures.

To demonstrate the relative importance of the various physical processes, the magnitudes of each term in Eq. 3.40 are plotted in Fig. 3.3 as a function of altitude. The terms are all multiplied by $3/2N_\alpha k_B$ and expressed in units of $\mathrm{eVcm^{-3}s^{-1}}$. Clearly at low altitudes local heating and cooling dominate all other processes. At these altitudes the temperatures can be obtained by simply solving algebraic equations. At higher altitudes thermal diffusion (term 3), nonlocal photoelectron heating (term 1), local cooling (term 2), and perpendicular advection (term 4a) are all important processes. Expansion and contraction (terms 5a and 5b) are always insignificant, and parallel advection (term 4b) is small because parallel diffusion

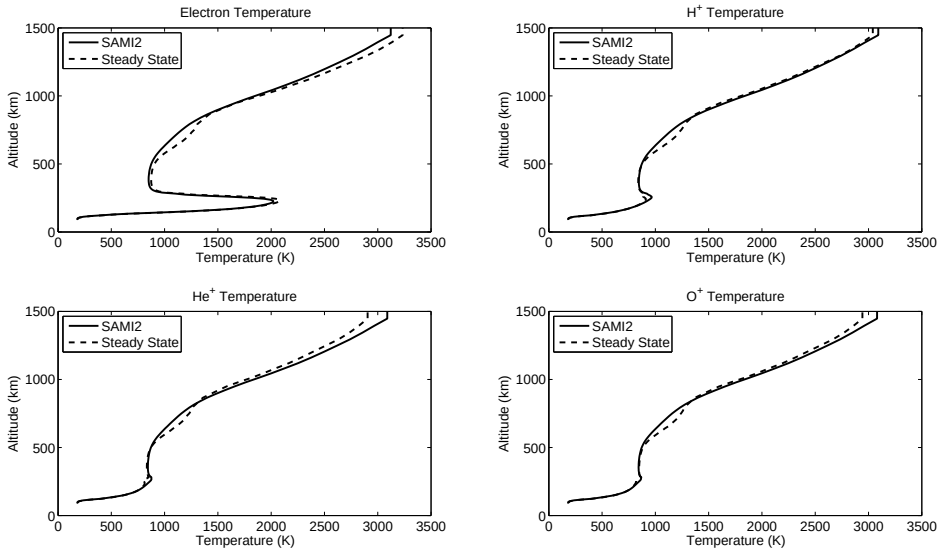

Figure 3.2: Vertical profiles of temperatures produced by SAMI2 and the steady state model for the reference case at 14 LT. These profiles represent a cut through the full solution at the magnetic equator.

acts to smooth out parallel gradients much more efficiently.

Fig. 3.4 demonstrates the validity of the steady state model for various times of day. The solid line is the electron temperatures produced by SAMI2 during the second 24 hours of the 48 hour reference case at 1011 km over the magnetic equator, and the diamonds are electron temperatures from the corresponding runs of the steady state model. During most of the day the steady state solution is only slightly above the true solution. The discrepancies are worst just after sunrise, when the temperatures are changing rapidly and a steady state solution is not expected to be appropriate, and just before sunset, during the prereversal enhancement. The steady state solutions are the most accurate during the early afternoon. During the night the steady state solutions are simply equal to the neutral temperature because there is no photoelectron heating. The true nighttime temperatures are higher than the neutral temperatures due to heat which persists from the daytime.

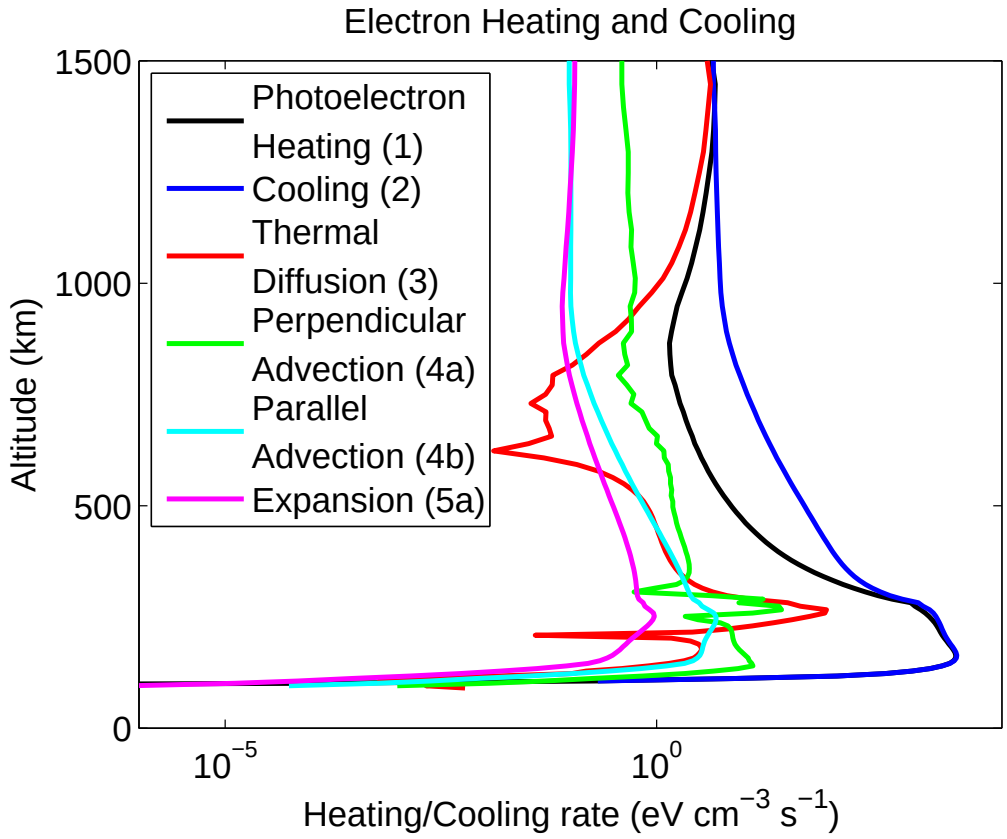

Figure 3.3: A vertical cut of the magnitudes of the electron heating/cooling rates at the final model solution. The numbers in the legend identify the terms in Eq. 3.40 corresponding to each curve. The curve labeled "cooling" is the sum of all local cooling processes due to electron-ion and electron-neutral collisions.

This residual heat lasts all the way until sunrise on the following day.

3.4 Sensitivity Studies

The steady state model provides an expedient way to repeatedly predict temperatures at a single time for a variety of different physical conditions. We have used the model to conduct a series of numerical experiments which test the sensitivities of the topside equatorial temperatures to a variety of physical processes. We have

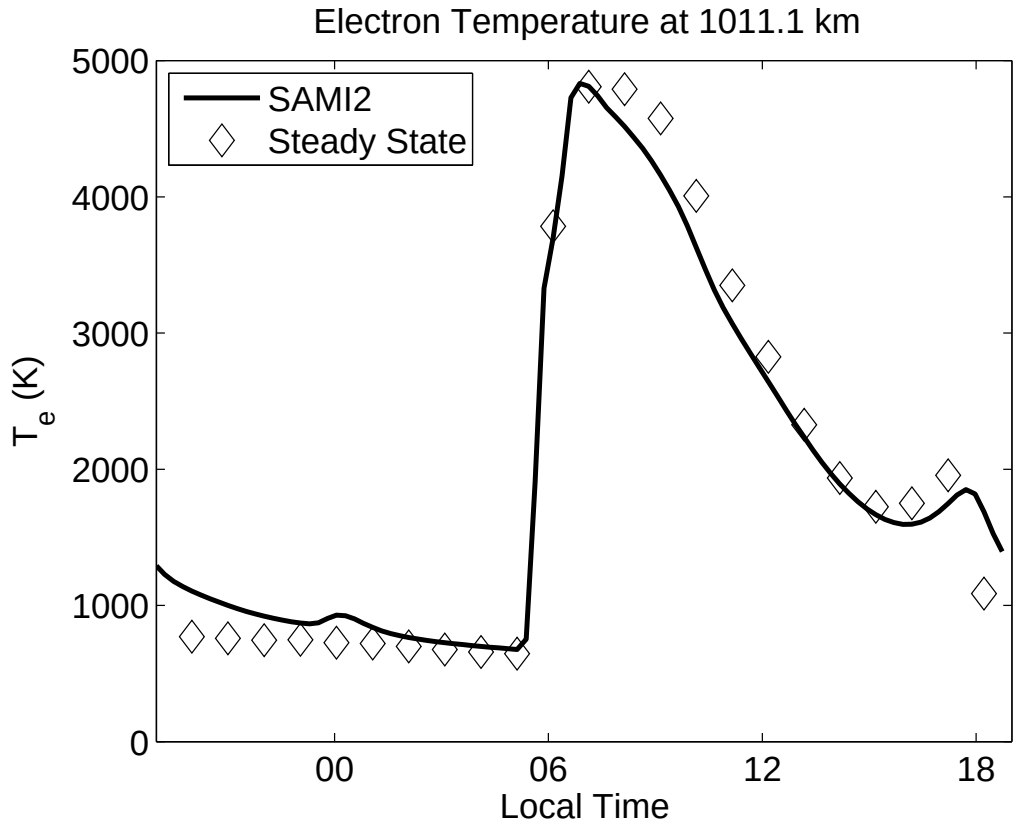

Figure 3.4: Electron temperatures produced by SAMI2 and the steady state model for various times of day. During much of the day the steady state solution is still approximately correct.

focused on the temperatures at 14 LT because at this time of day the steady state model is most accurate.

3.4.1 Effects of Electric Fields

Hysell et al. [2009] have shown that the topside temperatures are extremely sensitive to variations in the electric field. To fully illustrate the response we have run SAMI2 for three full days for the reference case discussed above, but after local noon on the third day we double the electric field. Fig. 3.5 illustrates the response

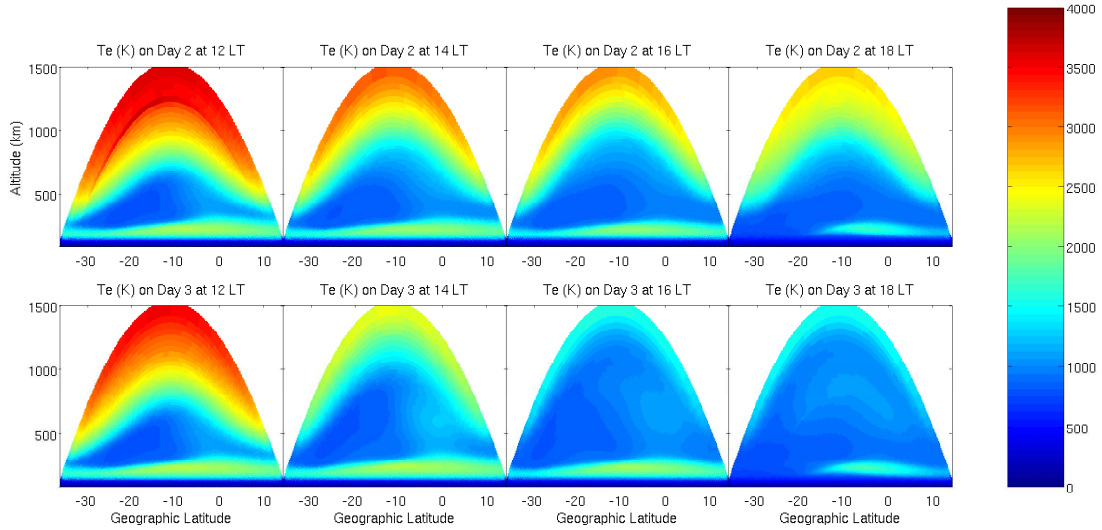

Figure 3.5: Electron temperatures in Kelvin for selected times during the afternoon of the second and third day of the SAMI2 run. The first day is omitted because it potentially contains transients. The second day corresponds to the reference case. On the third day after local noon the electric field is doubled. The temperatures on the third day are consistently lower than those on the second.

of the electron temperature and Fig. 3.6 illustrates the corresponding response of the electron density. During the afternoon the electric fields are eastward, meaning that the plasma drifts upwards. Lifting the plasma results in a reduction of the electron temperature and the formation of equatorial arcs via the fountain effect.

Electric fields affect the topside temperatures through both direct and indirect means. The direct effects stem from terms in the temperature equation which explicitly depend on $\mathbf{u}_\perp$, namely the perpendicular advection and expansion/contraction terms. Flux tubes always expand as they are lifted to higher altitude, meaning that $\nabla \cdot \mathbf{u}_\perp$ is positive. Furthermore, in the topside ∇T points upwards, so $\mathbf{u}_\perp \cdot \nabla T$ is also positive. Thus both perpendicular advection and expansion will cool the topside.

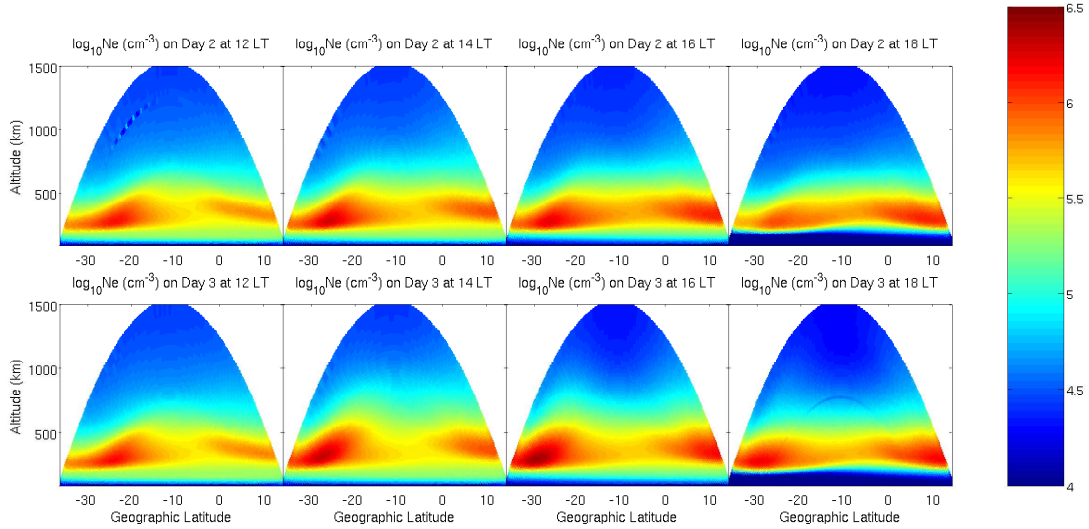

Figure 3.6: Electron densities corresponding to the electron temperatures in Fig. 3.5. Clearly the increased electric fields on the third day moves the equatorial arcs to higher latitudes.

The redistribution of plasma by the electric fields results in many more complicated indirect effects. Increasing the vertical drift raises the O^+ to H^+ transition height. Changing the ion composition changes the local cooling rates. Furthermore, the topside heating is strongly coupled to the off-equatorial F-region both through field aligned thermal diffusion and nonlocal heating from photoelectrons.

To determine the relative importance of all of these effects we have run our steady state model for a number of different cases. We have generated electron and ion density profiles by running SAMI2 for the reference case and for the reference case with the electric field multiplied by 1.5. Fig. 3.7 shows the result of the model when run at 14 LT using:

1. The standard densities and no other modifications,

2. The standard densities and the perpendicular advection terms multiplied by

1.5,

3. The standard densities and the expansion terms multiplied by 1.5,
4. The standard electron densities with the ion densities adjusted such that the ion fractions match those from the modified SAMI2 run,
5. The standard densities but photoelectron heating rates computed using the modified electron densities,
6. The modified densities but photoelectron heating rates computed using the standard electron densities,
7. The modified densities with self consistent photoelectron heating rates and both perpendicular advection and expansion multiplied by 1.5.

The first and last cases have consistently higher temperatures than their corresponding SAMI2 results due to discrepancies between the steady state and the true solutions discussed earlier, not due to any other physical processes. The other cases are all designed to isolate the different processes which are altered by the electric fields. Fig. 3.7 clearly demonstrates that changes to the nonlocal photoelectron heating have the largest individual effect. The strong dependence of the nonlocal photoelectron heating on the electron density at 300 km is immediately apparent from Eq. 4.82. All of the other terms provide smaller but comparable amounts of cooling individually throughout the topside. The exception is perpendicular advection which cools most of the lower altitudes but heats the very highest altitudes simulated.

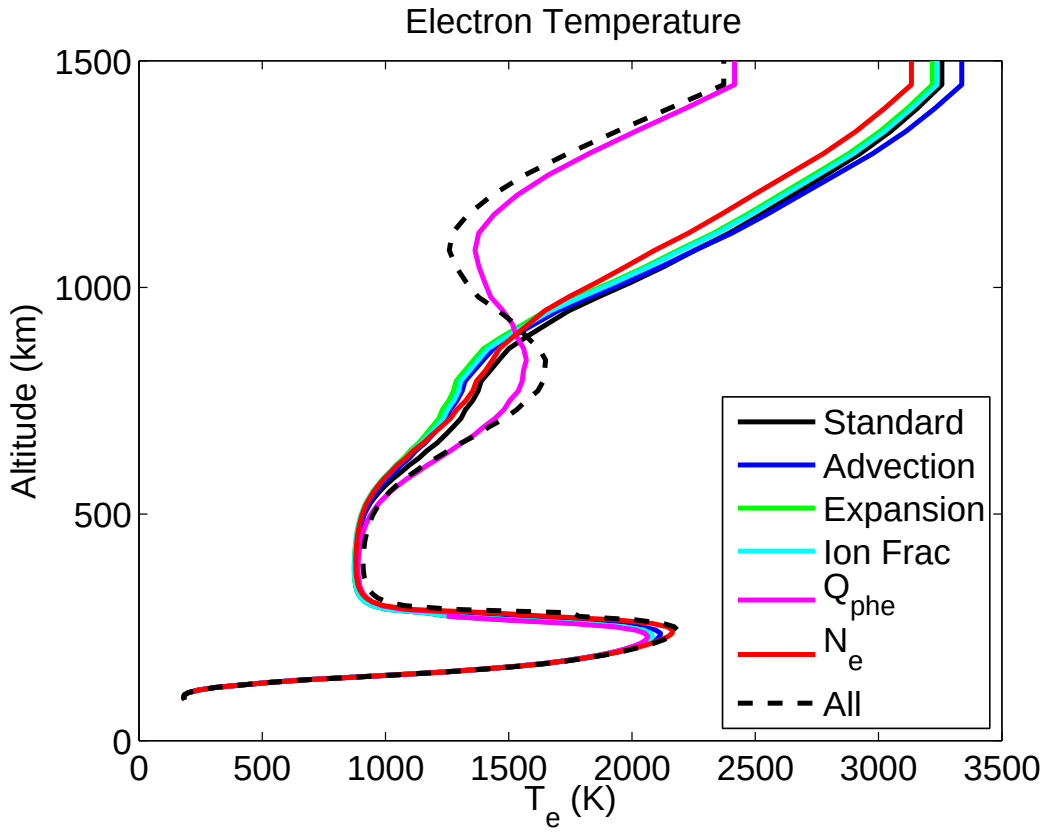

Figure 3.7: Steady state electron temperature profiles over the magnetic equator with the electric field scaled by 1.5. The curve labeled "Standard" is the reference case and the curve labeled "All" is the solution with all the effects of the increased electric field included. The other curves are solutions when only one term is adjusted for the increased electric fields at a time as explained in the text.

3.4.2 Effects of Meridional Neutral Winds

The effects of meridional neutral winds on the topside temperatures can be understood in a similar fashion to the effects of electric fields. Neutral winds directly change the temperature equation by changing the parallel advection and expansion/compression terms, but these terms are usually small compared to the other physical processes. However, the meridional winds can also redistribute plasma and thus also have strong indirect effects on the topside temperatures just like

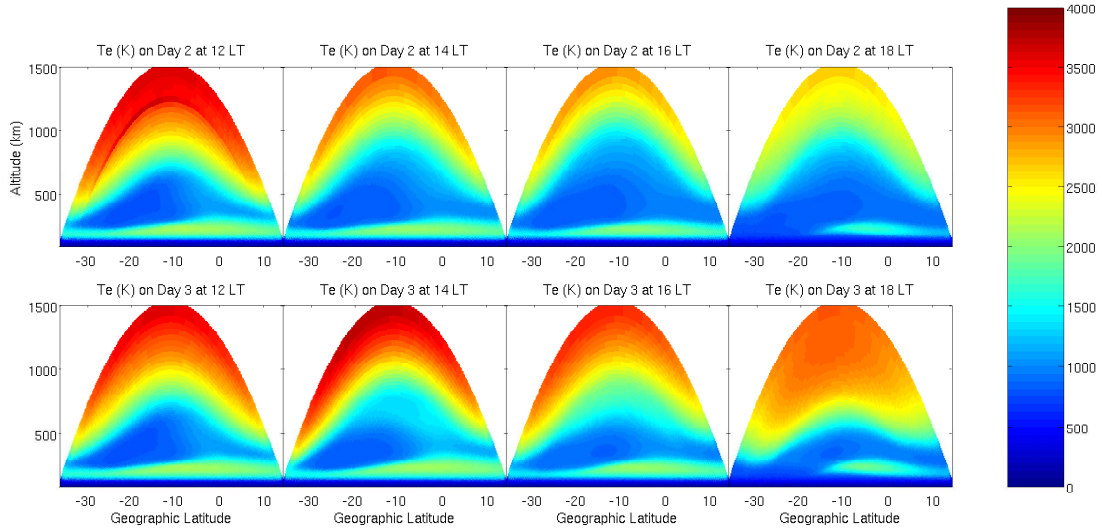

Figure 3.8: Electron temperatures in Kelvin for selected times during the afternoon of the second and third day of the SAMI2 run. The second day corresponds to the reference case. On the third day after local noon the neutral winds are doubled. The temperatures on the third day are consistently higher than those on the second.

electric fields.

We have performed another three-day run of SAMI2 where the meridional winds are doubled after noon on the final day. Fig. 3.8 and Fig. 3.9 illustrate the evolution of the electron temperature and electron density respectively. The winds produced by the HWM93 in the upper thermosphere have a strong southward component. These winds create an asymmetry between the equatorial arcs. The northern arc is raised in altitude and depleted while the southern arc is lowered in altitude and enhanced. The total amount of plasma in both arcs is actually decreased for increasing winds because as the southern arc is lowered in altitude recombination becomes more important.

The steady state model can be used once again to isolate the relative importance

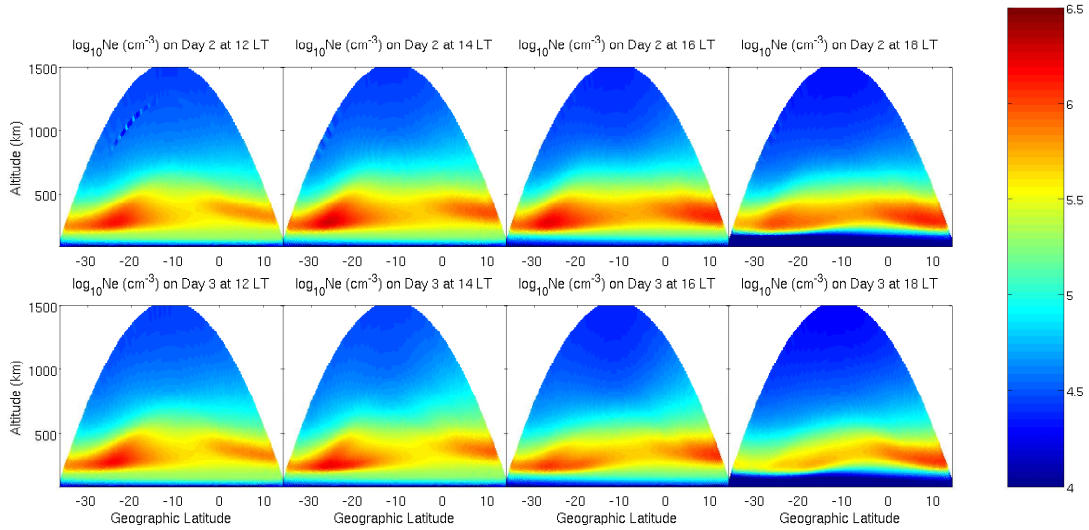

Figure 3.9: Electron densities corresponding to the electron temperatures in Fig. 3.8. The increased winds on the third day exaggerate the asymmetry between the two equatorial arcs and decrease the total integrated plasma density along any given field line.

of the pathways through which meridional winds affect temperatures. Ion and electron densities and ion parallel velocities were generated by running SAMI2 both with normal winds and with winds scaled by 2. Fig. 3.10 shows runs of the model at 14 LT using:

1. Standard densities and velocities,
2. Standard densities and velocities with photoelectron heating rates computed using the modified electron densities,
3. Standard velocities and modified densities with photoelectron heating rates computed using the standard electron densities.
4. Standard densities but modified ion and neutral velocities,
5. Modified densities, velocities, and photoelectron heating rates.

The direct effect of changing the parallel advection by changing the velocities produces a slight cooling of the topside. However, the total effect of increasing the winds is a substantial heating of the topside. Once again the rearrangement of the plasma along the flux tubes has a substantial indirect effect on the temperature. Exactly like the electric field case the largest effect comes from changing the nonlocal photoelectron heating. Increasing the meridional winds causes the total integrated density along the flux tube to decrease because the wind depletes the upwind portion of the field line, and forces the downwind portion of the field line downwards where recombination is stronger. This means that the integral in Eq. 4.82 is larger. Physically this integral models the attenuation of the nonlocal heating as the electrons travel further along the field lines. Adjusting the densities, and thus the parallel thermal diffusion, without changing photoelectron heating also appreciably increases the topside temperatures.

In all of the examples presented thus far the adiabatic compression/expansion has always been insignificant compared to other processes. These effects have been shown to create significant ion heating, however, in SAMI3 simulations of equatorial spread-F where the flow velocities are much faster [*Huba et al.*, 2009]. The occasional satellite observations of troughs and enhancements in ion temperature at night have also been attributed to adiabatic compression/expansion [*Bailey and Heelis*, 1980; *Venkatraman and Heelis*, 1999a, b]. These structures are thought to be associated with strong trans-equatorial neutral winds. The ions are constrained to move along the magnetic field lines as they are pushed by the wind, so the ions in the downwind hemisphere are compressed by the converging magnetic field and the ions in the upwind hemisphere expand due to the diverging magnetic field. Thus a strong meridional wind should expand and cool the ions the upwind hemisphere, creating a trough, and compress and heat the ions the

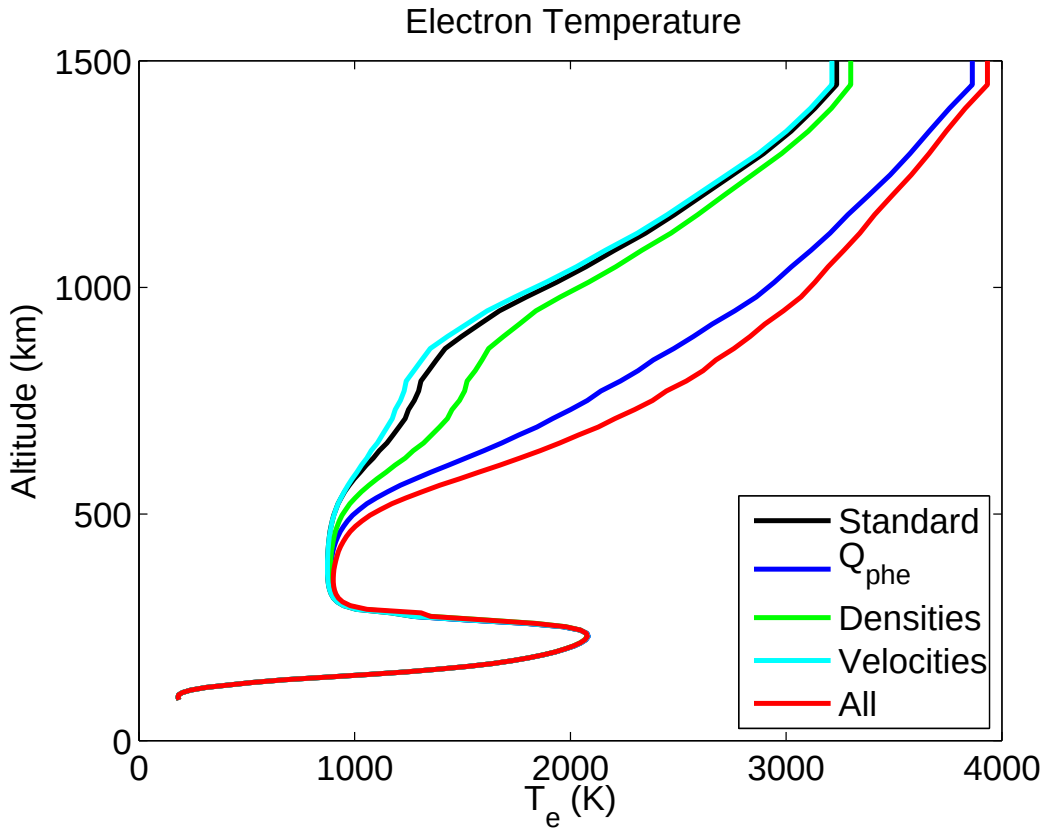

Figure 3.10: Steady state electron temperature profiles over the magnetic equator with the winds scaled by 2. The curve labeled "Standard" is the reference case and the curve labeled "All" is the solution with all the effects of the increased winds included. The other curves are solutions when only one term is adjusted for the increased winds at a time as explained in the text.

downwind hemisphere, creating an enhancement.

We have attempted to reproduce these effects using SAMI2. The four panels in the upper left of Fig. 3.11 show the O^+ temperature at 1 local time for four different SAMI2 runs. The top left and center left panels are for the same date and conditions as the reference case, which correspond to solar minimum. The top center and center panels are for the year 2002 and an F10.7 of 190, which are solar maximum conditions, with all other parameters unchanged. During solar maximum the O^+-H^+ transition height is much higher, meaning that a larger

proportion of the topside is composed of O^+. Satellite observations have shown that ion temperature troughs are much more pronounced during solar maximum for this reason [*Venkatraman and Heelis*, 1999b]. The top left and top center panels use the HWM93 model to generate the neutral winds. The HWM93 winds for both the solar minimum and solar maximum conditions are plotted in the bottom two panels. In both cases the winds in the topside are southwards at the equator, but eventually change sign in the southern hemisphere. The center left and center panels assume a constant, uniform neutral wind of 100 m/s southward. This is the simplest way to create a strong trans-equatorial flow. Both of the simulations with the HWM93 winds show very little latitudinal dependence of the O^+ temperatures. The simulation at solar maximum using the strong uniform winds, however, shows a pronounced temperature maximum in the downwind hemisphere as well a trough slightly upwind of the magnetic equator. Similar yet much less pronounced features are visible in the simulation at solar minimum using the uniform winds. These four simulations thus corroborate the main conclusions of *Bailey and Heelis* [1980]; troughs and enhancements in ion temperature are possible at night if strong trans-equatorial flows exist and are much more pronounced during solar maximum when larger amounts of O^+ are present in the topside.

To prove that these troughs and enhancements are indeed the result of the neutral wind and not a remnant of structures created by asymmetric heating during the daytime we have run the steady state model using the uniform wind for the solar maximum conditions at 1 local time. The steady state model was run using the densities and ion velocities produced by the SAMI2 run with the same conditions. The center right panel of Fig. 3.11 shows steady state O^+ temperatures. The SAMI2 temperatures (center panel) and the steady state temperatures (center right panel) do not match because the steady state model cannot account for heat

which persists from the daytime. Normally the steady state model sets the ion temperatures almost exactly equal to the neutral temperatures at night since since there are no significant heat sources. For reference the MSIS neutral temperatures used for all of the solar max runs are plotted in the top right panel of Fig. 3.11. In this case, however, the steady state ion temperatures show an enhancement in the downwind hemisphere and a temperature minimum at high altitudes and in the upwind hemisphere which are not present in the neutral temperatures. This proves that the compression and expansion driven by the wind are acting as a direct source of ion heating and cooling.

3.4.3 Effects of the Nonlocal Heating Parameter

The nonlocal heating model used in our model relies on an unknown parameter, C_{qe}. Fig. 3.12 shows several runs of the model for a variety of different values of the parameter for the reference case. Clearly the temperatures below 300 km are unaffected because this parameter only appears in the model of the nonlocal photoelectron heating above 300 km. Above 300 km all of the profiles have the same qualitative shape, but the absolute temperatures increase dramatically with increasing C_{qe}. Thus none of the model results presented above should be regarded as strictly reliable predictions of the absolute temperatures and direct comparisons to data or other models will almost certainly be inaccurate. Nonetheless, the qualitative shapes of the profiles and the changes to the profiles caused by changing physical conditions predicted by this model are still meaningful.

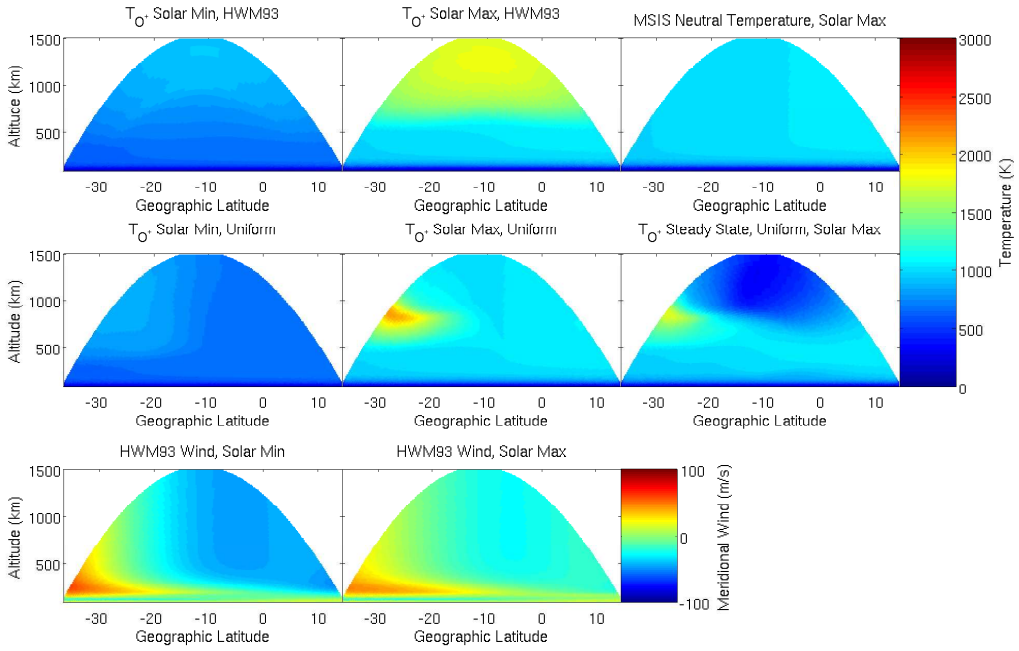

Figure 3.11: Summary plots illustrating the effects of neutral winds at night on ion temperature. All of the plots correspond to 1 local time. The plots are (a) oxygen ion temperatures from a SAMI2 run at solar minimum using HWM93 winds (top left), (b) oxygen ion temperatures from a SAMI2 run at solar maximum using HWM93 winds (top center), (c) oxygen ion temperatures from a SAMI2 run at solar minimum using a constant, uniform 100 m/s southward wind (center left), (d) oxygen ion temperatures from a SAMI2 run at solar maximum using a constant, uniform 100 m/s southward wind (center), (e) HWM93 winds for solar minimum conditions (bottom left), (f) HWM93 winds for solar maximum conditions (bottom center), (g) MSIS neutral temperatures for solar maximum conditions (top right), and (h) oxygen ion temperatures from the steady state model using the same parameters as the center panel (center right).

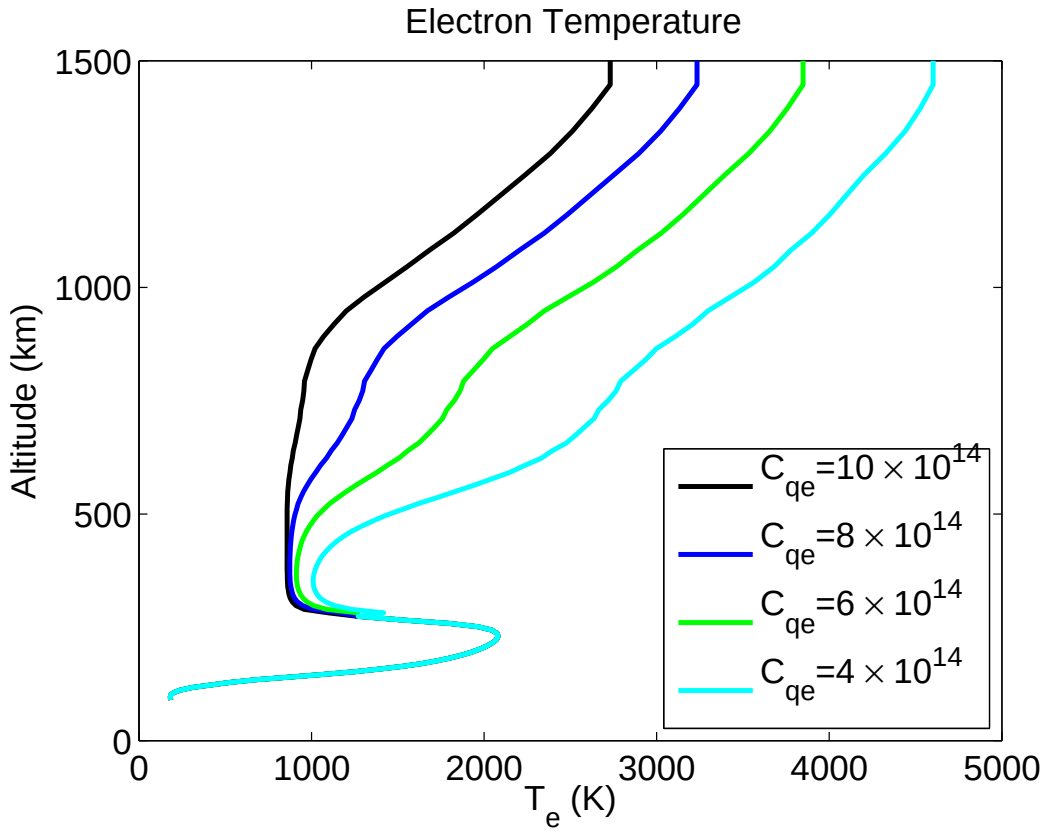

Figure 3.12: Steady state electron temperature profiles over the magnetic equator for various values of the nonlocal heating attenuation parameter, C_{qe}. The value of 8×10^{-14} cm^2 is the standard value used in all of the other plots.

3.5 Comparison of SAMI2 to Jicamarca data

March 25, 2009 was an exceptionally quiet day on which Jicamarca ran a full profile mode. This day is used as the reference case for SAMI2-PE in Sec. 6.1. This section displays some results from the standard SAMI2 for the same day for comparison. Three simulations were performed using three different values of the nonlocal heating parameter, C_{qe}. Figs. 3.13 and 3.14 show the electron densities and temperatures respectively from these three simulations along with the Jicamarca measurements. The electron densities in the three simulations are

all similar to each other and agree well with the measurements. The differences in the densities are most pronounced in the topside, where the simulations with higher C_{qe} have slightly higher topside plasma densities. When the temperatures are higher the pressure gradients along the field lines can hold more plasma up at high altitudes. The band of strong radar returns around 150 km in the electron density data is not actually a layer of large electron density, but rather the result of coherent scatter from 150 km echoes [see *Chau and Kudeki*, 2006b, for a review of this phenomenon]. Thus the absence of this layer in the simulations is not cause for concern.

The electron temperatures, however, differ substantially from the data and from one simulation to the next. Below 300 km the electron temperatures from the three simulations are identical because C_{qe} has no effect on these altitudes. These low altitude electron temperatures agree reasonably well with the data. In the topside, however, changing C_{qe} can change the temperatures by over 1000 K. The discrepancies with the data in the topside are worst at sunrise where the simulations overestimate the temperatures by 1000-2000 K. In the afternoon the simulations produce more reasonable temperature values, but the shapes of the temperature profiles with increasing altitude is wrong, as illustrated in Fig. 3.15. If C_{qe} is tuned such that the temperatures matches the data at some reference altitude, then the simulation will underestimate the temperatures below that reference altitude and overestimate the temperatures above that reference altitude. These errors are $\sim$500-1000 K which is 25-50% of the measured values. Thus even in the afternoon there is no one value of C_{qe} which can generate satisfactory agreement with the data. This weakness of SAMI2 is the motivation for reexamining the physics of photoelectron heating in more detail and creating SAMI2-PE.

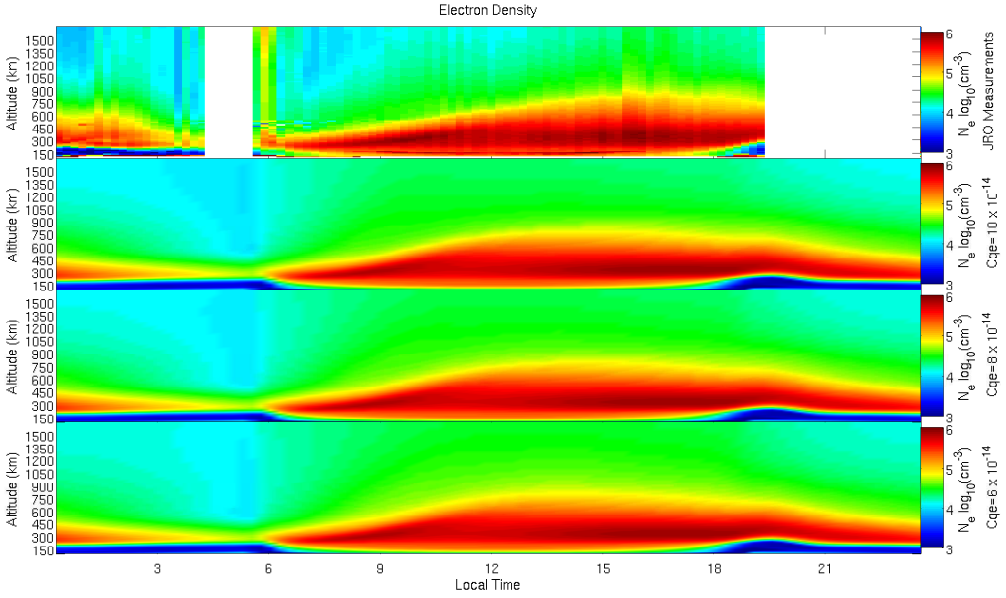

Figure 3.13: RTI plots of electron densities on March 25, 2009 measured by Jicamarca (top) and modeled by SAMI2 (bottom 3 plots). Each vertical strip in these RTI plots is a cut through the equatorial plane of the 2-D simulations. The values used for C_{qe} in the various SAMI2 simulations are indicated on the right hand side.

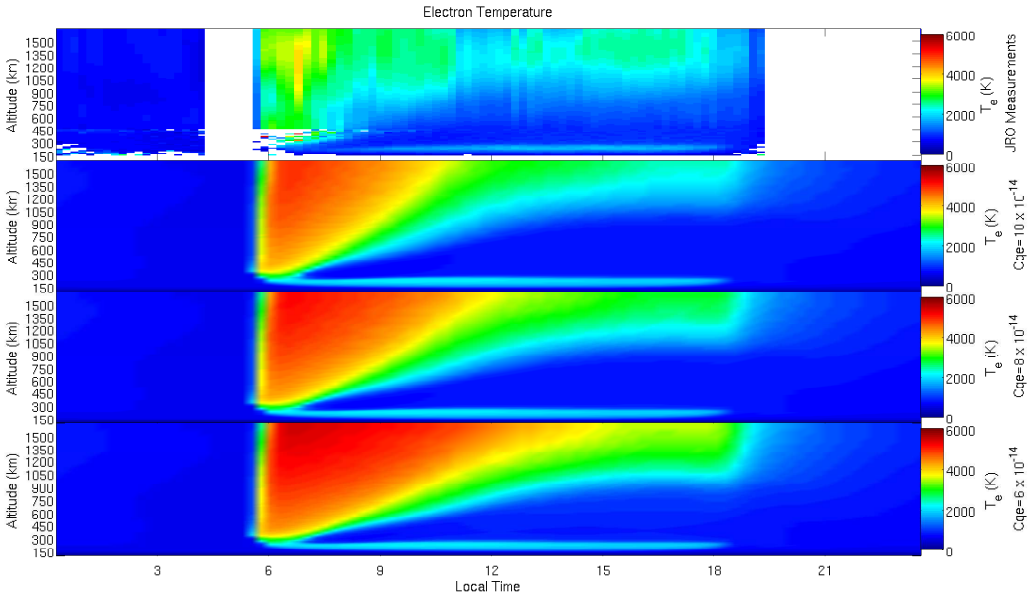

Figure 3.14: RTI plots of measured and modeled electron temperatures on March 25, 2009 in the same format as Fig. 3.13.

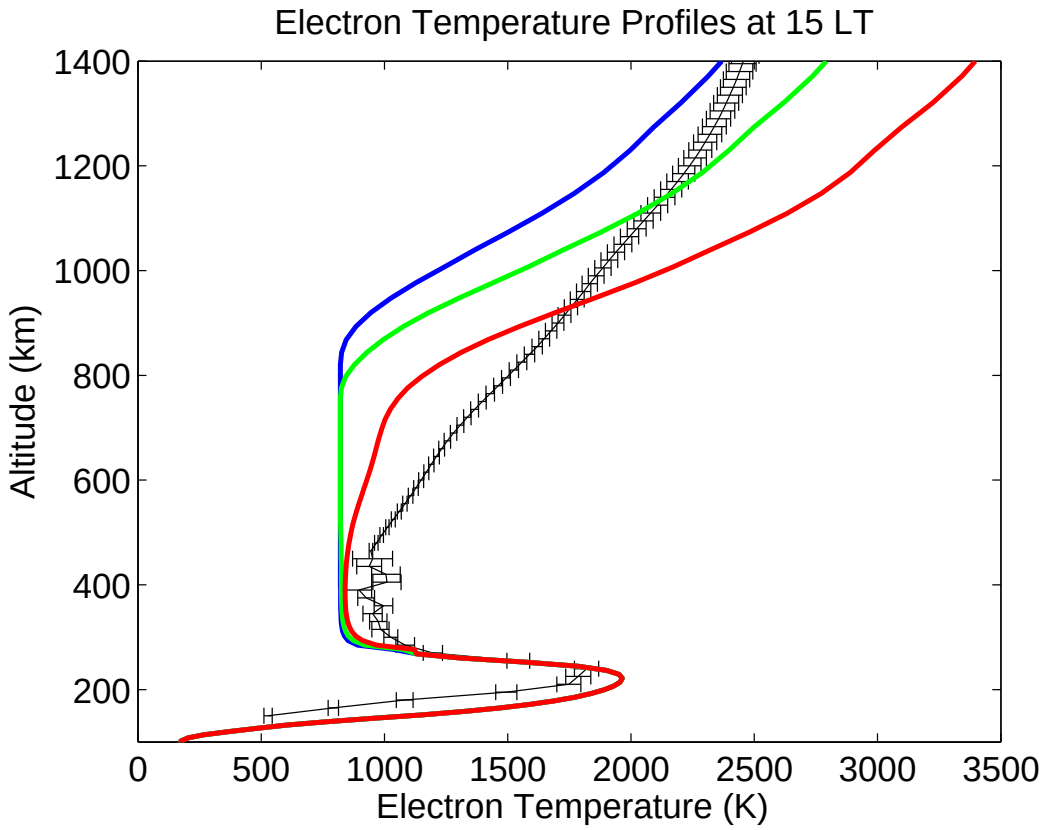

Figure 3.15: Measured and modeled electron temperature profiles above the magnetic equator at 15 LT on March 25, 2009. The black dots with errorbars are the Jicamarca measurements. The solid lines are SAMI2 simulations using different values of C_{qe}.

CHAPTER 4

PHYSICS OF PHOTOELECTRONS

In the development of Ch. 3 photoelectron heating was treated as an external heat source. This chapter seeks a physical description of this heat source by considering the photoelectrons as a portion of the total electron population. Most ionospheric electrons are at energies of ~ 0.2 eV, but the newly produced photoelectrons have typical energies of 10-100 eV. These photoelectrons will be a tiny part of the total electron density, but their relative importance will increase for higher moments of the electron distribution function. A crucial assumption used in Ch. 3 to close the system of fluid equations was that the heat flow vector, a third moment, was small and could be expressed in terms of lower moments of the distribution function. Photoelectrons will make a significant contribution to the heat flow vector, and thus this assumption is not valid. A practical way to proceed is to assume the total electron distribution function can be divided into thermal and suprathermal portions, $f_e = f_{th} + f_{pe}$, where the thermal portion has large low moments but negligible high moments and the suprathermal portion has negligible low moments but significant high moments. Numerous authors have made this division by calling all electrons below a threshold energy "thermal" and all electrons above that energy "suprathermal" [in particular see *Krinberg* [1973] and *Hoegy* [1984] for detailed discussions of this division]. A photoelectron-thermal electron heating rate can only be defined once the total electron population is divided, and thus the value of the heating rate depends on the way the division is performed [*Hoegy*, 1984].

An alternative to the *Hoegy* [1984] method of defining a fixed energy above which all electrons are deemed to be photoelectrons is to look at the relative sizes of the moments of the two parts of the distribution function. We assume that

all moments of f_{th} above the third are negligible such that the fluid equations are a sensible description of the thermal population. Furthermore we assume the zeroth, first, and second moments of f_{pe} are negligible such that $N_e \approx N_{th}$, $N_e \mathbf{u}_e \approx N_{th} \mathbf{u}_{th}$ and $\mathbf{P}_e \approx \mathbf{P}_{th}$. With these assumptions the total electron continuity and momentum equations are unaffected by the photoelectrons. The total electron energy equation can be written as

$$\frac{\partial}{\partial t}\left(\frac{3}{2}p_e\right) + \mathbf{u}_e \cdot \nabla\left(\frac{3}{2}p_e\right) + \frac{5}{2}p_e\left(\nabla \cdot \mathbf{u}_e\right) + \nabla \cdot \left(\mathbf{q}_{th} + \mathbf{q}_{pe}\right) + \tau_e : \nabla \mathbf{u}_e \tag{4.1}$$
$$= Q_{h\nu} + Q_{phe} - Q_{phe} - L_{pe} - L_{th},$$

where $Q_{h\nu}$ is the rate at which the total electron population gains energy from photoionizations, L_{pe} is the rate at which the photoelectron population loses energy, and L_{th} is the rate at which the thermal electron population loses energy. The energy loss term can be separated into two terms because the electron-ion and electron-neutral collision terms are linear in f_e. The term Q_{phe} which is both added and subtracted from the right hand side is the rate at which the thermal electron population gains energy from the photoelectron population. This equation can be separated into two equations,

$$\frac{\partial}{\partial t}\left(\frac{3}{2}p_e\right) + \mathbf{u}_e \cdot \nabla\left(\frac{3}{2}p_e\right) + \frac{5}{2}p_e\left(\nabla \cdot \mathbf{u}_e\right) + \nabla \cdot \mathbf{q}_{th} + \tau_e : \nabla \mathbf{u}_e = Q_{phe} - L_{th} \tag{4.2}$$

$$\nabla \cdot \mathbf{q}_{pe} = Q_{h\nu} - Q_{phe} - L_{pe}, \tag{4.3}$$

where the first equation is a version of Eq. 3.4 for the thermal electrons only. If the third moment of f_{th} is assumed to be small this equation can be closed by assuming the thermal electron heat flow vector, $\mathbf{q}_{th}$, is related to the thermal electron temperature via $\mathbf{q}_{th\parallel} = -\lambda_{th} \nabla_{\parallel} T_{th}$ [*Schunk and Nagy*, 2009]. When discussing collisions with thermal electrons in Sec. 4.3.2 we will approximate the thermal

distribution as Maxwellian, although if we assumed a perfect Maxwellian thermal distribution when deriving the thermal electron energy equation all the physics of thermal diffusion would be lost since Maxwellians have third moments of 0 [*Schunk and Nagy*, 2009]. Eq. 4.3 is not useful because an equation for the photoelectron heat flow vector would involve even higher moments of f_{pe}. The only way to proceed is to use a kinetic equation to solve for f_{pe} directly instead of ever taking its moments. Once f_{pe} is known Q_{phe} can be calculated directly from a moment of the photoelectron-electron collision term (see Sec. 4.3.3).

The practice of dividing the distribution function may not seem to have helped since it still necessitates solving a kinetic equation. However, approximations can be made which make the kinetic equation for f_{pe} substantially easier to solve than the Boltzmann equation for the entire electron gas. In particular, the guiding center approximation can be applied to photoelectrons to reduce the number of phase space variables (see Sec. 4.1) and the nonlinear collision terms representing photoelectron-photoelectron interactions can be neglected relative to the linear collision terms representing photoelectron-electron, photoelectron-ion, and photoelectron-neutral interactions (see Sec. 4.3).

4.1 Photoelectron transport equation in the guiding-center approximation

Numerous authors have derived simplified kinetic equations for photoelectron using a variety of different approaches [see *Walt et al.* [1967], *Mantas* [1975], *Strickland et al.* [1976], *Khazanov et al.* [1994], *Schunk and Nagy* [2009] Sec. 9.4, and references therein for examples]. This section presents a complete derivation which, like

Khazanov et al. [1994], uses the Boltzmann equation in an arbitrary phase space as the starting point.

A general form of a kinetic equation is [e.g. *Krall and Trivelpiece*, 1973; *Ichimaru*, 2004]

$$\frac{df}{dt} = \check{q} + \frac{\delta f}{\delta t}, \tag{4.4}$$

where $f(\mathbf{X})d\mathbf{X}$ is the number of particles between $\mathbf{X}$ and $\mathbf{X} + d\mathbf{X}$ in phase space and $\check{q}$ is the rate at which particles are produced in that phase space element. The term $\frac{\delta f}{\delta t}$ is the rate at which particles enter minus the rate at which particles leave that phase space element due to collisions. The total time derivative on the left hand side is taken along the path a single particle would take in the absence of interactions with other particles. The production function q is discussed in Sec. 4.2 and the collision term $\frac{\delta f}{\delta t}$ is discussed in Sec. 4.3. The remainder of this section is devoted to the left hand side of this equation, which represents the transport of photoelectrons.

The units of these quantities depend on the phase space variables chosen. A common phase space is a set of three position coordinates, $\mathbf{r}$, and three velocity coordinates, $\mathbf{v}$. Expanding the total derivative with the chain rule then substituting the equations of motion of a single electron neglecting gravity yields the familiar form [e.g. *Bellan*, 2006]:

$$\frac{\partial f}{\partial t} + \frac{\partial \mathbf{r}}{\partial t} \cdot \frac{\partial f}{\partial \mathbf{r}} + \frac{\partial \mathbf{v}}{\partial t} \cdot \frac{\partial f}{\partial \mathbf{v}} = \check{q} + \frac{\delta f}{\delta t} \tag{4.5}$$

$$\frac{\partial f}{\partial t} + \mathbf{v} \cdot \frac{\partial f}{\partial \mathbf{r}} - \frac{e}{m}(\mathbf{E} + \mathbf{v} \times \mathbf{B}) \cdot \frac{\partial f}{\partial \mathbf{v}} = \check{q} + \frac{\delta f}{\delta t}. \tag{4.6}$$

Ionospheric problems are naturally described in a phase space which reflects an offset and tilted dipole magnetic field. The velocity coordinates can be expressed in

spherical coordinates relative to the magnetic field, (v, μ, φ), where v is the speed of the electron, $\mu = \cos\theta$ is the cosine of the pitch angle, i.e. the angle between $\mathbf{v}$ and $\mathbf{B}$, and φ is an azimuth angle around the magnetic field. The speed coordinate can be replaced by kinetic energy, $\mathcal{E} = mv^2/2$. Using these coordinates instead of the velocity coordinates, the orthogonal dipolar coordinates, $(s = R_E q_d, p_d, \phi_d)$ instead of the position coordinates, and applying the chain rule to Eq. 4.4 yields a kinetic equation for the photoelectron distribution function.

$$\frac{\partial \tilde{f}}{\partial t} + \frac{\partial s}{\partial t}\frac{\partial \tilde{f}}{\partial s} + \frac{\partial p_d}{\partial t}\frac{\partial \tilde{f}}{\partial p_d} + \frac{\partial \phi_d}{\partial t}\frac{\partial \tilde{f}}{\partial \phi_d} + \frac{\partial \mathcal{E}}{\partial t}\frac{\partial \tilde{f}}{\partial \mathcal{E}} + \frac{\partial \mu}{\partial t}\frac{\partial \tilde{f}}{\partial \mu} + \frac{\partial \varphi}{\partial t}\frac{\partial \tilde{f}}{\partial \varphi} = q + \frac{\delta \tilde{f}}{\delta t}. \tag{4.7}$$

The distribution function in the above equation is defined as the number of photoelectrons per unit volume per unit energy per unit solid angle and has units of $\mathrm{cm}^{-3}\mathrm{eV}^{-1}\mathrm{ster}^{-1}$. The relationship between this distribution function and the distribution function in Eq. 4.6 by can be determined by insisting that both will integrate to the total electron density, i.e.

$$N_e = \int_{-\infty}^{\infty} d\mathbf{v} f = \int_0^{\infty} d\mathcal{E} \int_{-1}^{1} d\mu \int_0^{2\pi} d\varphi \tilde{f}. \tag{4.8}$$

Switching to spherical coordinates in velocity space in the first integral,

$$N_e = \int_0^{\infty} v^2 dv \int_0^{\pi} \sin\theta d\theta \int_0^{2\pi} d\varphi f = \int_0^{\infty} d\mathcal{E} \int_{-1}^{1} d\mu \int_0^{2\pi} d\varphi \tilde{f}, \tag{4.9}$$

then using the definitions $\mu = \cos\theta$, $d\mu = \sin\theta d\theta$, $\mathcal{E} = mv^2/2$, and $d\mathcal{E} = mvdv$ yields

$$N_e = \int_0^{\infty} v^2 dv \int_{-1}^{1} d\mu \int_0^{2\pi} d\varphi f = \int_0^{\infty} mv\, dv \int_{-1}^{1} d\mu \int_0^{2\pi} d\varphi \tilde{f}. \tag{4.10}$$

This equality holds when

$$\tilde{f}(s, p_d, \phi_d, \mathcal{E}, \mu, \varphi) = \frac{v}{m} f(\mathbf{r}, \mathbf{v}) = \frac{2^{1/2}\mathcal{E}^{1/2}}{m^{3/2}} f(\mathbf{r}, \mathbf{v}). \tag{4.11}$$

The new production function, q, and collision operator, $\frac{\delta \tilde{f}}{\delta t}$, are defined in an analogous manner.

The terms in Eq. 4.7 involving time derivatives of a coordinate (e.g. $\frac{\partial s}{\partial t}$) must be determined from the equations of motions of an undisturbed photoelectron. If the electric and magnetic fields are changing slowly in time compared to a gyroperiod and slowly in space compared to the distance the particle travels during one gyroperiod then the guiding center approximation applies and the equations of motions simplify substantially [see *Bellan*, 2006, Ch. 3]. The gyroperiod of an ionospheric electron is $2\pi m_e/(eB) = 1.43 \times 10^{-6}$ s using $B = 0.25 \times 10^{-4}$ T for the magnetic equator. In the ionosphere the electric fields change on time scales of minutes and hours and the magnetic field is dominated by the geomagnetic field which changes on time scales of years. The velocity of a 100 eV electron is 5.93×10^6 m/s, so the distance this electron would travel in a gyroperiod is merely 8.48 m; the spatial variation of the electric and magnetic fields in the ionosphere will be on scales of 10s or 100s of km. Thus the guiding center approximation is easily justified for photoelectrons in the ionosphere. When using the guiding center approximation the distribution function can be assumed to be independent of φ, i.e. $\frac{\partial \tilde{f}}{\partial \varphi} = 0$, thus eliminating one phase space variable entirely.

The remaining five equations of motion needed in Eq. 4.7 are easily obtained from the drift equations [*Bellan*, 2006]. The motion of a photoelectron in the s direction is given by

$$\frac{\partial s}{\partial t} = \frac{ds}{d\ell} v \cos\theta = b_s \mu \sqrt{\frac{2\mathcal{E}}{m}}. \tag{4.12}$$

In the guiding center approximation the first adiabatic invariant [e.g. *Bellan*, 2006],

$$M \equiv \frac{m v_\perp^2}{2B} = \frac{(1-\mu^2)\mathcal{E}}{B}, \tag{4.13}$$

is constant, i.e.

$$0 = \frac{dM}{dt} = \frac{\partial s}{\partial t}\frac{\partial M}{\partial s} + \frac{\partial \mu}{\partial t}\frac{\partial M}{\partial \mu}. \tag{4.14}$$

Differentiating Eq. 4.13, substituting Eq. 4.12, and rearranging yields a second equation of motion,

$$\frac{\partial \mu}{\partial t} = -b_s\sqrt{\frac{2\mathcal{E}}{m}}\frac{(1-\mu^2)}{2B}\frac{\partial B}{\partial s}. \tag{4.15}$$

For a dipole magnetic field the variation of the magnetic field strength obeys [*Schunk and Nagy*, 2009]

$$\frac{b_s}{B}\frac{\partial B}{\partial s} = \frac{1}{B}\frac{\partial B}{\partial \ell} = \frac{1}{r_e}\frac{9\cos\theta_e + 15\cos^3\theta_e}{(1+3\cos^2\theta_e)^{3/2}} \equiv \delta B. \tag{4.16}$$

The terms $\frac{\partial p_d}{\partial t}$ and $\frac{\partial \phi_d}{\partial t}$ are related to the drifts of the photoelectrons perpendicular to **B**. All of these drifts motions are negligibly small compared to the parallel velocity of a photoelectron, so both of these terms are effectively 0. For example, consider a 30 eV photoelectron traveling on a field line whose apex altitude is ∼1000 km. The path length from 300 km altitude in one hemisphere to 300 km altitude in the other along this field line is approximately 6500 km. The parallel velocity of this photoelectron is 5.93×10^5 m/s$\sqrt{\mathcal{E}}\mu = 3.25 \times 10^6\mu$ m/s. If the photoelectron is traveling parallel to **B** (i.e. $\mu = 1$) the trip from one hemisphere to the other takes 2 s. This photoelectron will experience three types of drifts 1) $\mathbf{E} \times \mathbf{B}$ drift, 2) curvature drift, and 3) ∇B drift. The $\mathbf{E} \times \mathbf{B}$ drift experienced by a particle is independent of the velocity. A typical vertical $\mathbf{E} \times \mathbf{B}$ drift in the equatorial ionosphere is 25 m/s, meaning the example photoelectron would only move a total of 50 m during its 2 s journey. The grid cells in the model will be several km wide so this is insignificant.

The curvature drift velocity of an electron is [e.g. *Bellan*, 2006]

$$\mathbf{v}_{curvature} = -\frac{1}{eB^2}\left(\frac{mv_{\parallel}^2\hat{\mathbf{R}}}{R}\right) \times \mathbf{B}, \tag{4.17}$$

where R is the instantaneous radius of curvature of the field line and $\hat{\mathbf{R}}$ is a unit vector pointing from the center of curvature to the point on the field line. In the equatorial plane of the Earth $\hat{\mathbf{R}}$ points upwards and $\mathbf{B}$ points north so $-\hat{\mathbf{R}} \times \mathbf{B}$ points east. In the worst case where $\mu = 1$ the magnitude of this velocity will be $v_{curvature} = 2\mathcal{E}/(eBR)$. Dipole magnetic field lines are circles with diameters equal to R_E plus the apex altitude, so for a field line with an apex altitude of 1000 km, $R = (R_E + 1000)/2 = 3685.5$ km. The magnetic field strength in the equatorial plane is $B = B_0 R_E^3/r^3$ where $B_0 = 0.25 \times 10^{-4}$ T. Thus at 1000 km $B = 0.1614 \times 10^{-4}$. Using these numbers a 30 eV electron would experience a curvature drift of only 1 m/s.

Finally, the ∇B drift experienced by an electron is [e.g. *Bellan*, 2006]

$$\mathbf{v}_{\nabla B} = \frac{mv_{\perp}^2}{2eB^3}\nabla B \times \mathbf{B}. \tag{4.18}$$

In the equatorial plane ∇B points down so $\nabla B \times \mathbf{B}$ points east, just like the curvature drift. Furthermore, in the equatorial plane $\nabla B = \partial B/\partial r = -3B/r$. The worst case for this drift is when $\mu = 0$, in which case the magnitude of the drift is $v_{\nabla B} = 3\mathcal{E}/(eBr)$, which is 0.76 m/s for the example photoelectron considered above.

The final term needed in Eq. 4.7 is $\partial\mathcal{E}/\partial t$, which is the work done on the photoelectrons by electric fields; $\partial\mathcal{E}/\partial t = -e\mathbf{v} \cdot \mathbf{E} = -ev_{\parallel}E_{\parallel}$. The perpendicular electric fields do no work because the perpendicular velocities of the guiding centers are dominated by the $\mathbf{E}\times\mathbf{B}$ drift, which is perpendicular to $\mathbf{E}_{\perp}$. Parallel ambipolar electric fields exist in the equatorial ionosphere due to electron pressure gradients,

but they are too small to have an appreciable impact on photoelectrons. The ambipolar electric field forms to balance ion gravity [*Schunk and Nagy*, 2009]. The steady state ion and electron momentum equations, neglecting the force of gravity on electrons but not on ions, are

$$0 = eE_{\parallel} - \frac{1}{N_e}\nabla p_i - m_i g \cos I \tag{4.19}$$

$$0 = -eE_{\parallel} - \frac{1}{N_e}\nabla p_e, \tag{4.20}$$

where I is the magnetic dip angle. In the simple case where $T_e = T_i$ such that $p_e = p_i$ these equations reduce to

$$E_{\parallel} = \frac{m_i g}{2e} \cos I. \tag{4.21}$$

At 300 km altitude on a field line whose apex altitude is 1000 km $\cos I = 0.2288$ and $g = 8.94$ m/s^2. In an O^+ plasma the ambipolar electric field at this point would be 1.71×10^{-9} V/cm. If this field were constant along the entire half of the field line a photoelectron would lose 0.56 eV over the 3250 km journey from 300 km to the apex at 1000 km. This is an overestimate because as the photoelectron goes up the field line g, $\cos I$ and the mean m_i all decrease. Below it is shown that Coulomb collisions with ambient electrons can be modeled as a retarding force whose typical magnitude is 10^{-8} eV/cm, which is larger than that caused by the ambipolar electric fields.

At higher latitudes the amount of energy lost by a photoelectron as it travels up the field line can be significant. In this case one must account for where this extra energy goes. By Newton's third law, the electric field which retards the photoelectron motion must be simultaneously accelerating the rest of the plasma. This accelerating force can be viewed as an augmentation to the ambipolar electric field created by the suprathermal electrons. The energy lost by the photoelectrons

is thus equal to the mechanical work done by this additional field on the plasma. Suprathermal electron transport including parallel electric fields has been studied in the contexts of the aurora [*Min et al.*, 1993], plasmaspheric refilling [*Liemohn et al.*, 1997] and ion outflows in the polar wind [*Tam et al.*, 1995; *Khazanov et al.*, 1997, 1998; *Tam et al.*, 1998]. This thesis, however, is primarily concerned with the low latitude ionosphere and will ignore these effects.

Inserting the two equations of motion, Eqs. 4.15 and 4.12, into Eq. 4.7 and neglecting all the other terms yields the simplified kinetic equation

$$\frac{\partial \tilde{f}}{\partial t} + b_s \mu \sqrt{\frac{2\mathcal{E}}{m}} \frac{\partial \tilde{f}}{\partial s} - \sqrt{\frac{2\mathcal{E}}{m}} \frac{(1-\mu^2)}{2} \delta B \frac{\partial \tilde{f}}{\partial \mu} = q + \frac{\delta \tilde{f}}{\delta t}. \tag{4.22}$$

Conventionally this equation is written in terms of photoelectron fluxes rather than the distribution function itself. The fluxes are defined as

$$\Phi \equiv \sqrt{\frac{2\mathcal{E}}{m}} \tilde{f}. \tag{4.23}$$

If a unit area element is oriented with its normal in the θ, φ direction, then Φ is the number of electrons crossing this area element at normal incidence per unit energy per second per unit solid angle. Fluxes defined this way have units of $\mathrm{cm}^{-2}\mathrm{s}^{-1}\mathrm{eV}^{-1}\mathrm{ster}^{-1}$. Using these fluxes, switching spatial coordinates from s to the true distance traveled along a field line, ℓ, and rearranging terms transforms the simplified kinetic equation, Eq. 4.22, into the form of a conservation law with net source terms:

$$\sqrt{\frac{m}{2\mathcal{E}}} \frac{\partial \Phi}{\partial t} + \mu \frac{\partial \Phi}{\partial \ell} - \delta B \frac{\partial}{\partial \mu} \left[\frac{1-\mu^2}{2} \Phi \right] = \mu \delta B \Phi + q + \frac{1}{v} \frac{\delta \Phi}{\delta t}. \tag{4.24}$$

The new term which appears on the right hand side, $\mu \delta B \Phi$, increases the photoelectron flux as the field lines grow closer together. The new collision term $\frac{1}{v}\frac{\delta \Phi}{\delta t}$ is identical to $\frac{\delta \tilde{f}}{\delta t}$. This alternate notation is used, however, to emphasize that this

term is the rate at which the photoelectron flux changes per unit distance traveled. The units of the collision term are the units of Φ divided by length.

4.2 Production of suprathermal electrons

The primary source of suprathermal electrons in the ionosphere is photoionization by solar EUV and soft X-rays [see *Schunk and Nagy*, 2009, Ch. 9 for an overview]. The determination of the production rate of photoelectrons requires three steps: specification of the EUV spectrum outside of the atmosphere (Sec. 4.2.1), calculation of the EUV spectrum at a given point inside the atmosphere (Sec. 4.2.2), and calculation of the energy dependent production rate of photoelectrons from the EUV spectrum (Sec. 4.2.3). Suprathermal electrons can also be produced by energetic electron impact, which is discussed below as part of the discussion of inelastic collisions (Sec. 4.3.1). A third source of suprathermal electrons is the quenching of metastable excited neutral species (Sec. 4.2.5). All three of these terms are summed to produce the production function, q, in Eq. 4.24.

4.2.1 The solar EUV spectrum

We specify the EUV spectrum outside of the atmosphere, $F_\infty(\lambda)$, using a version of the empirical HEUVAC model [*Richards et al.*, 2006]. HEUVAC is based on the measured F74113 solar reference spectrum with scaling factors applied based on the F10.7 solar radio flux index. We have adapted the standard HEUVAC model such that we can specify both wavelength bins and individual lines. We use one hundred and five 1 nm wide bins from 1.8 nm to 105.0 nm and eighteen individual

Bright Solar Lines		
Wavelength (nm)	Energy (eV)	Ion(s)
25.630	48.4	Si X - He II
28.415	43.6	Fe XV
30.331	40.9	Si XI
30.378	40.8	He II
33.541	37.0	Fe XVI
36.807	33.7	Mg IX
46.522	26.7	Ne VIII
55.437	22.4	O VI
58.433	21.2	He I
60.976	20.3	Mg X
62.973	19.7	O V
70.336	17.6	O III
76.515	16.2	N IV
77.041	16.1	Ne VIII
78.771	15.7	O IV
79.015	15.7	O IV
97.702	12.7	C III
102.572	12.1	H I (Lyman-β)

Table 4.1: Wavelengths of important lines in the solar EUV spectrum and their associated ions.

lines. These lines correspond to exceptionally bright lines in the solar spectrum associated with specific ionic transitions. The line wavelengths and their associated ions are tabulated in Table 4.1. Each of these lines is regarded as a special line in HEUVAC and given its own scaling factors.

The modeled solar flux on our wavelength grid is plotted in Fig. 4.1 for a variety of different F10.7 values. The shape of the spectrum is complicated but remains relatively constant with solar activity. By far the brightest line is the He II line at 30.4 nm (40.8 eV). Also of note is the abrupt order of magnitude drop at below 17 nm (above 73 eV). Later we will show that these two features of the solar spectrum have obvious signatures in the photoelectron spectra.

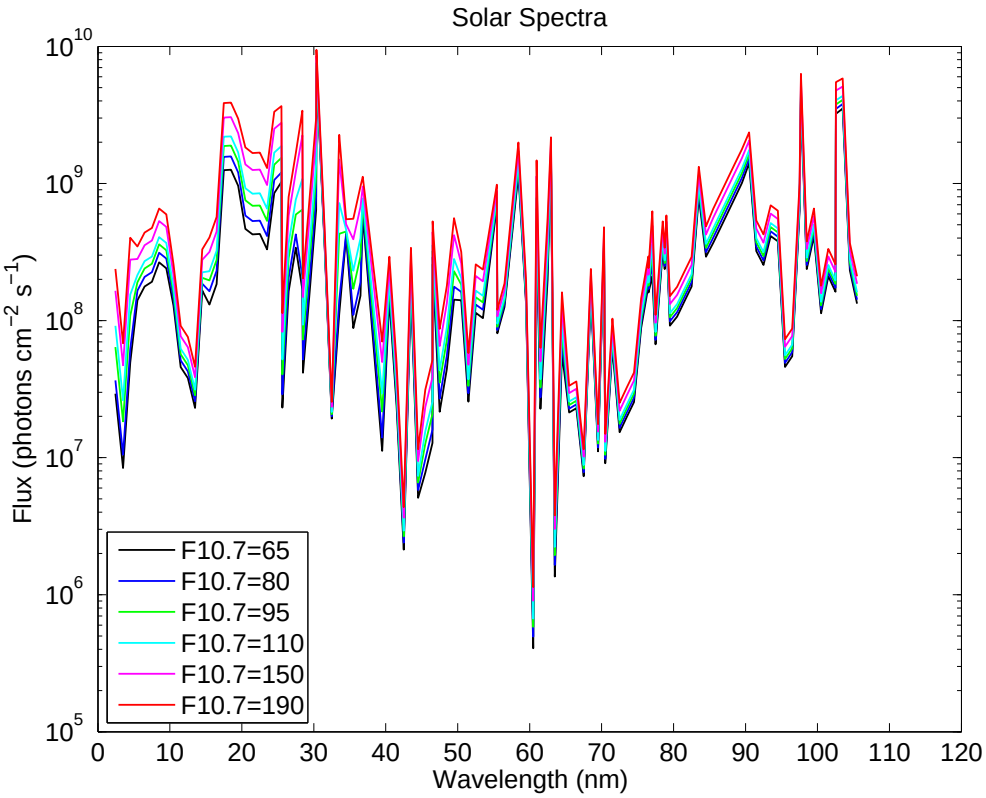

Figure 4.1: HEUVAC solar spectra at the resolution used in SAMI2-PE for a variety of different F10.7.

4.2.2 Transport and absorption of solar EUV in the atmosphere

The scattering of solar EUV is negligible compared to its absorption, meaning the flux inside the atmosphere can be modeled with the simple Beer-Lambert law [*Schunk and Nagy*, 2009]

$$\frac{dF(\lambda)}{d\zeta} = \sum_n \sigma_n^{abs}(\lambda) N_n(z) F(\lambda), \tag{4.25}$$

where $\sigma_n^{abs}(\lambda)$ is the absorption cross section associated with neutral species n at wavelength λ and ζ is a spatial coordinate which increases along the line from the point of interest towards the sun. The attenuated EUV flux inside the atmosphere

is computed as

$$F(\lambda) = F_\infty(\lambda) \exp\left[-\sum_n \sigma_n^{abs}(\lambda) \int_{\zeta_0}^{\infty} N_n(z)\, d\zeta \right]. \tag{4.26}$$

Numerically evaluating the integral in the exponential term is computationally expensive and requires a 3-D specification of the neutral density profiles. A simple approximation is to assume a plane stratified atmosphere (i.e. a flat Earth with no horizontal gradients). In this case $d\zeta = dz \sec\chi$, where χ is the solar zenith angle, and

$$\int_{\zeta_0}^{\infty} N_n(z)\, d\zeta \approx \int_{z_0}^{\infty} N_n(z) \sec\chi\, dz. \tag{4.27}$$

If it is further assumed that the neutral scale height, H, is constant such that $N_n(z) = N_n(z_0)\exp(-(z - z_0)/H)$ then this integral can be expressed in closed form;

$$\int_{z_0}^{\infty} N_n(z) \sec\chi\, dz \approx N_n(z_0) H \sec\chi. \tag{4.28}$$

A better approximation is to still assume that the neutral densities only depend on altitude and the scale height is constant, but to use a spherical planet. In this approximation

$$\int_{\zeta_0}^{\infty} N_n(z)\, d\zeta \approx N_n(z_0) H(z_0) \mathrm{Ch}(z_0, \chi), \tag{4.29}$$

where $\mathrm{Ch}(z_0, \chi)$ is the Chapman grazing incidence function [*Chapman*, 1931]. SAMI2 uses this approximation and computes the Chapman grazing incidence function numerically using the algorithm of *Smith and Smith* [1972].

In SAMI2 only considers photoabsorption from O, O_2, and N_2. The photoabsorption cross sections for these species have been tabulated at high resolution by *Fennelly and Torr* [1992]. For SAMI2-PE we construct photoabsorption cross sections for each bin in our solar spectrum from flux weighted averages of the high

resolution cross sections from *Fennelly and Torr* [1992] over the wavelength bins. Fig. B.1 presents an example of these cross sections when a reference spectrum with F10.7=80 is used to do the flux weighted averages.

Although small, the scattering of solar EUV is not precisely 0, meaning some solar EUV can scatter around the planet into the nightside. At night SAMI2 computes the intensity of scattered radiation at 102.6 (Lyman β), 58.4 (He I), and 30.4 nm (He II) using a model developed by *Strobel et al.* [1974]. Unfortunately the daytime and nighttime EUV fluxes produced by the original code in SAMI2 do not smoothly connect to each other; the daytime routine when the sun is just above the horizon produces much lower results than the nighttime routine when the sun is just below the horizon. In the present work we have resolved this issue by adding an extra contribution to the daytime results equal to the nighttime results evaluated with the sun at the critical solar zenith angle. This extra contribution is negligible throughout most of the day, but guarantees continuity at sunrise and sunset. In practice the electron heating and secondary production produced by photoelectrons arising from photoionization at night are negligibly small and can be ignored to expedite the calculations.

4.2.3 Photoionization processes

For a given EUV spectrum inside the atmosphere, the number of photoelectrons with energy $\mathcal{E}$ produced per unit volume per steradian per second by a single photoionization process of neutral species n is

$$q_n^p = \Upsilon(\theta, \varphi)\sigma_n^p(\lambda_p)N_n(\ell)F(\lambda_p) \tag{4.30}$$

where $\sigma_n^p(\lambda_p)$ is the photoionization cross section for species n at wavelength λ_p for the process p and $\Upsilon(\theta, \varphi)$ is a function with units of ster^{-1} which defines the pitch angle distribution of the newly produced photoelectrons (see Sec. 4.2.4). For an isotropic distribution $\Upsilon(\theta, \varphi) = 1/(4\pi)$. The energy of the resultant photoelectron is related to the wavelength λ_p by

$$\mathcal{E} = \frac{hc}{\lambda_p} - T_p \tag{4.31}$$

where h is Planck's constant, c is the speed of light, and T_p is the appropriate photoionization threshold for the process in question. In general there will be multiple photoionization processes for each neutral species. We consider all of the processes for O, O_2, and N_2 tabulated in *Conway* [1988]. For wavelengths shorter than 2.3 nm we use the cross sections from *Conway* [1988] directly. For longer wavelengths we use the higher resolution cross sections from *Fennelly and Torr* [1992]. *Fennelly and Torr* [1992] do not enumerate partial cross sections for all of the various processes for O_2 and N_2, so we construct these cross sections by weighting the *Fennelly and Torr* [1992] cross sections by branching ratios inferred from *Conway* [1988]. We also consider photoionization of He and N in the model, but do not bother to consider all of the different branching ratios for these minor species. All ionizations of these species are considered to have thresholds equal to the ionization thresholds of these species, 24.6 and 14.4 eV respectively. The N cross sections used come from *Fennelly and Torr* [1992] and the He cross sections come from *Kirby et al.* [1979]. The high resolution cross sections for all of these processes are adapted to the moderate resolution wavelength grid used for the solar spectrum by computing flux weighted averages over each bin, just like absorption cross sections in Fig. B.1. Figs. B.2, B.3, B.4, B.5, and B.6 plot the flux averaged partial photoionization cross sections for all of the photoionization processes of O, O_2, N_2 considered using the solar spectrum at F10.7=80 for the averages.

Furthermore, Fig. B.7 plots the flux weighted total ionization cross sections which are used to compute the ion production rates. For the molecular species non-dissociating ionizations (e.g. $O_2 + h\nu \rightarrow O_2^+ + e^*$) are separated from dissociating ionizations (e.g. $O_2 + h\nu \rightarrow O^+ + O + e^*$).

The electrons in atoms like O and N are arranged in two energy shells, which are called the K-shell and L-shell in X-ray notation. Most of the important photoionization processes involve the ejection of L-shell (valence) electrons. However, soft X-rays can be sufficiently energetic to remove K-shell electrons. The K-shell binding energies are 400 eV for N and 537.1 eV for O. Atoms with a missing K-shell electron are extremely unstable; a L-shell electron will quickly transition into the K-vacancy. The K-shell is at a much lower potential than the L-shell, so this transition must involve an extra release of energy. The atom could release this energy by emitting an X-ray, but it is far more probable for the atom to eject a second L-shell electron with the necessary amount of kinetic energy. This is known as the Auger effect and the second ejected electron is known as an Auger electron. Specifically the process described would be labeled as a K-LL Auger process. *Moddeman et al.* [1971] review K-LL Auger processes and present detailed measurements of the Auger spectra of several gases, including N_2 and O_2. The Auger spectra typically consist of a single "normal" line and several weaker "satellite" lines. The "normal" lines correspond to cases when the orbitals of all the other electrons in the atom are not disturbed when the K-vacancy is formed. The numerous "satellite" lines correspond to cases where the formation of the K-vacancy is accompanied by the excitation of other electrons. The "normal" and "satellite" lines span a relatively small range of energies ($\sim$50 eV), and thus for aeronomical calculations it is sufficient to assume that all Auger electrons are produced at the energy of the "normal" line (362 eV for N and 500 eV for O) [*Winningham et al.*,

1989]. [*Winningham et al.*, 1989] have shown that the inclusion of these Auger electrons, particularly those at 362 eV produced from ionization of N_2, is essential to accurately capturing the high energy (> 60 eV) portion of the photoelectron spectrum.

4.2.4 Angular distribution of newly produced photoelectrons

Photoelectrons are not produced isotropically, but rather are ejected with an angular probability distribution which is peaked in the direction of the electric field of the incident electromagnetic wave and is zero in both the directions parallel to wavevector and parallel to the magnetic field of the wave. In the non-relativistic limit this probability distribution is

$$\Psi(\vartheta, \psi) = \frac{3}{8\pi} \sin^2 \vartheta \cos^2 \psi, \tag{4.32}$$

where ϑ is the angle between the wavevector and the photoelectron velocity and ψ is the angle between the electric field and the photoelectron velocity [*Heitler*, 1954]. For randomly polarized light the dependence on ψ disappears. This can be written as

$$\begin{aligned} \Psi(\theta, \varphi) = \frac{3}{8\pi}(1 &- \cos^2 \theta \cos^2 \beta \\ &- 2 \cos\theta \sin\theta \cos\varphi \sin\beta \cos\beta \\ &- \sin^2 \theta \cos^2 \varphi \sin^2 \beta), \end{aligned} \tag{4.33}$$

where β is the angle between the magnetic field and $\hat{\zeta}$, which is a vector pointing from the point of interest towards the sun, θ is the angle between the photoelectron velocity vector and the magnetic field, and φ is the angle between the photoelectron

velocity vector and $\hat{\zeta} \times \mathbf{B}$. Fast gyromotions will randomize the photoelectron distribution in φ, so

$$\begin{aligned}\Upsilon(\mu) &= \frac{1}{2\pi}\int_0^{2\pi} \Psi(\mu,\varphi)\, d\varphi \\ &= \frac{3}{16\pi}\left[1+\cos^2\beta+\left(1-3\cos^2\beta\right)\mu^2\right], \end{aligned} \tag{4.34}$$

which is equivalent to the result derived by *Mariani* [1964]. In terms of the solar zenith angle, χ, the solar azimuth angle, δ, the magnetic dip angle, I, and the magnetic declination angle D,

$$\begin{aligned}\cos\beta =& \sin\chi\sin\delta\cos I\sin D + \sin\chi\cos\delta\cos I\cos D \\ &- \cos\chi\sin I. \end{aligned} \tag{4.35}$$

4.2.5 Quenching of excited species such as $\mathrm{N}(^2\mathrm{D})$

The excited species $\mathrm{N}(^2\mathrm{D})$ has a radiative lifetime of close to one day, so it is primarily de-excited by inelastic collisions with other neutral species and electrons [*Richards*, 1986]. When a thermal electron collides with $\mathrm{N}(^2\mathrm{D})$ it gains 2.4 eV and is thus promoted into the photoelectron population. The average energy of the promoted electrons is thus $k_B T_e + 2.4$ eV. For simplicity we neglect the width of the thermal distribution and assume all the promoted electrons appear at this average energy. With this assumption the production rate due to quenching is

$$q^{quench} = \frac{1}{4\pi} k_1 N_{\mathrm{N}(^2\mathrm{D})} N_e \delta\left(\mathcal{E} - k_B T_e - 2.4\text{ eV}\right) \tag{4.36}$$

where k_1 is the reaction rate for $\mathrm{N}(^2\mathrm{D}) + \mathrm{e} \rightarrow \mathrm{N}(^4\mathrm{S}) + \mathrm{e} + 2.4$ eV [*Richards*, 1986]. The factor of $1/(4\pi)$ is for an isotropic pitch-angle distribution. Typically this extra heat source has the largest effect in the lower F-region ($\sim$240 km) [*Richards*, 1986].

Chemical Reactions Involving $N(^2D)$	
Reaction	Rate (cm^3s^{-1})
$N_2^+ + O \rightarrow NO^+ + N(^2D)$	$\beta_1 = 1.4 \times 10^{-10} \left(\frac{300}{T_n}\right)^{0.44}$
$N_2^+ + e \rightarrow 2N(^2D)$	$\beta_2 = 2.1 \times 10^{-7} \left(\frac{300}{T_e}\right)^{0.39}$
$NO^+ + e \rightarrow O + N(^2D)$	$\beta_3 = 3.4 \times 10^{-7} \left(\frac{300}{T_e}\right)^{0.85}$
$N(^2D) + e \rightarrow N(^4S) + e^*$	$k_1 = 6.5 \times 10^{-10} \left(\frac{T_e}{300}\right)^{0.5}$
$N(^2D) + O \rightarrow N(^4S) + O$	$k_2 = 6.0 \times 10^{-13}$
$N(^2D) + O_2 \rightarrow NO + O$	$k_3 = 6.0 \times 10^{-12}$

Table 4.2: Chemical reactions involving $N(^2D)$ and their reaction rates [*Aponte et al.*, 1999].

SAMI2 does not solve for the density of $N(^2D)$, but this density is easy to estimate if $N(^2D)$ is assumed to be in local equilibrium. The reactions which create and destroy $N(^2D)$ and their reaction rates are tabulated in Table 4.2. In terms of these rates the steady state density of $N(^2D)$ is [*Aponte et al.*, 1999]

$$N_{N(^2D)} = \frac{\beta_1 N_{N_2^+} N_O + 2\beta_2 N_{N_2^+} N_e + \beta_2 N_{NO^+} N_e}{k_1 N_e + k_2 N_O + k_3 N_{O_2}}. \tag{4.37}$$

The density of $N(^2D)$ is indirectly coupled to the densities of many other species through all the chemical processes that can produce NO^+ and N_2^+ [see *Huba et al.*, 2000a, for a complete list of the reactions in SAMI2]. The density of neutral NO is particularly important since NO participates in several charge exchange reactions which produce NO^+. The NRLMSISE-00 model does not predict the density of neutral NO so SAMI2 estimates it using the empirical model [*Mitra*, 1968; *Bailey and Balan*, 1996]

$$N_{NO} = 0.4 \exp\left(-\frac{3700}{T_n}\right) N_{O_2} + 5 \times 10^{-7} N_O \text{ cm}^{-3}. \tag{4.38}$$

In reality the neutral NO density in the lower thermosphere is highly variable and has been the subject of several modeling studies [see *Barth et al.*, 2003; *Bailey et al.*,

2002, and references therein]. The *Mitra* [1968] empirical model was originally created using D-region data, so its applicability to the lower F-region is suspect. A more recent model for the NO density has been developed by *Marsh et al.* [2004] which fits empirical orthogonal functions to the Student Nitric Oxide Explorer (SNOE) satellite measurements. Unfortunately, the SNOE measurements only cover the altitude region from 97.5 km to 150 km, so this model cannot predict the NO density in the lower F-region.

4.3 Photoelectron collision processes

The rate of change of the distribution function of species s due to collisions with species t in the conventional $(\mathbf{r}, \mathbf{v})$ phase space is given by the well known Boltzmann collision integral [e.g. *Schunk and Nagy*, 2009]

$$\frac{\delta f_s}{\delta t} = \int d\mathbf{v}_t' d\Omega dT \sigma_{st}(g_{st}, \alpha, T) g_{st}(f_s(\mathbf{v}_s) f_t(\mathbf{v}_t) - f_s(\mathbf{v}_s') f_t(\mathbf{v}_t')), \tag{4.39}$$

where $g_{st} = |\mathbf{v}_s' - \mathbf{v}_t'|$ is the relative velocity before the collision and $\sigma_{st}(g_{st}, \alpha, T) d\Omega dT$ is the partial cross section for the collision process in question. In general this cross section is a function of the relative velocity, the scattering angle, α, and the change in energy caused by the collision, T. The velocities $\mathbf{v}_s'$ and $\mathbf{v}_t'$ are before the collision and $\mathbf{v}_s$ and $\mathbf{v}_t$ are after the collision (note that *Schunk and Nagy* [2009] use the opposite convention for the primed and unprimed velocities). In general the Boltzmann collision integral is a complicated nonlinear operator, but for collisions involving photoelectrons in the ionosphere several simplifying limits apply.

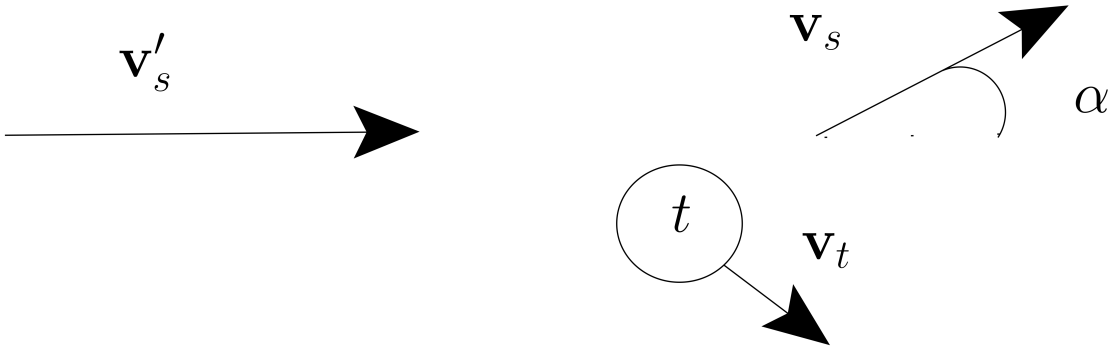

Figure 4.2: Scattering geometry for a binary collision.

4.3.1 Collisions with Neutrals

Mantas [1975] presents a compact derivation of the photoelectron-neutral collision term. In this section we will show that this result can also be obtained by manipulating the Boltzmann collision integral.

For the collision geometry illustrated in Fig. 4.2, in the frame of reference where $\mathbf{v}_t' = 0$, conservation of momentum requires that

$$m_s v_s' = m_t v_{tx} + m_s v_s \cos\alpha \rightarrow v_{tx} = \frac{m_s}{m_t}\left(v_s' - v_s \cos\alpha\right) \tag{4.40}$$

$$0 = m_t v_{ty} + m_s v_s \sin\alpha \rightarrow v_{ty} = -\frac{m_s}{m_t} v_s \sin\alpha. \tag{4.41}$$

In the case of electron-neutral collisions, $m_s/m_t \ll 1$, so both components of $\mathbf{v}_t$ will be negligibly small.

Furthermore, photoelectrons move so much faster than the neutrals that both the mean and random thermal velocities of the neutrals can be ignored. In this approximation the neutral distribution function can be written as a delta function

$$f_t(\mathbf{v}_t') = N_t \delta(\mathbf{v}_t'). \tag{4.42}$$

Inserting this into the Boltzmann collision integral and taking the integral over $\mathbf{v}_t'$

yields

$$\frac{\delta f_s}{\delta t} = -N_t \mathbf{v}'_s f_s(\mathbf{v}'_s) \int d\Omega dT \sigma_{st}(\mathbf{v}'_s, \alpha, T) + N_t \int d\Omega dT \sigma_{st}(\mathbf{v}'_s, \alpha, T) \mathbf{v}'_s f(\mathbf{v}_s). \tag{4.43}$$

In the second term the distribution function cannot be taken out of the integral because the velocity after the collision depends on both the scattering angle and the change in energy caused by the collision. The first term in this expression is the rate at which electrons scatter out of a phase space element, and the second term is the rate at which electrons scatter into the a phase space element from all other possible phase space elements. Using the definitions $\Phi = v^2/mf$ and $\frac{1}{v}\frac{\delta \Phi}{\delta t} = \frac{v}{m}\frac{\delta f}{\delta t}$ and changing the coordinates from $\mathbf{v}_s$ and α to energy and pitch angle, this operator can be rewritten as

$$\frac{1}{v}\frac{\delta \Phi}{\delta t} = -N_t \Phi(\ell, \mathcal{E}, \mu) \frac{1}{2} \int_{\mathcal{E}}^{\infty} d\mathcal{E}' \int_{-1}^{1} d\mu' \sigma_{st}(\mathcal{E}', \mathcal{E}, \mu', \mu) + \tag{4.44}$$

$$N_t \frac{1}{2} \int_{\mathcal{E}}^{\infty} d\mathcal{E}' \int_{-1}^{1} d\mu' \sigma_{st}(\mathcal{E}', \mathcal{E}, \mu', \mu) \Phi(\ell, \mathcal{E}', \mu'), \tag{4.45}$$

where $\mathcal{E}'$ and μ' are the energy and pitch-angle cosine before the collision and $\mathcal{E}$ and μ are the energy and pitch-angle cosine after the collision. The lower bounds of the integrals over $\mathcal{E}'$ will be $\mathcal{E}$ instead of 0 in the case where collisions cannot increase the energy of a photoelectron (i.e. $\mathcal{E}' \geq \mathcal{E}$). For the special case of elastic collisions the partial cross sections will be of the form

$$\sigma_{st}(\mathcal{E}', \mathcal{E}, \mu', \mu) = \sigma_e(\mathcal{E}, \mu', \mu) \delta(\mathcal{E}' - \mathcal{E}), \tag{4.46}$$

meaning that for elastic collisions the collision operator simplifies to

$$\frac{1}{v}\frac{\delta \Phi}{\delta t} = -N_t \Phi(\ell, \mathcal{E}, \mu) \frac{1}{2} \int_{-1}^{1} d\mu' \sigma_e(\mathcal{E}, \mu', \mu) + \tag{4.47}$$

$$N_t \frac{1}{2} \int_{-1}^{1} d\mu' \sigma_{st}(\mathcal{E}, \mu', \mu) \Phi(\ell, \mathcal{E}, \mu'). \tag{4.48}$$

In general there are a multiples different neutral species, and multiple different types of collision processes associated with each species. The full electron-neutral collision operator is a sum over all processes and species [c.f. *Mantas*, 1975; *Strickland et al.*, 1976],

$$\left[\frac{1}{v}\frac{\delta\Phi}{\delta t}\right]_n = -\sum_n(\bar{\sigma}_{an}+\bar{\sigma}_{en})N_n\Phi(\ell,\mathcal{E},\mu) + \sum_n N_n\frac{1}{2}\int_{-1}^{1}d\mu'\sigma_{en}(\mathcal{E},\mu',\mu)\Phi(\ell,\mathcal{E},\mu') + \sum_{n,p} N_n\frac{1}{2}\int_{\mathcal{E}}^{\infty}d\mathcal{E}'\int_{-1}^{1}d\mu'\sigma_{an}^{p}(\mathcal{E}',\mathcal{E},\mu',\mu)\Phi(\ell,\mathcal{E}',\mu'). \tag{4.49}$$

We have adopted the notation $\sigma_{an}^{p}(\mathcal{E}',\mathcal{E},\mu',\mu)$ for the partial cross section for inelastic collisions which move photoelectrons from $(\mathcal{E}',\mu')$ to $(\mathcal{E},\mu)$ through inelastic process p with neutral species n. The partial elastic cross section, $\sigma_{en}(\mathcal{E},\mu',\mu)$, is defined in an analogous manner. The total cross sections at $(\mathcal{E},\mu)$ are the sums over all processes of the integrals of the partial cross sections over all energies and pitch angles, $(\mathcal{E}'',\mu'')$, to which a photoelectron could go, i.e.

$$\bar{\sigma}_{an}(\mathcal{E},\mu) \equiv \sum_p \frac{1}{2}\int_0^{\mathcal{E}}d\mathcal{E}''\int_{-1}^{1}d\mu''\sigma_{an}^{p}(\mathcal{E},\mathcal{E}'',\mu,\mu'') \tag{4.50}$$

$$\bar{\sigma}_{en}(\mathcal{E},\mu) \equiv \frac{1}{2}\int_{-1}^{1}d\mu''\sigma_{en}(\mathcal{E},\mu,\mu'') \tag{4.51}$$

In this study we will follow *Stolarski* [1972] and *Swartz* [1976] and only consider the simple case of isotropic scattering from collisions. In this case the partial cross sections are independent of μ' and μ, so the collision operator simplifies to

$$\left[\frac{1}{v}\frac{\delta\Phi}{\delta t}\right]_n = -\sum_n(\bar{\sigma}_{an}+\bar{\sigma}_{en})N_n\Phi(\ell,\mathcal{E},\mu,t) + \sum_n \bar{\sigma}_{en}N_n\frac{1}{2}\int_{-1}^{1}d\mu'\Phi(\ell,\mathcal{E},\mu',t) + \sum_{n,p} N_n\int_{\mathcal{E}}^{\infty}d\mathcal{E}'\sigma_{an}^{p}(\mathcal{E}',\mathcal{E})\frac{1}{2}\int_{-1}^{1}d\mu'\Phi(\ell,\mathcal{E}',\mu',t). \tag{4.52}$$

Stamnes [1980] has investigated the use of anisotropic elastic and inelastic collisions for calculations involving auroral electrons, but the expressions used in that study are only valid when $\mathcal{E} > 1$ keV. Exact forms of the phase function for lower energies are not known, but should be very nearly isotropic.

The final term in Eq. 4.52 represents the cascade production of photoelectrons with energy $\mathcal{E}$ from other energies. The cascade production can be computed once all the fluxes at higher energies are known. Thus the photoelectron transport equations can be solved one energy at a time, working downwards in energy. The energy redistribution algorithm for computing the cascade production is described in Sec. 5.2, and while solving the photoelectron transport equation at a given energy this term is combined with all of the other production terms in q. The quantity called $\hat{q}$ in Ch. 2 is the sum of what has been called q throughout this chapter with this final cascade production term.

Throughout this thesis the subscript x appearing on the letter σ will be used for inelastic collisions which excite but do not ionize the neutral, i will be used for ionizing collisions, and a will be used for either variety. For ionizing collisions the final term in Eq. 4.52 only accounts for the degraded primaries. The secondary production at energy $\mathcal{E}_s$ is included as part of q, and can be written as

$$q^{sec}(\mathcal{E}_s) = \sum_{n,p} N_n \int_{T_p}^{\infty} d\mathcal{E}' \sigma_{in}^{p}(\mathcal{E}', \mathcal{E}' - T_p - \mathcal{E}_s) \frac{1}{2} \int_{-1}^{1} d\mu' \Phi(\ell, \mathcal{E}', \mu', t), \qquad (4.53)$$

where T_p is the ionization threshold for process p.

For all of the elastic and inelastic collisions with neutrals, only atomic oxygen, molecular oxygen, and molecular nitrogen are considered. The empirical expressions, tables of parameters, and plots of the cross sections are all in Appendix C

4.3.2 Photoelectron collisions with the ambient plasma

Coulomb collisions between electrons and between electrons and ions are long range interactions which nearly always result in small angle changes. Instead of using the Boltzmann collision integral, which assumes binary interactions, Coulomb collisions are traditionally described using a Fokker-Planck collision operator which models the net effects of a large number of small angle collisions. The appendix of *Khazanov et al.* [1994] presents a brief derivation of an approximate form of the Fokker-Planck operator for photoelectrons. This section repeats that derivation and shows many of the detailed intermediate steps.

For ordinary Coulomb collisions in a warm plasma the rate of change of the distribution function of species T as a result of all field particles F is [see *Bellan*, 2006, Ch. 13 for a complete derivation]

$$\frac{\delta f_T}{\delta t} = \sum_{F=i,e} \mathcal{F}\left(f_T, f_F\right) \tag{4.54}$$

where the Fokker-Planck operator is

$$\mathcal{F}\left(f_T, f_F\right) = \frac{e^4 \ln\Lambda}{4\pi\epsilon_0^2 m_T^2}\left[-\frac{\partial}{\partial \mathbf{v}}\cdot\left(f_T\frac{\partial h_F}{\partial \mathbf{v}}\right) + \frac{1}{2}\frac{\partial}{\partial \mathbf{v}}\frac{\partial}{\partial \mathbf{v}} : \left(f_T\frac{\partial^2 g_F}{\partial \mathbf{v}\partial \mathbf{v}}\right)\right] \tag{4.55}$$

and the Rosenbluth potentials, h_F and g_F, are linear functions of f_F [*Rosenbluth et al.*, 1957];

$$h_F(\mathbf{v}) = \left(1 + \frac{m_T}{m_F}\right)\int \frac{f_F(\mathbf{v}')}{|\mathbf{v}-\mathbf{v}'|}\, d\mathbf{v}' \tag{4.56}$$

$$g_F(\mathbf{v}) = \int |\mathbf{v}-\mathbf{v}'| f_F(\mathbf{v}')\, d\mathbf{v}'. \tag{4.57}$$

The dependencies of the Rosenbluth potentials on the distributions functions means that in general Fokker-Planck equations are nonlinear. However, the fact that the Rosenbluth potentials are linear in the distribution functions means that

if the total electron distribution function is the sum of a thermal distribution and a photoelectron distribution, $f_e = f_{th} + f_{pe}$, then the total electron collision term can be neatly separated into a thermal electron term and a photoelectron term;

$$\frac{\delta f_e}{\delta t} = \frac{\delta f_{th}}{\delta t} + \frac{\delta f_{pe}}{\delta t} \tag{4.58}$$

$$\frac{\delta f_{th}}{\delta t} = \mathcal{F}\left(f_{th}, f_{th}\right) + \mathcal{F}\left(f_{th}, f_i\right) + \mathcal{F}\left(f_{th}, f_{pe}\right) \tag{4.59}$$

$$\frac{\delta f_{pe}}{\delta t} = \mathcal{F}\left(f_{pe}, f_{th}\right) + \mathcal{F}\left(f_{pe}, f_i\right) + \mathcal{F}\left(f_{pe}, f_{pe}\right). \tag{4.60}$$

The first two terms in $\frac{\delta f_{pe}}{\delta t}$ are linear in f_{pe} whereas the final term is nonlinear. However, if the total photoelectron density is much less than the total thermal electron density this final term will be small compared to the first term and may be neglected. If f_{th} and f_i are furthermore assumed to be Maxwellians then $\frac{\delta f_{pe}}{\delta t}$ can be expressed as a linear function of f_{pe} which depends on the electron and ion densities and temperatures.

When the distribution function of the field particles is isotropic then the corresponding Rosenbluth potentials will only depend on the scalar speed of the particles, v. In this case the Fokker-Planck operator can be simplified to

$$\begin{aligned}\frac{4\pi\epsilon_0^2 m_T^2}{e^4 \ln\Lambda}\mathcal{F}\left(f_T, f_F\right) = &-\frac{\partial}{\partial \mathbf{v}} \cdot \left(f_T h'_F(v)\frac{\mathbf{v}}{v}\right) \\ &+ \frac{1}{2}\frac{\partial}{\partial \mathbf{v}}\frac{\partial}{\partial \mathbf{v}} : \left\{ f_T \left[g''_F(v)\frac{\mathbf{vv}}{v^2} + \frac{g'_F(v)}{v}\left(\mathbf{I} - \frac{\mathbf{vv}}{v^2}\right)\right]\right\},\end{aligned} \tag{4.61}$$

where primes denote differentiation with respect to the scalar v. This can then be rearranged using tensor identities

$$\begin{aligned}\frac{4\pi\epsilon_0^2 m_T^2}{e^4 \ln\Lambda}\mathcal{F}\left(f_T, f_F\right) = &-\frac{\partial}{\partial \mathbf{v}} \cdot \left[f_T \left(h'_F(v) + \frac{g'_F(v)}{v^2}\right)\frac{\mathbf{v}}{v}\right] \\ &+ \frac{1}{2}\frac{\partial}{\partial \mathbf{v}}\frac{\partial}{\partial \mathbf{v}} : \left(f_T g''_F(v)\frac{\mathbf{vv}}{v^2}\right) \\ &+ \frac{1}{2}\frac{\partial}{\partial \mathbf{v}} \cdot \left(\mathbf{I} - \frac{\mathbf{vv}}{v^2}\right) \cdot \frac{\partial}{\partial \mathbf{v}}\left(f_T \frac{g'_F(v)}{v}\right).\end{aligned} \tag{4.62}$$

Transforming to spherical coordinates and assuming azimuthal symmetry (i.e. $\frac{\partial f_T}{\partial \varphi} = 0$) yields

$$\frac{4\pi\epsilon_0^2 m_T^2}{e^4 \ln\Lambda}\mathcal{F}\left(f_T, f_F\right) = -\frac{1}{v^2}\frac{\partial}{\partial v}\left[f_T\left(v^2 h_F'(v) + g_F'(v)\right)\right] \tag{4.63}$$

$$+\frac{1}{2v^2}\frac{\partial^2}{\partial v^2}\left(v^2 f_T g_F''(v)\right)$$

$$+\frac{1}{2}\frac{g_F'(v)}{v^3}\frac{1}{\sin\theta}\frac{\partial}{\partial\theta}\sin\theta\frac{\partial f_T}{\partial\theta}. \tag{4.64}$$

The physical significances of these three terms are now apparent. The first term is a dynamical friction which slows down the photoelectrons, the second is a diffusion term in the speed (or energy) coordinate, and the final term is pitch-angle diffusion.

For Maxwellian distributions the Rosenbluth potentials can be approximated as [see *Bellan*, 2006, Ch. 13 assignment 2]

$$h_F(v) \approx \left(1 + \frac{m_T}{m_F}\right)\frac{N_F}{v} \tag{4.65}$$

$$g_F(v) \approx \left(v + \frac{3V_F^2}{2v}\right)N_F, \tag{4.66}$$

where N_F is the density of the field particles and $V_F = \sqrt{k_B T_F/m_F}$ is their thermal speed. Substituting these expressions yields

$$\frac{4\pi\epsilon_0^2 m_T^2}{e^4 \ln\Lambda}\mathcal{F}\left(f_T, f_F\right) = \frac{N_F}{v^2}\left\{\frac{\partial}{\partial v}\left[f_T\left(\frac{m_T}{m_F} + \frac{3V_F^2}{2v^2}\right)\right]\right. \tag{4.67}$$

$$+\frac{3V_F^2}{2}\frac{\partial^2}{\partial v^2}\left(\frac{f_T}{v}\right)$$

$$\left.+\frac{1}{2}\left(\frac{1}{v} - \frac{3V_F^2}{v^3}\right)\frac{1}{\sin\theta}\frac{\partial}{\partial\theta}\sin\theta\frac{\partial f_T}{\partial\theta}\right\}.$$

This can be simplified further by noting that $m_e/m_i \ll 1$ and both V_e and V_i are much smaller than typical photoelectron speeds (i.e. $V_F/v \ll 1$). Separating the thermal electron and ion terms and dropping the subscript *pe* from the

photoelectron distribution function gives

$$\left[\frac{\delta f}{\delta t}\right]_e = \frac{N_e e^4 \ln\Lambda}{4\pi\epsilon_0^2 m^2}\left\{\frac{1}{v^2}\frac{\partial f}{\partial v} + \frac{1}{2v^3}\frac{1}{\sin\theta}\frac{\partial}{\partial\theta}\sin\theta\frac{\partial f}{\partial\theta}\right\} \tag{4.68}$$

$$\left[\frac{\delta f}{\delta t}\right]_i = \frac{N_i e^4 \ln\Lambda}{4\pi\epsilon_0^2 m^2}\frac{1}{2v^3}\frac{1}{\sin\theta}\frac{\partial}{\partial\theta}\sin\theta\frac{\partial f}{\partial\theta}. \tag{4.69}$$

The dynamical friction caused by the ions is a factor of m_e/m_i smaller than that caused by the electrons and thus can be neglected. However, by quasineutrality $N_e = N_i$ so both the ions and electrons create the same amount of pitch angle diffusion. Combining these two terms, using the definitions $\frac{1}{v}\frac{\delta\Phi}{\delta t} = \frac{v}{m}\frac{\delta f}{\delta t}$ and $\Phi = v^2/mf$ and transforming from v and θ to $\mathcal{E}$ and μ yields a simple combined collision term for interactions between photoelectrons and the ambient plasma

$$\left[\frac{1}{v}\frac{\delta\Phi}{\delta t}\right]_{e+i} = \frac{N_e e^4 \ln\Lambda}{8\pi\epsilon_0^2}\left\{\frac{\partial}{\partial\mathcal{E}}\left(\frac{\Phi}{\mathcal{E}}\right) + \frac{1}{2\mathcal{E}^2}\frac{\partial}{\partial\mu}\left[\left(1-\mu^2\right)\frac{\partial\Phi}{\partial\mu}\right]\right\}. \tag{4.70}$$

This is the expression used by *Khazanov et al.* [1994]. It is of the generic form

$$\left[\frac{1}{v}\frac{\delta\Phi}{\delta t}\right]_{e+i} = \frac{\partial}{\partial\mathcal{E}}\left[L(\mathcal{E})\Phi\right] + D(\mathcal{E})\frac{\partial}{\partial\mu}\left[(1-\mu^2)\frac{\partial\Phi}{\partial\mu}\right], \tag{4.71}$$

where $L(\mathcal{E})$ is the energy loss rate and $D(\mathcal{E})$ is the pitch-angle diffusion rate.

The above derivation assumes the only type of interaction between the photoelectrons and the plasma are classical Coulomb collisions. Very fast particles, however, can also produce plasma waves via Cherenkov emission, and these effects can be incorporated into more sophisticated forms of the Fokker-Planck equation [*Perkins*, 1965; *Itikawa and Aono*, 1966]. Furthermore, for electrons with energies above 14 eV the classical distance of closest approach during a Coulomb collision can be shorter than the deBroglie wavelength of the electrons, meaning that additional quantum mechanical corrections must be applied [*Schunk and Hays*, 1971]. Fortunately a simple empirical expression exists for the energy lost per distance traveled which covers both the quantum and non-quantum regimes [*Swartz et al.*,

1971];

$$L(\mathcal{E}) = \frac{3.37 \times 10^{-12} N_e^{0.97}}{\mathcal{E}^{0.94}} \left(\frac{\mathcal{E} - k_B T_e}{\mathcal{E} - 0.53 k_B T_e} \right)^{2.36} \frac{\text{eV}}{\text{cm}}, \tag{4.72}$$

where N_e is the electron density in cm^{-3}, $\mathcal{E}$ is expressed in eV, T_e is the thermal electron temperature in K, and $k_B = 8.618 \times 10^{-5} \text{eV/K}$ is Boltzmann's constant. Fig. 4.3 compares this expression to the classical result for an electron density of 10^5 cm^{-3} and a variety of different temperatures. The largest differences are at energies very near to $k_B T_e$. However, at these low energies the assumption that $\mathcal{E} \gg k_B T_e$ no longer applies so these expressions for $L(\mathcal{E})$ cease to be meaningful. A more important difference is that the *Swartz et al.* [1971] expression decays slightly more slowly than $\mathcal{E}^{-1}$, meaning the loss rates are higher than the classical result at the highest energies.

No compact empirical expression for the diffusion rate, $D(\mathcal{E})$, exists which accounts for all of the physics contained in Eq. 4.72, so we will simply use the classical result.

$$D(\mathcal{E}) = \frac{e^4 \ln \Lambda N_e}{16 \pi \epsilon_0^2 \mathcal{E}^2} = \left(1.3 \times 10^{-13} \text{eV}^2 \text{cm}^2\right) \ln \Lambda \frac{N_e}{2\mathcal{E}^2}, \tag{4.73}$$

where the Coulomb logarithm is [e.g. *Bellan*, 2006]

$$\ln \Lambda = \ln \left[\frac{4\pi\epsilon_0}{e^2} \frac{mv^2}{2} \sqrt{\frac{\epsilon_0 k_B T_e}{N_e e^2}} \right] \tag{4.74}$$

$$= 15.75 + \ln \left[\mathcal{E}(\text{eV}) \right] + \ln \left[\lambda_D(\text{cm}) \right]. \tag{4.75}$$

In the topside, where pitch-angle diffusion matters most, typical densities and temperatures are 10^5 cm^{-3} and 2000 K respectively. These correspond to Debye lengths of $\lambda_D \approx 1$ cm. Using this Debye length, photoelectron energies ranging from 10 to 500 eV correspond to Coulomb logarithms ranging from 18 to 22. For simplicity the Coulomb logarithm is fixed at 20 in the model and its variation with

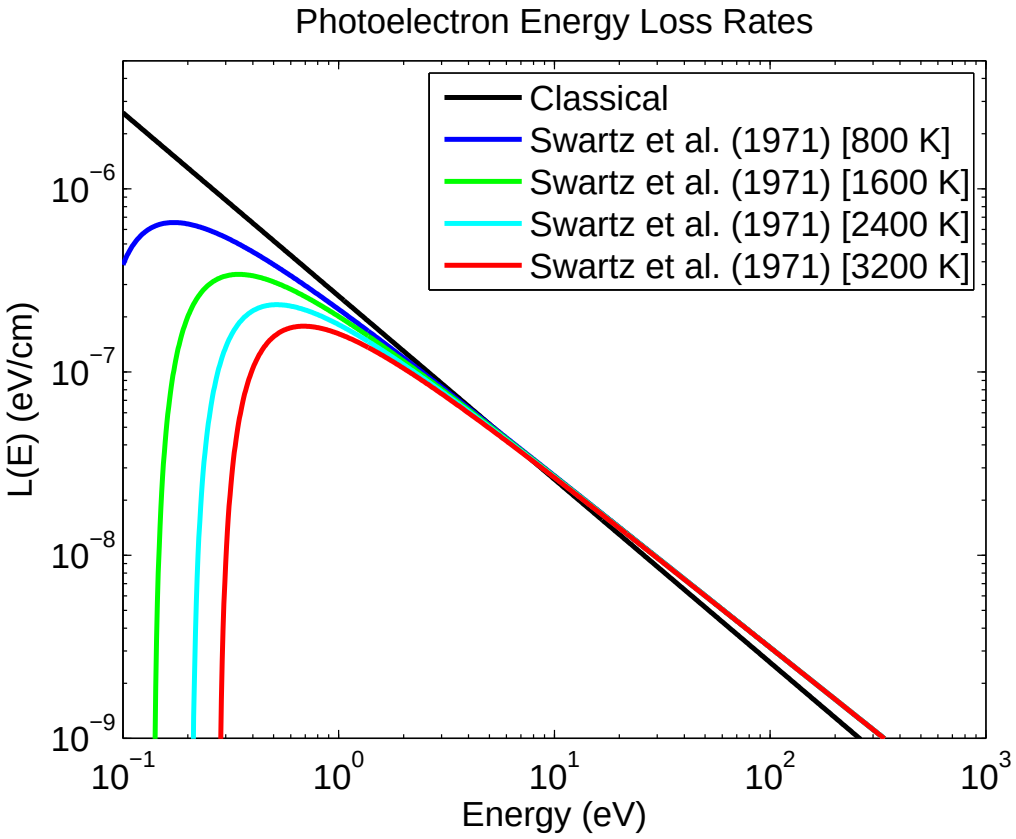

Figure 4.3: Comparison of the classical energy loss rate with the *Swartz et al.* [1971] empirical expression for an electron density of 10^5 cm^{-3}.

energy, density, and temperature is ignored. The sensitivity of the results to the exact choice of the Coulomb logarithm is discussed in Sec. 6.3.

4.3.3 Ambient electron heating rates

The final term in Eq. 4.59 is the effect of photoelectrons on the thermal electrons. Taking the second moment of this term gives a concrete definition of the thermal electron heating rate,

$$Q_{phe} \equiv \int \frac{1}{2} m v^2 \mathcal{F}\left(f_{th}, f_{pe}\right)\, d\mathbf{v}. \tag{4.76}$$

The energy gained by the thermal electron distribution from electron-photoelectron interactions must equal the energy lost by the photoelectron distribution through photoelectron-electron collisions, so an equivalent expression for the electron heating rate is

$$Q_{phe} = -\int \frac{1}{2} m v^2 \mathcal{F}\left(f_{pe}, f_{th}\right)\, d\mathbf{v}. \tag{4.77}$$

Inserting Eq. 4.71 into Eq. 4.77 gives a more useful expression for the electron heating rate.

$$Q_{phe} = -\int_0^{2\pi} d\varphi \int_{-1}^{1} d\mu \int_0^{\infty} d\mathcal{E}\, \mathcal{E} \left[\frac{1}{v}\frac{\delta\Phi}{\delta t}\right]_e. \tag{4.78}$$

The integral over the pitch angle diffusion portion of $\left[\frac{1}{v}\frac{\delta\Phi}{\delta t}\right]_e$ is zero because

$$\int_{-1}^{1} d\mu \frac{\partial}{\partial \mu}\left[\left(1-\mu^2\right)\frac{\partial \Phi}{\partial \mu}\right] = 0. \tag{4.79}$$

The integral over the energy loss portion of $\left[\frac{1}{v}\frac{\delta\Phi}{\delta t}\right]_e$ can be written as

$$Q_{phe} = -\int_0^{\infty} d\mathcal{E}\, \mathcal{E} \frac{\partial}{\partial \mathcal{E}}\left[L(\mathcal{E})\bar{\Phi}\right], \tag{4.80}$$

where

$$\bar{\Phi} \equiv \int_0^{2\pi} d\varphi \int_{-1}^{1} d\mu\, \Phi. \tag{4.81}$$

Using integration by parts and insisting that $\lim_{\mathcal{E}\to\infty} \mathcal{E}\bar{\Phi} = 0$ yields the familiar formula [e.g. *Schunk and Nagy*, 2009]

$$Q_{phe} = \int_0^{\infty} L(\mathcal{E})\bar{\Phi}\, d\mathcal{E} \tag{4.82}$$

The problem with Eq. 4.82 is the previously presented expressions for $L(\mathcal{E})$ are only valid in the limit where $\mathcal{E} \gg k_B T_e$, and thus the integral cannot be extended all the way to $\mathcal{E} = 0$. *Hoegy* [1984] has discussed this problem in detail. The proposed solution is to arbitrarily select an energy $\mathcal{E}_t$ and assume below this energy $\Phi = 0$.

Furthermore, assume any photoelectron which goes below this energy instantly becomes a thermal electron. With these assumptions the expression for the heating rate is

$$Q_{phe} = \int_0^{\mathcal{E}_t} \mathcal{E}\bar{q}(\mathcal{E})\, d\mathcal{E} - \int_{\mathcal{E}_t}^{\infty} \mathcal{E}\frac{\partial}{\partial \mathcal{E}}\left[L(\mathcal{E})\bar{\Phi}\right]\, d\mathcal{E}, \tag{4.83}$$

where $\bar{q}$ is the production rate of photoelectrons at energy $\mathcal{E}$ integrated over all solid angles, including cascade production associated with inelastic collisions. In the notation of the previous sections

$$\bar{q}(\mathcal{E}) = \int_0^{2\pi} d\varphi \int_{-1}^{1} d\mu \left\{ q(\mathcal{E}) + \sum_{n,p} N_n \int_{\mathcal{E}}^{\infty} d\mathcal{E}' \sigma_{an}^{p}(\mathcal{E}', \mathcal{E}) \frac{1}{2} \int_{-1}^{1} d\mu' \Phi(\ell, \mathcal{E}', \mu') \right\}, \tag{4.84}$$

where q is the sum of direct photoproduction, secondary production, and production due to quenching. The first term in Eq. 4.83 is energy transfered to the thermal electron population by photoelectrons which instantly thermalize after either being produced or cascading below $\mathcal{E}_t$. The second term is analogous to Eq. 4.80. Integration by parts of this term yields

$$Q_{phe} = \int_0^{\mathcal{E}_t} \mathcal{E}\bar{q}(\mathcal{E})\, d\mathcal{E} + \mathcal{E}_t L(\mathcal{E}_t)\bar{\Phi}(\mathcal{E}_t) + \int_{\mathcal{E}_t}^{\infty} L(\mathcal{E})\bar{\Phi}\, d\mathcal{E}. \tag{4.85}$$

The new "surface term" which appears after integration by parts represents energy which is transfered to the thermal electrons by photoelectrons which cascade below $\mathcal{E}_t$ due to Coulomb collisions and instantly thermalize.

Clearly $\mathcal{E}_t$ needs to be selected such that $\mathcal{E}_t \gg k_B T_e$ so that $L(\mathcal{E}_t)$ is well defined. *Schunk and Nagy* [1978] and *Hoegy* [1984] assume $\mathcal{E}_t$ should be near the energy where the total distribution deviates detectably from a Maxwellian, which is around 2 eV. We, however, will chose to set $\mathcal{E}_t$ to much lower value because if $\mathcal{E}_t$ is too large then systematic overestimation of Q_{phe} can result. For example, consider a population of 1.8 eV electrons. If $\mathcal{E}_t$ were 2 eV then this population

would instantly transfer 100% of its energy to the thermal population. However, 1.8 eV is above the threshold for vibrational excitation of N_2 (1.5 eV), meaning that some fraction of the energy in this 1.8 eV population should be going towards exciting N_2 molecules an not towards heating the ambient electrons. This type of error can be completely avoided if $\mathcal{E}_t$ is set to an energy which is below the lowest inelastic collision threshold. In fact, if transport effects are negligible the computed Q_{phe} will be independent of the chosen $\mathcal{E}_t$ for any $\mathcal{E}_t$ which is lower than the lowest inelastic collision threshold. Consider two energies $\mathcal{E}_{t1}$ and $\mathcal{E}_{t2}$ such that $\mathcal{E}_{t2} > \mathcal{E}_{t1}$. On the interval $[\mathcal{E}_{t1}, \mathcal{E}_{t2}]$ assume $L(\mathcal{E})$ is defined and nonzero, all inelastic cross sections are zero, and transport is negligible. On the interval the transport equation integrated over all solid angles reduces to

$$0 = \bar{q} + \frac{\partial}{\partial \mathcal{E}} \left[L(\mathcal{E}) \bar{\Phi} \right]. \tag{4.86}$$

Note the pitch angle diffusion and elastic collision terms integrate to 0. The solution to this equation on the interval is

$$\bar{\Phi}(\mathcal{E}) = \frac{L(\mathcal{E}_{t2})}{L(\mathcal{E})} \bar{\Phi}(\mathcal{E}_{t2}) + \frac{1}{L(\mathcal{E})} \int_{\mathcal{E}}^{\mathcal{E}_{t2}} \bar{q}(\mathcal{E}')\, d\mathcal{E}'. \tag{4.87}$$

Eq. 4.85 evaluated at $\mathcal{E}_{t1}$ is

$$Q_{phe} = \int_0^{\mathcal{E}_{t1}} \mathcal{E} \bar{q}(\mathcal{E})\, d\mathcal{E} + \mathcal{E}_{t1} L(\mathcal{E}_{t1}) \Phi(\mathcal{E}_{t1}) + \int_{\mathcal{E}_{t1}}^{\infty} L(\mathcal{E}) \bar{\Phi}(\mathcal{E})\, d\mathcal{E} \tag{4.88}$$

$$= \int_0^{\mathcal{E}_{t1}} \mathcal{E} \bar{q}(\mathcal{E})\, d\mathcal{E} + \mathcal{E}_{t1} L(\mathcal{E}_{t1}) \Phi(\mathcal{E}_{t1}) + \int_{\mathcal{E}_{t1}}^{\mathcal{E}_{t2}} L(\mathcal{E}) \bar{\Phi}(\mathcal{E})\, d\mathcal{E} + \int_{\mathcal{E}_{t2}}^{\infty} L(\mathcal{E}) \bar{\Phi}(\mathcal{E})\, d\mathcal{E}. \tag{4.89}$$

Inserting the solution, Eq. 4.87, into the third term yields

$$\int_{\mathcal{E}_{t1}}^{\mathcal{E}_{t2}} L(\mathcal{E})\bar{\Phi}(\mathcal{E})\,d\mathcal{E} = \int_{\mathcal{E}_{t1}}^{\mathcal{E}_{t2}} L(\mathcal{E}_{t2})\bar{\Phi}(\mathcal{E}_{t2})\,d\mathcal{E} + \int_{\mathcal{E}_{t1}}^{\mathcal{E}_{t2}} d\mathcal{E} \int_{\mathcal{E}}^{\mathcal{E}_{t2}} \bar{q}(\mathcal{E}')\,d\mathcal{E}'. \tag{4.90}$$

$$= (\mathcal{E}_{t2} - \mathcal{E}_{t1})L(\mathcal{E}_{t2})\bar{\Phi}(\mathcal{E}_{t2}) + \int_{\mathcal{E}_{t1}}^{\mathcal{E}_{t2}} \bar{q}(\mathcal{E}')(\mathcal{E}' - \mathcal{E}_{t1})\,d\mathcal{E}' \tag{4.91}$$

$$= (\mathcal{E}_{t2} - \mathcal{E}_{t1})L(\mathcal{E}_{t2})\bar{\Phi}(\mathcal{E}_{t2}) + \int_{\mathcal{E}_{t1}}^{\mathcal{E}_{t2}} \mathcal{E}\bar{q}(\mathcal{E})\,d\mathcal{E} \tag{4.92}$$

$$+ \mathcal{E}_{t1}\left[L(\mathcal{E}_{t2})\bar{\Phi}(\mathcal{E}_{t2}) - L(\mathcal{E}_{t1})\bar{\Phi}(\mathcal{E}_{t1})\right],$$

where the final step involves resubstituting the differential equation, Eq. 4.86. Substituting this expression into Eq. 4.89 and collecting terms yields

$$Q_{phe} = \int_0^{\mathcal{E}_{t2}} \mathcal{E}\bar{q}(\mathcal{E})\,d\mathcal{E} + \mathcal{E}_{t2}L(\mathcal{E}_{t2})\bar{\Phi}(\mathcal{E}_{t2}) + \int_{\mathcal{E}_{t2}}^{\infty} L(\mathcal{E})\bar{\Phi}(\mathcal{E})\,d\mathcal{E}, \tag{4.93}$$

which is Eq. 4.85 evaluated at $\mathcal{E}_{t2}$.

The ideal choice for $\mathcal{E}_t$ is thus any energy which is below the lowest inelastic collision threshold yet still high enough for $\mathcal{E}_t \gg k_B T_e$. Unfortunately this is not always possible since the threshold for vibrational excitation of O_2 is 0.25 eV, which corresponds to $T_e = 2900K$. SAMI2-PE compromises by setting the effective $\mathcal{E}_t$ to be $\frac{3}{2}k_B T_e$ rounded up to the next highest energy cell boundary. Any theoretical description of ionospheric electrons which attempts to divide the total electron population into thermal and suprathermal portions will inevitably be forced into some kind of compromise like this which creates uncertainties in the "no man's land" where $\mathcal{E} > k_B T_e$ but $\mathcal{E} \not\gg k_B T_e$. Applications where the exact shape of the distribution function in this energy range are important should use fully kinetic models instead of dividing the distribution function. *Vlasov et al.* [2004] discuss one such model for the application of predicting red line airglow during HF heating experiments.

CHAPTER 5

NUMERICAL METHODS FOR PHOTOELECTRON TRANSPORT CALCULATIONS

The photoelectron transport equation, Eq. 4.24, only involves the direction parallel to the magnetic field, so all of the new routines for SAMI2-PE appear inside the parallel transport portion of SAMI2. The photoelectron transport calculations are done after the photoproduction calculations are performed but before the momentum, continuity and energy equations are solved. Thus whenever the state variables N_e and T_e appear in the photoelectron transport routine the values being used are those from the previous time step. The photoelectron transport routine takes the photoelectron production rates as an input and produces thermal electron heating rates and secondary production rates. The secondary production rates are added to the photoionization rates and the chemical production rates to form the total production rate which is passed to the parallel continuity equation solvers. The thermal electron heating rates are passed to the parallel electron temperature equation solver.

Numerical methods for photoelectron transport calculations must preserve two key attributes of the continuous equations presented in Ch. 4. First, the photoelectron flux must be non-negative everywhere. Second, energy must be conserved throughout the entire system. Sec. 5.1 presents a numerical scheme for solving the photoelectron transport equation based on finite volume methods which both guarantees non-negativity and conservation of number of particles. Conservation of number of particles guarantees conservation of energy for calculations done at a single energy. By assumption photoelectrons only go downwards in energy so the photoelectron transport equation can be solved one energy at a time, starting at

the highest and working downwards. Sec. 5.2 describes an algorithm for computing the production rates at each energy based the fluxes at all higher energies which is based on the algorithm of *Swartz* [1985]. This algorithm adjusts the inelastic collision cross sections and direct production rates in such a way that energy will be conserved on a discrete, non-uniformly spaced energy grid. Finally, Sec. 5.3 gives a discrete expression for the ambient electron heating rates by summing all the energy lost by the photoelectrons to the thermal electrons. The resulting expression is a discrete analogue of Eq. 4.85.

5.1 Photoelectron transport as a conservation law: Finite volume methods

The photoelectron transport equation, Eq. 4.24, is a conservation law of the form

$$\frac{1}{v}\frac{\partial}{\partial t}\Phi + \frac{\partial}{\partial \ell}F + \frac{\partial}{\partial \mu}G = \frac{\partial}{\partial \mathcal{E}}H + S, \tag{5.1}$$

where the flux terms are

$$F = \mu\Phi, \tag{5.2}$$

$$G = -\delta B\frac{1-\mu^2}{2}\Phi, \tag{5.3}$$

$$H = L(\mathcal{E})\Phi, \tag{5.4}$$

and the net source terms are

$$S = \mu\delta B\Phi + D(\mathcal{E})\frac{\partial}{\partial \mu}\left[(1-\mu^2)\frac{\partial \Phi}{\partial \mu}\right] + C_n(\Phi) + q \tag{5.5}$$

Conservation laws are naturally treated with finite volume methods [*LeVeque*, 2002]. We associate a $\Delta\ell \times \Delta\mu$ rectangular cell with each point in $\ell - \mu$ space. In

terms of the grid points in s constructed by SAMI2,

$$\Delta\ell_i = \int_{(s_i+s_{i-1})/2}^{(s_{i+1}+s_i)/2} \frac{ds}{b_s(s)} \approx \frac{s_{i+1}-s_{i-1}}{2b_s(s_i)}, \tag{5.6}$$

where the approximation is valid because b_s varies slowly over a cell. Our discretized equation takes the form

$$\begin{aligned}\frac{1}{v}\frac{\partial}{\partial t}\phi_{i,j,k} &+ \frac{1}{\Delta\ell_i}\left[F_{i+1/2,j,k} - F_{i-1/2,j,k}\right] \\ &+ \frac{1}{\Delta\mu_k}\left[G_{i,j,k+1/2} - G_{i,j,k-1/2}\right] \\ &= \left[H_{i,j+1/2,k} - H_{i,j-1/2,k}\right] + S_{i,j,k},\end{aligned} \tag{5.7}$$

where the subscripts define the discrete photoelectron fluxes and net sources in terms of the continuous functions as

$$\phi_{i,j,k} \equiv \frac{1}{\Delta\ell_i\Delta\mu_k}\int_0^{2\pi} d\varphi \int_{\mathcal{E}_j-\Delta\mathcal{E}_j/2}^{\mathcal{E}_j+\Delta\mathcal{E}_j/2} d\mathcal{E} \int_{\ell_i-\Delta\ell_i/2}^{\ell_i+\Delta\ell_i/2} d\ell \int_{\mu_k-\Delta\mu_k/2}^{\mu_k+\Delta\mu_k/2} d\mu\, \Phi(\ell,\mathcal{E},\mu,t), \tag{5.8}$$

$$S_{i,j,k} \equiv \frac{1}{\Delta\ell_i\Delta\mu_k}\int_0^{2\pi} d\varphi \int_{\mathcal{E}_j-\Delta\mathcal{E}_j/2}^{\mathcal{E}_j+\Delta\mathcal{E}_j/2} d\mathcal{E} \int_{\ell_i-\Delta\ell_i/2}^{\ell_i+\Delta\ell_i/2} d\ell \int_{\mu_k-\Delta\mu_k/2}^{\mu_k+\Delta\mu_k/2} d\mu\, S(\ell,\mathcal{E},\mu,t). \tag{5.9}$$

The term $F_{i-1/2,j,k}$ is the total flux entering the cell around (ℓ_i, μ_k) through the face adjacent to the cell around (ℓ_{i-1}, μ_k) and $F_{i+1/2,j,k}$ is the flux leaving the cell around (ℓ_i, μ_k) through the face adjacent to the cell around (ℓ_{i+1,μ_k}). The fluxes in μ-space, $G_{i,j,k-1/2}$ and $G_{i,j,k+1/2}$, and in energy space, $H_{i,j+1/2,k}$ and $H_{i,j-1/2,k}$, are defined in analogous manners. The only way to construct these flux functions from linear combinations of the photoelectron fluxes while retaining the conservation properties of the original PDE is the donor cell upwinded (DCU) method, which is a special case of Godunov's method [*LeVeque*, 2002]. This scheme is only first order

accurate, but all higher order linear schemes cannot be total variation diminishing (TVD) as stated by Godunov's theorem [*LeVeque*, 2002].

Photoelectrons are assumed to only go downwards in energy, so upwinded differencing of the first term in Eq. 4.71 results in

$$H_{i,j+1/2,k} = \frac{1}{\Delta\mathcal{E}_{j+1}} L(\mathcal{E}_j + \Delta\mathcal{E}_j/2)\phi_{i,j+1,k} \tag{5.10}$$

$$H_{i,j-1/2,k} = \frac{1}{\Delta\mathcal{E}_j} L(\mathcal{E}_j - \Delta\mathcal{E}_j/2)\phi_{i,j,k}. \tag{5.11}$$

The term $-H_{i,j-1/2,k}$ is a type of loss from bin j and the term $+H_{i,j+1/2,k}$ is a type of cascade production into bin j from the bin above. It is intuitive to define an effective cross section for interations with thermal electrons as

$$\sigma_{th,i,j} = \frac{1}{N_e}\frac{1}{\Delta\mathcal{E}_j} L(\mathcal{E}_j - \Delta\mathcal{E}_j/2), \tag{5.12}$$

such that $H_{i,j-1/2,k} = \sigma_{th,i,j} N_e \phi_{i,j,k}$.

In ℓ-space the upwind direction is entirely determined by the sign of μ so

$$F_{i-1/2,j,k} = \begin{cases} \mu_k \phi_{i-1,j,k} & \mu_k > 0 \\ \mu_k \phi_{i,j,k} & \mu_k < 0 \end{cases} \tag{5.13}$$

$$F_{i+1/2,j,k} = \begin{cases} \mu_k \phi_{i,j,k} & \mu_k > 0 \\ \mu_k \phi_{i+1,j,k} & \mu_k < 0 \end{cases}. \tag{5.14}$$

In μ-space the upwind direction is entirely determined by the sign of $-\delta B$, which depends on the hemisphere. We choose to number the discrete pitch-angle cosines such that μ_1 is closest to -1 and $\mu_{n_{st}}$ is closest to $+1$, where n_{st} is the total

number of streams considered. Using this convention

$$G_{i,j,k-1/2} = \begin{cases} -\delta B_i \frac{1-\mu_{k-1}^2}{2} \phi_{i,j,k-1} & \delta B_i < 0 \text{ (South)} \\ -\delta B_i \frac{1-\mu_k^2}{2} \phi_{i,j,k} & \delta B_i > 0 \text{ (North)} \end{cases} \tag{5.15}$$

$$G_{i,j,k+1/2} = \begin{cases} -\delta B_i \frac{1-\mu_k^2}{2} \phi_{i,j,k} & \delta B_i < 0 \text{ (South)} \\ -\delta B_i \frac{1-\mu_{k+1}^2}{2} \phi_{i,j,k+1} & \delta B_i > 0 \text{ (North)} \end{cases}. \tag{5.16}$$

By definition $|\mu| \leq 1$ so the fluxes in μ-space through cell faces located at $\mu = \pm 1$ must be zero, i.e.

$$G_{i,j,1-1/2} = G_{i,j,n_{st}+1/2} = 0. \tag{5.17}$$

The net source term $S_{i,j,k}$ and the $H_{i,j\pm 1/2,k}$ terms can be reorganized into two pieces. The first piece is a production term which is independent of the flux at the current energy, $q_{i,j,k}$. This term is the sum of the photoproduction, cascade production, $H_{i,j+1/2,k}$, secondary production, and production due to the quenching of N(^{2}D) (see Sec. 5.2 for details). The other term can be written as a linear combination of the discrete photoelectron fluxes at the current energy.

$$\begin{aligned} T_{i,j,k} =& \mu_k \delta B_i \phi_{i,j,k} - \sigma_{th,i,j} N_e \phi_{i,j,k} \\ & - \sum_n (\check{\sigma}_{an,j} + \bar{\sigma}_{en,j}) N_n \phi_{i,j,k} \\ & + \frac{1}{2} \sum_n \bar{\sigma}_{en,j} N_n \sum_\alpha g_\alpha \phi_{i,j,\alpha} \\ & + D(\mathcal{E}_j) \Delta_k^2 (\phi_{i,j,k-1}, \phi_{i,j,k}, \phi_{i,j,k+1}). \end{aligned} \tag{5.18}$$

The total inelastic cross section needs to be changed to a modified total cross section, $\check{\sigma}_{an,j}$, for reasons which are discussed in Sec. 5.2. The locations of the centers of the cells in μ and the weights $g_\alpha = \Delta\mu_\alpha$ are chosen such that the second to last term in the above equation approximates the elastic collision integral

in the second to last term in Eq. 4.52 according to an optimal quadrature rule. This approximation transforms Eq. 4.24 from an integro-differential equation to a system of coupled differential equations. The same approximation is commonly used in the radiative transfer literature where it is known as the finite ordinate approximation [*Chandrasekhar*, 1950]. If the photoelectron flux as a function of μ is approximately a polynomial then the most accurate quadrature rule available is Gauss-Legendre quadrature [e.g. *Press et al.*, 2007]. The number of μ_k is always chosen to be an even number so that none of the μ_k are 0. Electrons whose pitch-angle cosines are exactly 0 travel in a circular orbit around the field line without ever being transported along the field line.

The final term in Eq. 5.18 is a discrete approximation of the second term in Eq. 4.71 which describes the pitch-angle diffusion. A flux-differencing method yields the following approximation [e.g. *LeVeque*, 2002]

$$\Delta_k^2 \equiv \begin{cases} -b_k\phi_{i,j,k} + b_k\phi_{i,j,k+1} & k = 1 \\ a_k\phi_{i,j,k-1} - (a_k + b_k)\phi_{i,j,k} + b_k\phi_{i,j,k+1} & k \neq 1 \text{ and } k \neq n_{st} \\ a_k\phi_{i,j,k-1} - a_k\phi_{i,j,k} & k = n_{st} \end{cases} \tag{5.19}$$

where

$$a_k = \frac{1 - \mu_{k-1/2}^2}{g_k\left(\mu_k - \mu_{k-1}\right)} \tag{5.20}$$

$$b_k = \frac{1 - \mu_{k+1/2}^2}{g_k\left(\mu_{k+1} - \mu_k\right)}. \tag{5.21}$$

The time derivative term in Eq. 5.1 is always negligible, so the discrete equations, Eqs. 5.7 - 5.21, can be written in steady state as a linear system. For

notational convenience define a linear operator $\mathbf{M}_{i,j,k}$ such that

$$\begin{aligned}\mathbf{M}_{i,j,k}\phi = &\left[F_{i+1/2,j,k} - F_{i-1/2,j,k}\right] + \left[G_{i,j,k+1/2} - G_{i,j,k-1/2}\right] - T_{i,j,k} \\ =&q_{i,j,k}.\end{aligned} \tag{5.22}$$

On a grid containing n_z points along a field line and n_{st} pitch angles $\mathbf{M}$ will be an $n_z n_{st} \times n_z n_{st}$ matrix where all of the nonzero values are located within n_{st} entries above or below the main diagonal. The system is solved using SGBMV from LAPACK [*Anderson et al.*, 1992], which performs LU decomposition and backsubstitution in a way which is efficient for banded matrices [e.g. *Press et al.*, 2007]. The asymptotic complexity of this algorithm is $O(n_z n_{st}^2)$ for matrices like $\mathbf{M}$.

The boundary conditions for Eq. 5.22 are set as follows. At the highest energy bin the cascade production, secondary production, and $H_{i,j+1/2,k}$ are all set to zero. There is no need for a boundary condition at the low end of the energy grid since photoelectrons only move down in energy. Below 120 km transport is assumed to be negligible, so the F flux terms through this lower boundary are set to 0. The photoelectron distribution for lower altitudes could be computed by solving the local equilibrium equation

$$\begin{aligned}0 = &-\sigma_{th,i,j} N_e \phi_{i,j,k} - \sum_n (\check{\sigma}_{an,j} + \bar{\sigma}_{en,j}) N_n \phi_{i,j,k} \\ &+ \frac{1}{2} \sum_n \bar{\sigma}_{en} N_n \sum_\alpha g_\alpha \phi_{i,j,\alpha} + D(\mathcal{E}_j)\Delta_k^2 + q_{i,j,k}.\end{aligned} \tag{5.23}$$

However, both the heating rates and the cascade production only depend on the integral of the flux over the pitch-angle distribution. The latter statement is only true because isotropic collisions are assumed. Integrating Eq. 5.23 over all pitch angles and solving for the total flux yields the simple equation

$$\phi_{i,j}^{tot} = \sum_k g_k \phi_{i,j,k} = \frac{\sum_k g_k q_{i,j,k}}{\sigma_{th} N_e + \sum_n \check{\sigma}_{an,j} N_n}. \tag{5.24}$$

Note that the elastic collision and pitch-angle diffusion terms disappear completely after integrating over the pitch-angle distribution. To save computation time, at energies below 2 eV transport is assumed to be negligible and this local equilibrium equation is solved instead for every position. These local calculations are continued down to an energy of $3/2k_BT_e$. Any photoelectrons which cascade below this point are assumed to instantly join the thermal population.

The μ coordinate is only defined between -1 and 1, meaning that no photoelectrons can ever be allowed to cross the $\mu = \pm 1$ cell boundaries. The finite difference rules given by Eqs. 5.15, 5.16, 5.17, and 5.19 satisfy this condition. Implicit in these finite difference rules are the four boundary conditions

$$\left.\frac{1-\mu^2}{2}\phi\right|_{\mu=\pm 1} = 0 \tag{5.25}$$

$$\left.\left(1-\mu^2\right)\frac{\partial\phi}{\partial\mu}\right|_{\mu=\pm 1} = 0. \tag{5.26}$$

These boundary conditions are satisfied as long as ϕ and its derivative with respect to μ are finite at $\mu = \pm 1$.

5.1.1 Numerical pitch-angle diffusion and higher order corrections to the mirror force term

Finite differencing the mirror force term using Eqs. 5.15 and 5.16 leads to an extra source of numerical pitch-angle diffusion. Numerical diffusion can cause particles which should stay in the loss cones and travel all the way to the conjugate hemisphere to leak into the mirror traps and become stuck in the plasmasphere. This potentially leads to systematic overestimation of the heating rates in the plasmasphere.

The approximate value of this numerical diffusion can be estimated by rewriting the finite difference approximation in terms of a second order Taylor expansion:

$$-\delta B\frac{\partial}{\partial\mu}\left[\frac{1-\mu^2}{2}\phi\right] \approx -\frac{\delta B}{\Delta\mu_k}\left\{\frac{1-\mu_k^2}{2}\phi_k - \frac{1-\mu_{k-1}^2}{2}\phi_{k-1}\right\} \tag{5.27}$$
$$\approx -\frac{\delta B}{\Delta\mu_k}\left\{\frac{1-\mu_k^2}{2}\phi_k - \frac{1-\mu_{k-1}^2}{2}\left[\phi_k - \Delta\mu_k\left.\frac{\partial\phi}{\partial\mu}\right|_{\mu_k} + \frac{\Delta\mu_k^2}{2}\left.\frac{\partial^2\phi}{\partial\mu^2}\right|_{\mu_k}\right]\right\}.$$

The pitch-angle diffusion due to Coulomb collisions is

$$D(\mathcal{E})\frac{\partial}{\partial\mu}\left[\left(1-\mu^2\right)\frac{\partial\phi}{\partial\mu}\right] = D(\mathcal{E})\left\{\left(1-\mu^2\right)\frac{\partial^2\phi}{\partial\mu^2} - 2\mu\frac{\partial\phi}{\partial\mu}\right\}. \tag{5.28}$$

Comparing the second order terms in both expression gives an estimate of the numerical pitch-angle diffusion:

$$D_{numerical} \approx \delta B\frac{\Delta\mu}{2}. \tag{5.29}$$

The term δB is given by Eq. 4.16; for a colatitude of 60° on a magnetic field line having an apex radius of 1.15 R_E (apex height of 955 km) $\delta B = 2\times10^{-10}$ cm^{-1}. For eight pitch-angle bins a typical value of the numerical diffusion is thus 2.5×10^{-11} cm^{-1}. The pitch-angle diffusion due to Coulomb collisions of a 10 eV electron in a 10^4 cm^{-3} plasma is 1.3×10^{-10} cm^{-1}, which is an order of magnitude larger than the numerical diffusion. The pitch-angle diffusion due to Coulomb collisions scales as $N_e/\mathcal{E}^2$, whereas the numerical diffusion is only a weak function of position through δB. Thus for lower electron densities or higher energies the pitch-angle diffusion due to Coulomb collisions can be comparable to or lower than the numerical diffusion. Nonetheless, the numerical diffusion is smaller than that due to Coulomb collisions over the majority of the domain considered, meaning that it is not a significant source of error.

Khazanov et al. [1979] and *Khazanov et al.* [1993] created a numerical treatment of the mirror force term which creates no numerical diffusion whatsoever. They

rewrite the equation in terms of the pitch-angle cosines the electrons would have if they traveled to the equatorial plane without making any collisions,

$$\mu_0(\ell, \mu) \equiv \frac{\mu}{|\mu|}\sqrt{1 - \frac{B_0}{B(\ell)}\,(1-\mu^2)}, \tag{5.30}$$

where B_0 is the magnetic field strength at the apex of the field line. We chose not to make this transformation because it greatly complicates the integrals over pitch angles which appear in the collision operator. The model of *Khazanov et al.* [1994] uses the transformation to μ_0, but treats all collisions as continuous loss processes using operators of the same form as Eq. 4.71, and thus avoids the need to transform collision integrals. In this work we are focused on the ionosphere, where the collision integrals dominate the photoelectron transport equation. In the plasmasphere and inner magnetosphere, however, large-angle collisions with neutrals can be neglected and the electron density, and thus the pitch-angle diffusion due to Coulomb collisions, is lower. Thus the transformation to μ_0 is helpful for studies of those regions.

Another way to reduce the numerical diffusion is to stay in μ-space and add higher order correction terms to the fluxes in μ-space (Eqs. 5.15 and 5.16). This method cannot completely remove numerical diffusion, but it can substantially reduce it. One possible second order accurate scheme is to use centered differences instead of upwind differences to approximate the mirror force term. Unfortunately, by Godunov's theorem, no linear scheme which is higher than first order accurate can be total variation diminishing (TVD) [e.g. *LeVeque*, 2002]. Thus a scheme using centered differences could potentially produce spurious oscillations. In practice these oscillations can sometimes cause the computed fluxes to be negative numbers, which is unphysical.

A way to generate a higher order accurate scheme which still preserves positivity

is to employ flux limiters. Standard references describing the use of flux limiters are usually written for time dependent equations [e.g. *Trac and Pen*, 2003; *LeVeque*, 2002], however these formulas are easily adapted to steady state solvers. Consider a 1-D advection equation with production and a linear loss term

$$\frac{1}{v}\frac{\partial n}{\partial t} + \frac{\partial n}{\partial x} = q - Ln, \tag{5.31}$$

where n is some quantity (e.g. density), v is an advection velocity, x is a spatial coordinate and t is a time coordinate. If q, L, and the initial n are positive everywhere then n will remain positive everywhere for all time. Assume v is positive, consider a uniformly spaced grid with cell widths Δx, and let N_i^j be the total density in cell i at time j. The second order accurate time advance equation using flux limiters is [c.f. *LeVeque*, 2002, Eq. 6.40]

$$\begin{aligned}\frac{1}{v}\frac{N_i^{j+1} - N_i^j}{\Delta t} + \Bigg\{ \frac{N_i^j - N_{i-1}^j}{\Delta x} \\ + \frac{1}{2}\left(1 - \frac{v\Delta t}{\Delta x}\right)\left[\psi(r_{i+1/2}^j)\frac{N_{i+1}^j - N_i^j}{\Delta x} - \psi(r_{i-1/2}^j)\frac{N_i^j - N_{i-1}^j}{\Delta x}\right]\Bigg\} = q_i^j - L_i^j N_i^j\end{aligned} \tag{5.32}$$

where $\psi(r)$ is the flux limiter function, and $r_{i\pm1/2}^j$ are the ratios of successive gradients. For $v > 0$ these are

$$r_{i-1/2}^j = \frac{N_{i-1}^j - N_{i-2}^j}{N_i^j - N_{i-1}^j} \tag{5.33}$$

$$r_{i+1/2}^j = \frac{N_i^j - N_{i-1}^j}{N_{i+1}^j - N_i^j}. \tag{5.34}$$

Eq. 5.32 becomes the Lax-Wendroff scheme if $\psi(r) = 1$ [*LeVeque*, 2002]. If the flux limiters are chosen appropriately the scheme will be TVD and the positivity property will be preserved.

Suppose $v \to \infty$ and $\Delta t \to \infty$ in such a way that $v\Delta t \to 0$ (i.e. $\Delta t \to 0$ faster than $v \to \infty$). The Courant number $v\Delta t/\Delta x$ will go to 0 for finite Δx. The first

term in Eq. 5.32 will not necessarily go to infinity as $v\Delta t \to 0$ because $N_i^{j+1} - N_i^j$ also goes to 0 as $\Delta t \to 0$. By definition

$$\lim_{\Delta t \to 0} \frac{N_i^{j+1} - N_i^j}{\Delta t} \equiv \frac{\partial N_i^j}{\partial t}. \tag{5.35}$$

If this derivative is finite then

$$\lim_{v \to \infty} \lim_{\Delta t \to 0} \frac{1}{v} \frac{N_i^{j+1} - N_i^j}{\Delta t} = \lim_{v \to \infty} \frac{1}{v} \frac{\partial N_i^j}{\partial t} = 0. \tag{5.36}$$

In these limits Eq. 5.32 reduces to a steady state equation where the sources are balanced by transport terms;

$$\frac{N_i^j - N_{i-1}^j}{\Delta x} + \frac{1}{2}\left[\psi(r_{i+1/2}^j)\frac{N_{i+1}^j - N_i^j}{\Delta x} - \psi(r_{i-1/2}^j)\frac{N_i^j - N_{i-1}^j}{\Delta x}\right] = q_i^j - L_i^j N_i^j. \tag{5.37}$$

Note that if $\psi(r) = 1$ this equation reduces to

$$\frac{N_{i+1}^j - N_{i-1}^j}{2\Delta x} = q_i^j - L_i^j N_i^j, \tag{5.38}$$

which is a centered difference approximation of the steady state differential equation. Eq. 5.32 is guaranteed to conserve number of particles and have non-negative solutions for all Courant numbers less than 1. Eq. 5.37 is a limiting case of Eq. 5.32, and thus it retains these important properties.

For the case of the mirror force term in the photoelectron transport equation the advection speed is not a constant and can have both signs. Furthermore, the μ-grid in SAMI2-PE is nonuniform. *LeVeque* [2002] describes how to write time dependent finite volume schemes with flux limiters for both of these general cases. Steady state expressions can be generated from these schemes by taking limits like in the example given above. The final expressions for the fluxes in μ-space in the

southern hemisphere ($\Delta B_i < 0$) are

$$G_{i,j,k-1/2} = -\delta B_i \frac{1-\mu_{k-1}^2}{2}\phi_{i,j,k-1} - \delta B_i \frac{g_{k-1}}{g_k + g_{k-1}}\psi(r_{i,j,k-1/2})\left[\frac{1-\mu_k^2}{2}\phi_{i,j,k} - \frac{1-\mu_{k-1}^2}{2}\phi_{i,j,k-1}\right] \tag{5.39}$$

$$G_{i,j,k+1/2} = -\delta B_i \frac{1-\mu_k^2}{2}\phi_{i,j,k} - \delta B_i \frac{g_k}{g_k + g_{k+1}}\psi(r_{i,j,k+1/2})\left[\frac{1-\mu_{k+1}^2}{2}\phi_{i,j,k+1} - \frac{1-\mu_k^2}{2}\phi_{i,j,k}\right] \tag{5.40}$$

and in the northern hemisphere ($\Delta B_i < 0$) are

$$G_{i,j,k-1/2} = -\delta B_i \frac{1-\mu_k^2}{2}\phi_{i,j,k} + \delta B_i \frac{g_k}{g_k + g_{k-1}}\psi(r_{i,j,k-1/2})\left[\frac{1-\mu_k^2}{2}\phi_{i,j,k} - \frac{1-\mu_{k-1}^2}{2}\phi_{i,j,k-1}\right] \tag{5.41}$$

$$G_{i,j,k+1/2} = -\delta B_i \frac{1-\mu_{k+1}^2}{2}\phi_{i,j,k+1} + \delta B_i \frac{g_{k+1}}{g_k + g_{k+1}}\psi(r_{i,j,k+1/2})\left[\frac{1-\mu_{k+1}^2}{2}\phi_{i,j,k+1} - \frac{1-\mu_k^2}{2}\phi_{i,j,k}\right]. \tag{5.42}$$

The appropriate ratios of successive gradients in the southern hemisphere are

$$r_{i,j,k-1/2} = \frac{\xi_{i,j,k-2}}{\xi_{i,j,k-1}} \tag{5.43}$$

$$r_{i,j,k+1/2} = \frac{\xi_{i,j,k-1}}{\xi_{i,j,k}}, \tag{5.44}$$

and in the northern hemisphere are

$$r_{i,j,k-1/2} = \frac{\xi_{i,j,k}}{\xi_{i,j,k-1}} \tag{5.45}$$

$$r_{i,j,k+1/2} = \frac{\xi_{i,j,k+1}}{\xi_{i,j,k}}, \tag{5.46}$$

where

$$\xi_{i,j,k} = \frac{\frac{1-\mu_{k+1}^2}{2}\phi_{i,j,k+1} - \frac{1-\mu_k^2}{2}\phi_{i,j,k}}{\mu_{k+1} - \mu_k}. \tag{5.47}$$

LeVeque [2002] reviews the properties which the flux limiter function, $\psi(r)$, must have for the scheme to be TVD. The most conservative choice is the minmod

limiter

$$\psi_{minmod}(r) = \text{minmod}(1, r), \tag{5.48}$$

the most aggressive choice is the superbee limiter

$$\psi_{superbee}(r) = \max[0, \min(1, 2\text{r}), \min(2, \text{r})], \tag{5.49}$$

and all other TVD limiters lie between these bounds [*LeVeque*, 2002]. A commonly used intermediate limiter is the van Leer limiter [*van Leer*, 1974]

$$\psi_{van\ Leer}(r) = \frac{r + |r|}{1 + |r|}. \tag{5.50}$$

Each of these limiters has the properties [*LeVeque*, 2002]

$$\psi(0) = 0 \tag{5.51}$$

$$\psi(1) = 1 \tag{5.52}$$

$$\psi\left(\frac{1}{r}\right) = \frac{\psi(r)}{r}. \tag{5.53}$$

The boundary conditions

$$G_{i,j,1-1/2} = G_{i,j,n_{st}+1/2} = 0, \tag{5.54}$$

still apply when using higher order corrections. However, the high order correction formulas involve fluxes which are more than one cell away from the interface in question. Thus these two boundary conditions are not sufficient. The high order correction formulas can be derived by imagining that the continuous function is being reconstructed from the discrete data using linear segments in each cell where the slope in each cell depends on the value in that cell, the downwind cell, and the two upwind cells. A simple fix near the boundaries is to assume that the slopes are 0 in the lowest and highest cells (i.e. use a zero order reconstruction instead of

a first order reconstruction when adjacent to a boundary). This change will cause the high order correction to disappear from one of the fluxes. In the southern hemisphere the altered term is

$$G_{i,j,1+1/2} = -\delta B_i \frac{1-\mu_1^2}{2} \phi_{i,j,1}, \tag{5.55}$$

and in the northern hemisphere the altered term is

$$G_{i,j,n_{st}-1/2} = -\delta B_i \frac{1-\mu_{nst}^2}{2} \phi_{i,j,n_{st}}. \tag{5.56}$$

The introduction of flux limiter functions makes the $G_{i,j,k\pm1/2}$ terms nonlinear in ϕ. The resulting nonlinear system of equations can be solved iteratively. On the first iteration the higher order correction terms are omitted. On each subsequent iteration, the $r_{i,j,k\pm1/2}$ terms are evaluated using the ϕ from the previous iteration. The matrix which is inverted in each iteration contains extra terms involving $\psi(r_{i,j,k\pm1/2})$ which depend on the solution from the previous iteration. This matrix will have the same size and sparsity as the matrix did when the higher order corrections are omitted. This iterative algorithm converges quickly; tests suggest that in practice four iterations are usually sufficient. However, since the matrix inversions are the slowest part of the program the need to iterate four times increases the computation time by nearly a factor of four. By default these high order corrections are omitted from SAMI2-PE because of this additional computational expense. Sec. 6.3.1 compares simulations with and without the high order corrections. In the region of interest for this thesis (i.e. below 1500 km at low latitudes) the high order corrections only have a small effect on the computed heating rates and temperatures.

5.2 Energy degradation and reapportionment

The standard energy grid in SAMI2-PE uses 0.25 eV bins up to 10 eV, 1 eV bins from 10 to 60 eV, 10 eV bins from 60 to 100 eV, 50 eV bins from 100 to 450 eV, and 100 eV bins from 450 to 650 eV. Special care must be taken when working on a discrete, nonuniform energy grid to conserve energy. SAMI2-PE adopts an algorithm originally developed by *Swartz* [1985] to accomplish this.

The total discrete production function is a combination of photoproduction, production due to quenching, cascade production due to excitation collisions, production due to degraded primaries from ionizing collisions, secondary production from ionizing collisions, and cascade production from Coulomb collisions, i.e.

$$q_{i,m,k} = q^{ph}_{i,m,k} + q^{quench}_{i,m,k} + q^{ex}_{i,m,k} + q^{dp}_{i,m,k} + q^{sec}_{i,m,k} + q^{Coulomb}_{i,m,k}. \tag{5.57}$$

In the notation of the previous section

$$q^{Coulomb}_{i,m,k} = H_{i,m+1/2,k} = \sigma_{th,i,m+1} N_e \phi_{i,m+1,k}. \tag{5.58}$$

All of the others types of discrete production need to be treated specially on a discrete grid.

The total photoproduction rate is a combination of many different photoionization processes, p, resulting from many different photon wavelengths, λ, i.e.

$$q^{phot}_{i,m,k} = \sum_p \sum_\lambda q^{phot,p,\lambda}_{i,m,k} \tag{5.59}$$

The wavelength bins are sufficiently narrow that it is reasonable to assume that each wavelength bin only produces photoelectrons in a single energy bin via a particular photoionization process. Let $\mathcal{E}_\beta$ be the midpoint of the closest bin the grid to the true photoelectron energy, $\mathcal{E}^{p,\lambda} = hc/\lambda - T_p$. The discrete production

rate in the bin around $\mathcal{E}_m$ is computed as

$$q_{i,m,k}^{phot,p,\lambda} = 2\pi\Upsilon(\mu_k)\frac{\mathcal{E}^{p,\lambda}}{\mathcal{E}_m}\sigma_n^p(\lambda)N_n(\ell_i)F(\lambda)\delta_{\beta m}. \tag{5.60}$$

In this context $F(\lambda)$ is the solar flux. The final $\delta_{\beta m}$ is a Kronecker delta function and n is the index of whichever neutral species process p ionizes. If the extra factor of $\frac{\mathcal{E}^{p,\lambda}}{\mathcal{E}_m}$ were neglected then energy would be created or destroyed by rounding from $\mathcal{E}^{p,\lambda}$ to $\mathcal{E}_m$ [*Swartz*, 1985]. The extra factor of 2π is included because the discrete production rate, $q_{i,m,k}$, has already been integrated over all φ. Note that since $\Upsilon(\mu)$ is quadratic in μ,

$$\int_{-1}^{1} d\mu\, \Upsilon(\mu) = \sum_k g_k \Upsilon(\mu_k), \tag{5.61}$$

is precisely correct for a Gauss-Legendre quadrature rule, so using anisotropic photoproduction with a coarse μ grid does not result in particles being artificially created or destroyed. Just like the discrete photoproduction rates, the discrete production rate due to quenching of N(^{2}D) includes an extra factor to compensate for the energy mismatch between nearest bin center and the true mean energy of the newly promoted electrons

$$q_{i,j,k}^{quench} = \frac{1}{2}\frac{k_B T_e + 2.4}{\mathcal{E}_j} k_1 N_{\mathrm{N}(^2\mathrm{D})} N_e. \tag{5.62}$$

The second portion of the *Swartz* [1985] algorithm involves adjusting the inelastic collision cross sections. Inelastic collisions which excite neutral molecules will cause a photoelectron to lose a discrete amount of energy equal to the excitation threshold. Thus special care must be taken when adapting the cascade production integral in Eq. 4.52 to a discrete energy grid. When considering isotropic collisions, it is convenient to define an average discrete flux,

$$\bar{\phi}_{i,j} \equiv \frac{1}{2}\sum_k g_k \phi_{i,j,k}. \tag{5.63}$$

For a uniformly spaced energy grid the cascade production into bin m from bin j due to excitation process p with threshold T_p is written as

$$q_{i,m,k}^{ex,j,p} = \hat{\sigma}_{xn}^{p}(\mathcal{E}_j) N_n(\ell_i) \bar{\phi}_{i,j} \tag{5.64}$$

where n is the index of whichever neutral species is involved in process p and $\mathcal{E}_m$ is the closest energy cell midpoint to $\mathcal{E}_j - T_p$. The total cascade production into bin m is the sum of contributions from all higher energy bins and from all processes, i.e.

$$q_{i,m,k}^{ex} = \sum_{p} \sum_{j=m+1}^{j_{max}} q_{i,m,k}^{ex,j,p}. \tag{5.65}$$

Inevitably $\mathcal{E}_m$ will not equal $\mathcal{E}_j - T_p$, so to prevent energy from being created or destroyed by rounding $\mathcal{E}_j - T_p$ to $\mathcal{E}_m$, the method of *Swartz* [1985] uses an adjusted cross section,

$$\hat{\sigma}_{xn}^{p} = \frac{T}{\mathcal{E}_j - \mathcal{E}_m} \int_{\mathcal{E}_j - T_p - \epsilon}^{\mathcal{E}_j - T_p + \epsilon} d\mathcal{E} \sigma_{xn}^{p}(\mathcal{E}_j, \mathcal{E}), \tag{5.66}$$

where ϵ is any small positive number. This adjustment causes collisions for which $\mathcal{E}_j - \mathcal{E}_m > T_p$ to be less frequent in order to compensate for the energy being lost by rounding down and vice versa.

For nonuniformly spaced grids the width, $\Delta\mathcal{E}_j$, of the bin centered at $\mathcal{E}_j$ can be wider than the bins around $\mathcal{E}_j - T_p$. In this case the the method of [*Swartz*, 1985] spreads the cascade production over a group of energy bins whose total width equals $\Delta\mathcal{E}_j$. The widths of the energy bins are all integer multiples of 0.25 eV so this is always possible. The highest bin in this group is chosen such that it contains the energy $\mathcal{E}_j - T_p + \Delta\mathcal{E}_j/2$. The production into bin α of the group is

$$q_{i,\alpha,k}^{ex,j,p} = \tilde{\sigma}_{xn\alpha}^{p}(\mathcal{E}_j) N_n(\ell_i) \bar{\phi}_{i,j}. \tag{5.67}$$

The weighted adjusted cross sections are given by

$$\tilde{\sigma}^p_{xn\alpha} = \frac{\Delta\mathcal{E}_\alpha}{\Delta\mathcal{E}_j}\hat{\sigma}^p_{xn}. \tag{5.68}$$

In this case the $\mathcal{E}_m$ used in Eq. 5.66 to compute the effective cross section is the weighted average of middle energies of all the bins in the group, i.e.

$$\mathcal{E}_m = \frac{1}{\Delta\mathcal{E}_j}\sum_\alpha \Delta\mathcal{E}_\alpha\mathcal{E}_\alpha. \tag{5.69}$$

Ionizing collisions cause a discrete loss in energy equal to the ionization threshold, T_p, plus a variable loss in energy equal to the energy of the secondary. By convention the less energetic of the two electrons involved in an ionizing collision is called the secondary electron and the more energetic electron is called the degraded primary. To conserve energy the energy of the degraded primary, $\mathcal{E}_p$, and the energy of the secondary, $\mathcal{E}_s$, must satisfy $\mathcal{E}_p + \mathcal{E}_s = \mathcal{E} - T_p$. Thus the maximum possible secondary energy which could conserve energy while still being smaller than $\mathcal{E}_p$ is $(\mathcal{E} - T_p)/2$. Let $s^{p,j}_{max}$ denote the index of the energy bin containing this maximum secondary energy for ionizing collisions of process p beginning in bin j. For every energy bin index s between 1 and $s^{j,p}_{max}$ the degraded primaries are tracked by performing a cascade production calculation in exactly the same way as it is for an excitation collision using $T + \mathcal{E}_s$ as the new effective threshold. The adjusted cross sections for each s is

$$\hat{\sigma}^{p,j,s}_{in} = \frac{T_p + \mathcal{E}_s}{\mathcal{E}_j - \mathcal{E}_m}\int_{\mathcal{E}_j - T_p - \mathcal{E}_s - \Delta\mathcal{E}_s/2}^{\mathcal{E}_j - T_p - \mathcal{E}_s + \Delta\mathcal{E}_s/2} d\mathcal{E}\,\sigma^p_{in}(\mathcal{E}_j, \mathcal{E}) \approx \frac{T_p + \mathcal{E}_s}{\mathcal{E}_j - \mathcal{E}_m}\sigma^p_{in}(\mathcal{E}_j, \mathcal{E}_j - T_p - \mathcal{E}_s)\Delta\mathcal{E}_s. \tag{5.70}$$

Again the production is spread over a group of bins spanning the width of $\Delta\mathcal{E}_j$. The cascade production in bin α of this group due to degraded primaries from ionizing collisions of process p coming from bin j and producing secondaries in bin

s is

$$q_{i,\alpha,k}^{dp,p,j,s} = \tilde{\sigma}_{in,\alpha}^{p,j,s} N_n(\ell_i) \bar{\phi}_{i,j} \tag{5.71}$$

where the weighted corrected cross section is defined as

$$\tilde{\sigma}_{in,\alpha}^{p,j,s} = \frac{\Delta \mathcal{E}_\alpha}{\Delta \mathcal{E}_j} \hat{\sigma}_{in}^{p,s}. \tag{5.72}$$

The total production into bin α due to degraded primaries from ionizing collisions of process p coming from bin j is

$$q_{i,\alpha,k}^{dp,p,j} = \sum_{s=1}^{s_{max}^{p,j}} q_{i,\alpha,k}^{dp,p,j,s}. \tag{5.73}$$

It is convenient to define a total weighted adjusted cross section for degraded primaries,

$$\bar{\tilde{\sigma}}_{in,\alpha}^{p,j} \equiv \sum_{s=1}^{s_{max}^{p,j}} \tilde{\sigma}_{in,\alpha}^{p,j,s} \tag{5.74}$$

such that

$$q_{i,\alpha,k}^{dp,p,j} = \bar{\tilde{\sigma}}_{in,\alpha}^{p,j} N_n(\ell_i) \bar{\phi}_{i,j}. \tag{5.75}$$

The total discrete production due to degraded primaries is given by summing over all processes and energies,

$$q_{i,\alpha,k}^{dp} = \sum_{p} \sum_{j=\alpha+1}^{j_{max}} q_{i,\alpha,k}^{dp,p,j}. \tag{5.76}$$

The secondary production rate in bin s is computed such that there is one secondary for every degraded primary. The secondary production rate in bin s associated with ionizing collisions of process p from bin j is

$$q_{i,s,k}^{sec,p,j} = \hat{\sigma}_{in}^{p,j,s} N_n(\ell_i) \bar{\phi}_{i,j}. \tag{5.77}$$

Again the total discrete secondary production rate is obtained by summing over all processes and energies, i.e.

$$q_{i,s,k}^{sec} = \sum_{p} \sum_{j=s+1}^{j_{max}} q_{i,s,k}^{sec,p,j}. \tag{5.78}$$

Ionizing collisions also create ions which must be tracked. Let the operator $\delta_{n\gamma}^{p}$ be 1 if process p transforms neutrals of species n to ions of species γ and 0 otherwise. The contribution from energy $\mathcal{E}_j$ and process p to the production rate of ion γ is

$$P_{i,\gamma}^{sec,p,j} = \delta_{n\gamma}^{p} \sum_{s=1}^{s_{max}^{p,j}} \sum_{k} g_k q_{i,s,k}^{sec,p,j}, \tag{5.79}$$

It is convenient to define a secondary production cross section

$$\breve{\sigma}_{in}^{p,j} \equiv \sum_{s=1}^{s_{max}^{p,j}} \hat{\sigma}_{in}^{p,j,s}, \tag{5.80}$$

such that

$$P_{i,\gamma}^{sec,p,j} = 2\delta_{n\gamma}^{p} \breve{\sigma}_{in}^{p,j} N_n(\ell_i) \bar{\phi}_{i,j}. \tag{5.81}$$

The total production rate which is ultimately passed to the continuity equation solvers is the sum over all processes and energies, i.e.

$$P_{i,\gamma}^{sec} = \sum_{p} \sum_{j=1}^{j_{max}} P_{i,\gamma}^{sec,p,j} \tag{5.82}$$

To conserve the number of particles the total number lost from a given bin must equal the total number which cascade into all the other bins. This can be enforced numerically by defining the modified total inelastic cross section in Eq. 5.18 in terms of the modified partial cross sections, Eqs. 5.66 and 5.70, as

$$\breve{\sigma}_{an,j} = \breve{\sigma}_{xn,j} + \breve{\sigma}_{in,j}, \tag{5.83}$$

where

$$\breve{\sigma}_{xn,j} \equiv \sum_p \hat{\sigma}_{xn}^{p,j} \tag{5.84}$$

$$\breve{\sigma}_{in,j} \equiv \sum_p \sum_s \hat{\sigma}_{in}^{p,j,s} \tag{5.85}$$

Throughout the SAMI2-PE code six different types of adjusted inelastic cross sections are used: $\tilde{\sigma}_{xn,\alpha}^{p,j}$, $\bar{\tilde{\sigma}}_{in,\alpha}^{p,j}$, $\hat{\sigma}_{in}^{p,j,s}$, $\breve{\sigma}_{in}^{p,j}$, $\breve{\sigma}_{xn,j}$, and $\breve{\sigma}_{in,j}$. All of these cross sections can be computed once at the beginning of the program after the energy grid has been defined. These cross sections are stored in lookup tables called `wcsigex`, `wcsigion`, `wcsigsec`, `sigionp`, `sigex`, and `sigion` respectively.

5.3 Ambient electron heating rates

Based on Eq. 5.12, at each step down through the energy grid energy leaves bin (j,k) at a rate of $\sigma_{th,i,j} N_e \phi_{i,j,k} \mathcal{E}_j / 2\pi$ eVcm^{-3}s^{-1}ster^{-1} and enters bin $(j-1,k)$ at a rate of $\sigma_{th,i,j} N_e \phi_{i,j,k} \mathcal{E}_{j-1} / 2\pi$ eVcm^{-3}s^{-1}ster^{-1}. The total amount of energy transfered to the thermal population through this process is thus

$$\sum_{j=j_{min}}^{j_{max}} (\mathcal{E}_j - \mathcal{E}_{j-1}) \sigma_{th,i,j} N_e \sum_k g_k \phi_{i,j,k} \text{ eVcm}^{-3}\text{s}^{-1}. \tag{5.86}$$

The energy index j_{max} is the index of the highest energy bin the grid, whereas j_{min} is the lowest energy bin whose lower boundary is greater than $3/2 k_B T_e$. This sum is a discrete approximation of the integral in the third term Eq. 4.85.

All electrons which are produced in bins below j_{min} are assumed to instantly transfer their energy to the thermal population. The total heating rate can thus

be written as

$$Q_{phe}(\ell_i) = \sum_{j=1}^{j_{min}-1} \mathcal{E}_j \sum_k g_k q_{i,j,k} + \sum_{j=j_{min}}^{j_{max}} (\mathcal{E}_j - \mathcal{E}_{j-1}) \sigma_{th,i,j} N_e \sum_k g_k \phi_{i,j,k}. \qquad (5.87)$$

The new first term in this expression is a discrete approximation of the first two terms in Eq. 4.85 added together. Note that by convention $q_{i,j,k}$ includes the cascade production from the bin above due to Coulomb collisions (i.e. $H_{i,j+1/2,k} = \sigma_{th,i,j+1} N_e \phi_{i,j,k}$). Thus the first term in Eq. 5.87 includes a term which is equivalent to $\mathcal{E}_{j_{min}-1} \sigma_{th,i,j_{min}} N_e \sum_k g_k \phi_{i,j_{min},k}$, which is a discrete approximation of the "surface term" in Eq. 4.85.

CHAPTER 6

SAMI2-PE MODEL RESULTS

This chapter presents examples of results from numerous runs of SAMI2-PE and compares them to other models and real Jicamarca data. While these results frequently show promising similarity to Jicamarca data, they certainly do not reproduce the data perfectly. The model contains many uncertainties about the cross sections, reaction rates, collision frequencies and other transport coefficients as well as many simplifying assumptions (e.g. isotropic collisions), all of which could introduce systematic biases between the data and the model. Furthermore, SAMI2-PE requires a priori specifications of the neutral atmospheric parameters, electric fields, and solar fluxes. The empirical models used for these parameters contain significant amounts of uncertainty as well. Despite all these weaknesses of the model, the results presented here are still useful because they provide insight into the workings of the low latitude ionosphere system. The discussion in this chapter focuses on which physical processes are most important in various regions under various conditions and how quantities change in response different kinds of forcing rather than dwelling on why the data and the model do not match. It is shown that photoelectron transport is a crucial part of how the thermosphere, ionosphere, and plasmasphere work together as a system.

6.1 Example results

We will demonstrate the performance of the model by studying a single day in detail. All of the example simulation results shown in this section correspond to March 25, 2009, which was chosen as a reference day because Jicamarca ran a

long pulse/Faraday experiment which achieved excellent data coverage on this day. This day was also exceptionally quiet; the daily and 81 day averaged $F10.7$ solar radio fluxes were 68.2 and 69.2 $\mathrm{Wm^{-2}Hz^{-1}}$ respectively, and the Ap geomagnetic index was only 4.0 nT. Each simulation is for the magnetic longitude passing over Jicamarca ($-11.95°, -76.87°$ geographic), uses 151 points along a field line, uses 90 field lines extending to a maximum altitude of 1650 km at the magnetic equator, and begins at local midnight on the previous day (i.e. 5 UT on March 24, 2009). The first 24 hours of the simulation are ignored because they potentially contain transient behavior created by the assumed initial conditions.

The reference case uses eight pitch-angle bins, the model of *Scherliess and Fejer* [1999] for the electric fields, the HWM93 model for the neutral winds [*Hedin et al.*, 1991], and the NRLMSISE-00 model for the neutral densities and temperatures [*Picone et al.*, 2002]. Fig. 6.1 summarizes the state of this simulation at 5:48 LT, which is during sunrise. The top eight panels show the photoelectron fluxes in all eight streams for the energy bin between 20 and 21 eV. The bottom four panels plot the total photoproduction rate, the electron heating rate, the electron temperature, and the electron density. At sunrise the heating rates peak first between 300 and 400 km. The photoelectron fluxes at high altitudes are lower for lower absolute values of μ, i.e. particles at higher pitch angles. This is both because higher pitch-angle particles take a longer time to travel along a field line, and thus make more collisions, and because the hyperbolic term in the transport equation which enforces the conservation of the first adiabatic invariants moves flux from higher pitch angles to lower pitch angles as the field lines spread apart. High pitch angles and high altitudes correspond to the section of phase space where the trapped orbits exist. The only ways for particles to be on a trapped orbit are if they are produced locally or scattered from a low pitch angle to high pitch angle by

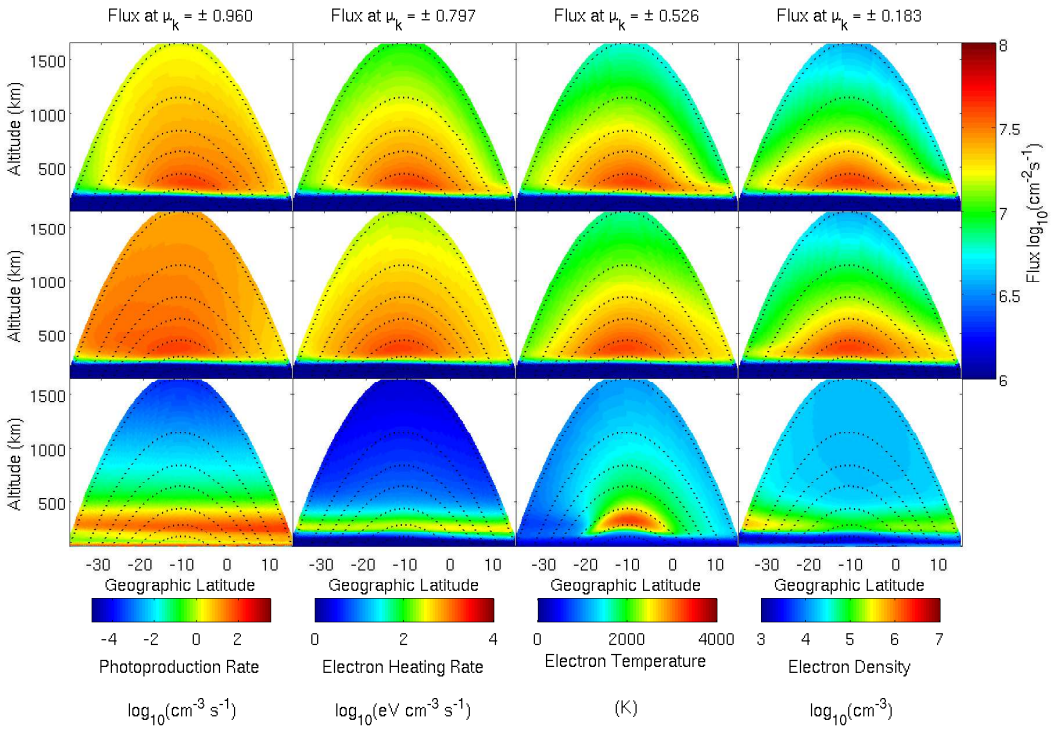

Figure 6.1: Summary of the reference simulation at 5:48 LT, during sunrise. The top eight panels depict the photoelectron fluxes in the 20-21 eV bin. The top four panels are for photoelectrons traveling to the north (positive μ) and the middle four panels are for photoelectrons traveling to the south (negative μ). The bottom four panels plot the total photoproduction rates, the electron heating rates, the electron temperatures, and the electron densities. The horizontal axis of each plot shows the geographic latitude; Jicamarca is located at $-11.95°$ latitude. The dotted curves in each panel show the positions of a few magnetic field lines.

a collision. Both collisions and photoionizations are relatively infrequent at high altitudes due to the relatively lower neutral densities.

Fig. 6.2 summarizes the state of the same simulation at 15:15 LT using the same format as Fig. 6.1. The photoelectron fluxes are in general lower than at dawn because both the electron density and the neutral densities are higher in the afternoon. This is especially true for the field lines connected to the equatorial arcs. In the afternoon the fountain effect creates regions of high electron density in the

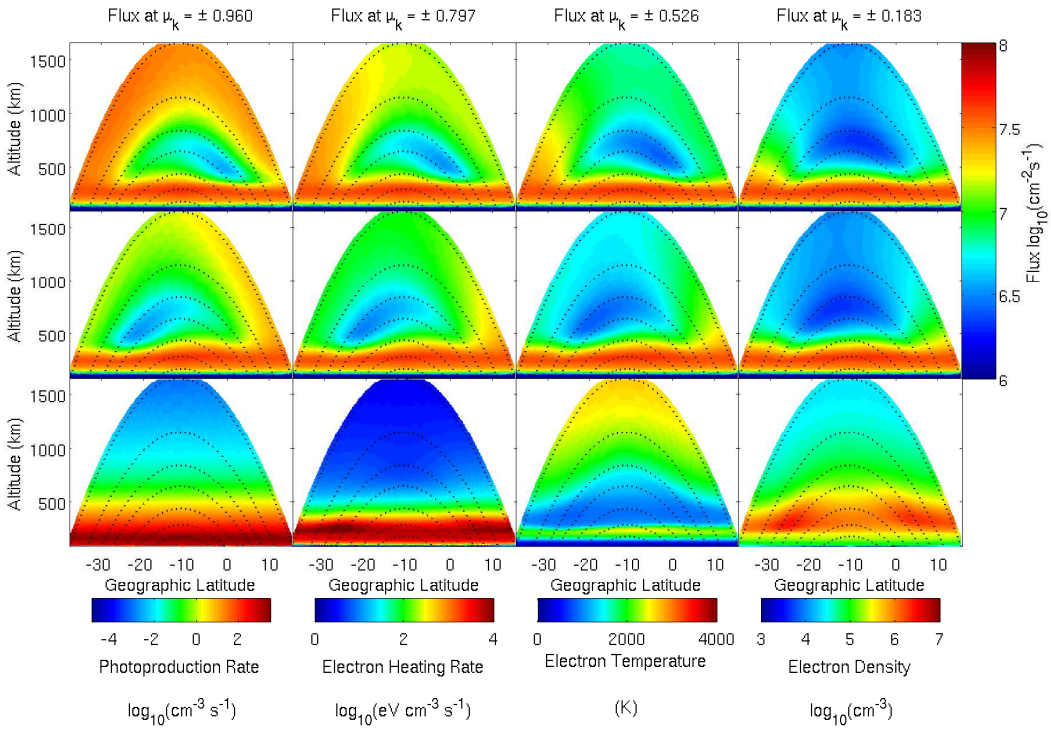

Figure 6.2: Summary of the reference simulation at 15:15 LT in the same format as Fig. 6.1. The most notable features of this snapshot are the "shadows" of the equatorial arcs in the fluxes.

F-regions $\sim 15°$ north and south of the magnetic equator known as the equatorial arcs. The photoelectron fluxes display pronounced local minima in the afternoon located on the same field lines as the equatorial arcs and the formation and evolution of these minima parallels the formation and evolution of the equatorial arcs themselves. These minima can be thought of as "shadows" of the equatorial arcs. The shadows appear in the conjugate ionosphere from their controlling equatorial arcs and are more pronounced for higher pitch angle particles which take a longer time to travel through an equatorial arc.

6.1.1 Photoelectron spectral shapes

The above plots have only shown fluxes for the 20-21 eV bin. As an illustration of the shape of the photoelectron flux spectra the total fluxes at the magnetic equator as a function of energy and altitude are plotted in Fig. 6.3 for the reference simulation at the same local time as Fig. 6.2. The total fluxes plotted are defined in terms of the discrete fluxes as

$$\phi_{tot,i,j} = \frac{1}{\Delta\mathcal{E}_j} \sum_k g_k \phi_{i,j,k}, \tag{6.1}$$

such that they have the same units as the continuous fluxes, Φ, integrated over all solid angles. At altitudes below $\sim$ 200 km transport effects are negligible, so the structure of the photoelectron spectrum is entirely determined by the structure of the production and loss functions. The increased flux between 20 and 30 eV exists because the exceptionally bright 30.4 nm (41 eV) line in the solar spectrum primarily produces photoelectrons in this energy range. The depletion between 1.5 and 3 eV is the result of vibrational excitation of N_2, and the edge appearing at 2.5 eV comes from the quenching of $N(^2D)$. At high altitudes very few photoelectrons are produced locally. The high altitude spectra are smooth functions of energy because the photoelectrons make many different types of collisions before reaching these altitudes. Unlike the low altitude spectra which generally have increasing fluxes with decreasing energy since photoelectrons constantly move downwards in energy, the high altitude spectra have maxima between 15 and 20 eV. The lower energy photoelectrons have much more difficulty escaping to high altitudes. The fluxes at medium and low energies also show local minima as a function of altitude around 800 km which is a direct consequence of the equatorial arcs as discussed above.

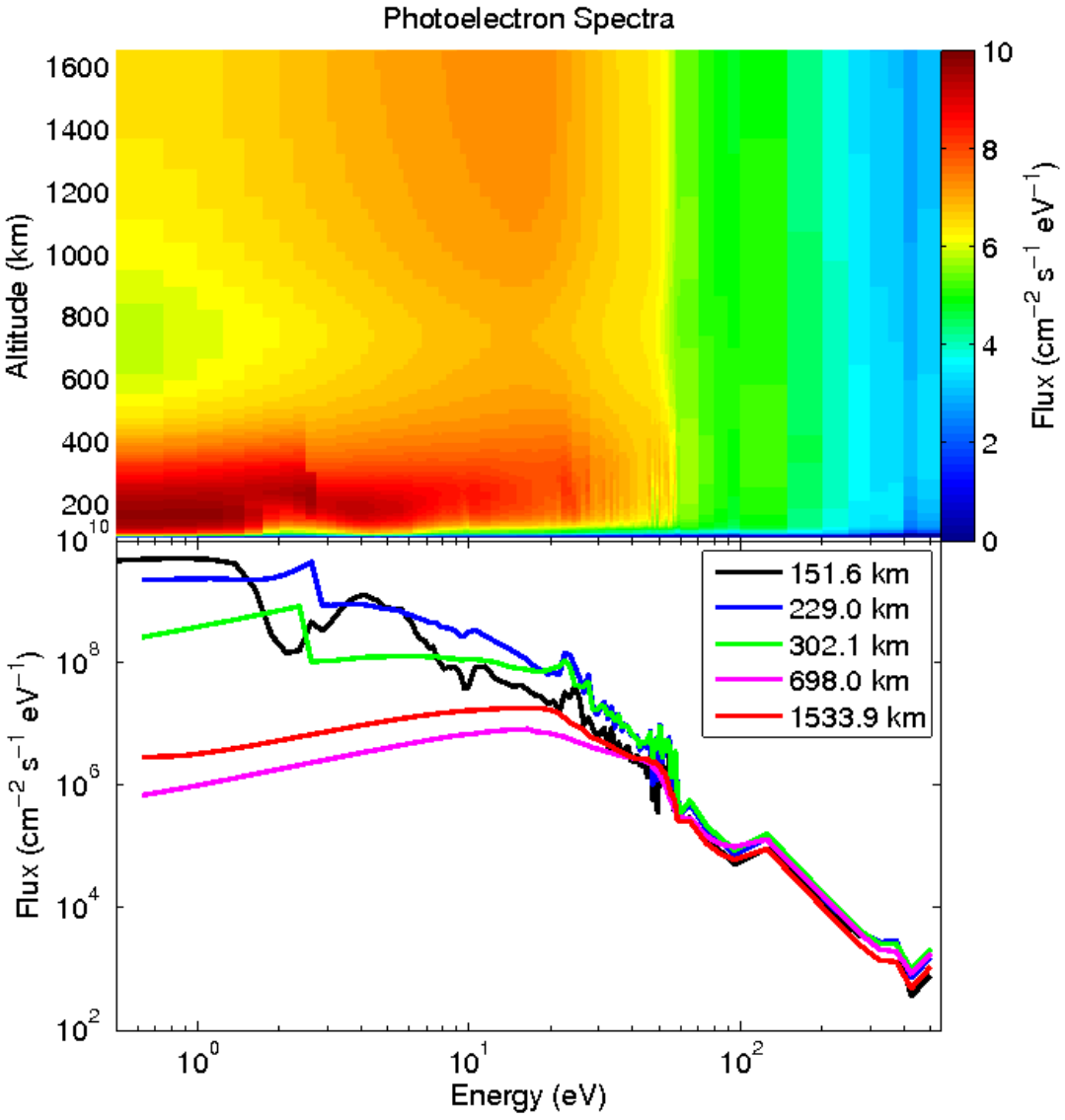

Figure 6.3: Top: Total photoelectron flux spectra as a function of energy and altitude above the magnetic equator at 15:15 LT for the reference simulation. The edges of each pixel are placed at the locations of the upper and lower boundaries of each energy bin in the discrete grid. Bottom: Total photoelectron flux spectra at a few representative altitudes.

6.1.2 Pitch-angle distributions

When discussing the pitch-angle distributions it is intuitive to look at average pitch-angle cosines for the northwards and southwards traveling portions of the photoelectron population. The discrete analogues of Eqs. 2.54 and 2.55 are

$$\langle \mu \rangle_{i,j}^{+} = \frac{\sum_{k=n_{st}/2+1}^{n_{st}} \mu_k g_k \phi_{i,j,k}}{\sum_{k=n_{st}/2+1}^{n_{st}} g_k \phi_{i,j,k}} \tag{6.2}$$

$$\langle \mu \rangle_{i,j}^{-} = -\frac{\sum_{k=1}^{n_{st}/2} \mu_k g_k \phi_{i,j,k}}{\sum_{k=1}^{n_{st}/2} g_k \phi_{i,j,k}}. \tag{6.3}$$

These quantities must be specified a priori in a two-stream code. For example, the FLIP two-stream code assumes $\langle \mu \rangle$ is 0.577 at low altitudes and only changes as a result of the magnetic mirror force. In a multi-stream model like SAMI2-PE the mean pitch-angle cosines can be computed self-consistently including transport effects. For a perfectly isotropic distribution the average pitch-angle cosines are 0.5. Higher numbers indicate the photoelectrons are more likely to be propagating close to parallel to **B**. Fig. 6.4 plots the average pitch-angle cosines for three different energies. In general, the mean pitch-angle cosines of the two streams are not equal and are functions of both position and energy. As expected, at low altitudes the distributions are almost perfectly isotropic as a result of frequent collisions. In the plasmasphere the average pitch-angle cosines become closer to 1 because the magnetic mirror force decreases the pitch-angle cosine as the magnetic field lines spread apart and because photoelectrons with higher pitch-angle cosines can more easily escape into the topside. The higher pitch-angle cosine particles undergo fewer collisions per distance traveled along the field line. This transport effect is more important at lower energies than higher energies, thus the average pitch-angle cosines in the topside are closer to 1 for lower energy particles. This transport effect causes the average pitch-angle cosine to become closer to 1 than one would expect from the effect of the magnetic mirror force alone. Furthermore, small regions

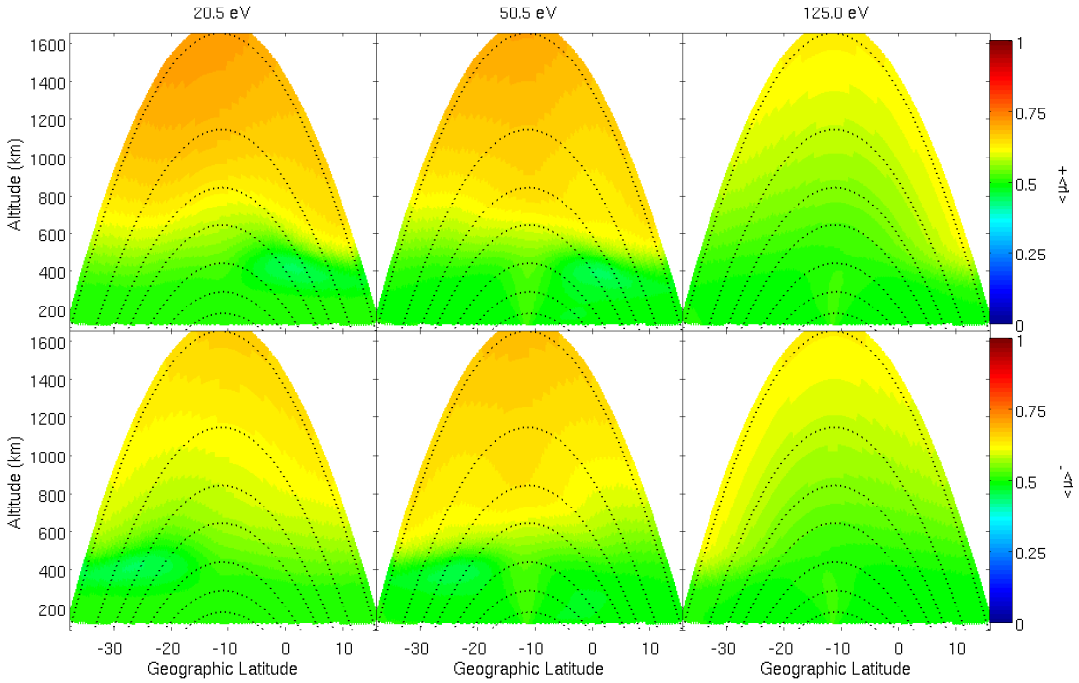

Figure 6.4: Average pitch-angle cosines for the northwards traveling ($\langle\mu\rangle^+$, top row) and southwards traveling ($\langle\mu\rangle^-$, bottom row) streams for three different energy bins. This plot corresponds to the reference simulation at 15:15 LT.

where the average pitch-angle cosines are less than 0.5 form in the "downwind" F-regions (i.e. the northern F-region for the northward propagating photoelectrons) as a result of an additional transport effect. Photoelectrons from the conjugate hemisphere with pitch-angle cosines closer to 1 will penetrate deeper than those with lower pitch-angle cosines. The lower pitch-angle cosine photoelectrons pile up at the top of the F-region without being able to penetrate to lower altitudes.

6.1.3 Comparison to Jicamarca Data

The upper two panels of Fig. 6.5 show the electron densities and temperatures over Jicamarca produced by the full profile procedure on March 25, 2009 [*Hysell et al.*, 2008]. The lower two panels of Fig. 6.5 show modeled electron densities and temperatures above the magnetic equator as a function of local time for the reference case. Both the data and the model agree on a number of features. The topside temperatures rise very quickly at dawn to $\sim$ 3500 K when the neutral and electron densities are lowest, decrease during the middle of the day as the electron density increases and the neutral atmosphere expands, then increase slightly again in the late afternoon as the neutral atmosphere begins to retract.

The modeled electron temperatures in the hot 250 km region are higher than the data. This remains true even when the quenching of N(^{2}D) is disabled. The electron density in the model below the F peak is lower than that in the data, which potentially explains why the electron temperatures at these altitudes are too high. In this altitude regime the cooling rates are either too low, the recombination rates are too high, or extra production terms which have been neglected, such as the ionization of NO by Lyman-α, are significant. Furthermore, uncertainties in the solar soft X-ray spectrum will substantially impact this region [e.g. *Solomon et al.*, 2001]. All of the photochemistry at these altitudes in SAMI2 needs to be reexamined in the future.

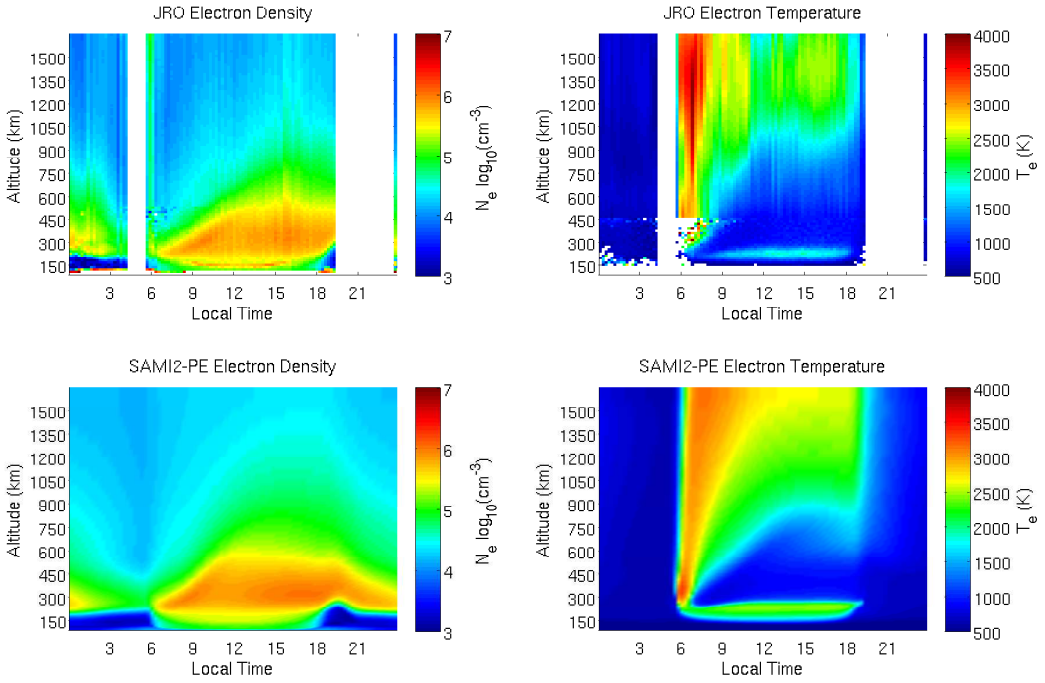

Figure 6.5: Top panels: Electron densities and temperatures derived from full profile analysis of Jicamarca data. White areas indicate missing data. The layer around 150 km is not a layer of enhanced electron density but rather coherent scatter from 150 km echoes. Bottom panels: SAMI2-PE electron densities and temperatures at the magnetic equator plotted as Range-Time-Intensity (RTI) plots like radar data from the reference simulation.

6.2 Importance of $N(^2D)$

The quenching of $N(^2D)$ is a dominant heat source for the thermal electrons in the lower F-region [*Richards*, 1986]. Fig. 6.6 shows temperature profiles both with and without quenching enabled and the electron temperature maximum at 250 km changes by over 50%. The heating from $N(^2D)$ scales with the density of NO^+, which itself depends on the density of neutral NO. The blue curve in Fig. 6.6 shows the effect of dividing the neutral NO density in the model in half when quenching is enabled. The electron temperatures in the hot 250 km region are highly sensitive

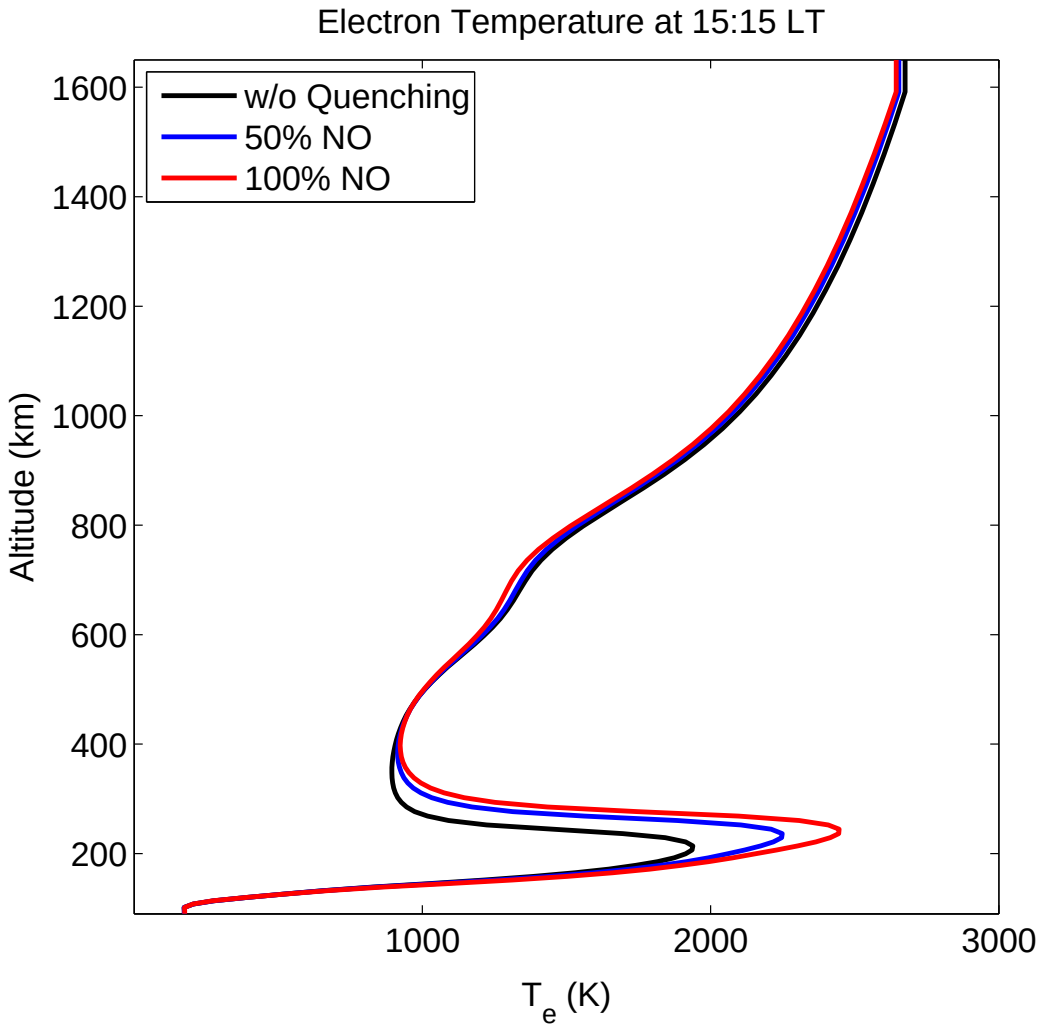

Figure 6.6: Electron temperature profiles at 15:15 LT over the magnetic equator with quenching disabled (black), quenching enabled with the neutral NO density reduced by 50% (blue), and quenching enabled using the full neutral NO density (red). The red curve is the reference simulation.

to this quantity.

Including quenching also has an effect on the topside temperatures even though there is no appreciable N(^{2}D) density at high altitudes. In general equatorial topside temperatures will decrease slightly when the off-equatorial F-region temperatures are increased due to an important feedback mechanism between the densities

and temperatures, which is illustrated in Fig. 6.7. The left panels show the electron density, heating rate, and temperature for a simulation without quenching. The center panels show the same quantities for the reference simulation (with quenching), and the right panels show the change between the two. Red regions are ones where the values from the simulation with quenching are larger. When quenching is enabled the temperature in the off-equatorial F-regions are increased, which creates a pressure gradient pointing up the field line and raises the height of the F-layer. The electron densities throughout the topside increase when the F-layer is raised. This causes photoelectrons to lose more energy to the thermal electrons on their way up into the topside, and thus the equatorial topside heating rates decrease slightly. The combined effect of having more plasma density in the topside and slightly lower heating rates is decreased topside temperatures.

6.3 Sensitivity to model parameters

The model is constructed with many degrees of freedom in how the energy and pitch-angle grids are chosen. To test the sensitivity of the results to these choices we have initialized the model with conditions from various times in the reference simulation and solved the photoelectron transport problem for a single time step using a wide variety of grids. The reference simulation was consistently within 5% of extremely high energy resolution simulations. Fig. 6.8 shows a few examples of these one step tests performed at 15:15 LT. The top left panel shows the change relative to a 64-stream in simulations using fewer pitch-angle bins. The top right and bottom left panels show the changes produced by constructing the energy grids in different ways. The top right panel changes the width of the energy bins below 10 eV. The bottom left panel changes the location of the transition from 0.25 eV

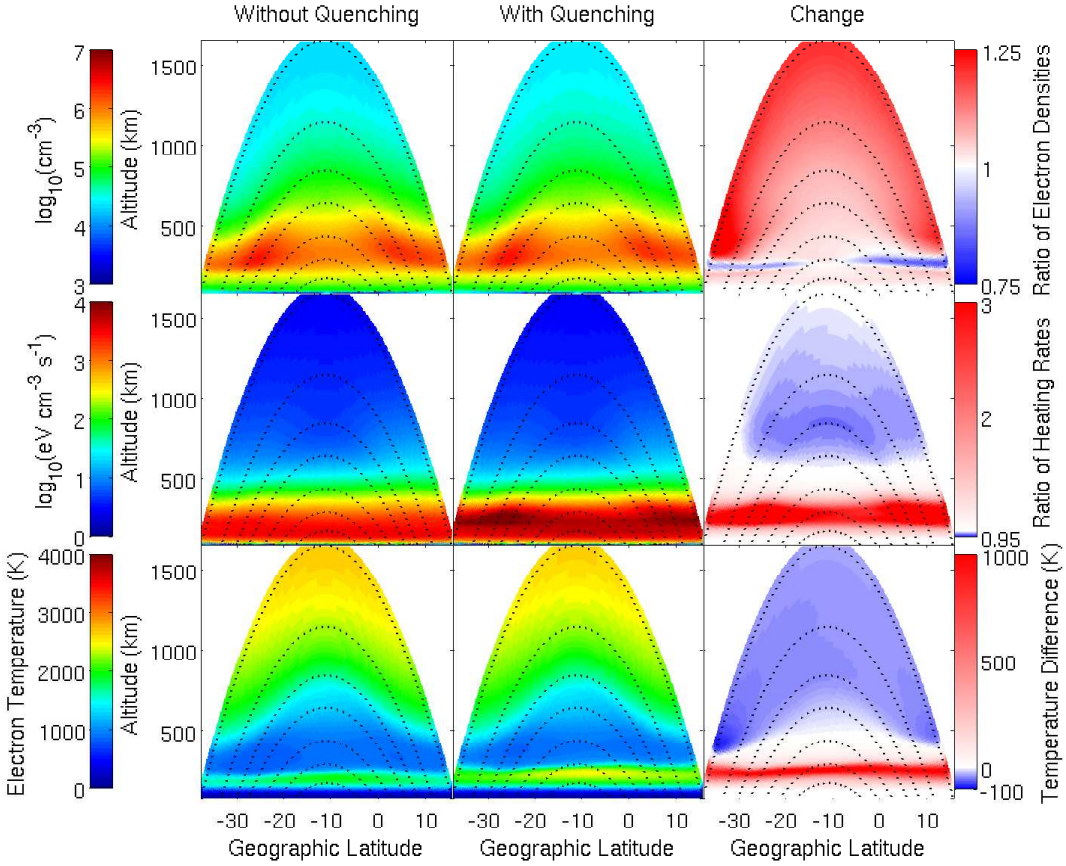

Figure 6.7: Comparisons of simulations with and without the quenching of $N(^2D)$. The left panels show, from top to bottom, the electron densities, electron heating rates, and electron temperatures from a simulation without quenching at 15:15 LT. The middle panels are these same quantities from the reference simulation, which includes quenching. The right panels show the changes. For the densities and heating rates the changes plotted are the ratios of the densities/heating rates with quenching to those without quenching. The temperature changes plotted are the temperatures with quenching minus the temperatures without quenching. In each of these three plots white represents no change. Note the highly asymmetric colorbars used for the change in heating rates and temperatures.

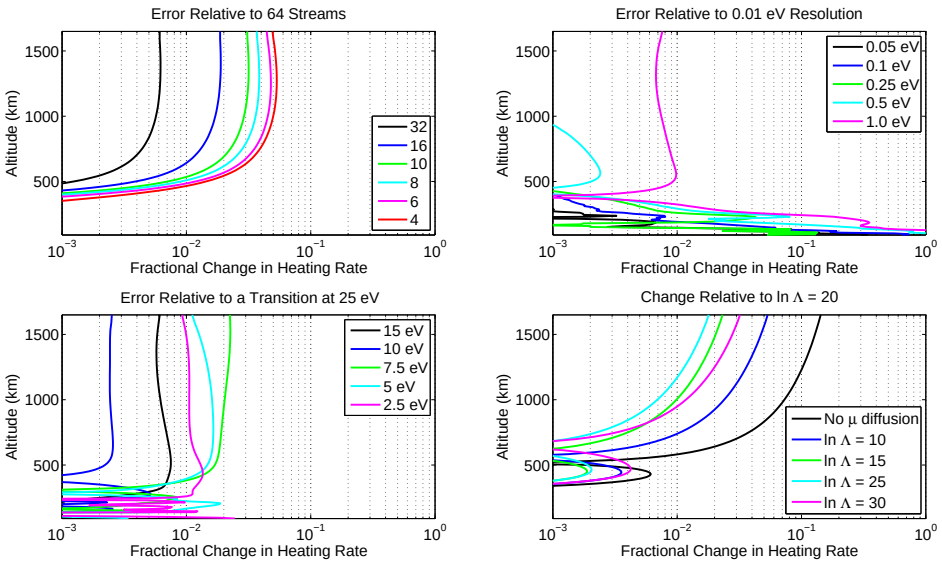

Figure 6.8: Fractional changes in the heating rates from one step tests for the reference case at 15:15 LT. See the text for descriptions of each of these tests. Each plot only shows the equatorial plane.

bins to 1 eV bins. Finally, the bottom right panel shows the effect of changing the amount of pitch-angle diffusion by altering the Coulomb logarithm.

6.3.1 Pitch-angle resolution, pitch-angle diffusion, and the treatment of the magnetic mirror force

The model results are potentially much more sensitive to changes in the pitch-angle resolution than Fig. 6.8 indicates if less pitch-diffusion is assumed. Fig. 6.9 shows a polar plot of the pitch-angle distributions from one step tests at 18 LT using 64 pitch-angle bins for the energy bin from 20 to 21 eV at 1534 km at the magnetic equator. Each of these tests was performed with identical initial conditions but using different amounts of pitch-angle diffusion. These pitch-angle distributions are primarily determined by the transport properties of the photoelectrons and

the magnetic field geometry, not by the pitch-angle distribution assumed for the photoproduction. When no pitch-angle diffusion whatsoever is used the pitch-angle distributions have narrow spikes near 0° and 180°, which are the result of the magnetic mirror force pushing photoelectrons towards $\mu = \pm 1$ as the field lines spread apart. Lower pitch-angle resolution simulations cannot resolve these spikes, and thus the heating rates produced by 4- and 8-stream simulations with no pitch-angle diffusion can systematically overestimate the topside heating rates by 20% and 10% respectively compared to 64-stream simulations. This problem is resolved by including some pitch-angle diffusion. Even a small amount of pitch-angle diffusion can remove the spike from the pitch-angle distributions. When the Coulomb logarithm in Eq. 4.73 is set to 10 the biases in 4- and 8-stream simulations relative to 64-stream simulations are reduced to 3% and less than 1% respectively. For values of the Coulomb logarithm larger than 10 these biases actually increase instead of decreasing further. For 8-stream simulations the biases relative to 64 streams are 3% and 4% for Coulomb logarithms of 20 and 30 respectively. Increasing pitch-angle diffusion not only removes the spikes near 0° and 180°, but also increases the number of photoelectrons near 90°, where magnetic mirroring is important.

The examples in Fig. 6.9 are all generated without using the higher order corrections described in Sec. 5.1.1. The effects of these higher order corrections can be tested using further one step tests. Fig. 6.10 shows results generated by initializing simulation with results from the reference case at 18 LT, then taking a single step using 64-streams using different types of high order corrections. The plot labeled "DCU" using the simple donor cell upwinded method (i.e. no higher order corrections). All the other plots use higher order corrections with different flux limiters, and are arranged in order of decreasing diffusivity. These plots show

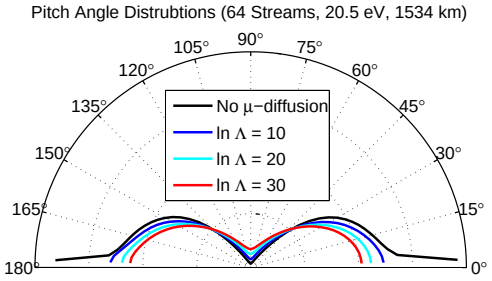

Figure 6.9: Pitch-angle distributions from single step tests using 64 streams for various different amounts of pitch-angle diffusion. Each test was initialized with conditions at 18 LT from the reference simulation. Each plot is for the 20 to 21 eV bin, at the magnetic equator, and at 1534 km. These plots are on a linear scale and each dashed semicircle represents a change of 10^7 cm^{-2}s^{-1}. The angles 0° and 180° correspond to photoelectrons traveling parallel to **B** northwards and southwards respectively.

the photoelectron fluxes for the energy bin centered at 375 eV as a function of pitch-angle cosine and the dipole coordinate, q_d, along the magnetic field line whose apex altitude is 1147 km. The colors are on a linear scale which has been engineered to highlight the subtle differences between these plots. The circular region in the center of each of these plots corresponds to the trapped region. As expected, the amount of flux in the trapped region noticeably decreases for the less diffusive numerical scheme. Fig. 6.11 shows these same results as a polar plot of the pitch angle distributions at the magnetic equator. The schemes using the higher order corrections slightly decrease the fluxes near 90° and increase the fluxes in the parallel directions.

The effects of higher order corrections on lower energy electrons are somewhat more complicated to interpret. Figs. 6.12 and 6.13 show the same information as Figs. 6.10 and 6.13 for the energy bin centered at 20.5 eV. In the color plots the

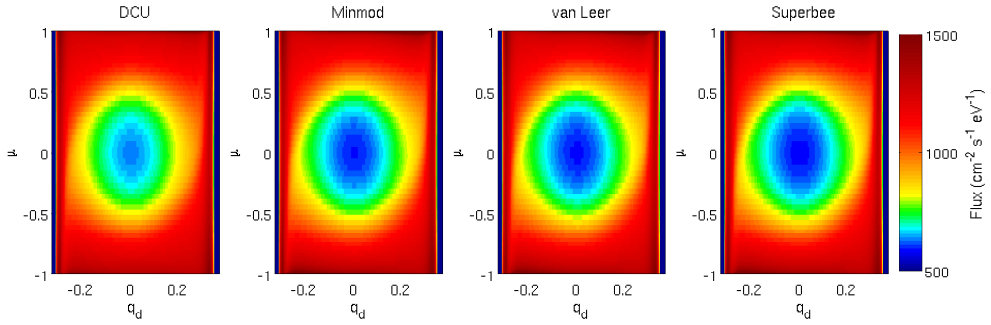

Figure 6.10: Photoelectron fluxes at 375 eV as a function of pitch-angle cosine, μ, and the dipole coordinate, q_d, along the field line with an apex altitude of 1147 km. The left plot uses no higher order corrections, and the other plots use the minmod, van Leer, and superbee flux limiters respectively. In each case the model was initialized using the reference case at 18 LT and uses 64 streams.

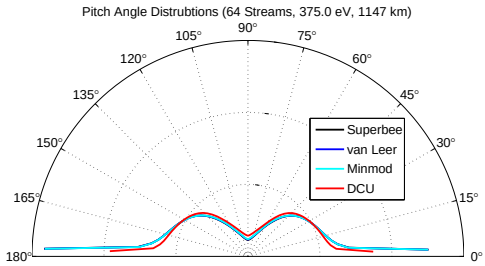

Figure 6.11: Polar plot of the pitch-angle distributions at 375 eV at 1147 km above the magnetic equator. The four curves correspond to cuts through the $q_d = 0$ planes of the four plots in Fig. 6.10.

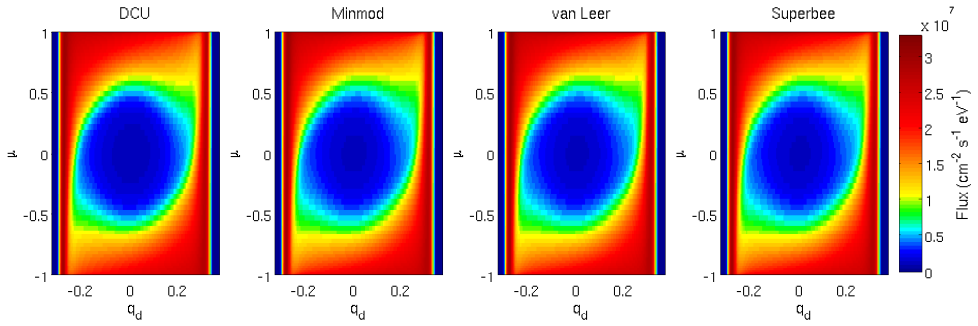

Figure 6.12: Photoelectron fluxes at 20.5 eV in the same format as Fig. 6.10 for the same four simulations.

fluxes in the trapped regions appear to increase slightly when the higher order corrections are applied instead of decrease. However, the higher order corrections are still increasing the fluxes in the parallel directions, meaning that in a relative sense the fluxes in the trapped regions are going down. When the higher order corrections are applied the total amount of flux reaching high altitudes increases because when the mean pitch-angle cosine is closer to 1 the photoelectrons have an easier time escaping to high altitudes. Transport effects are not important at 375 eV because the escape probabilities for such high energy photoelectrons are very high no matter what the pitch angles are.

It is not obvious whether the heating rates in the plasmasphere should increase or decrease in the plasmasphere when the higher order correction terms are used. Decreasing the trapped fluxes should decrease the plasmaspheric heating rates, however increasing the escape probabilities of the lower energy electrons by moving the mean pitch angle cosines closer to 1 should increase the plasmaspheric heating rates. In the low latitude ionosphere at altitudes below 1500 km both of these effects appear to be small, meaning the higher order corrections are unimportant in practice. Fig. 6.14 shows RTI plots of the electron temperatures for a simulation without higher order corrections and a simulation using the superbee

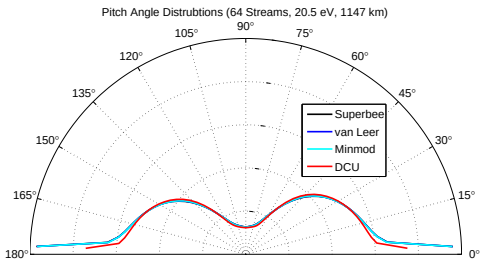

Figure 6.13: Polar plot of the pitch-angle distributions at 20.5 eV at 1147 km above the magnetic equator for the same four simulations as in Fig. 6.11.

flux limiter. Each of these simulations was performed for the reference day, but with quenching of N(^{2}D) turned off and using 16-streams. To save time, the photoelectron transport solutions were only computed once every 60$^{\text{th}}$ time step, and were assumed to be constant for the time steps in between. Sec. 7.4 discusses this method for accelerating the code in more detail. It produces small errors in the middle of the day, but introduces significant biases around sunrise and sunset. The bottom panel of Fig. 6.14 shows the arithmetic difference between the temperatures in these two simulations. The differences are almost 0 at low altitudes, as expected. At high altitudes the plasmaspheric temperatures decrease by 20-30 K when higher order corrections are added, which is a $\sim$1% change. The decrease is somewhat larger immediately after sunrise. The additional computation expense of an iterative solver is substantial, so given the small sizes of the temperature differences adding the higher order corrections is not worthwhile.

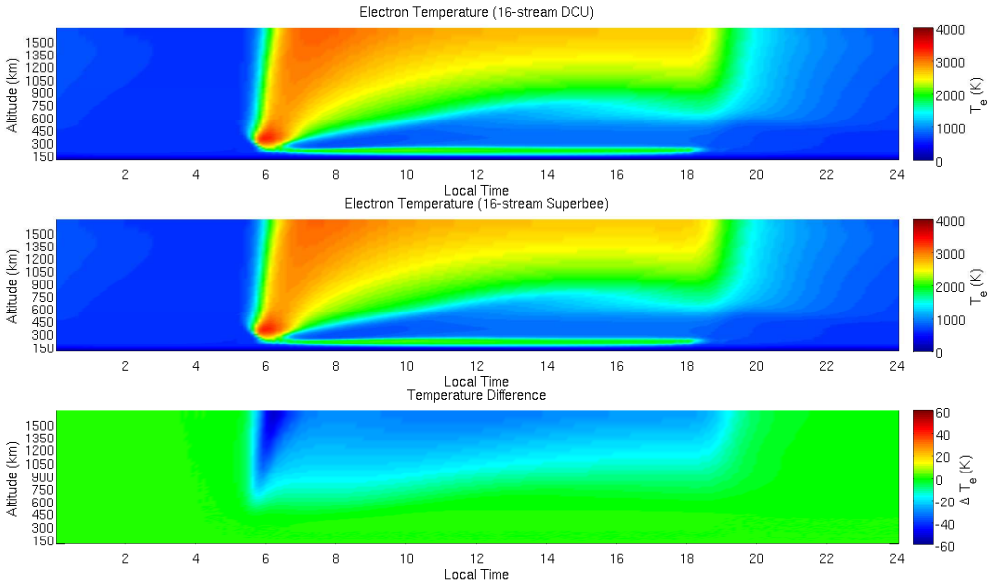

Figure 6.14: RTI plots of electron temperatures produced by a standard 16-stream simulation (top), a 16-stream simulations using higher order corrections with the superbee flux limiter (middle), and the arithmetic difference between the two (bottom).

6.4 Sensitivity to drivers

The modeled topside temperatures are also sensitive to changes in the many empirical models used as inputs to SAMI2-PE. Fig. 6.15 compares the measured electron temperatures to the SAMI2-PE results above the magnetic equator for several runs with adjusted drivers. The left panel shows the temperatures at 1005 km as a function of local time and the right panel shows the temperatures at 15:15 LT as a function of altitude. The blue curves correspond to the reference case. The green curves show the effect of replacing HWM93 with the more recent HWM07 model of the neutral winds [*Drob et al.*, 2008]. The HWM07 winds result in less electron density in the topside and corresponding higher temperatures, especially at dawn. The NRLMSISE-00 model does not accurately reflect just how low the neutral densities become during solar minima, especially during the unusually quiet solar

minimum during late 2008 and early 2009 [*Emmert et al.*, 2010; *Solomon et al.*, 2010, 2011]. The cyan curves show the effect of adjusting the NRLMSISE-00 model to use an exospheric temperature which is 14 K lower, 12% lower atomic oxygen density at the lower boundary of the thermosphere, and 3% lower density of all other species at the lower boundary of the thermosphere, as recommended by *Emmert et al.* [2010] from analysis of satellite drag measurements. These adjustments also result in less electron density and higher electron temperatures in the topside. The magenta curves show the effect of decreasing the vertical drifts predicted by the model of *Scherliess and Fejer* [1999] by 25%, which also results in less topside electron density and higher topside electron temperatures, especially in the afternoon when the equatorial arcs are fully formed. In this case the inflection in the temperature profile around 800 km from the shadowing effect of the equatorial arcs disappears because now the neutrals are controlling photoelectron escape. Finally, the red curves in Fig. 6.15 show the effect of using HWM07 winds, the adjusted NRLMSISE-00 neutral densities and temperatures, and the reduced electric fields simultaneously. All of these simulations produce nearly identical temperatures below 400 km, where everything is local, but the topside temperatures vary by over 30%. Uncertainties in the winds, electric fields, and neutral densities are thus the dominant source of error in the model in the topside.

Also shown in Fig. 6.15 are temperatures from a simulation using the old empirical electron heating model for two different values of the free parameter, C_{qe}, (dashed lines) and the temperatures from the empirical plasmasphere temperature model of *Titheridge* [1998] (dash-dotted line). During the day the Titheridge temperatures have reasonable values and the correct slope with increasing altitude, but they do not capture the local time dependence correctly. The local time dependence in this model was constructed using a simple harmonic expan-

sion which made no attempt to capture the large temperature increases at dawn at the equator [*Titheridge*, 1998]. The simulations using the old electron heating model can capture the qualitative shape of the temperatures with local time, but are quantitatively much further from the data than the Titheridge model. These temperatures are consistently much too high at dawn and too low in the afternoon for most values of C_{qe}. These temperatures also increase with increasing altitude too quickly.

The mechanisms by which changes in the neutral winds, electric fields, and neutral densities affect the equatorial topside electron temperatures can be more throughly understood by looking at changes in the off-equatorial F-regions. The following subsections explore the connections between the topside electron temperatures and neutral winds, electric fields, and neutral densities and temperatures respectively in more detail.

6.4.1 Neutral winds

Fig. 6.16 compares the reference case to a run with the HWM93 winds multiplied by two at 15 LT. The left column shows the electron density, electron thermal energy density, and electron temperatures from the reference case. The electron thermal energy density is defined as

$$\mathcal{W}_e = \frac{3}{2} k_B N_e T_e. \tag{6.4}$$

The center column of Fig. 6.16 shows the same quantities for the run with the winds doubled, and the right column shows the amount of change between the two runs. In March at the longitude of Jicamarca the meridional component of the HWM93 winds is predominantly southward. Thus increasing the winds causes the

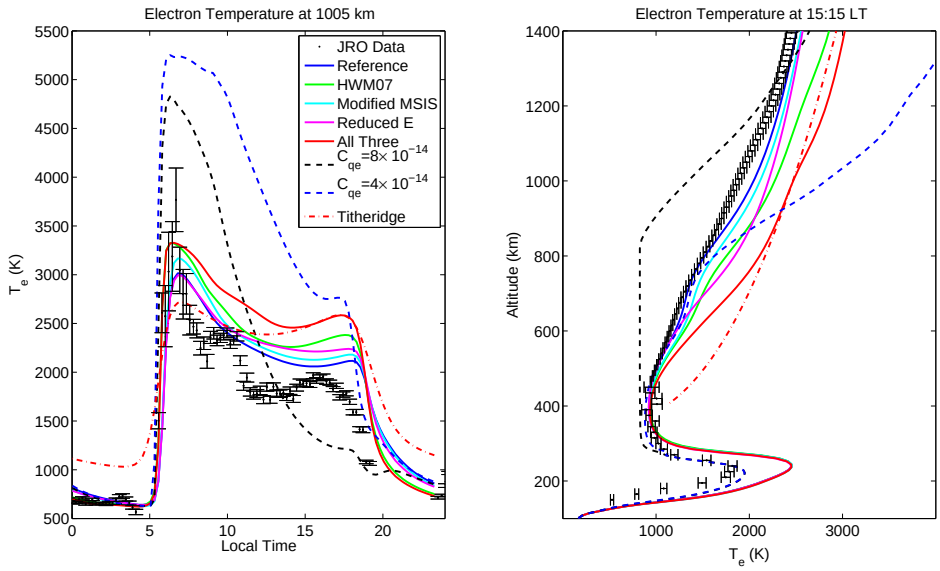

Figure 6.15: Comparison of temperatures from many different simulations to the Jicamarca data. The left panel shows temperatures at 1005 km as a function of local time and the right panel shows temperatures at 15:15 LT as a function of altitude. The solid curves are all SAMI2-PE runs. The solid blue curve is the reference simulation. The green curve replaces HWM93 with HWM07, the cyan curve makes modifications to the NRLMSISE-00 model as described in the text, and the magenta curve uses electric fields which have been reduced by 25%. The red curve uses all three of these modifications simultaneously. The dashed curves are SAMI2-PE runs with the photoelectron model disabled and the old empirical heating model from SAMI2 used instead with two different values of the free parameter, C_{qe}. Finally, the red dashed-dotted curve is the *Titheridge* [1998] empirical plasmaspheric temperature model.

F-region ionosphere in the southern hemisphere to be pushed downwards. At lower altitudes neutral molecular species are more prevalent. These neutral molecular species charge exchange with atomic ions to produce molecular ions, which recombine faster than the atomic ions via dissociative recombination processes. Thus decreasing the altitude of the F-region also results in a decrease in the electron densities. This effect is most obvious on the field lines containing the equatorial

arcs. The increased winds will raise the F-region in the northern hemisphere and slow the recombination rate in the north, however the increased recombination in the south outweighs the decreased recombination in the north. The field line integrated electron densities decrease as a result of the increased winds. The electron densities in the topside will also decrease with the increased winds such that these high altitudes remain in diffusive equilibrium with the off-equatorial F-regions.

The affect of the increased neutral winds on the topside electron temperatures are more complicated because there are multiple effects involved. If all of the heat flows into and out of the topside remained constant then one would expect the temperatures to increase as the electron densities decreased such that the electron thermal energy densities remained constant. However, the changes to the electron density profiles affect both the transport of photoelectrons up into the topside and the thermal diffusion back down to the F-regions. Fig. 6.17 compares the total photoelectron fluxes at 20 eV, the electron heating rates, and the thermal diffusion rates for the same two simulations as Fig. 6.16. The decreased electron densities make it easier for photoelectrons to reach the topside, especially on the field lines connected to the equatorial arcs.

The increased photoelectron fluxes do not necessarily imply increased electron heating rates, however, since the electron heating rates are roughly proportional to the product between electron density and photoelectron flux. At $\sim$ 1200 the increase in the photoelectron fluxes in small, but the decrease in the total plasmaspheric electron densities is substantial, resulting in decreased electron heating rates at these altitudes. The decreased plasmaspheric density means there are fewer thermal electrons around to "catch" energy from photoelectrons as they travel through the plasmasphere from one hemisphere to the other. On the field lines connected

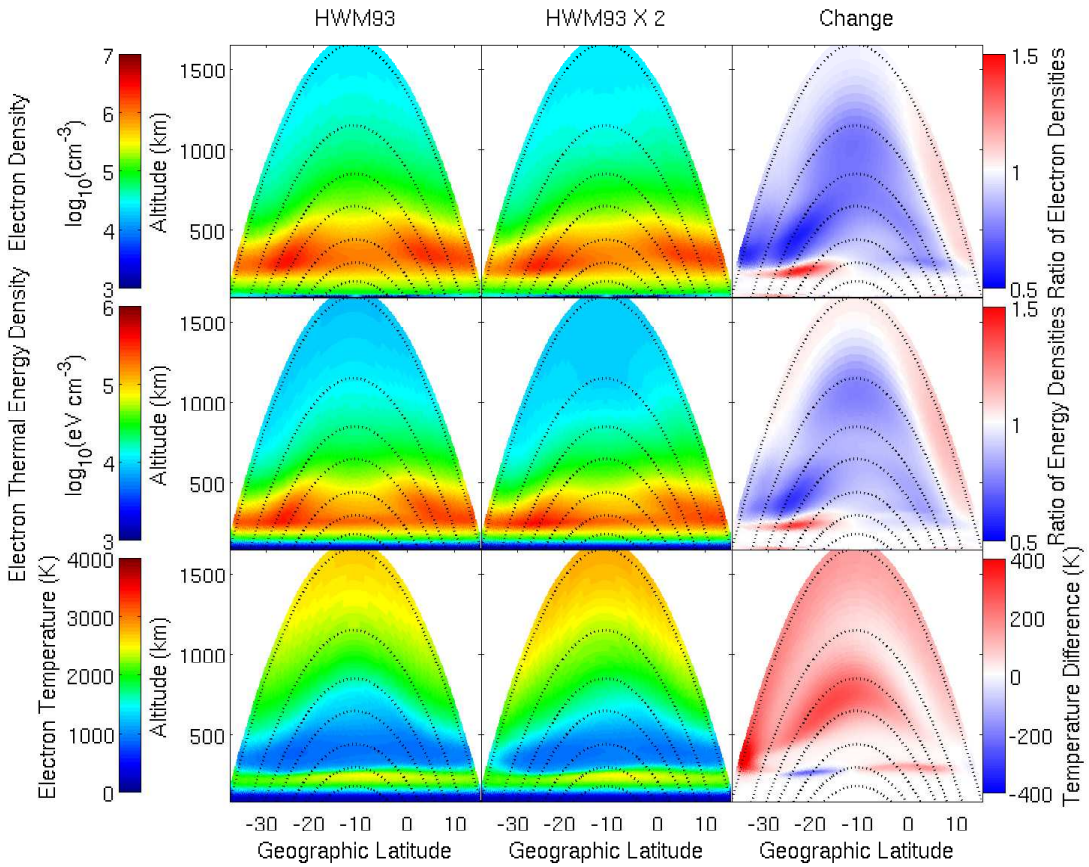

Figure 6.16: Comparisons of the reference simulation to a simulation using the HWM93 winds times two at 15 LT. In each plot the vertical axis is altitude and the horizontal axis is latitude. The dotted lines show the positions of a few magnetic field lines. The left column corresponds to the reference simulation, the middle column corresponds to the simulation with the winds doubled, and the right column shows the change between the two. The left and middle columns use the color scales on the left hand side. The right column uses the color scales on the right hand side. In the right column red colors means the values in the middle column are higher than those in the left column. The top row shows electron densities on a log scale and expresses the change as a ratio. The middle row shows the electron thermal energy densities on a log scale and also expresses the change as a ratio. The bottom row shows the electron temperatures on a linear scale and expresses the change as an arithmetic difference.

to the equatorial arcs, however, the increase in the photoelectron fluxes outweighs the decreases in the plasma densities, resulting in increased heating rates on these field lines.

The temperatures in the topside are primarily determined by the balance between the heating rates and the thermal diffusion rates back down the field lines. When the heating rates increase, the magnitude of the thermal diffusion rates must also increase. In the bottom panels of Fig. 6.17 these thermal diffusion rates are plotted on a log scale. The values are only plotted above 300 km and only where the sign of the diffusion rates corresponds to a cooling process. The thermal diffusion rates can be increased by increasing the temperatures and thus the thermal diffusivities (recall $\lambda_e \propto T_e^{5/2}$) or by increasing the temperature gradients. In the simulation with increased winds both effects happen; the topside electron temperatures increase which both raises thermal diffusivity in the topside and exaggerates the temperature gradient between the F-regions and the topside. Increased temperatures do not necessarily mean increased thermal energy densities, however. The increased thermal diffusion down the field lines actually trumps the increased heating rates throughout most of the topside, resulting in decreased electron thermal energy densities in the topside. It is not a contradiction to say the thermal energy densities decrease while the temperatures increase because temperature is a measure of the energy per electron and the electron density is also decreasing in this case.

Fig. 6.18 compares the reference case to a run performed with the HWM07 neutral wind model [*Drob et al.*, 2008] at 15 LT. The top panels show the projection of the neutral wind vector onto the direction of $\mathbf{B}$ for the two models, with negative numbers indicating southward flows. The HWM93 winds are uni-

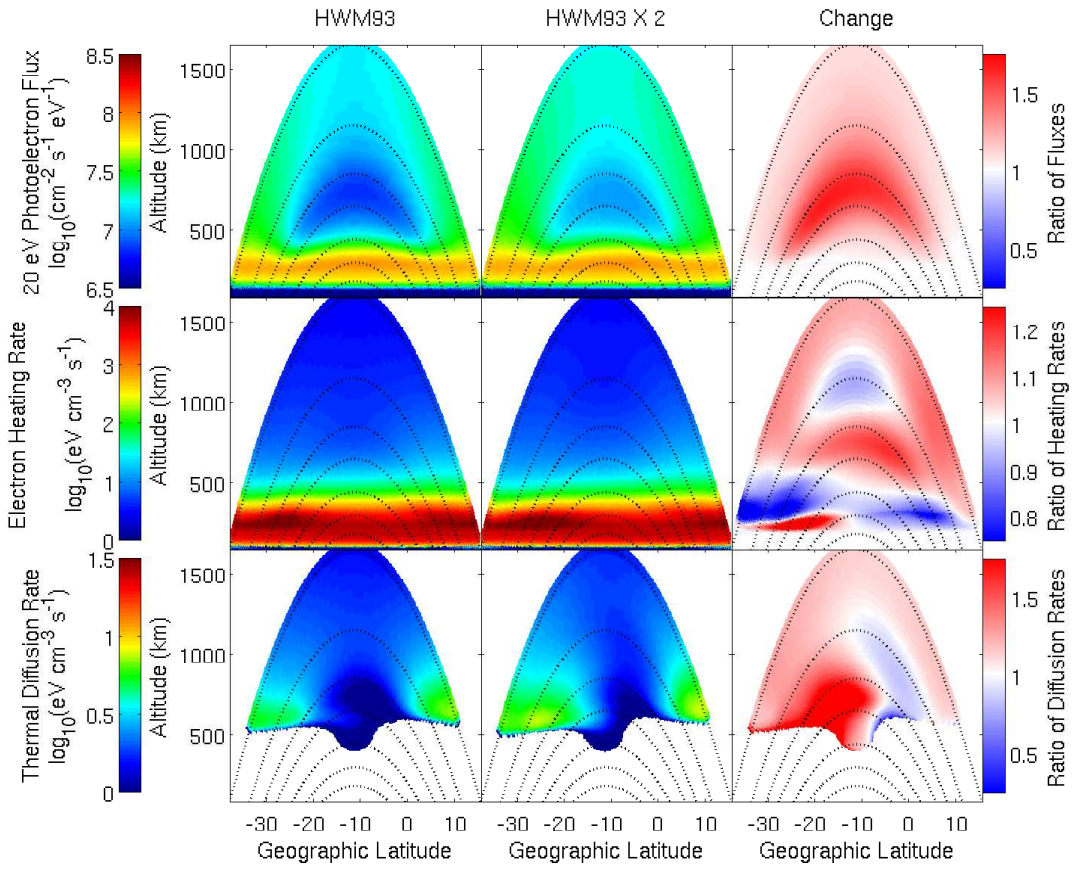

Figure 6.17: Comparisons of additional parameters from the reference simulation and the simulation using the HWM93 winds times 2 in a similar format to Fig. 6.16. The top column shows the total flux at 20 eV, the middle column shows the electron heating rates, and the bottom column shows the electron thermal diffusion rates. All quantities in the left and middle columns are plotted on log scales and the changes in the right column are all expressed as ratios. For the thermal diffusion rates the values are only plotted for altitudes above 300 km and when the sign of the thermal diffusion rate corresponds to a cooling process.

formly southward, but the HWM07 winds change sign at high altitudes such that they diverge away from the magnetic equator. The as a result the F-regions in both the southern and northern hemisphere are pushed to lower altitudes where they recombine faster. The result is a substantial decrease in the electron density along all of the flux tubes. The plasmaspheric densities must decrease when the F-region densities decrease to maintain diffusion equilibrium. Like in the case of doubling the HWM93 winds presented above, this decrease in topside densities is accompanied by a substantial increase in the topside temperatures.

6.4.2 Electric fields

Changes to the electric fields have similar effects to changes to the meridional winds. Fig. 6.19 compares the reference case to a run with the $\mathbf{E}\times\mathbf{B}$ drifts reduced by 25% in the same format as Fig. 6.16. The equatorial arcs are formed in the afternoon via the well known fountain effect [e.g. *Schunk and Nagy*, 2009; *Kelley*, 2009]; the vertical $\mathbf{E}\times\mathbf{B}$ drifts point upwards in the afternoon, lifting the equatorial plasma to higher altitudes. The plasma then slides down the field lines and piles up in the equatorial arcs just above and below the magnetic equator. The densities in the equatorial topside are determined by a balance between the lifting of the equatorial F-region plasma and diffusion down into the off-equatorial F-regions. When the $\mathbf{E}\times\mathbf{B}$ drifts are reduced the topside electron densities decrease and the equatorial arcs which form are less dense and closer to the magnetic equator. Just like the cases presented above, the decrease in topside plasma densities are accompanied by increased electron temperatures but decreased electron thermal energy densities. Like the cases presented above, this result can be understood as an interplay between changes in the photoelectron transport and the thermal

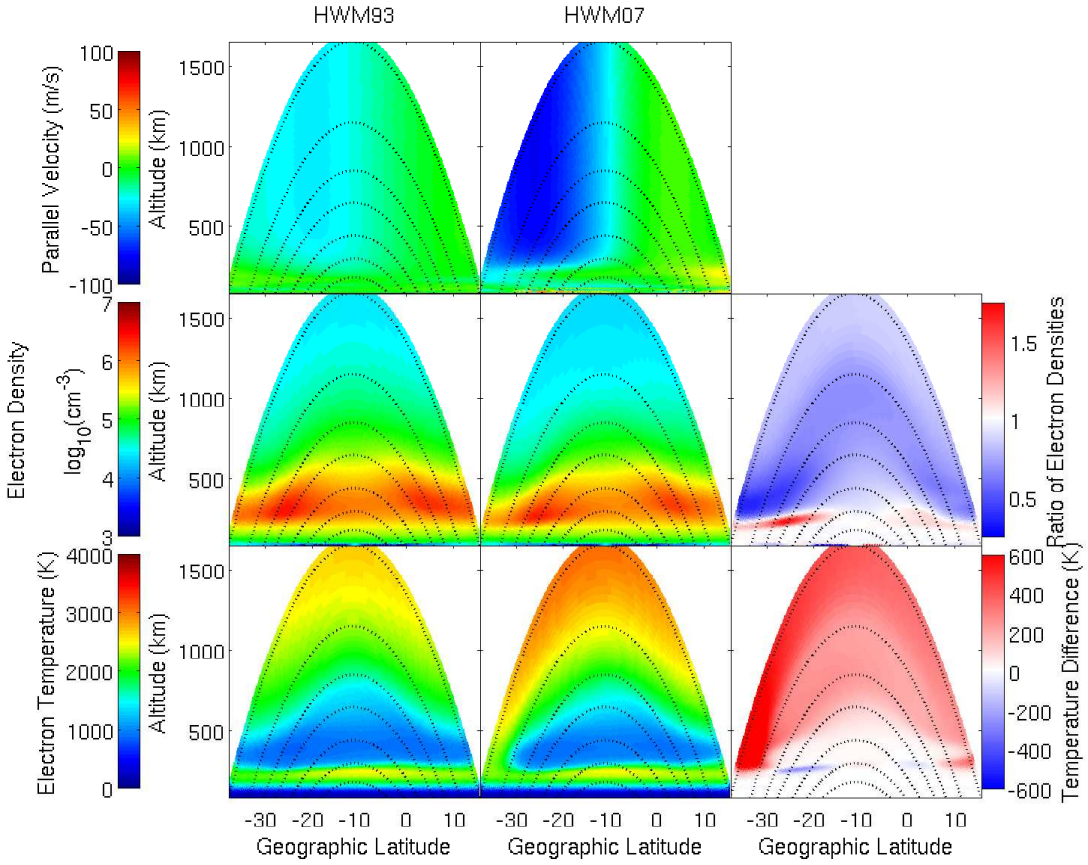

Figure 6.18: Comparison of the reference simulation to a simulation using HWM07 winds at 15 LT in a similar format to Fig. 6.16. The middle and bottom rows show the electron densities and electron temperatures in an identical format to the top and bottom rows of Fig. 6.16. The top row shows the projection of the horizontal winds onto the direction of **B**, with positive numbers corresponding to northward flows.

diffusion.

6.4.3 Neutral densities and temperatures

The changes to the neutral densities will also have effects on the electron densities and temperatures. Lower neutral densities will lower the photoproduction

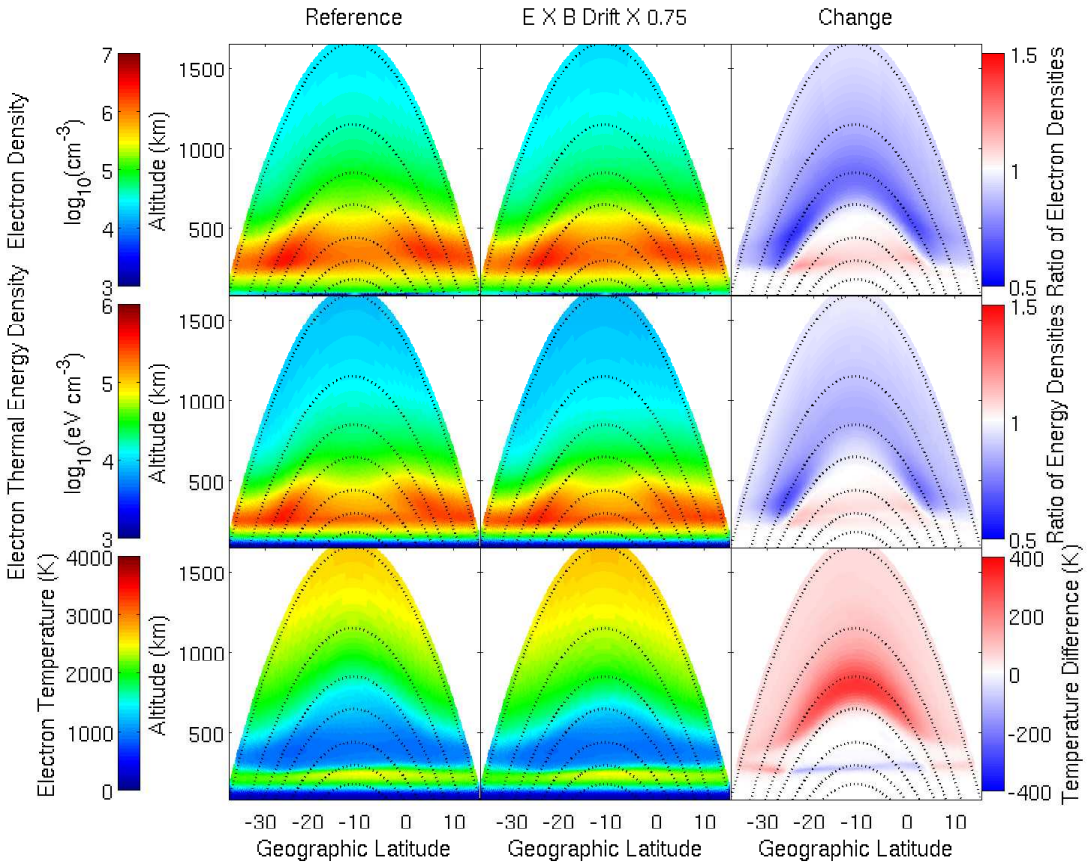

Figure 6.19: Comparison of the reference simulation and a simulation where the $\mathbf{E} \times \mathbf{B}$ drifts are multiplied by 0.75 at 15 LT. The format is identical to that of Fig. 6.16.

rates thus lowering the electron densities, lower the electron and ion cooling rates through collisions, slightly change thermal diffusivities, and decrease the photoelectron collision frequencies causing photoelectron to travel further. Fig. 6.20 compares the reference case to a run with the NRLMSISE-00 neutral densities uniformly decreased by 20%. The decrease in the electron densities resulting from the decreased photoproduction rates appears to be the most important effect. Even though photoproduction is negligible at high altitudes, the topside densities also decrease when the photoproduction rates decrease to maintain diffusive equilibrium. Like in the cases above of increased winds and decreased electric fields,

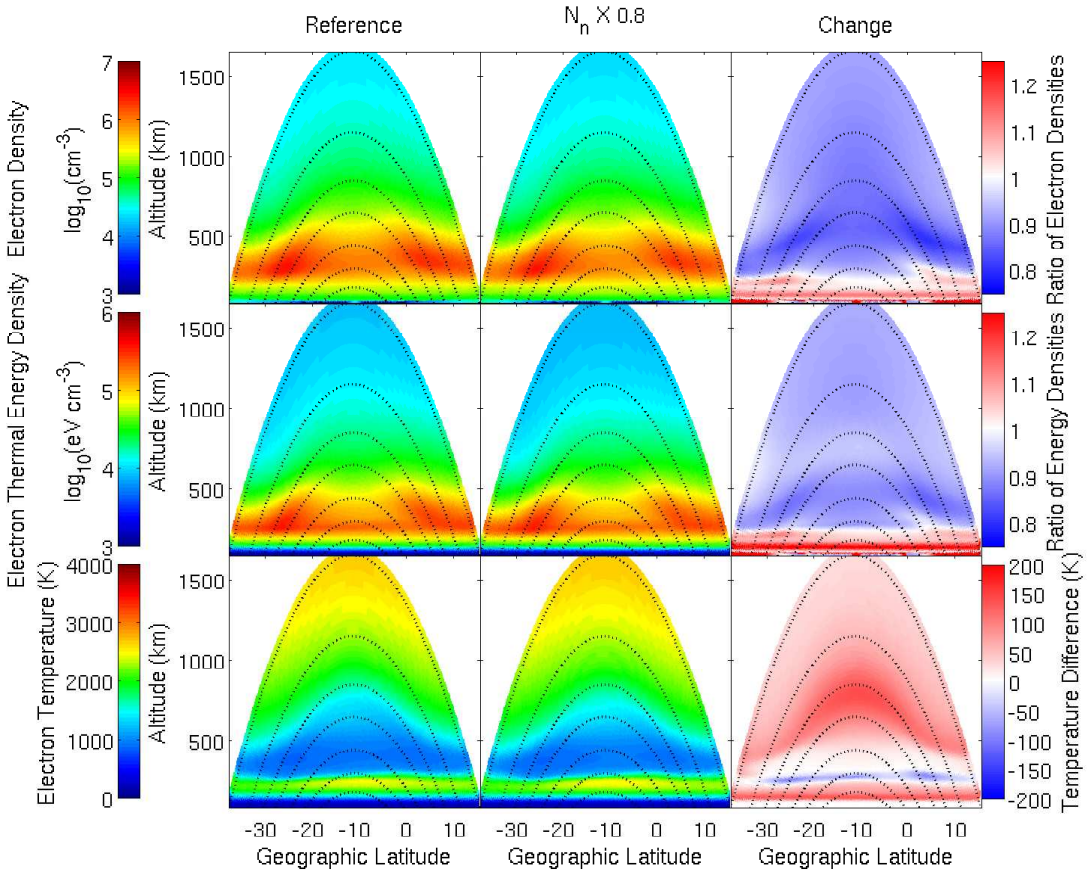

Figure 6.20: Comparison of the reference simulation and a simulation where the neutral densities are multiplied by 0.8 at 15 LT. The format is identical to that of Fig. 6.16.

this decrease in electron density is accompanied by an increase in the electron temperatures but a decrease in the electron thermal energy densities.

Changes to the neutral exospheric temperature are somewhat more interesting than changes to the neutral densities. Changes to the neutral temperatures alter the density profiles because the neutral atmosphere must be in hydrostatic equilibrium. Decreasing the exospheric temperature decreases the neutral scale height, resulting in decreases in the neutral densities which become larger with increasing altitude. Fig. 6.21 illustrates the effects of decreasing the exospheric temperatures

by 100 K. At low altitudes the decreased neutral temperatures result in decreased plasma temperatures because the electron-neutral cooling terms are proportional to $T_e - T_n$. Furthermore, the decreased temperatures alter the chemical reaction rates such that the amount of N(^{2}D) is decreased, which is a large heat source in the lower F-region. At high altitudes the decreased neutral temperatures result in slightly increased plasma temperatures, however. When the temperatures decrease the high altitude neutral densities decrease. As in the case presented above, reduced neutral densities leads to reduced topside plasma densities and higher topside plasma temperatures.

Fig. 6.22 compares the reference simulation to the simulation using the adjustments to NRLMSISE-00 suggested by *Emmert et al.* [2010]. The adjustments both reduce the neutral densities at the bottom of the thermosphere and reduce the exospheric temperature. The reduction in exospheric temperature decreases the neutral scale height, meaning the percent change in the neutral density increases with increasing altitude, reaching a nearly 50% reduction at 1500 km. Nonetheless, the most pronounced effects on the electron densities appear in the F-regions, where photoproduction is important. The decreases in the plasma density in the topside appear to maintain diffusive equilibrium with the decreased F-regions, not because of a large decrease in the photoproduction at these altitudes. Like all of the other examples presented above, these decreased topside densities are accompanied by increased electron temperatures.

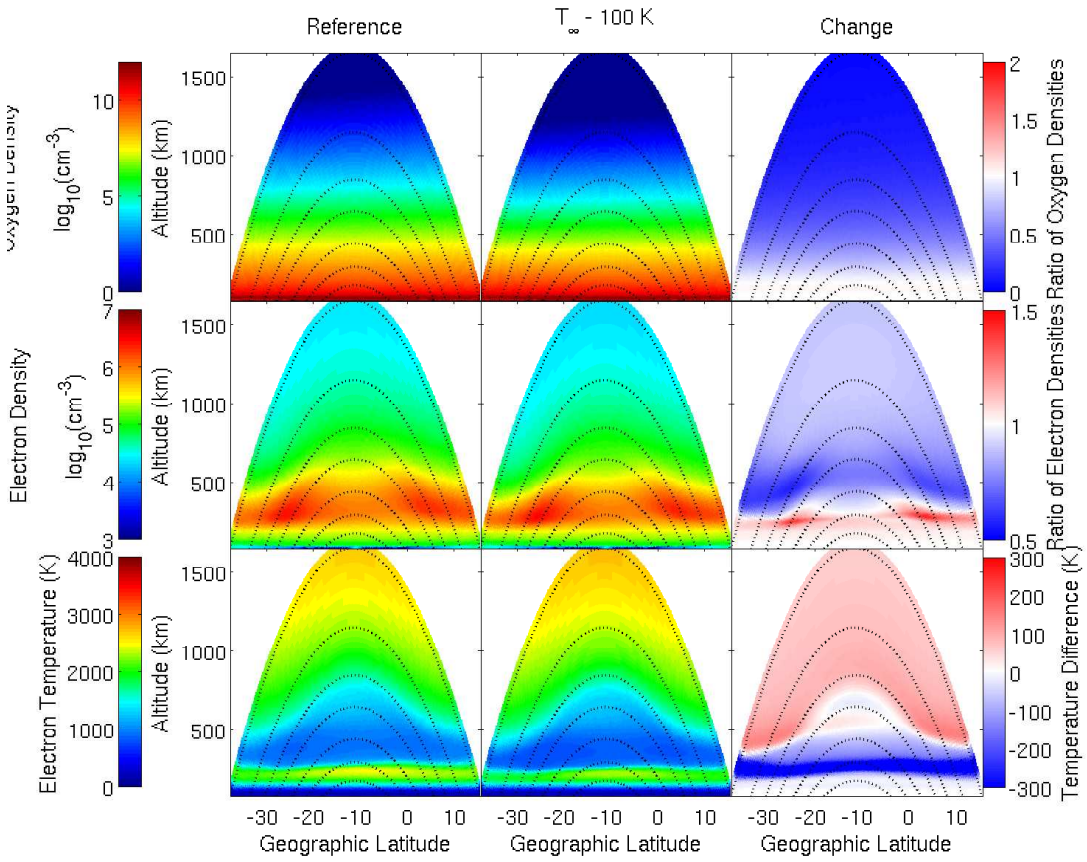

Figure 6.21: Comparison of the reference simulation and a simulation where the exospheric temperature is reduced by 100 K at 15 LT. The format is similar to that of Fig. 6.16, except the top panel shows the neutral atomic oxygen densities.

6.5 Day-to-day Variability

All the results presented so far have been for a single day. The top panel of Fig. 6.23 shows electron temperature measurements from six consecutive days of full profile data from Jicamarca, which is one of the longest continuous experiments run since the introduction of the full profile mode. These days are July 8-13, 2008, which were also geomagnetically quiet and in extremely low solar minimum conditions (F10.7=67.7, Ap=3.0). The middle panel shows electron temperatures from a SAMI2-PE run covering the same time period and the bottom panel plots the

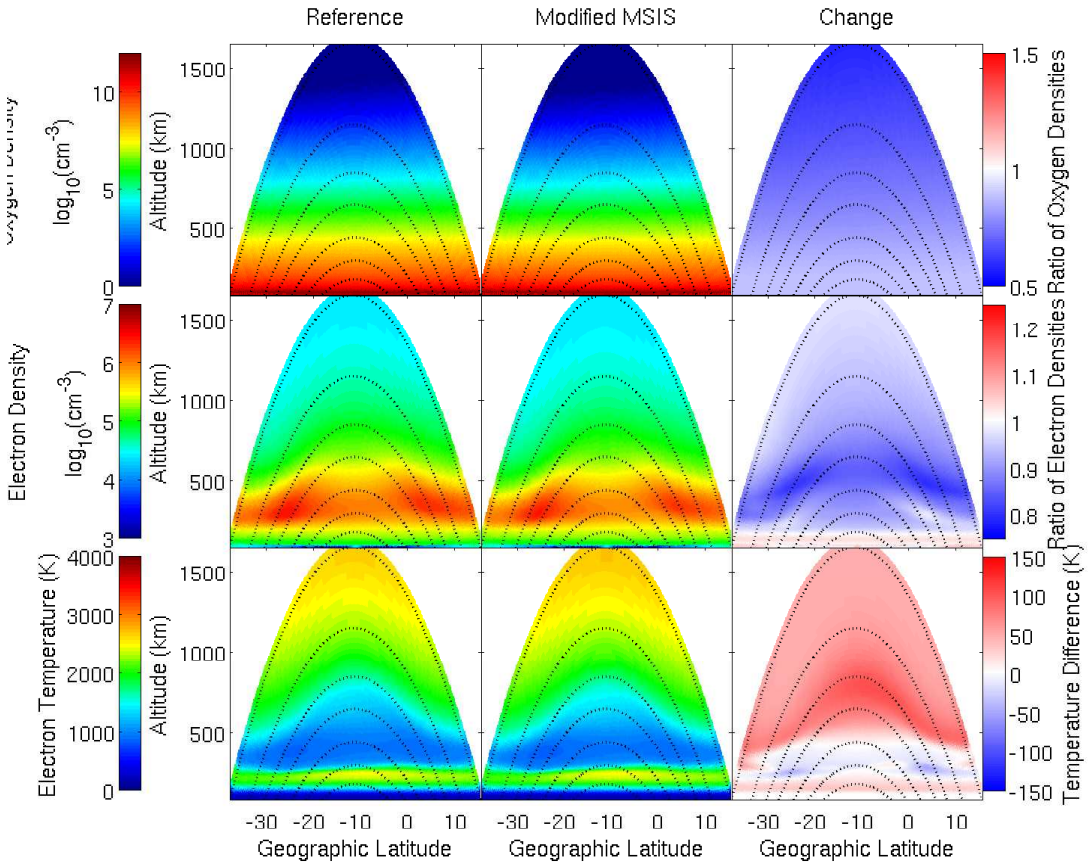

Figure 6.22: Comparison of the reference simulation and a simulation using the modifications to NRLMSISE-00 recommended by *Emmert et al.* [2010] (see text). The format is identical to that of Fig. 6.21.

data and model results at a single altitude on the same plot. The model produces nearly identical results from one day to the next, but the data show a large degree of day-to-day variability. The daytime topside electron temperatures routinely differ by 500 K or more from one day to the next. Figs. 6.24 and 6.25 show the corresponding data and model results for the electron densities and electron thermal energy densities. These parameters also exhibit a substantial amount of day-to-day variability which is not captured by the model.

For expediency, the SAMI2-PE run presented here was performed with only 4

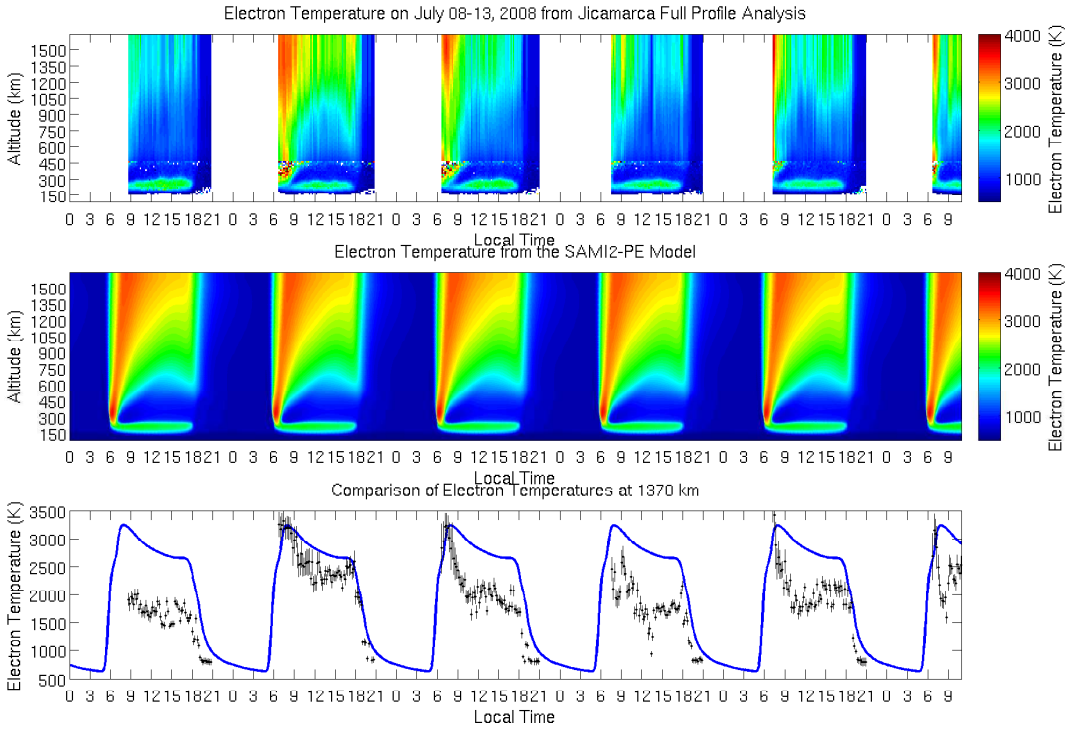

Figure 6.23: Measured and modeled electron temperatures for July 8-13, 2008. The top panel shows the measured electron temperatures as a function of local time and altitude. The middle panel shows the modeled temperatures in the same format. The bottom panel plots the measured and modeled temperatures at an altitude of 1370 km. The measurements are plotted as black dots with 1 standard deviation error bars and the model results are plotted as a solid blue line.

pitch angle bins and the low resolution 45 bin energy grid. As discussed above, this resolution results in some systematic bias in the model. This bias is both smaller than the difference between the model and the data and smaller than the day-to-day differences in the data. Thus, these low resolution runs are still instructive to study despite their inaccuracies. Also, the run was performed with quenching of $N(^2D)$ disabled since with the current neutral NO model and nitrogen ion chemistry enabling this term produces unreasonable overestimations of the temperatures in the F_1-region.

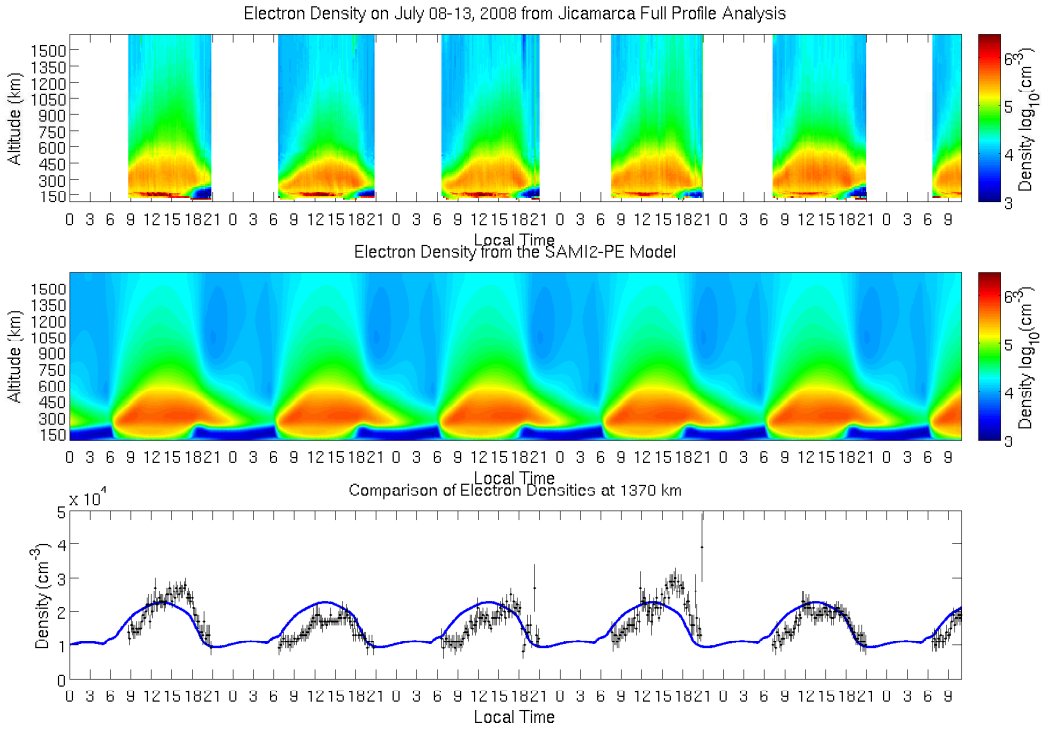

Figure 6.24: Measured and modeled electron densities for July 8-13, 2008. These plots are formatted the same way as in Fig. 6.23 except the top and middle panels are in a logarithmic scale.

Even with heating due to quenching disabled the electron temperatures and thermal energy densities are consistently higher than the data at all altitudes and most local times during the day. An easy solution to this is to tune down the solar flux. Fig. 6.26 shows the effect of multiplying the solar fluxes by 0.66 at 240 km. These data are taken from ultra low solar minimum conditions where the F10.7 index is lower than any of the days used to construct the empirical scalings used in the EUVAC and HEUVAC models [*Richards et al.*, 1994, 2006]. Thus it is plausible the HEUVAC would be overestimating the solar flux during this period. However, since the F10.7 index is steady throughout the entire week it is unlikely that the solar EUV flux is varying substantially. Thus this tuning of the solar fluxes fixes some of the systematic bias between the data and the model, but cannot explain

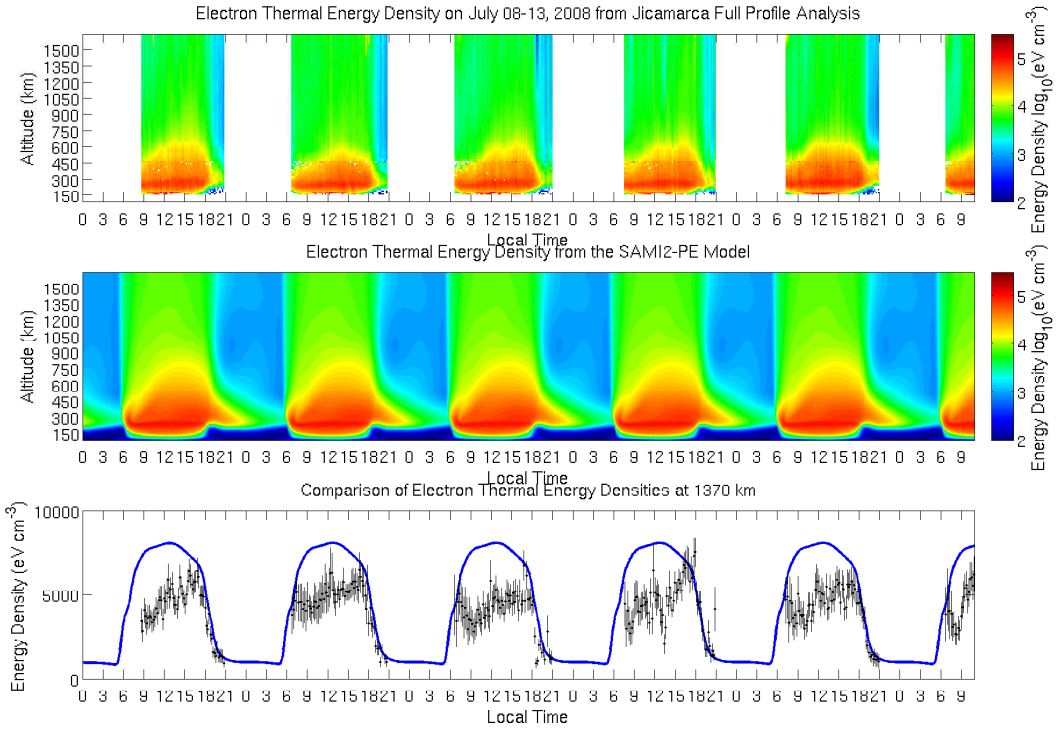

Figure 6.25: Measured and modeled electron thermal energy densities for July 8-13, 2008. These plots are formatted the same way as in Fig. 6.24.

the day-to-day variability.

The best candidates for sources of variability are variations in the $\mathbf{E} \times \mathbf{B}$ drift and variations in the neutral winds. Variations in the neutral densities and temperatures could also play a role, but Sec. 6.4.3 showed that relatively large variations in the neutral densities and temperatures (i.e. 20% density and 100 K) can only produce temperature changes of 100-200 K. Realistically variations in the neutral densities and temperatures cannot be large enough to explain the observed changes of $\sim$500 K or more from day-to-day.

The Jicamarca data presented were collected with the antenna in an oblique pointing position, meaning no direct measurements of the drifts are available from

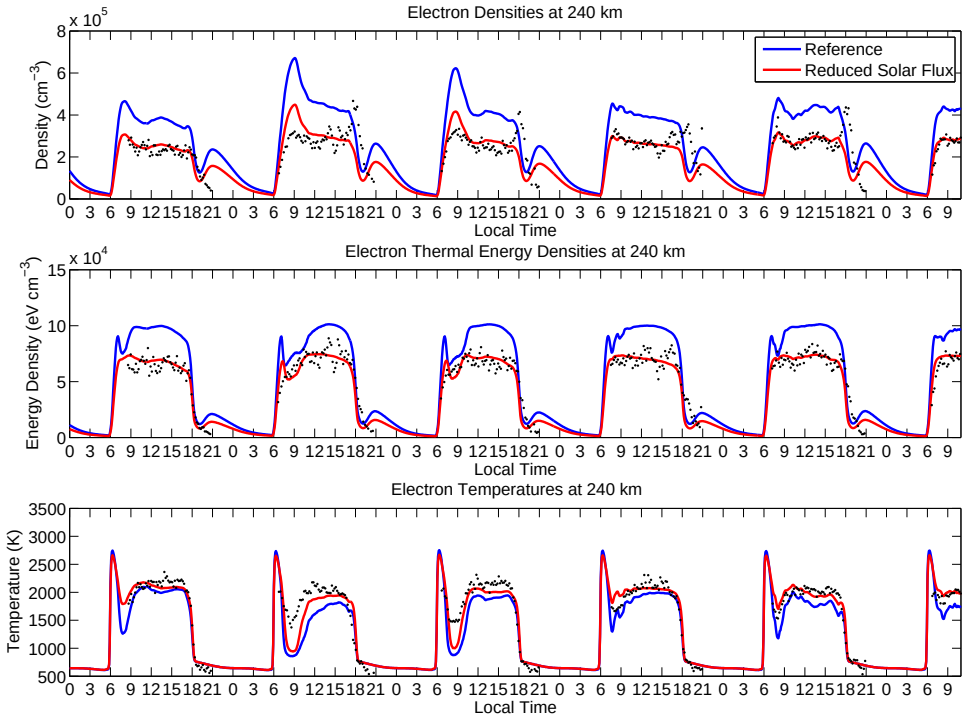

Figure 6.26: Comparison of two simulations at 240 km. The panels show the electron densities, the electron thermal energy densities, and electron temperatures respectively at 240 km altitude above the magnetic equator. The black dots are the Jicamarca measurements. The blue "reference" curve is from the same simulations presented in Figs. 6.23, 6.24 and 6.25. The red curve is the simulation with the solar fluxes multiplied by 0.66.

the incoherent scatter radar itself. However, the vertical drifts can be estimated from magnetometer data. The JRO staff maintain several magnetometers in South America, including one at Jicamarca on the magnetic equator, and one in Piura, which is a few degrees away from the magnetic equator. During the day, the difference in the horizontal components measured by these two magnetometers, called ΔH, is primarily related to the current flowing in the equatorial electrojet, which is in turn related to the zonal electric field which are responsible for the vertical $\mathbf{E} \times \mathbf{B}$ drifts. A neutral network is used to estimate the vertical drifts associated with ΔH measurements made at Jicamarca [*Anderson et al.*, 2004]. The

bottom panel of Fig. 6.27 shows these estimates along with the *Scherliess and Fejer* [1999] model values for the week of July 8-13, 2008. A SAMI2-PE simulation was performed for this week with the solar fluxes multiplied by 0.66 and using vertical drifts which were interpolated from these data. At night when the ΔH estimates are not available the *Scherliess and Fejer* [1999] model is used instead. The top three panels of Fig. 6.27 compare the results from this simulation to the simulation where the solar fluxes were multiplied by 0.66 but the *Scherliess and Fejer* [1999] model was used at all times (i.e. the simulation used for Fig. 6.26). As expected from the discussion in Sec. 6.4.2, days were the electric field was higher than the *Scherliess and Fejer* [1999] model have lower temperatures and vice versa. This explains some, but not all, of the observed variability. For the last 4 days the drifts inferred from ΔH are very similar to the *Scherliess and Fejer* [1999] model, so little difference is observed between the two models.

Unfortunately no simple proxy for the meridional winds over Jicamarca is available for July 8-13, 2008. *Richards* [1991] created a method for estimating the meridional winds from the height of F-peak determined by a mid-latitude ionosonde. In principle this method could be employed in the future using off-equatorial ionosondes on the same magnetic longitude as Jicamarca. A chain of ionosondes near Jicamarca's longitude are currently being deployed as part of the Low Latitude Sensor Network (LISN), however none of these, except the ionosonde at Jicamarca itself, were in place in 2008. Fig. 6.28 shows results from a variety of SAMI2-PE simulations using different sets of winds. Like Fig. 6.27, each simulation multiplies the solar fluxes by 0.66 and uses $\mathbf{E} \times \mathbf{B}$ drifts interpolated from the ΔH measurements during the day. The winds used in each simulation are scaled versions of the HWM93 and HWM07 models. When the scaling factor is negative the direction of the winds are reversed. The simulation with no winds whatsoever

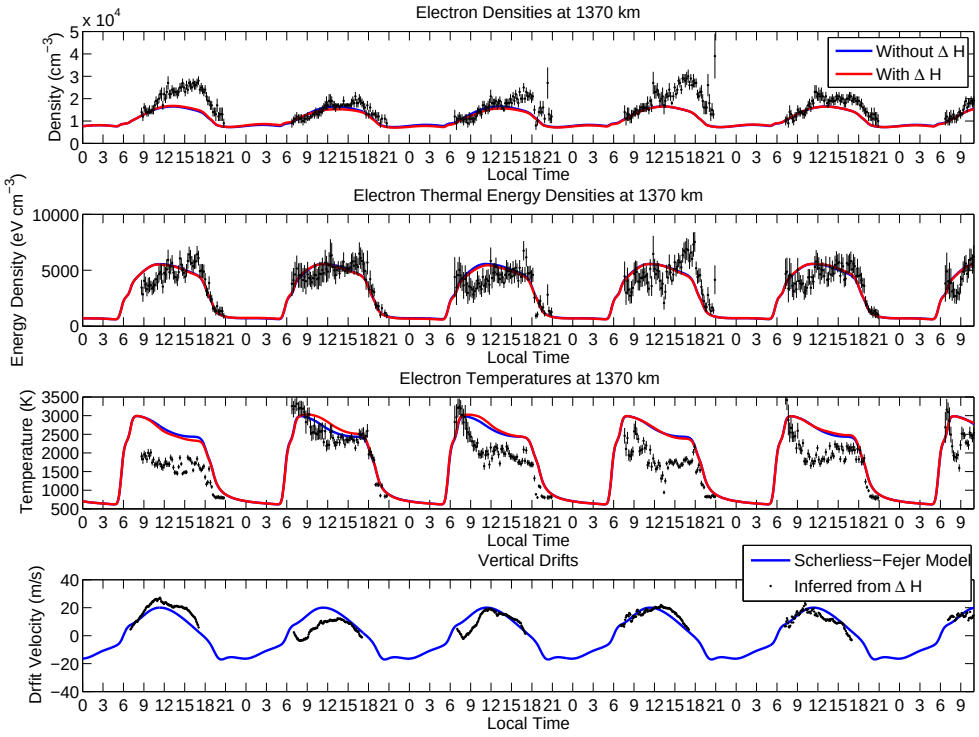

Figure 6.27: Comparisons of simulations using measured and modeled $\mathbf{E} \times \mathbf{B}$ drifts. The bottom panel shows vertical $\mathbf{E} \times \mathbf{B}$ drifts inferred from ΔH measurements along with those from the *Scherliess and Fejer* [1999] model. The top three panels show the electron densities, thermal energy densities, and temperatures at 1370 km. The black dots with errorbars are the Jicamarca measurements. The blue curve corresponds to the same simulation as the red curve in Fig. 6.26. The red curve is for a simulation which uses the ΔH measurements in addition to reducing the solar fluxes.

matches the data for the electron thermal energy densities best of all. The two most drastic simulations are those using HWM07 and HWM07 with the sign reversed. The HWM93 and HWM07 winds in July are similar to those in March presented in the top panels of Fig. 6.18. The HWM93 winds point predominantly southward, while the HWM07 winds switch sign in the northern hemisphere, resulting in winds which diverge away from the magnetic equator. Thus in the simulation where the sign of HWM07 is reversed the winds are converging on the magnetic

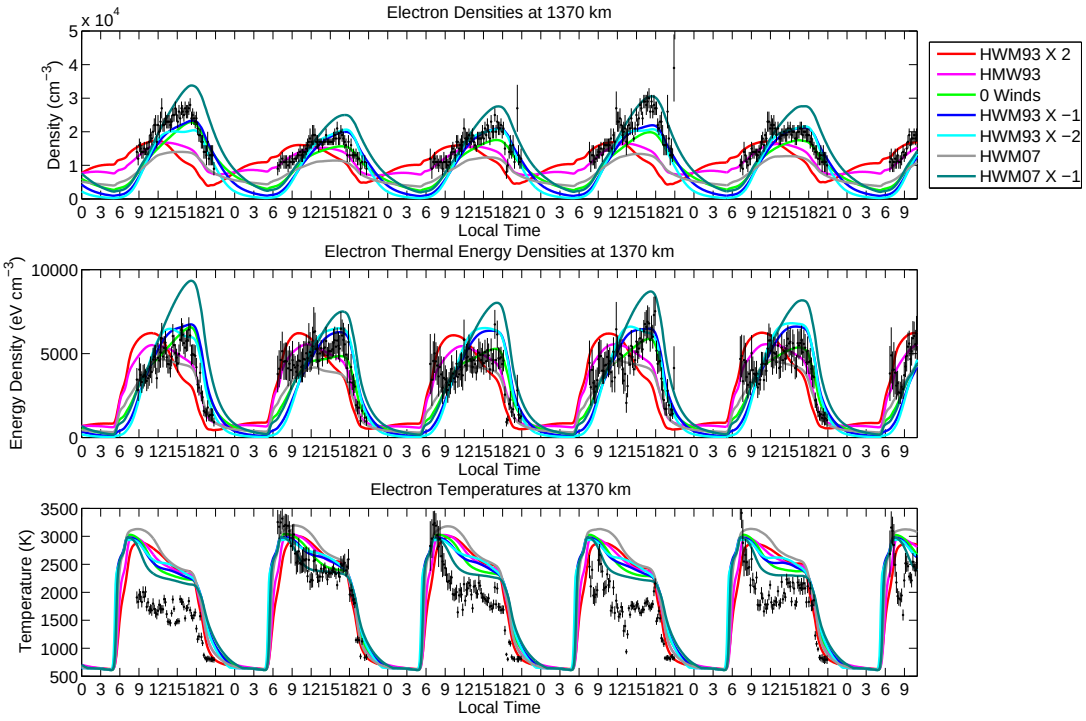

Figure 6.28: Comparisons of simulations using many different neutral wind profiles at 1370 km in the same format as Fig. 6.26. In each simulation the fluxes are reduced and the ΔH measurements are used. Thus the magenta curve labeled "HWM93" is the same simulation as the red curve in Fig. 6.27.

equator the winds push plasma up into the plasmasphere from both hemispheres. The switch from diverging winds to converging winds increases the plasmaspheric electron densities by a factor of 3 and lowers the electron temperatures by nearly 500 K. Thus changes to the meridional winds can have dramatic effects on the densities and temperatures in the plasmasphere.

In general the temperatures in Fig. 6.28 are consistently higher than the data. None of the runs can reproduce the cold temperatures observed on the first day. This probably indicates that SAMI2-PE systematically overestimates the plasmaspheric temperatures. The section on future work in Ch. 7 will discuss possible reasons for this problem in more detail.

CHAPTER 7

CONCLUSIONS AND RECOMMENDATIONS FOR FUTURE WORK

This thesis revisited the old problems of photoelectron transport and ionospheric energetics to interpret recently improved plasma temperature measurements made at the Jicamarca Radio Observatory. These efforts have produced an extended version of the 2-D SAMI2 ionospheric model, called SAMI2-PE, which includes photoelectron transport. The new electron heating model is a significant improvement over the semi-empirical model used in SAMI2. The electron temperatures above the F-peak from the modified model qualitatively reproduce the shape of the measurements as functions of time and altitude and quantitatively agree with the measurements, even during the rapid temperature increase at dawn. For the reference day (March 25, 2009) the modeled and measured temperatures in the topside are within $\sim$30% or less during the entire day. In the topside the modeled temperatures can change by $\sim$30% or more when the background winds or electric fields are changed. Sec. 7.3 discusses additional sources of uncertainty and bias which may still be present in the model.

The photoelectron transport model created for SAMI2-PE is yet another addition to the long history of suprathermal electron transport modeling. Sec. 7.1 reviews the similarities and differences between SAMI2-PE and other existing suprathermal electron transport models. This section also speculates on the future evolution of photoelectron transport modeling. The greatest advantage of SAMI2-PE is the ability to run 24 hour or longer simulations on a 2-D grid and produce plots that look like Jicamarca data. The numerous simulations presented in Ch. 6 with slightly differing inputs have illuminated ways the thermosphere, ionosphere,

and plasmasphere work together as a system at low-latitudes. Sec. 7.2 summarizes these lessons. Unfortunately, the computational complexity of the model currently prohibits transitioning to 3-D. Sec. 7.4 gives several recommendations for ways to simplify the computations and accelerate the code. SAMI2-PE was created with the low-latitude topside ionosphere specifically in mind, however it has many other potential applications. Extending the model to auroral latitudes would be straightforward. The energy grid would need to be extended to higher energies, provisions for anisotropic scattering would need to be included, and the boundary conditions at the top of the field line would need to be changed properly. Given the detailed studies of electron aurora which have already been performed [e.g. *Solomon*, 1993; *Lummerzheim and Lilensten*, 1994], however, there is little motivation to do this. SAMI2-PE can also be used to predict the effects of suprathermal electrons produced during ionospheric modification experiments.

7.1 Relationship of SAMI2-PE to other suprathermal electron transport models

This thesis comes 44 years after *Nisbet* [1968] published one of the earliest photoelectron transport models. Sec. 2.4 shows that the equations solved by previous photoelectron transport models are either equivalent to, or approximations of, the equations solved in SAMI2-PE. One physical effect which is neglected in SAMI2-PE but included in several other existing suprathermal electron transport models is the effect of parallel electric fields. The discussion in Ch. 4 justifies the omission of parallel electric fields in the low-latitude ionosphere.

Most of the past photoelectron transport models were made to perform the

calculations once in a specified background atmosphere instead of doing the calculations self consistently for every time step and field line inside an ionospheric model like SAMI2-PE. Currently ionospheric models with embedded photoelectron solvers are relatively rare, but given the increasing computer power and the importance of photoelectron calculations, some kind of photoelectron transport routine will likely be a standard element of most ionospheric models in the future. Hopefully the synthesis of the literature on photoelectrons presented in this thesis will be pedagogically useful to future students wishing to work with future ionospheric models which contain photoelectron transport routines.

Time dependent single field line ionosphere-plasmasphere models with embedded photoelectron transport routines began to appear in the mid-1980s with the development of FLIP [*Young et al.*, 1980; *Richards and Torr*, 1983; *Torr et al.*, 1990; *Richards and Torr*, 1990, 1996] and the model of *Khazanov et al.* [1984]. SUPIM [*Bailey and Balan*, 1996] then used the same two-stream photoelectron model as FLIP in a 2-D model ionosphere-plasmasphere model. Most recently, the Ionosphere-Plasmasphere-Electrodynamics (IPE) model [*Maruyama et al.*, 2011] has become the first 3-D global ionosphere-plasmasphere model to contain an embedded photoelectron transport routine. IPE is a 3-D Lagrangian generalization of the FLIP model. At each time step IPE runs the FLIP model, including its two-stream photoelectron transport routine, on every field line, then solves for the electrostatic potential with a 2-D potential solver, and finally advects each field line according to the resulting $\mathbf{E} \times \mathbf{B}$ drifts. In principle the photoelectron routine from SAMI2-PE could be inserted directly into SAMI3 to produce another global, electrodynamic model with an embedded photoelectron transport solver, but the strategies for accelerating the code discussed in Sec. 7.4 need to be explored more fully before this is practical. The photoelectron solver is SAMI2-PE is slower than

that from FLIP because it includes more physics. FLIP uses a two-stream model and uses the average energy loss approximation introduced by *Richards and Torr* [1983] for inelastic collisions, whereas SAMI2-PE uses a multi-stream model and considers 39 different types of inelastic collisions using the *Swartz* [1985] energy degradation algorithm for each type. The use of multiple streams in particular introduces a substantial computational penalty because the matrix inversion in Eq. 5.22 is $O(n_{st}^2 n_z)$, and thus an eight-stream model is 16 times slower than a two-stream model. In the topside ionosphere, however, the extra complexity of a multi-stream model is worthwhile because anisotropic pitch angle distributions will form due to transport effects and the mirror force. The FLIP two-stream model assumes the mean pitch-angle cosines change in the plasmasphere the same way the pitch-angle cosine of a single collisionless electron would in a changing magnetic field, but Fig. 6.4 illustrates that the pitch-angle distributions are more complicated than that because of transport effects.

Like SAMI2-PE, the model of *Khazanov et al.* [1994] is a multi-stream model which includes the mirror force, but unlike SAMI2-PE this model treats all collisions as continuous processes with operators of the form

$$\frac{1}{v}\frac{\delta\Phi}{\delta t} = \frac{\partial}{\partial\mathcal{E}}\left[L(\mathcal{E})\Phi\right] + D(\mathcal{E})\frac{\partial}{\partial\mu}\left[(1-\mu^2)\frac{\partial\Phi}{\partial\mu}\right]. \tag{7.1}$$

Nonetheless, *Khazanov et al.* [1994] use a different numerical treatment of the mirror force. SAMI2-PE uses a fixed pitch-angle grid at all positions where the bin centers and widths are chosen such that the integrals over the pitch-angle distributions follow Gauss-Legendre quadrature rules. This "finite ordinate approximation" is believed to be optimal for radiative transfer problems [e.g. *Chandrasekhar*, 1950; *Stamnes et al.*, 1988]. When the collision operators are approximated in the form of Eq. 7.1, however, there is no advantage to using a Gauss-point grid. *Khazanov et al.* [1994] instead construct their pitch-angle grid to eliminate numerical

diffusion. The equations are transformed from the true pitch-angle cosine, μ, to the pitch-angle cosine the photoelectrons will have when the reach the magnetic equator, i.e.

$$\mu_0(\ell, \mu) \equiv \frac{\mu}{|\mu|}\sqrt{1 - \frac{B_0}{B(\ell)}\,(1 - \mu^2)}, \tag{7.2}$$

which is an invariant quantity along the phase-space trajectory of a collisionless photoelectron. The grid in μ_0 is then constructed such that different numbers of points are used at different positions. This variable transformation completely eliminates numerical pitch-angle diffusion. The numerical methods in SAMI2-PE, however, contain some numerical pitch-angle diffusion and thus can cause particles to become anomalously trapped. At the altitudes of interest in this study (below $\sim$ 1500 km), real pitch-angle diffusion due to collisions is always present and significant, meaning some numerical diffusion is not a serious problem. Sec. 5.1.1 introduced a higher-order scheme which partially removes the numerical diffusion, but the tests in Sec. 6.3.1 demonstrate that this higher-order scheme only changes the results by $\sim$1-2% at altitudes below 1500 km. The model of *Khazanov et al.* [1994] was designed with much higher altitudes in mind where collisions are less frequent and thus numerical diffusion would be a more serious issue.

The optimal treatment of the pitch-angle grid for coupled ionosphere-plasmasphere models is probably a hybrid approach which switches between different kinds of grids in different regions. Relying on the higher-order transport scheme to extend SAMI2-PE to much higher altitudes in the plasmasphere is not an efficient option since the iteration required for the higher-order scheme slows down the computations. A Gauss-point grid is not expected to be helpful at high altitudes in the plasmasphere since the collision operator for Coulomb collisions does not contain any integrals over the pitch-angle distribution. A more practical solution is to use a Gauss-point grid up to $\sim$1000 or 1500 km, then switch to using

a grid like that of *Khazanov et al.* [1994] at higher altitudes. This hybrid grid would have all the benefits of the finite ordinate approximation at altitudes where large-angle elastic collisions with neutrals are important while simultaneously eliminating numerical pitch-angle diffusion at high altitudes in the plasmasphere where the plasma is nearly collisionless.

7.2 Lessons learned about the low-latitude thermosphere-ionosphere-plasmasphere system

The numerous simulations performed throughout this thesis give insights into the ways the thermosphere, ionosphere, and plasmasphere work together as a system. The tests performed in Ch. 3 suggested that the topside plasma temperatures would respond to changes in the neutral winds and electric fields, even though the neutral winds have no direct connection to the nearly collisionless topside plasma. Neutral winds and electric fields will rearrange the distributions of electron density in the off-equatorial F-regions, especially on the field lines connected to the equatorial arcs. The off-equatorial F-regions are in turn connected to the equatorial topside ionosphere through material diffusion, thermal diffusion, and photoelectron transport effects, all of which are impacted by changes in the electron density distributions. Although the phenomenological photoelectron transport model in the original SAMI2 is not sufficient to reproduce Jicamarca data, the tests with SAMI2-PE in Ch. 6 show that the conclusions about the effects of neutral winds and electric fields from Ch. 3 are qualitatively correct. At low-latitudes the thermosphere, ionosphere, and plasmasphere form a simple system which is diagrammed in Fig. 7.1.

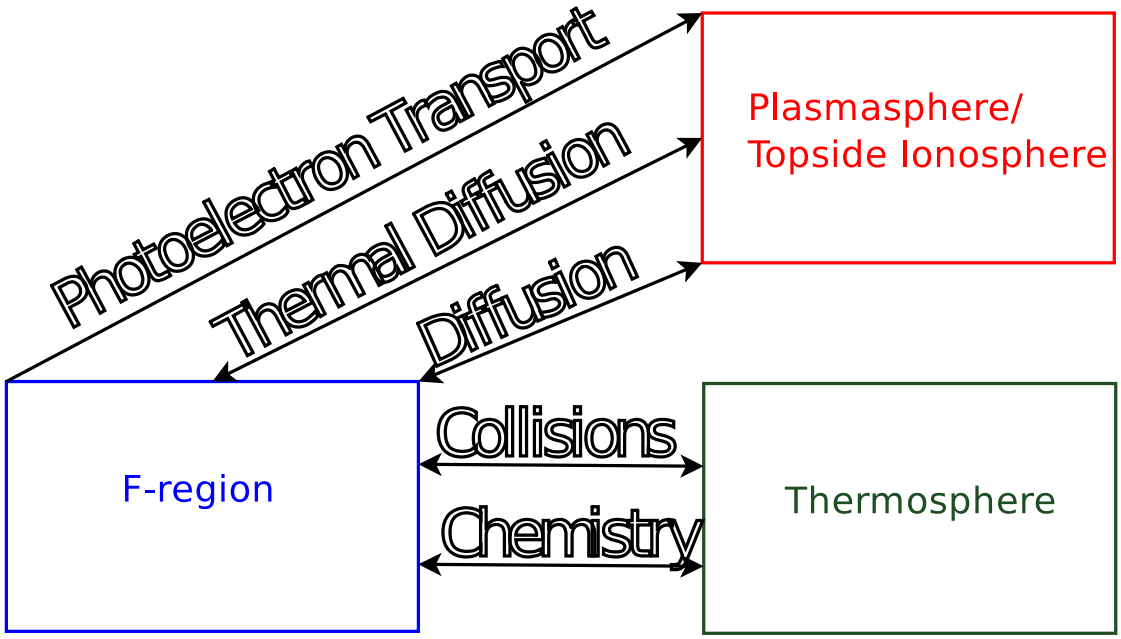

Figure 7.1: A simple diagram of the low-latitude thermosphere-ionosphere-plasmasphere system.

This simple and intuitive picture provides an easy explanation for how characteristics of the neutral thermosphere manifest themselves in the plasmasphere even though the neutral densities are negligible at plasmaspheric altitudes. For example, *Pedatella et al.* [2011] has shown that COSMIC total electron content (TEC) measurements both above and below 800 km exhibit wave 4 variations in longitude, which is a well known feature of the non-migrating tides. The system diagram in Fig. 7.1 not only provides a possible explanation for how wave 4 signatures could appear in the high altitude TEC measurements, but also suggests that similar longitudinal variations in the temperatures should also be present.

The sensitivity of Jicamarca temperature measurements to thermospheric winds suggests the tantalizing possibility of one day estimating winds by assimilating Jicamarca data into a model like SAMI2-PE. This task potentially suffers from observability problems which would need to be resolved. Obviously the entire prob-

lem is symmetric about the magnetic equator (e.g. a constant northward wind and a constant southward wind have the same effects on the equatorial plasmasphere), so either the wind directions would need to be known a priori, or off-equatorial data (e.g. from ionosondes or GPS receivers) would need to be incorporated. Furthermore, the effects of electric fields and neutral winds are impossible to differentiate when looking at the magnetic equator, thus direct measurement of electric fields would be needed. Currently the electric fields can be estimated from magnetometer data. Planned future upgrades to Jicamarca's phased array will permit electronic beam steering. A mode which alternates between perpendicular and oblique beam positions would allow for simultaneous measurements of temperatures and $\mathbf{E} \times \mathbf{B}$ drifts. Finally, uncertainties and systematic biases in the model would need to be carefully studied and characterized to do an error analysis of the derived winds.

7.3 Remaining sources of uncertainty and bias

While the agreements between SAMI2-PE and Jicamarca data are a promising improvement over the original SAMI2, a few types of discrepancies appear frequently which might indicate systematic biases remaining in SAMI2-PE. Firstly, the modeled topside temperatures are frequently higher than the measurements, indicating the fluxes in the plasmasphere are too high. One possibility is anomalous magnetic mirror trapping due to numerical pitch-angle diffusions, but the tests with and without the higher-order corrections performed in Sec. 6.3.1 suggests that this effect is relatively minor. Another possibility is an overestimation of the quasi-trapped plasmaspheric fluxes caused by an improper treatment of elastic collisions with neutrals. As explained by *Mantas et al.* [1978], elastic backscattering from the neutral thermospheres on either end of the field line can cause photoelectrons

to become quasi-trapped in the plasmasphere. The elastic cross sections used in SAMI2-PE are empirical fits to old data, and other models (e.g. GLOW) use different sets of cross sections. If the elastic cross sections are too high then too many photoelectrons will be quasi-trapped. Furthermore, SAMI2-PE only considers isotropic scattering whereas the proper phase functions for elastic collisions are somewhat peaked in the forward direction. Thus the backscattering of photoelectrons is likely being somewhat overestimated, leading to excess quasi-trapped photoelectrons in the plasmasphere.

Another problematic region for SAMI2-PE is the lower F-region ($\sim$240 km). Standard SAMI2 simulations, which use the empirical *Swartz and Nisbet* [1972] heating efficiency model at these altitudes, and SAMI2-PE simulations with the quenching of N(^{2}D) disabled appear to produce reasonable agreement with Jicamarca data. However, simulations with quenching enabled overestimate these temperatures by as much as 50%, suggesting the model is producing far too much N(^{2}D). *Aponte et al.* [1999] performed detailed studies of Jicamarca temperature measurements in the F-region and concluded that quenching of N(^{2}D) was a significant heat source in the lower F-region. However, *Aponte et al.* [1999] had no measurements of the densities of the minor ions N_2^+ and NO^+ available, both of which are crucial to determining the concentration of N(^{2}D). These ion concentrations had to be estimated from the major ion concentrations using a chemistry model. Both the chemistry models used by *Aponte et al.* [1999] and in SAMI2 will produce NO^+ through charge exchange with neutral NO, and thus are sensitive to assumed background neutral NO profile. Sec. 6.2 illustrates that the temperatures in the lower F-region produced by SAMI2-PE with quenching enabled can be changed significantly by changing the neutral NO profiles. A better model of the neutral NO density at $\sim$240 km is needed, along with a thorough reexamination

of the chemistry in SAMI2-PE at these altitudes.

7.4 Accelerating the computations

The reference simulation presented in Ch. 6 took a single processor roughly 18.5 h, whereas the original SAMI2 can run the same conditions in 28 min. The computation time is also dependent on the resolution chosen. A simulation using only 45 energy bins and 4 pitch angles can run in 4.5 h and the temperatures differ from the high resolution simulations by only 5%. Given these relatively long computation times for a 2-D model, a few other strategies for simplifying the computations should be considered before attempting to put photoelectrons into SAMI3.

Firstly, performing photoelectron heating calculations at night is a waste of time. SAMI2-PE can calculate the photoelectron spectra at night associated with the scattered radiation in the nighttime ionization model used in SAMI2, but the associated heating rates are negligible compared to the electron-neutral cooling rates. For the reference case switching off the photoelectron transport solver for all times when no point on the field line was in sunlight decreased the computation time from 18.5 h to 12.5 h.

A simple and effective way to speed up the code during the day is to not perform the photoelectron calculations at every single time step. Ionospheric models such as FLIP and TIE-GCM typically use time steps of 2-5 min. SAMI2, however, includes the nonlinear ion inertia term in the ion momentum equations and finite differences this term explicitly. Thus the Courant conditions in SAMI2 are set by the ion velocities. Typically the model uses 10 s time steps throughout most of the day, but these become as short as 1-2 s during sunrise. Figs. 7.2 and 7.3 illustrate

the effects of performing the photoelectron calculations once every n time steps for n of 10, 20, 40, and 60. A zero-order hold on the electron heating rates is used for the intermediate time steps. In each of these simulations photoelectron effects are ignored at night, so the first time step on which photoelectron calculations are performed each day is the one immediately after sunrise. The computation times for 48 hour simulations are 2 h 12 min, 1 h 38 min, 1 h 20 min, and 1 h 15 min for n of 10, 20, 40 and 60, respectively. Thus skipping every 10^{th} time step results in a factor of $\sim$6 speed up of the entire program, and there are diminishing returns for skipping more steps. When photoelectron calculations are performed for every time step they dominate the computation time, but they become a smaller fraction of the total computation time as the number of steps skipped is increased. During the middle of the day, even when skipping 60 steps, the modeled temperatures only change by 10 K or less. Significant errors appear at sunrise and sunset, however. During sunrise the electron heating rates are rising rapidly, so using a zero-order hold results in systematic underestimation of the temperatures. Similarly, during sunset the heating rates are decreasing rapidly so a zero-order hold results in systematic overestimation of the temperatures. These problems can be avoided by not skipping time steps near sunrise and sunset. The red curves in Figs. 7.2 and 7.3 come from a simulation where photoelectron calculations are ignored at night, done for every time step from sunrise to 9 LT, done for every 60^{th} time step from 9 to 17.5 LT, done for every time step from 17.5 LT to sunset. This 48 hour simulation took 7 h 31 min, most of which was spent on the sunrises on the two days.

In addition to skipping time steps, the code could be accelerated further by changing how the photoelectron calculations are performed. Currently collisions with neutrals are included at all positions, but at very high altitudes they should

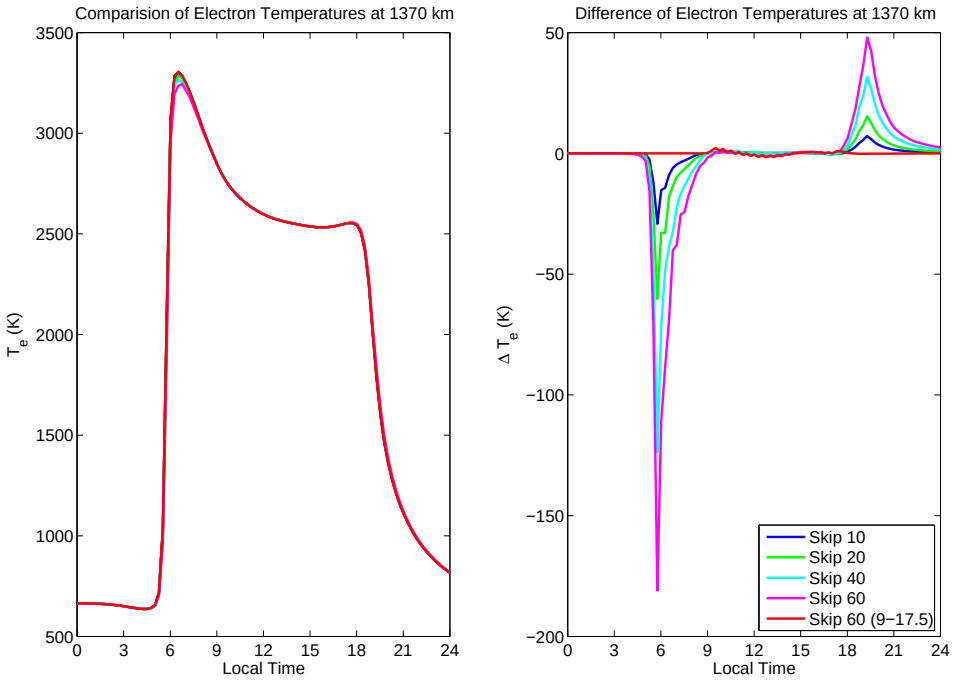

Figure 7.2: Left panel: Model electron temperatures at 1370 km as a function of local time for the second 24 hours of 48 hour simulations. Each simulation is for the reference case considered in Ch. 6, but ignores photoelectron calculations at night and skips different numbers of time steps (see text). Right panel: Differences between the modeled electron temperatures computed with and without skipping time steps.

be negligible compared to collisions with the ambient electrons. Ignoring inelastic collisions at high altitudes would allow the code to skip the energy reapportionment calculations in those cells; however, this is not expected to produce a substantial speed up because the reapportionment calculations are relatively fast and the uneven spacing of the grid points causes there to be fewer cells at high altitudes. The slowest part of the algorithm is the matrix inversion needed for the transport calculations. Ignoring elastic collisions at high altitudes would not make the matrix smaller, but it would make it sparser. The differential operator describing the pitch-angle diffusion caused by Coulomb collisions only couples adjacent

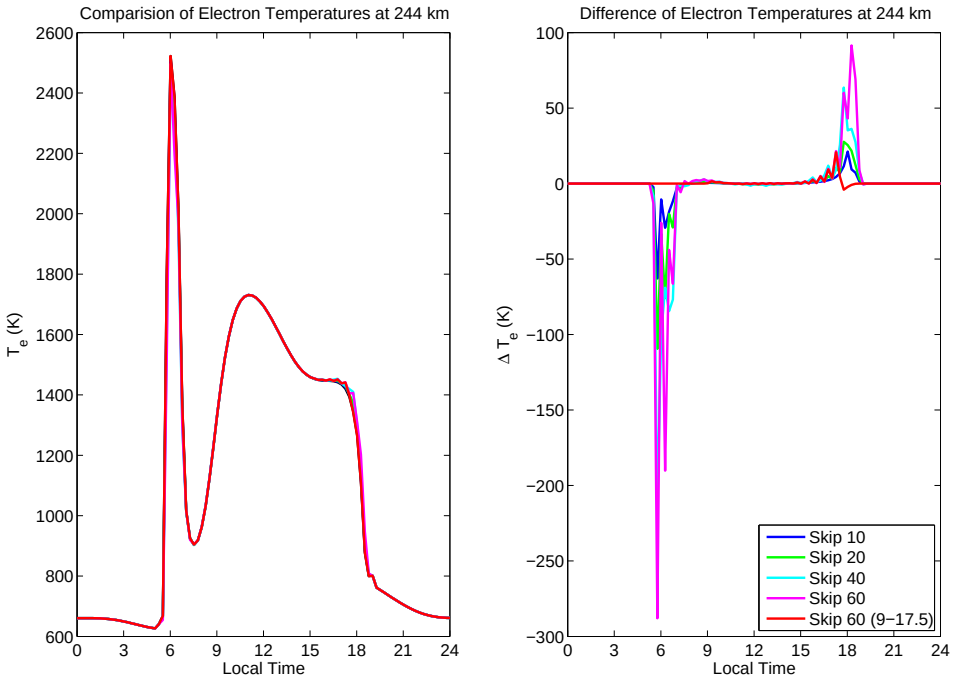

Figure 7.3: Same as Fig. 7.2 but for 244 km altitude.

pitch-angle bins, whereas the integral in the elastic collision term couples every pitch-angle bin to every other. The matrix could further be made both smaller and sparser by allowing the pitch-angle resolution to change with altitude. Fig. 6.4 suggests that the pitch-angle distributions below ∼400 km are always isotropic because of frequent elastic collisions. If the pitch-angle distributions are known to be isotropic, then multi-stream computations are a waste of time; the two-stream equations with $\langle\mu\rangle = 0.5$ are exact in the special case of isotropic distributions. Thus the portion of the grid with the highest spatial resolution could be using a lower pitch-angle resolution.

7.4.1 Empirical heating rate calculations

An alternative to accelerating the photoelectron transport model in SAMI2-PE to the point where it can be practically incorporated into 3-D models is to instead use SAMI2-PE to create better empirical models. The photoelectron population is coupled to the fluid equations governing the rest of the plasma through the secondary production and electron heating terms. Secondary production is most important at low altitudes where it is easily treated in a local empirical fashion by tabulating secondary to primary production ratios for each wavelength [e.g. *Solomon and Qian*, 2005]. Thus all that is needed is a new empirical heating rate model.

The electron heating rate in Eq. 4.85 is dominated by the final term

$$Q_{phe} = \int_{\mathcal{E}_t}^{\infty} d\mathcal{E}\, L(\mathcal{E}) \int_{-1}^{1} d\mu\, \Phi(\mathcal{E}, \mu), \tag{7.3}$$

which is a particular moment of the photoelectron distribution function. Consider the time dependent photoelectron transport equation written in the form

$$\begin{aligned} &\frac{\partial \Phi}{\partial t} + \sqrt{\frac{2\mathcal{E}}{m}} \left\{ \mu B \frac{\partial}{\partial \ell} \left(\frac{\Phi}{B} \right) - \delta B \frac{\partial}{\partial \mu} \left(\frac{1-\mu^2}{2} \Phi \right) \right\} = \\ &\sqrt{\frac{2\mathcal{E}}{m}} \left\{ q + \frac{\partial}{\partial \mathcal{E}} \left[L(\mathcal{E}) \Phi \right] + D(\mathcal{E}) \frac{\partial}{\partial \mu} \left[\left(1-\mu^2\right) \frac{\partial \Phi}{\partial \mu} \right] \right. \\ &- \sum_n (\bar{\sigma}_{an} + \bar{\sigma}_{en}) N_n \Phi(\ell, \mathcal{E}, \mu) \\ &+ \sum_n \bar{\sigma}_{en} N_n \frac{1}{2} \int_{-1}^{1} d\mu' \Phi(\ell, \mathcal{E}, \mu') \\ &\left. + \sum_{n,p} N_n \int_{\mathcal{E}}^{\infty} d\mathcal{E}' \sigma_{an}^{p}(\mathcal{E}', \mathcal{E}) \frac{1}{2} \int_{-1}^{1} d\mu' \Phi(\ell, \mathcal{E}', \mu') \right\}, \end{aligned} \tag{7.4}$$

and apply the operation $\int_{\mathcal{E}_t}^{\infty} d\mathcal{E} L(\mathcal{E}) \int_{-1}^{1} d\mu$ to the entire equation. The result is a

PDE governing the evolution of the electron heating rate of the form

$$\frac{\partial Q_{phe}}{\partial t} + B\frac{\partial}{\partial \ell}\left(\frac{FQ_{phe}}{B}\right) = P - \alpha N_e Q_{phe} - \sum_n \beta_n N_n Q_{phe} \tag{7.5}$$

where

$$F \equiv \frac{1}{Q_{phe}} \int_{\mathcal{E}_t}^{\infty} \sqrt{\frac{2\mathcal{E}}{m}} L(\mathcal{E}) \int_{-1}^{1} d\mu \, \mu \Phi, \tag{7.6}$$

$$P \equiv \int_{\mathcal{E}_t}^{\infty} d\mathcal{E} \sqrt{\frac{2\mathcal{E}}{m}} L(\mathcal{E}) \int_{-1}^{1} d\mu \, q \tag{7.7}$$

$$\alpha \equiv \frac{1}{Q_{phe}} \int_{\mathcal{E}_t}^{\infty} d\mathcal{E} \, \frac{Ł(\mathcal{E})}{N_e \sqrt{2\mathcal{E}m}} \int_{-1}^{1} d\mu \, \Phi \tag{7.8}$$

$$\beta_n \equiv \frac{1}{Q_{phe}} \int_{\mathcal{E}_t}^{\infty} d\mathcal{E} \sqrt{\frac{2\mathcal{E}}{m}} L(\mathcal{E}) \int_{-1}^{1} d\mu \, \{\bar{\sigma}_{an} \Phi - \sum_p \int_{\mathcal{E}}^{\infty} d\mathcal{E}' \sigma_{an}^p(\mathcal{E}', \mathcal{E}) \frac{1}{2} \int_{-1}^{1} d\mu' \Phi(\ell, \mathcal{E}', \mu') \Bigg\}. \tag{7.9}$$

Note that the mirror force, pitch-angle diffusion, and elastic collision terms drop out after integrating over all pitch angles and that it has been assumed that $\mathcal{E}_t$ is small. The production term P is simply a moment of the photoelectron production distribution, and thus straightforward to compute. It is proportional to the photoproduction rate. The other terms cannot be computed without knowing Φ itself. However, since Q_{phe} is a linear transformation of Φ, the terms F, α, and β_n are constants with respect to Φ (i.e. scaling Φ by a constant factor at all energies and pitch-angles would leave these numbers unchanged). If a large library of SAMI2-PE runs were generated for many different conditions empirical expressions for these "constants" could be determined. With these constants known, solving Eq. 7.5 in steady state is as easy as solving the parallel component of one of the fluid equations.

Eq. 7.5 reduces to other empirical forms in various limits. The time dependent term will probably always be negligible. At low altitudes transport effects, and

thus F, will be negligible and the equation reduces to

$$Q_{phe} = \frac{P}{\alpha N_e + \sum_n \beta_n N_n}, \tag{7.10}$$

i.e. the electron heating rate is directly proportional to the photoionization rate, just as *Swartz and Nisbet* [1972] assumed. At very high altitudes direct production, and thus P can be neglected, and the neutral densities become negligible compared to the electron densities. Eq. 7.5 then reduces to a simple transport equation of the form

$$B\frac{\partial}{\partial \ell}\left(\frac{FQ_{phe}}{B}\right) = -\alpha N_e Q_{phe}. \tag{7.11}$$

If it is furthermore assumed that B, F, and α are constants along the field line the solution to this equation is of the form

$$Q_{phe} = Q_{phe}(\ell_0) \exp\left[-C_{qe}\int_{\ell_0}^{\ell} N_e(\ell')\, d\ell'\right], \tag{7.12}$$

where $C_{qe} = \alpha/F$.

APPENDIX A

NUMERICAL METHODS FOR THE STEADY STATE TEMPERATURE MODEL

The steady state temperature model uses the same two-dimensional non-uniformly spaced grid in dipole coordinates as used by SAMI2-0.98 [*Huba et al.*, 2000a]. The steady state temperature equations, Eq. 3.40, for electrons, H^+, He^+, and O^+ are discretized around the point (i, j) as follows. The first coordinate, i, denotes the direction along $\mathbf{B}$, and the second denotes the perpendicular direction. Terms 1 and 2 only need to be evaluated at the point (i, j), but they will in general involve the temperatures of all four species at that point and they are highly nonlinear. Term 5a only depends on $T_{\alpha i}$ linearly. The divergence of $u_\parallel$ is computed from the $\mathbf{E}\times\mathbf{B}$ drift at the magnetic equator, $\mathbf{u}_\perp^{eq}$, and curvilinear factors which are specific to the dipole geometry. In terms of the spherical coordinate system centered on the eccentric dipole and the dipole coordinates,

$$\nabla\cdot\mathbf{u}_\perp = \frac{6\mathbf{u}_\perp^{eq}}{p_d R_E}\frac{\sin^2\theta_e(1+\sin^2\theta_e)}{(1+3\cos^2\theta_e)^2}. \tag{A.1}$$

Terms 3, 4b, and 5b only involve the temperatures of species α at $(i-1, j)$, (i, j), and $(i+1, j)$. Term 3 is discretized using a similar finite differencing scheme as in SAMI2.

$$\nabla_\parallel\cdot\lambda\nabla_\parallel T \approx b_s^2\left[\frac{\lambda_{i+1/2}}{\Delta s_i}\frac{T_{i+1}-T_i}{ds_i} - \frac{\lambda_{i-1/2}}{\Delta s_i}\frac{T_i - T_{i-1}}{ds_{i-1}}\right] \tag{A.2}$$

where the α subscripts and j indices have been omitted for simplicity, ds_i is change in the s coordinate between the points (i, j) and $(i-1, j)$, Δs_i is half of the change in the s coordinate between points $(i+1, j)$ and $(i-1, j)$, and

$$\lambda_{i+1/2} = \frac{1}{2}(\lambda_{i+1}+\lambda_i) \tag{A.3}$$

$$\lambda_{i-1/2} = \frac{1}{2}(\lambda_i+\lambda_{i-1}). \tag{A.4}$$

The dependence on λ_{i-1}, λ_i, and λ_{i+1} means that term 3 depends nonlinearly on $T_{\alpha i-1}$, $T_{\alpha i}$, and $T_{\alpha i+1}$.

Terms 4b and 5b can be combined and rewritten as two different terms.

$$\begin{aligned} &\mathbf{u}_{\alpha\|}\nabla_\| T_\alpha + \frac{2}{3}T_\alpha \nabla_\| \cdot \mathbf{u}_{\alpha\|} \\ &= \nabla_\| \cdot (\mathbf{u}_{\alpha\|} T_\alpha) - \frac{1}{3}T_\alpha \nabla_\| \cdot \mathbf{u}_{\alpha\|} \end{aligned} \tag{A.5}$$

The second of these terms is finite differenced as

$$\begin{aligned} -\frac{1}{3}\frac{1}{\Delta s_i}\Bigg[&\frac{1}{2}b_{si}(u_{i+1} - u_{i-1}) \\ &+\frac{1}{4}u_i(b_{si+1} - b_{si-1})\Bigg]. \end{aligned} \tag{A.6}$$

The first of these terms is approximated using an upwind scheme.

$$\nabla_\| \cdot (\mathbf{u}_{\alpha\|} T_\alpha) \approx \frac{A}{\Delta s_i}T_{i-1} + \frac{B}{\Delta s_i}T_i + \frac{C}{\Delta s_i}T_{i+1}, \tag{A.7}$$

where the coefficients A, B, and C depend on the signs of the parallel velocities. First the effective velocities at the left and right sides of the cell are defined.

$$u_r = \frac{1}{2}\left(b_{si}u_{\|i} + b_{si+1}u_{\|i+1}\right) \tag{A.8}$$

$$u_\ell = \frac{1}{2}\left(b_{si-1}u_{\|i-1} + b_{si}u_{\|i}\right) \tag{A.9}$$

If $u_r \geq 0$ and $u_\ell \geq 0$

$$A = -u_\ell \tag{A.10}$$

$$B = u_r \tag{A.11}$$

$$C = 0, \tag{A.12}$$

if $u_r \leq 0$ and $u_\ell \geq 0$

$$A = 0 \tag{A.13}$$

$$B = -u_\ell \tag{A.14}$$

$$C = u_r, \tag{A.15}$$

if $u_r \geq 0$ and $u_\ell \leq 0$

$$A = 0 \tag{A.16}$$

$$B = u_r - u_\ell \tag{A.17}$$

$$C = 0, \tag{A.18}$$

and finally if $u_r \leq 0$ and $u_\ell \geq 0$

$$A = -u_\ell \tag{A.19}$$

$$B = 0 \tag{A.20}$$

$$C = u_r. \tag{A.21}$$

Both of these terms are linear in $T_{\alpha i-1}$, $T_{\alpha i}$ and $T_{\alpha i+1}$.

Only term 4a couples adjacent field lines, but it is completely linear. It is discretized as

$$aT_{\alpha i,j-1} + bT_{\alpha i,j} + cT_{\alpha i,j+1}, \tag{A.22}$$

where the coefficients a, b, and c are also computed using an upwind scheme, and thus depend on the signs of $\mathbf{u}_\perp$. These coefficients are identical for all four species since the $\mathbf{E} \times \mathbf{B}$ drift is the same for all species. If $\mathbf{u}_{\perp i,j} \geq 0$ and $\mathbf{u}_{\perp i,j+1} \geq 0$

$$a = -\frac{A_{i,j}}{V_{i,j}}\mathbf{u}_{\perp i,j} \tag{A.23}$$

$$b = \frac{A_{i,j+1}}{V_{i,j}}\mathbf{u}_{\perp i,j+1} \tag{A.24}$$

$$c = 0, \tag{A.25}$$

if $\mathbf{u}_{\perp i,j} \leq 0$ and $\mathbf{u}_{\perp i,j+1} \geq 0$

$$a = 0 \tag{A.26}$$

$$b = \frac{A_{i,j+1}}{V_{i,j}}\mathbf{u}_{\perp i,j+1} - \frac{A_{i,j}}{V_{i,j}}\mathbf{u}_{\perp i,j} \tag{A.27}$$

$$c = 0, \tag{A.28}$$

if $\mathbf{u}_{\perp i,j} \geq 0$ and $\mathbf{u}_{\perp i,j+1} \leq 0$

$$a = -\frac{A_{i,j}}{V_{i,j}}\mathbf{u}_{\perp i,j} \tag{A.29}$$

$$b = 0 \tag{A.30}$$

$$c = \frac{A_{i,j+1}}{V_{i,j}}\mathbf{u}_{\perp i,j+1}, \tag{A.31}$$

and finally if $\mathbf{u}_{\perp i,j} \leq 0$ and $\mathbf{u}_{\perp i,j+1} \leq 0$

$$a = 0 \tag{A.32}$$

$$b = -\frac{A_{i,j}}{V_{i,j}}\mathbf{u}_{\perp i,j} \tag{A.33}$$

$$c = \frac{A_{i,j+1}}{V_{i,j}}\mathbf{u}_{\perp i,j+1}. \tag{A.34}$$

In each case $V_{i,j}$ is the volume of the cell at (i, j) and $A_{i,j}$ is the area of the face of the cell at (i, j) whose normal is perpendicular to $\mathbf{B}$.

The discretized temperature equations are nonlinear, and thus must be solved iteratively. Let $E_{\alpha,i,j}$ be the the evaluation of the discretized temperature equation for species α around the point (i, j) for the current guess of the temperature profiles. Clearly the problem is solved when $E_{\alpha,i,j} = 0$ for all i, j, and α. This problem can be solved with Newton's method by iteratively solving

$$\sum_{\beta,k,\ell} \frac{\partial E_{\alpha,i,j}}{\partial T_{\beta,k,\ell}} \delta T_{\beta,k,\ell} = -E_{\alpha,i,j} \tag{A.35}$$

for the changes to the guess of the temperatures, δT, subject to the boundary conditions. Contributions to the partial derivatives of E which come from the linear terms are trivial to compute, and contributions from the nonlinear terms are approximated using forward differences. Clearly this problem can be cast as a matrix equation of the form $\mathbf{Ax} = \mathbf{b}$ where the $\mathbf{A}$ matrix is very sparse.

Initially all of the temperatures are set equal to the neutral temperatures. Then Eq. A.35 is solved with the perpendicular advection terms (term 4a), and

the condition that the derivative at the top be 0 omitted. This corresponds to solving a one-dimensional problem along each field line. In this case the matrix is band diagonal with no non-zero entries more than 4 elements away from the main diagonal. Such systems are simple to solve by Gaussian elimination followed by backsubstitution [e.g. *Press et al.*, 2007]. The iteration continues until the rms change in the temperatures from the latest step is less than 1 K. The solution to this one-dimensional problem is then used as the initial guess for a more complicated two-dimensional solver.

Directly inverting the matrix with the perpendicular advection terms included is numerically unstable due to rounding errors. This difficulty is overcome using Tikhonov regularization. Instead of solving $\mathbf{Ax} = \mathbf{b}$ we attempt to minimize $||\mathbf{Ax} - \mathbf{b}||_2^2 + ||\mathbf{\Gamma x}||_2^2$, where the matrix $\mathbf{\Gamma} = \alpha\mathbf{I}$ is an extra condition which encourages the solution vector to be small. The $\mathbf{x}$ which minimizes this quantity is the solution to

$$\left(\mathbf{A}^T\mathbf{A} + \alpha^2\mathbf{I}\right)\mathbf{x} = \mathbf{A}^T\mathbf{b}. \tag{A.36}$$

This is again a band diagonal system which can be solved using the same technique as before. After some trial and error, a regularization parameter of $\alpha = 10^{-6}$ was chosen. Again the problem is iterated until the rms change in the temperatures is less than 1 K.

APPENDIX B

PHOTOABSORPTION AND PHOTOIONIZATION CROSS SECTIONS

The figures below show the various photoabsorption and photoionization cross sections used in SAMI2-PE. The data sources for the various cross sections are indicated in the caption. The methods used to integrate these cross sections onto the wavelength grid used in SAMI2-PE and to combine partial and total cross sections from multiple sources self consistently are described in secs. 4.2.2 and 4.2.3.

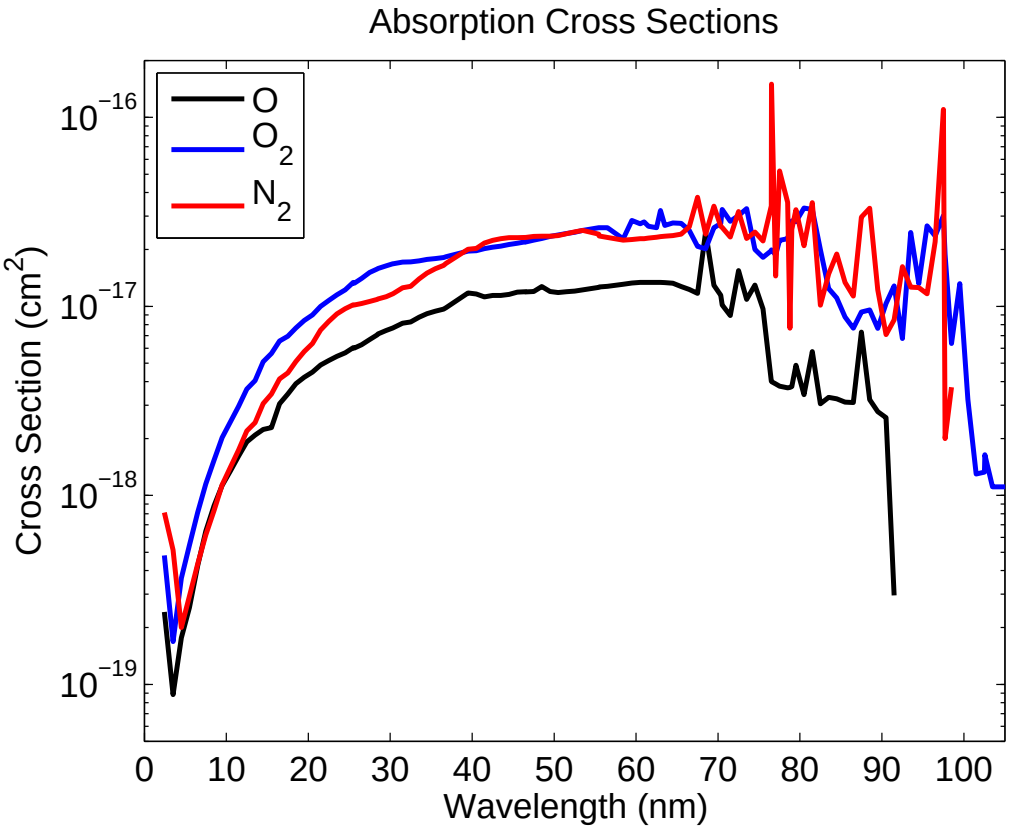

Figure B.1: Photoabsorption cross sections [*Fennelly and Torr*, 1992].

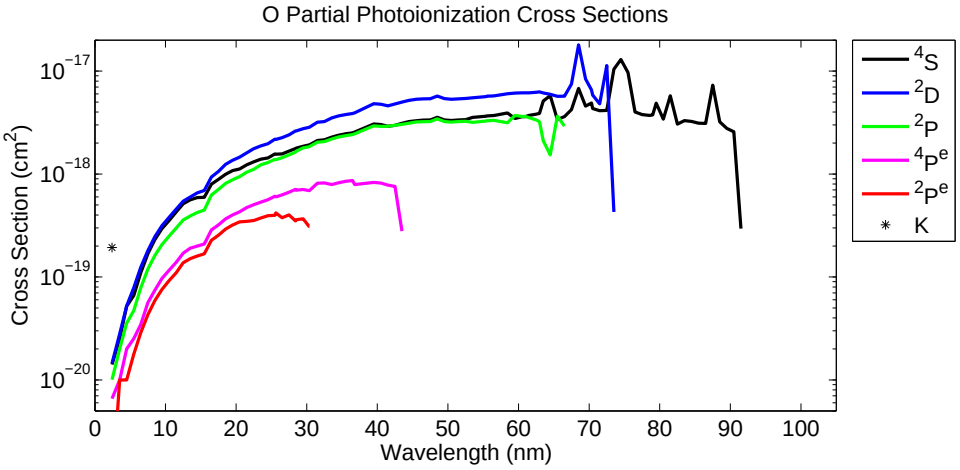

Figure B.2: Partial photoionization cross sections for atomic oxygen. The legend refers to the state of the resultant O^+ ion (see *Conway* [1988]).

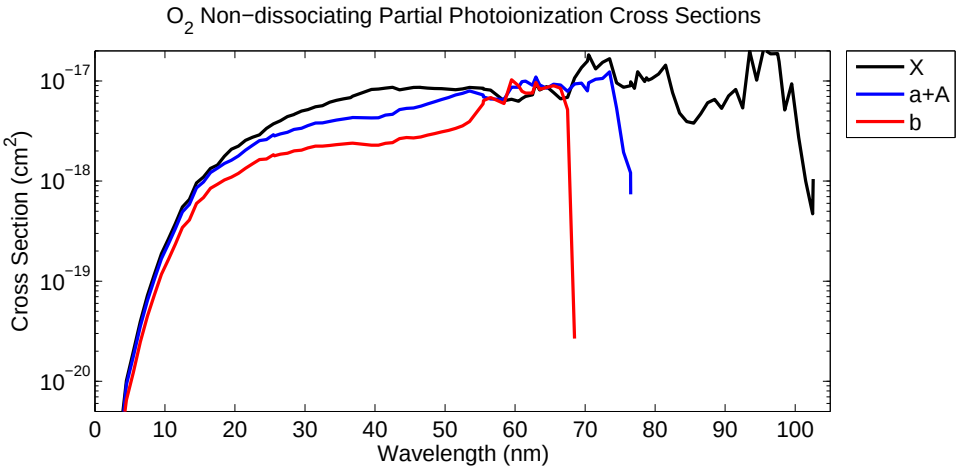

Figure B.3: Partial photoionization cross sections for non-dissociating reactions with molecular oxygen. The legend refers to the state of the resultant O_2^+ ion (see *Conway* [1988]).

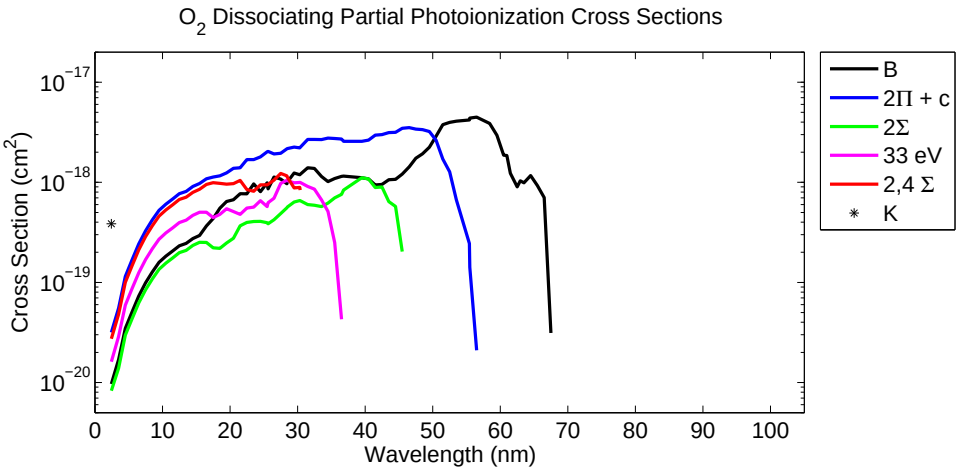

Figure B.4: Partial photoionization cross sections for dissociating reactions with molecular oxygen. The legend refers to the state of the resultant O^+ ion (see *Conway* [1988]).

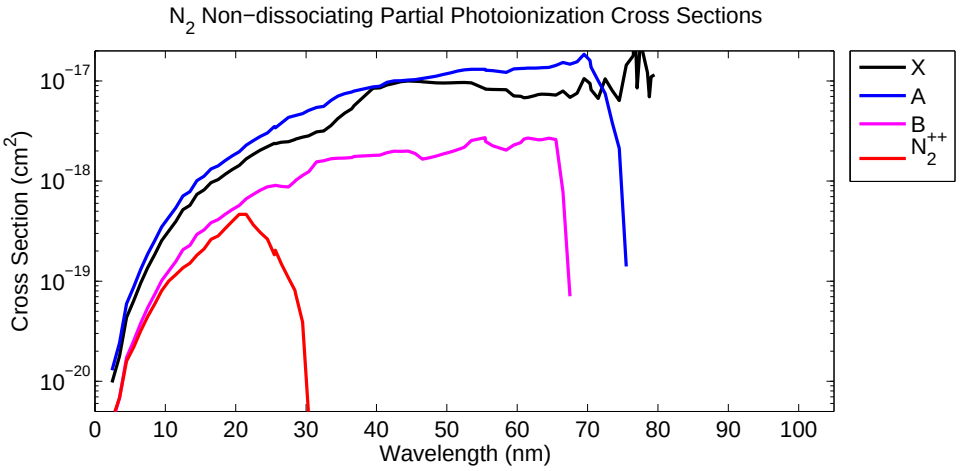

Figure B.5: Partial photoionization cross sections for non-dissociating reactions with molecular nitrogen. The legend refers to the state of the resultant N_2^+ ion (see *Conway* [1988]).

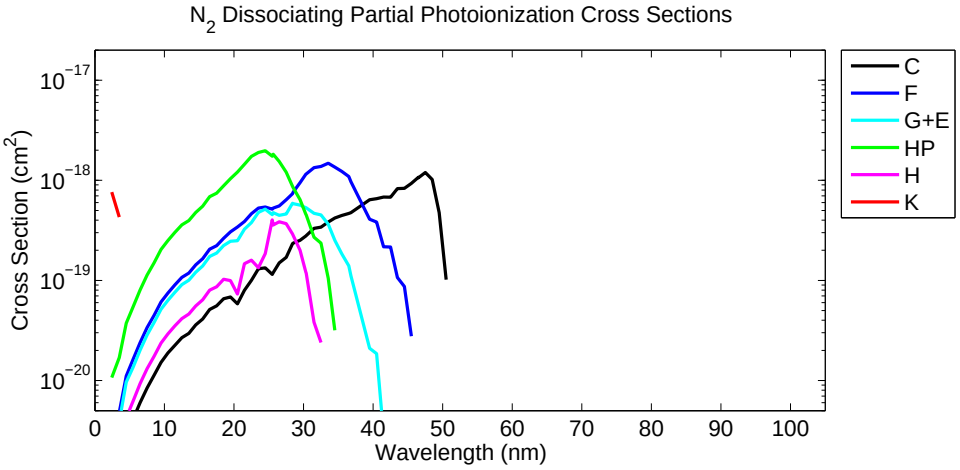

Figure B.6: Partial photoionization cross sections for dissociating reactions with molecular nitrogen. The legend refers to the state of the resultant N^+ ion (see *Conway* [1988]).

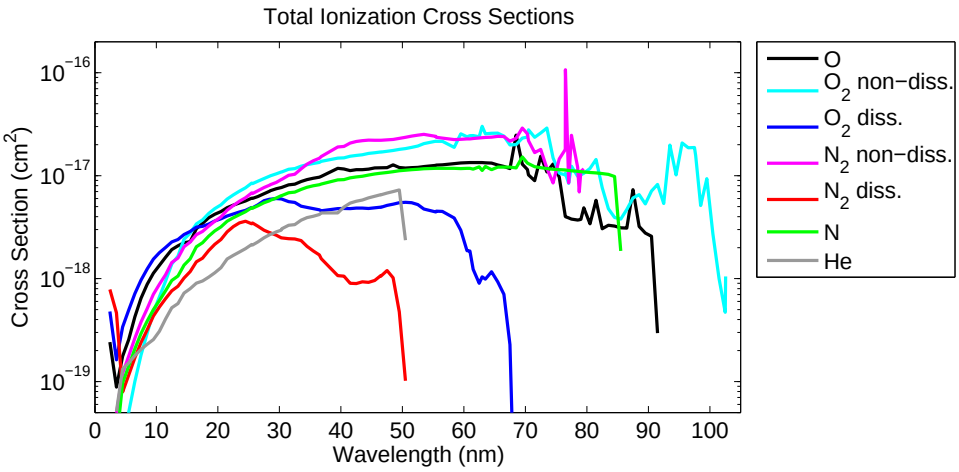

Figure B.7: Total photoionization cross sections. Helium cross sections come from *Kirby et al.* [1979]; all others come from *Fennelly and Torr* [1992].

APPENDIX C

PHOTOELECTRON-NEUTRAL COLLISION CROSS SECTIONS

The elastic cross sections used are the same as those in the FLIP [*Richards and Torr*, 1996] source code. In cm^2 they are.

$$\bar{\sigma}_{e,\mathrm{O}} = \begin{cases} 5.3 \times 10^{-16} \mathcal{E}^{0.146} \\ 5.3 \times 10^{-15} \left[1 - \frac{0.1}{\mathcal{E}}\right]^{55} \mathcal{E}^{-0.65} \end{cases} \tag{C.1}$$

$$\bar{\sigma}_{e,\mathrm{O_2}} = \begin{cases} 5.0 \times 10^{-16} \mathcal{E}^{0.301} \\ 8.53 \times 10^{-15} \left[1 - \frac{0.1}{\mathcal{E}}\right]^{64.3} \mathcal{E}^{-0.65} \end{cases} \tag{C.2}$$

$$\bar{\sigma}_{e,\mathrm{N_2}} = \begin{cases} 1 \times 10^{-15} + 1.5 \times 10^{-15} \exp\left[-\left(\frac{\mathcal{E}-2.2}{0.8}\right)^2\right] \\ 8.53 \times 10^{-15} \left[1 - \frac{0.1}{\mathcal{E}}\right]^{64.3} \mathcal{E}^{-0.65}, \end{cases} \tag{C.3}$$

where the top expression of each pair is for $\mathcal{E} < 10$ eV and the bottom expression is for $\mathcal{E} > 10$ eV. These cross sections are plotted in Fig. C.1.

The partial cross sections for inelastic collisions which excite but do not ionize the neutral are all modeled with analytic expressions of the form

$$\sigma^p_{xn}(\mathcal{E}', \mathcal{E}) = \frac{q_0 A}{T^2} \left[1 - \left(\frac{T}{\mathcal{E}'}\right)^{\gamma}\right]^{\nu} \left(\frac{T}{\mathcal{E}'}\right)^{\Omega} \delta(\mathcal{E}' - T - \mathcal{E}) \ \mathrm{cm}^2\mathrm{eV}^{-1}, \tag{C.4}$$

where $q_0 = 6.51 \times 10^{-14}$ $\mathrm{eV}^2\mathrm{cm}^2$, T is the threshold energy for the excitation in eV, and A, Ω, γ, and ν are dimensionless constants which are chosen such that the analytic expression matches experimental data while still transitioning smoothly from the cutoff at threshold to the appropriate high energy limit given by the Born-Bethe approximation [*Green and Stolarski*, 1972]. All of the excitations considered and the parameters used are summarized in Table C.1. The corresponding total cross sections are simply given by the term in front of the δ-function in Eq. C.4, and are plotted in Figs. C.2, C.3, and C.4.

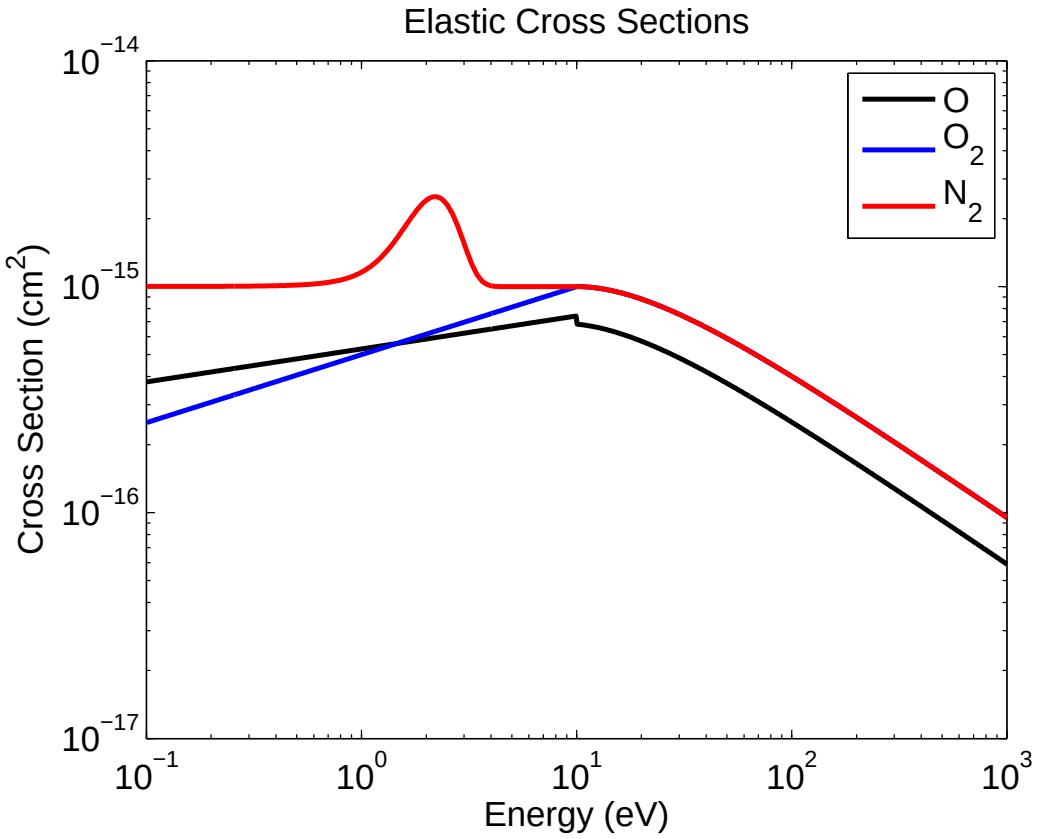

Figure C.1: Empirical elastic cross sections used.

The partial cross sections for ionizing collisions are modeled with a similar analytic form;

$$\sigma_{in}^{p}(\mathcal{E}',\mathcal{E}) = \begin{cases} \frac{q_0 A}{W^2}\left(\frac{T}{W}\right)^P \left[1-\left(\frac{W}{\mathcal{E}'}\right)^\gamma\right]^\nu \left(\frac{W}{\mathcal{E}'}\right)^\Omega \text{ cm}^2\text{eV}^{-1} & T \le W < \frac{\mathcal{E}'+T}{2} \\ 0 \text{ cm}^2\text{eV}^{-1} & \text{otherwise} \end{cases} \tag{C.5}$$

where q_0 is the same constant as before, T is the ionization threshold in eV, $W = \mathcal{E}' - \mathcal{E}$ is the total amount of energy lost by the primary electron in eV, and A, P, Ω, ν, and γ are dimensionless constants [*Banks and Kockarts*, 1973]. To conserve energy $W = \mathcal{E}' - \mathcal{E} = T + \mathcal{E}_s$ where $\mathcal{E}_s$ is the energy of the secondary. An ionizing collision begins with one free electron and ends with two. By convention the more energetic of these two electrons is labeled as the degraded primary and the less energetic is labeled as the secondary. Thus $\mathcal{E}_s$ must lie between 0 and

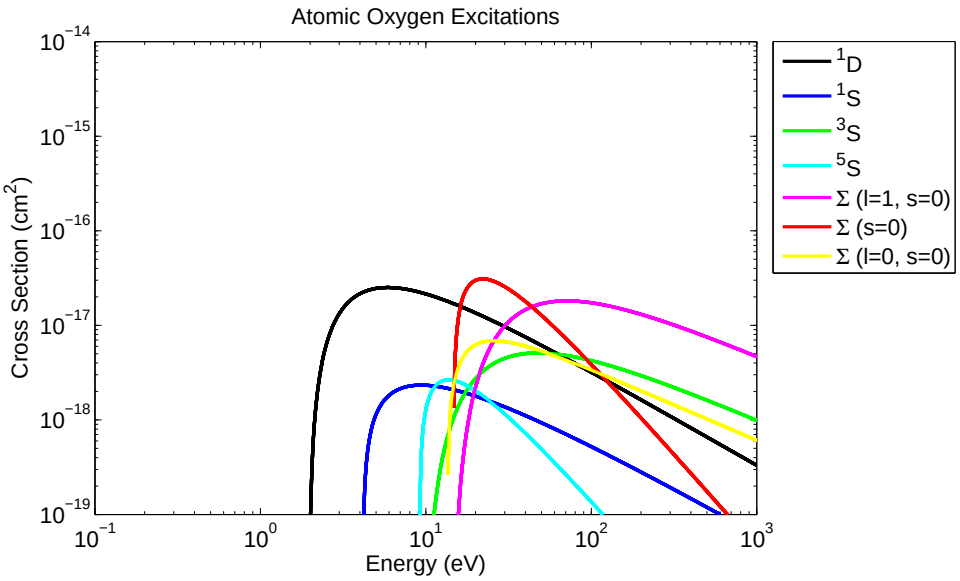

Figure C.2: Total inelastic cross sections for collisions involving excitations of atomic oxygen. These curves are computed using Eq. C.4 and parameters from Table C.1.

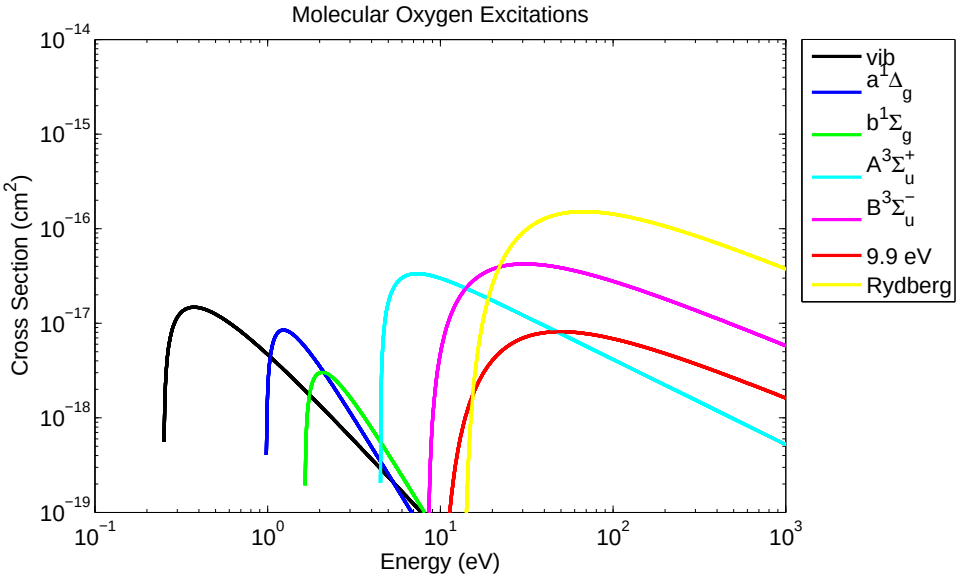

Figure C.3: Total inelastic cross sections for collisions involving excitations of molecular oxygen. These curves are computed using Eq. C.4 and parameters from Table C.1.

Electron Impact Excitation Collision Parameters						
Gas	State	T(eV)	A	Ω	ν	γ
O	^{1}D	1.96	0.01	1.0	2.0	1.0
	^{1}S	4.17	0.0042	1.0	1.0	0.5
	^{3}S	9.53	0.0465	0.75	3.0	1.0
	^{5}S	9.15	0.023	2.0	1.0	1.0
	$\Sigma(\Delta l = 1, \Delta s = 0)$	14.2	0.367	0.75	3.0	1.0
	$\Sigma(\Delta s = 1)$	14.7	0.694	2.0	1.0	1.0
	$\Sigma(\Delta l = 0, \Delta s = 0)$	13.5	0.043	0.75	1.0	2.0
O_2	$\sum$ vib.	0.25	9.57×10^{-5}	2.0	1.0	1.0
	$a^1\Delta_g$	0.98	0.0005	3.0	1.0	3.0
	$b^1\Sigma_g^+$	1.64	0.0005	3.0	1.0	3.0
	$A^3\Sigma_u+$	4.5	0.021	0.9	1.0	3.0
	$B^3\Sigma_u-$	8.4	0.23	0.75	2.0	1.0
	9.9 eV allowed	9.9	0.08	0.75	3.0	1.0
	$\sum$ Rydberg	13.5	2.77	0.75	3.0	1.0
N_2	$\sum$ vib.	1.4	1.5×10^5	16.0	9.0	1.0
	$A^3\Sigma_u+$	6.14	0.226	3.0	1.0	1.0
	$B^3\Pi_g$	7.30	0.178	3.0	1.0	3.0
	$C^3\Pi_u$	11.03	0.28	3.0	1.0	3.0
	$a^1\Pi_g$	9.10	0.136	1.0	1.0	1.0
	$b^1\Pi_u$	12.85	0.67	0.75	3.0	1.0
	$b'1\Sigma_u+$	14.0	0.33	0.75	3.0	1.0
	$\sum$ Rydberg	13.75	2.66	0.75	3.0	1.0

Table C.1: Parameters used with Eq. C.4 to compute cross sections for excitation collisions. The O_2 vibrational and N_2 vibrational terms are taken from *Swartz* [1972]. The rest of these parameters appear in *Banks and Kockarts* [1973].

$(\mathcal{E}'-T)/2$. All of the types of ionizing collisions considered and the parameters used are summarized in Table C.2. The corresponding total cross sections are obtained by integrating the partial cross sections over all possible secondary energies:

$$\begin{aligned}\sigma_{in}(\mathcal{E}) &= \int_{(\mathcal{E}-T)/2}^{\mathcal{E}-T} \sigma_{in}^p(\mathcal{E}, \mathcal{E}'')\, d\mathcal{E}'' \\ &= \int_T^{(\mathcal{E}+T)/2} \sigma_{in}^p(\mathcal{E}, \mathcal{E}'')\, dW'' \\ &= q_0 A T^P \mathcal{E}^{-\Omega} \sum_{k=0}^{\nu} (-1)^k \binom{\nu}{k} \mathcal{E}^{-k\gamma} \frac{\left(\frac{\mathcal{E}+T}{2}\right)^{k\gamma+\Omega-P-1} - T^{k\gamma+\Omega-P-1}}{k\gamma+\Omega-P-1},\end{aligned} \tag{C.6}$$

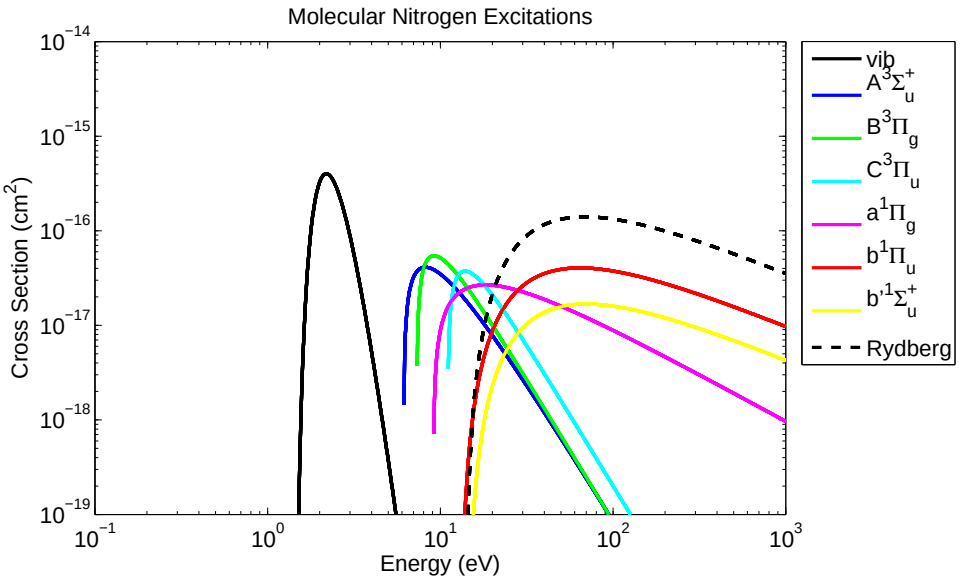

Figure C.4: Total inelastic cross sections for collisions involving excitations of molecular nitrogen. These curves are computed using Eq. C.4 and parameters from Table C.1.

where $W'' = \mathcal{E} - \mathcal{E}''$, and the final equation applies only for integer ν. These total cross sections are plotted in Figs. C.5, C.6, and C.7.

Electron Impact Ionization Parameters								
Gas	Final Ion	State	T(eV)	A	Ω	ν	γ	P
O	O^+	^4S	13.6	0.290	0.85	1.0	0.3	1.2
		^2D	16.9	0.360	0.85	1.0	0.3	1.2
		^2P	18.5	0.190	0.85	1.0	0.3	1.2
O_2	O_2^+	$X^2\Pi_g$	12.1	0.058	0.80	2.0	1.0	1.1
		$a^4\Pi_u$	16.1	0.150	0.80	2.0	1.0	1.1
		$A^2\Pi_u$	16.9	0.150	0.80	2.0	1.0	1.1
		$b^4\Sigma_g-$	18.2	0.130	0.80	2.0	1.0	1.1
		B	23.0	0.064	0.80	2.0	1.0	1.1
	O^+	^4S	18.0	0.400	0.93	3.0	1.0	1.1
	O^+	^2D	22.0	0.250	0.93	3.0	1.0	1.1
N_2	N_2^+	$X^2\Sigma_g+$	15.58	0.370	0.80	3.0	1.0	1.2
		$A^2\Pi_u$	16.73	0.160	0.83	1.0	1.0	1.2
		$B^2\Sigma_u+$	18.75	0.073	0.83	2.0	1.0	1.2
		$C^2\Pi_g$	22.0	0.056	0.83	2.0	1.0	1.2
		$D^2\Sigma_u+$	23.6	0.060	0.83	2.0	1.0	1.2
	N^+		25.0	0.380	0.96	2.0	1.0	1.2

Table C.2: Parameters used with Eq. C.5 to compute ionization cross sections. All of these parameters are taken from *Banks and Kockarts* [1973].

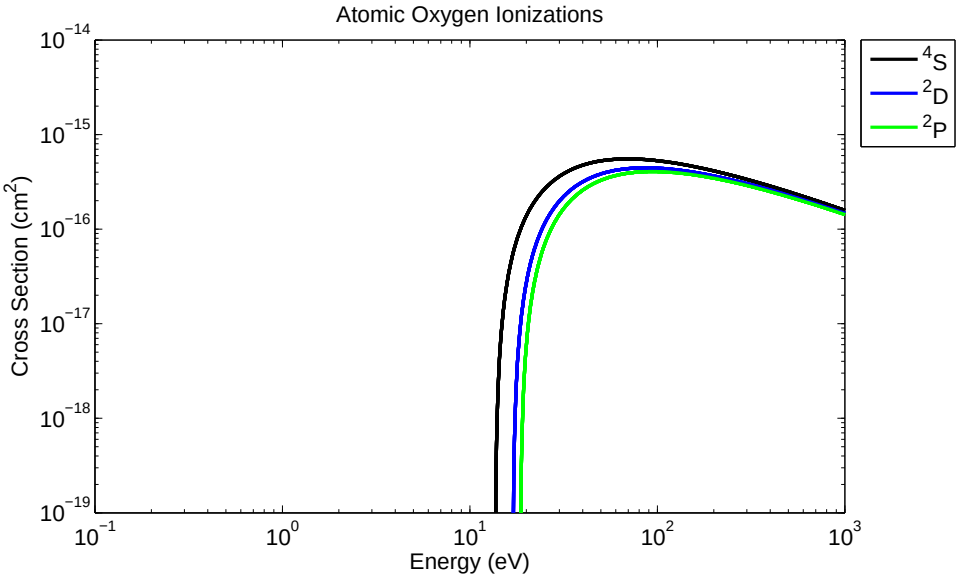

Figure C.5: Total inelastic cross sections for collisions involving impact ionization of atomic oxygen. These curves are computed using Eq. C.6 and parameters from Table C.2.

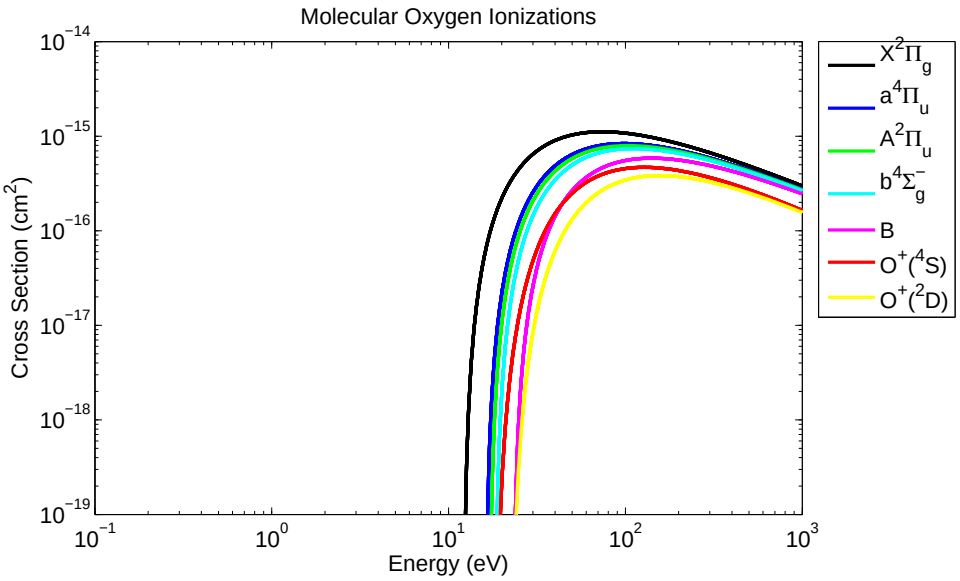

Figure C.6: Total inelastic cross sections for collisions involving impact ionization of molecular oxygen. These curves are computed using Eq. C.6 and parameters from Table C.2.

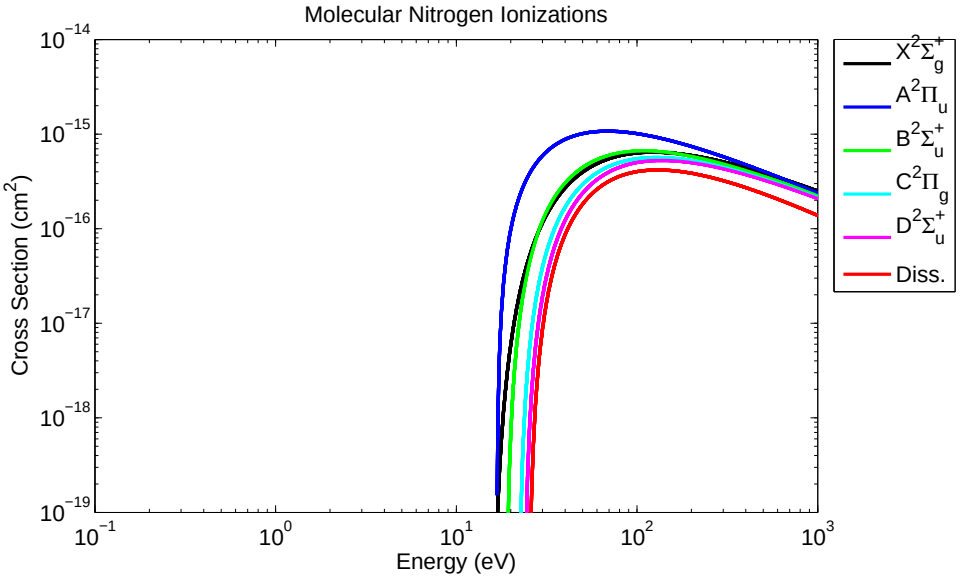

Figure C.7: Total inelastic cross sections for collisions involving impact ionization of molecular nitrogen. These curves are computed using Eq. C.6 and parameters from Table C.2.

BIBLIOGRAPHY

Anderson, D., A. Anghel, J. Chau, and O. Veliz, Daytime vertical $E \times B$ drift velocities inferred from ground-based magnetometer observations at low latitudes, *Space Weather*, *2*, S11,001, 2004.

Anderson, E., et al., *LAPACK's user's guide*, Society for Industrial and Applied Mathematics, Philadelphia, PA, USA, 1992.

Aponte, N., W. E. Swartz, and D. T. Farley, Electron energy balance in the F region above Jicamarca, *J. Geophys. Res.*, *104*, 10,041, 1999.

Aponte, N., M. P. Sulzer, and S. A. Gonzales, Correction of the Jicamarca electron-ion temperature ratio problem: verifying the effect of electron Coulomb collisions on the incoherent scatter spectrum, *J. Geophys. Res.*, *106*, 24,785, 2001.

Appleton, E. V., Regularities and irregularities in the ionosphere, I, *Proc. Roy. Soc. Ser. A*, *162*, 451, 1937.

Ashihara, O., and K. Takayanagi, Velocity distribution of ionospheric low-energy electrons, *Planet. Space Sci.*, *22*, 1201, 1974.

Bailey, G. J., and N. Balan, A low-latitude ionosphere-plasmasphere model, in *STEP: Handbook of Ionospheric Models*, edited by R. W. Schunk, pp. 173–206, Cent. for Atmos. and Space Sci., Logan, Utah, 1996.

Bailey, G. J., and R. A. Heelis, Ion temperature troughs induced by a meridional neutral air wind in the night-time equatorial topside ionosphere, *Planet. Space Sci.*, *28*, 895–906, 1980.

Bailey, G. J., R. J. Moffett, and W. E. Swartz, Effects of photoelectron heating and interhemisphere transport on day-time plasma temperatures at low latitudes, *Planet. Space Sci.*, *23*, 599, 1975.

Bailey, S. M., C. A. Barth, and S. C. Solomon, A model of nitric oxide in the lower thermosphere, *J. Geophys. Res.*, *107*, 1205, 2002.

Balan, N., K.-I. Oyama, G. J. Bailey, and T. Abe, Plasmasphere electron temperatures studies using satellite observations and a theoretical model, *J. Geophys. Res.*, *101*, 15,323, 1996a.

Balan, N., K.-I. Oyama, G. J. Bailey, and T. Abe, Plasmasphere electron temperature profiles and the effects of photoelectron trapping and an equatorial high-altitude heat source, *J. Geophys. Res.*, *101*, 21,689, 1996b.

Balan, N., K.-I. Oyama, G. J. Bailey, S. Fukao, S. Watanabe, and M. A. Abdu, A plasma temperature anomaly in the equatorial topside ionosphere, *J. Geophys. Res.*, *102*, 7485, 1997.

Banks, P. M., Charged particle temperatures and electron thermal conductivity in the upper atmosphere, *Annls. Geophys.*, *22*, 577, 1966.

Banks, P. M., and G. Kockarts, *Aeronomy*, Academic Press, New York, NY, USA, 1973.

Banks, P. M., and A. F. Nagy, Concerning the influence of eleastic scattering upon photoelectron transport and escape, *J. Geophys. Res.*, *75*, 1902, 1970.

Banks, P. M., C. R. Chappell, and A. F. Nagy, A new model for the interaction of auroral electrons with the atmosphere: Spectral degradation, backscatter, optical emission, and ionization, *J. Geophys. Res.*, *79*, 1459, 1974.

Barrett, J. L., and P. B. Hays, Spatial distribution of energy deposited in nitrogen by electrons, *J. Chem. Phys.*, *64*, 743, 1976.

Barth, C. A., K. D. Mankoff, S. M. Bailey, and S. C. Solomon, Global observations of nitric oxide in the thermosphere, *J. Geophys. Res.*, *108*, 1027, 2003.

Bellan, P. M., *Fundamentals of Plasma Physics*, Cambridge University Press, New York, NY, USA, 2006.

Berger, M. J., S. M. Seltzer, and K. Maeda, Energy deposition by auroral electrons in the atmosphere, *J. Atmos. Terr. Phys.*, *32*, 1015, 1970.

Berger, M. J., S. M. Seltzer, and K. Maeda, Some new results on electron transport in the atmosphere, *J. Atmos. Terr. Phys.*, *36*, 591, 1974.

Boggess, R. L., L. H. Brace, and N. W. Spencer, Langmuir probe measurements in the ionosphere, *J. Geophys. Res.*, *65*, 1627, 1959.

Booker, H. G., A theory of scattering by non-isotropic irregularities with application to radar reflections from the aurora, *J. Atmos. Terr. Phys.*, *8*, 204, 1956.

Bowles, K. L., Observations of vertical incidence scatter from the ionosphere at 41 Mc/s, *Phys. Rev. Lett.*, *1*, 454, 1958.

Brace, L. H., and R. F. Theis, Global empirical models of ionospheric electron temperatures in the upper F-region and plasmasphere based on in situ measurements from the Atomosphere Explorer-C, ISIS 1, and ISIS 2 satellites, *J. Atmos. Terr. Phys.*, *43*, 1317, 1981.

Buonsanto, M. J., M. Codrescu, B. A. Emery, C. G. Fesen, T. J. Fuller-Rowell, D. J. Melendez-Alvira, and D. P. Sipler, Comparisons of models and measurements at Millstone Hill during the January 24-26, 1993, minor storm interval, *J. Geophys. Res.*, *102*, 7267, 1997.

Callen, H. B., and T. A. Welton, Irreversibility and generalized noise, *Phys. Rev.*, *83*, 34, 1951.

Carlson, H. C., Ionospheric heating by magnetic conjugate-point photoelectrons, *J. Geophys. Res.*, *71*, 195, 1966.

Carru, H., M. Petit, and P. Waldteufel, Mesures de températures électroniques et ioniques par diffusion incohérente, *J. Atmos. Terr. Phys.*, *29*, 351, 1967.

Chandrasekhar, S., *Radiative Transfer*, Clarendon Press, 1950.

Chapman, S., The absorption and dissociative or ionizing effects of monochromatic radiation in an atmosphere on a rotating Earth, 2, Grazing incidence, *Proc. Phys. Soc. London*, *43*, 483, 1931.

Chapman, S., and T. G. Cowling, *The Mathematical Theory of Nonuniform Gases*, Cambridge University Press, New York, 1970.

Chau, J. L., and E. Kudeki, First *E*- and *D*- region incoherent scatter spectra observed over Jicamarca, *Ann. Geophys.*, *24*, 1305–1310, 2006a.

Chau, J. L., and E. Kudeki, Statistics of 150-km echoes over Jicamarca based on low-power VHF observations, *Ann. Geophys.*, *24*, 1305–1310, 2006b.

Cicerone, R. J., and S. Bowhill, Photoelectron escape fluxes obtained by a Monte Carlo technique, *Radio Sci.*, *5*, 49, 1970.

Cicerone, R. J., and S. Bowhill, Photoelectron fluxes in the ionosphere computed by a Monte Carlo method, *J. Geophys. Res.*, *76*, 8299, 1971.

Cicerone, R. J., W. E. Swartz, R. S. Stolarski, A. F. Nagy, and J. S. Nisbet, Thermalization and transport of photoelectrons: A comparison of theoretical approaches, *J. Geophys. Res.*, *78*, 6709, 1973.

Conway, R. R., Photoabsorption and photoionization cross sections of O, O_2, and N_2 for photoelectron production calculations: A compilation of recent laboratory measurements, *NRL Memo. Rep. 6155*, Nav. Res. Lab., Washington, D. C., 1988.

da Rosa, A. V., The theoretical time-dependent thermal behavior of the ionospheric electron gas, *J. Geophys. Res.*, *71*, 4107, 1966.

Dalgarno, A., and T. P. Degges, Electron cooling in the upper atmosphere, *Planet. Space Sci.*, *16*, 125, 1968.

Dalgarno, A., M. B. McElroy, and R. J. Moffett, Electron temperatures in the ionosphere, *Planet. Space Sci.*, *11*, 463, 1963.

Dougherty, J. P., and D. T. Farley, A theory of incoherent scattering of radio waves by a plasma, *Proc. Roy. Soc.*, *A259*, 79, 1960.

Dougherty, J. P., and D. T. Farley, A theory of incoherent scattering of radio waves by a plasma: 3. Scattering in a partly ionized gas, *J. Geophys. Res.*, *68*, 5473–5486, 1963.

Drob, D. P., et al., An empirical model of the Earth's horizontal wind fields: HWM07, *J. Geophys. Res.*, *113*, A12,304, 2008.

Drukarev, G., On the mean energy of electrons released in the ionization of gas, *J. Phys. USSR*, *10*, 81, 1946.

Emmert, J. T., J. L. Lean, and J. M. Picone, Record-low thermospheric density during the 2008 solar minimum, *Geophys. Res. Lett.*, *37*, L12,102, 2010.

Evans, J. V., Theory and practice of ionosphere study by Thomson scatter radar, *Proc. IEEE*, *57*, 496, 1969.

Evans, J. V., and I. J. Gastman, Detection of conjugate photoelectrons at Millstone Hill, *J. Geophys. Res.*, *75*, 807, 1970.

Farley, D. T., A theory of incoherent scattering of radio waves by a plasma, 4, The effect of unequal ion and electron temperatures, *J. Geophys. Res.*, *71*, 4091–4098, 1966.

Farley, D. T., Faraday rotation measurements using incoherent scatter, *Radio Sci.*, *4*, 143–152, 1969a.

Farley, D. T., Incoherent scatter correlation function measurements, *Radio Sci.*, *4*, 935–953, 1969b.

Farley, D. T., Multiple-pulse incoherent-scatter correlation function measurements, *Radio Sci.*, *7*, 661, 1972.

Farley, D. T., Early incoherent scatter observations at Jicamarca, *J. Atmos. Terr. Phys.*, *53*, 665, 1991.

Farley, D. T., J. P. Dougherty, and D. W. Barron, A theory of incoherent scattering of radio waves by a plasma, 2, Scattering in a magnetic field, *Proc. R. Soc., London Ser. A, 263*, 238–258, 1961.

Feautrier, P., Sur la résolution numérique de l'équation de transfert, *C. R. Acad. Sci. Paris.*, *258*, 3189, 1964.

Fejer, J. A., Radio wave scattering by an ionized gas in thermal equilibrium, *J. Geophys. Res.*, *65*, 2635–2636, 1960a.

Fejer, J. A., Scattering of radio wave by an ionized gas in thermal equilibrium, *Can. J. Phys.*, *38*, 1114–1133, 1960b.

Fejer, J. A., Radio wave scattering by an ionized gas in thermal equilibrium in the presence of a uniform magnetic field, *Can. J. Phys.*, *39*, 716–740, 1961.

Fennelly, J. A., and D. G. Torr, Photoionization and photoabsorption cross sections of O, N_2, O_2, and N for aeronomic calculations, *At. Data and Nucl. Data Tables*, *52*, 321, 1992.

Fok, M.-C., R. A. Wolf, R. W. Spiro, and T. E. Moore, Comprehensive computational model of Earth's ring current, *J. Geophys. Res.*, *106*, 8417, 2001.

Fried, B. D., and S. D. Conte, *The plasma dispersion function; the Hilbert transform of the Gaussian*, Academic Press, 1961.

Fuller-Rowell, T. J., G. H. Millward, A. D. Richmond, and M. V. Codrescu, Storm-time changes in the upper atmosphere at low latitudes, *J. Atmos. Solar-Terr. Phys.*, *64*, 1383, 2002.

Fuller-Rowell, T. J., et al., Impact of terrestrial weather on the upper atmosphere, *Geophys. Res. Lett.*, *35*, L09,808, 2008.

Gefan, G. D., and G. V. Khazanov, Non-steady-state conditions of filling up the geomagnetic trap with superthermal electrons, *Ann. Geophys.*, *8*, 519, 1990.

Geisler, J. E., and S. A. Bowhill, Ionospheric temperatures at sunspot minimum, *J. Atmos. Terr. Phys.*, *27*, 457, 1965a.

Geisler, J. E., and S. A. Bowhill, Exchange of energy between the ionosphere and the protonosphere, *J. Atmos. Terr. Phys.*, *27*, 1119, 1965b.

Gordon, W. E., Incoherent scattering of radio waves by free electrons with applications to space exploration by radar, *Proc. Inst. Radio Engr.*, *46*, 1824–1829, 1958.

Green, A. E. S., and R. S. Stolarski, Analytic models of electron impact cross sections, *J. Atmos. Terr. Phys.*, *34*, 1703, 1972.

Grün, A. E., Lumineszenz-photometrische messungen der energieabsorption im strahlungsfeld von elektronenquellen eindimensionaler fall in luft, *Z. Naturforsch.*, *12a*, 89, 1957.

Gustavsson, B., and B. Eliasson, HF radio wave acceleration of ionospheric electrons: Analysis of HF-induced optical enhancements, *J. Geophys. Res.*, *113. A08319*, doi:10.1029/2007JA012,913, 2008.

Hagfors, T., Density fluctuations in a plasma in a magnetic field, with applications to the ionosphere, *J. Geophys. Res.*, *66*, 1699–1712, 1961.

Hagfors, T., and R. A. Brockelman, A theory of collision dominated electron density fluctuations in a plasma with applications to incoherent scattering, *Phys. Fluids*, *14*, 1143, 1971.

Hanson, W. B., Electron temperatures in the upper atmosphere, *Space Res.*, *3*, 282, 1963.

Hanson, W. B., and R. Cohen, Photoelectron heating efficiency in the ionosphere, *J. Geophys. Res.*, *73*, 831, 1968.

Hanson, W. B., and F. S. Johnson, Electron temperatures in the ionosphere, *Mem. Soc. Roy. Sci. Liege*, *5*, 390, 1961.

Hedin, A., et al., Revised global model of thermospheric winds using satellite and ground-based observations, *J. Geophys. Res.*, *96*, 7657, 1991.

Hedin, A. E., Extension of the MSIS thermosphere model into the middle and lower atmosphere, *J. Geophys. Res.*, *96*, 1159–1172, 1991.

Heitler, W., *The Quantum Theory of Radiation*, 3^{rd} ed., Clarendon Press, 1954.

Hocking, W. K., Measurement of turbulent energy dissipation rates in the middle atmosphere by radar techniques: A review, *Radio Sci.*, *20*, 1403–1422, 1985.

Hoegy, W. R., Thermal electron heating rate: A derivation, *J. Geophys. Res.*, *89*, 977, 1984.

Holt, J. M., D. A. Rhoda, D. Tetenbaum, and A. P. van Eyken, Optimal analysis of incoherent scatter radar data, *Radio Sci.*, *27*, 435–447, 1992.

Huba, J. D., G. Joyce, and J. A. Fedder, Sami2 is Another Model of the Ionosphere (SAMI2): A new low-latitude ionosphere model, *J. Geophys. Res.*, *105*, 23,035, 2000a.

Huba, J. D., G. Joyce, and J. A. Fedder, The formation of an electron hole in the topside equatorial ionosphere, *Geophys. Res. Lett.*, *27*, 181, 2000b.

Huba, J. D., G. Joyce, and J. A. Fedder, Ion sound waves in the topside low latitude ionosphere, *Geophys. Res. Lett.*, *27*, 3181, 2000c.

Huba, J. D., G. Joyce, and J. Krall, Three-dimensional equatorial spread F modeling, *Geophys. Res. Lett.*, *35*, L10,102, 2008.

Huba, J. D., G. Joyce, J. Krall, and J. Fedder, Ion and electron temperature evolution during equatorial spread F, *Geophys. Res. Lett.*, *36*, L15,102, 2009.

Hysell, D. L., Incoherent scatter experiments at Jicamarca using alternating codes, *Radio Sci.*, *35*, 1425–1436, 2000.

Hysell, D. L., F. S. Rodrigues, J. L. Chau, and J. D. Huba, Full profile incoherent scatter analysis at Jicamarca, *Ann. Geophys.*, *26*, 59, 2008.

Hysell, D. L., J. L. Chau, and J. D. Huba, Topside measurements at Jicamarca during solar minimum, *Ann. Geophys.*, *27*, 427, 2009.

Hysell, D. L., R. H. Varney, M. N. Vlasov, E. Nossa, B. Watkins, T. Pedersen, and J. D. Huba, Estimating the electron energy distribution during ionospheric modification from spectrographic airglow measurements, *J. Geophys. Res.*, *117*, A02,317, 2012.

Ichimaru, S., *Statistical Plasma Physics*, vol. 1, Westview Press, 2004.

Itikawa, Y., and O. Aono, Energy change of a charged particle moving in a plasma, *Phys. Fluids*, *9*, 1259, 1966.

Jackson, J. D., *Classical Electrodynamics*, 3rd ed., John Wiley and Sons, 1999.

Jasperse, J. R., Boltzmann-Fokker-Plank model for the electron distribution in the Earth's ionosphere, *Planet. Space Sci.*, *24*, 33, 1976.

Jasperse, J. R., Electron distribution function and ion concentrations in the Earth's lower ionosphere from Boltzmann-Fokker-Plank theory, *Planet. Space Sci.*, *25*, 743, 1977.

Kelley, M. C., *The Earth's Ionosphere: Plasma Physics and Electrodynamics*, 2nd ed., Academic Press, 2009.

Khazanov, G. V., and M. W. Liemohn, Nonsteady state ionosphere-plasmasphere coupling of superthermal electrons, *J. Geophys. Res.*, *100*, 9669, 1995.

Khazanov, G. V., and M. W. Liemohn, Transport of photoelectrons in the nightside magnetosphere, *J. Geophys. Res.*, *107*, 1064, 2002.

Khazanov, G. V., M. A. Koen, and S. I. Burenkov, Numerical solution of the kinetic equation for photoelectrons in the plasmasphere with consideration of free and captive zones, *Cosmic Res.*, *17*, 894, 1979.

Khazanov, G. V., M. A. Koen, Y. V. Konikov, and I. M. Sidorov, Simulation of ionosphere-plasmasphere coupling taking into account ion inertia an temperature anisotropy, *Planet. Space Sci.*, *32*, 585, 1984.

Khazanov, G. V., M. W. Liemohn, T. I. Gombosi, and A. F. Nagy, Non-steady-state transport of superthermal electrons in the plasmasphere, *Geophys. Res. Lett.*, *20*, 2821, 1993.

Khazanov, G. V., T. Neubert, and G. D. Gefan, A unified theory of ionosphere-plasmasphere transport of suprathermal electrons, *IEEE Trans. Plasma Sci.*, *22*, 187, 1994.

Khazanov, G. V., T. E. Moore, M. W. Liemohn, V. K. Jordanova, and M.-C. Fok, Global, collisional model of high-energy photoelectrons, *Geophys. Res. Lett.*, *23*, 331, 1996.

Khazanov, G. V., M. W. Liemohn, and T. E. Moore, Photoelectron effects on the self-consistent potential in the collisionless polar wind, *J. Geophys. Res.*, *102*, 7509, 1997.

Khazanov, G. V., M. W. Liemohn, E. N. Krivorutsky, and T. E. Moore, Generalized kinetic description of a plasma in an arbitrary field-aligned potential energy structure, *J. Geophys. Res.*, *103*, 6871, 1998.

Khazanov, G. V., M. W. Liemohn, J. U. Kozyra, and D. L. Gallagher, Global energy deposition to the topside ionosphere from superthermal electrons, *J. Atmos. Solar-Terr. Phys.*, *62*, 947, 2000.

Kirby, K., E. R. Constantinides, S. Babeu, M. Oppenheimer, and G. A. Victor, Photoionization and photoabsorption cross sections of He, O, N_2, and O_2 for aeronomic calculations, *At. Data and Nucl. Data Tables*, *23*, 63, 1979.

Kozelov, B. V., Influence of the dipolar magnetic field on transport of proton-H atom fluxes in the atmosphere, *Ann. Geophys.*, *11*, 697, 1993.

Kozelov, B. V., and V. E. Ivanov, Monte-Carlo calculation of proton-hydrogen atom transport in N_2, *Planet. Space Sci.*, *40*, 1503, 1992.

Kozelov, B. V., and V. E. Ivanov, Effective energy loss per electron-ion pair in proton aurora, *Ann. Geophys.*, *12*, 1071, 1994.

Krall, J., J. D. Huba, and J. A. Fedder, Simulation of field-aligned H^+ and He^+ dynamics during late-stage plasmasphere refilling, *Ann. Geophys.*, *26*, 1507, 2008.

Krall, N. A., and A. W. Trivelpiece, *Principles of Plasma Physics*, McGraw Hill Book Company, 1973.

Krinberg, I. A., Description of the photoelectron interaction with ambient electrons in the ionosphere, *Planet. Space Sci.*, *21*, 523, 1973.

Kudeki, E., and M. Milla, Incoherent scatter spectrum theory for modes propagating perpendicular to the geomagnetic field, *J. Geophys. Res.*, *111*, A06,306, 2006.

Kudeki, E., and M. Milla, Incoherent scatter spectral theories - part I: A general framework and results for small magnetic aspect angles, *IEEE Trans. Geosci. Remote Sens.*, *49*, 315, 2011.

Kudeki, E., S. Bhattacharyya, and R. F. Woodman, A new approach in incoherent scatter *F* region E x B drift measurements at Jicamarca, *J. Geophys. Res.*, *104*, 28,145–28,162, 1999.

Lehtinen, M. S., Statistical theory of incoherent scatter radar measurements, *Tech. Rep. 86/45*, Eur. Incoherent Scatter Sci. Assoc., Kiruna, Sweden, 1986.

Lehtinen, M. S., and I. Häggström, A new modulation principle for incoherent scatter measurements, *Radio Sci.*, *22*, 625–634, 1987.

Lehtinen, M. S., A. Huuskonen, and J. Pirttilä, First experiences of full-profile analysis with GUISDAP, *Ann. Geophys.*, *14(12)*, 1487–1495, 1996.

Lehtinen, M. S., A. Huuskonen, and M. Markkanen, Randomization of alternating codes: Improving incoherent scatter measurements by reducing correlations of gated correlation function estimates, *Radio Sci.*, *32*, 2271, 1997.

Lejeune, G., "Two-stream" photoelectron distributions with interhemispheric coupling: A mixing of analytical and numerical methods, *Planet. Space Sci.*, *27*, 561, 1979.

LeVeque, R. J., *Finite Volume Methods for Hyperbolic Problems*, Cambridge University Press, Cambridge, United Kingdom, 2002.

Liemohn, M. W., and G. V. Khazanov, Nonsteady state coupling processes in superthermal electron transport, in *Cross-Scale Coupling in Space Plasmas, Geophys. Monogr. Ser.,* vol. 93, edited by J. L. Horwitz, N. Singh, and J. L. Burch, pp. 181–191, AGU, Washington, D. C., 1995.

Liemohn, M. W., G. V. Khazanov, T. E. Moore, and S. M. Guiter, Self-consistent superthermal electron effects on plasmaspheric refilling, *J. Geophys. Res.*, *102*, 7523, 1997.

Lindemann, F. A., and G. M. B. Dobson, A theory of meteors, and the density and temperature of the outer atmosphere to which it leads, *Proc. Roy. Soc. Ser. A*, *102*, 411, 1923.

Link, R., Feautrier solution of the electron transport equation, *J. Geophys. Res.*, *97*, 159, 1992.

Lummerzheim, D., and J. Lilensten, Electron transport and energy degradation in the ionosphere: Evaluation of the numerical solutions, comparison with laboratory experiments and auroral observations, *Ann. Geophys.*, *12*, 1039, 1994.

Lummerzheim, D., M. H. Rees, and H. R. Anderson, Angular dependent transport of auroral electrons in the upper atmosphere, *Planet. Space Sci.*, *37*, 109, 1989.

Mantas, G. P., Theory of photoelectron thermalization and transport in the ionosphere, *Planet. Space Sci.*, *23*, 337, 1975.

Mantas, G. P., H. C. Carlson, and V. B. Wickwar, Photoelectron flux buildup in the plasmasphere, *J. Geophys. Res.*, *83*, 1, 1978.

Mariani, F., Pitch-angle distribution of the photoelectrons and origin of the geomagnetic anomaly in the F_2 layer, *J. Geophys. Res.*, *69*, 556, 1964.

Maris, H. B., and E. O. Hulburt, Note on the ultraviolet light of the sun as the origin of aurorae and magnetic storms, *Terr. Magn. Atmos. Elec.*, *33*, 229, 1928.

Marsh, D. R., S. C. Solomon, and A. E. Reynolds, Empirical model of nitric oxide in the lower thermosphere, *J. Geophys. Res.*, *109*, A07,301, 2004.

Martyn, D. F., and O. O. Pulley, The temperatures and constituents of the upper atmosphere, *Proc. Roy. Soc. Ser. A*, *154*, 455, 1936.

Maruyama, N., P. G. Richards, T. Fang, L. Mayer, C. Negrea, T. J. Fuller-Rowell, M. Codrescu, A. D. Richmond, and A. I. Maute, Towards consistent understanding of the coupling between the ionosphere and plasmasphere, Abstract SA41B-1861 presented at 2011 Fall Meeting, AGU, San Francisco, Calif., 5-9 Dec., 2011.

McClure, J. P., Diurnal variation of neutral and charged particle temperatures in the equatorial *f* region, *J. Geophys. Res.*, *74*, 279, 1969.

Milla, M., and E. Kudeki, F-region electron density and T_e/T_i measurements using incoherent scatter power data collected at ALTAIR, *Ann. Geophys.*, *24*, 1333, 2006.

Milla, M., and E. Kudeki, Incoherent scatter spectral theories - part II: Modeling the spectrum for modes propagating perpendicular to **B**, *IEEE Trans. Geosci. Remote Sens.*, *49*, 329, 2011.

Millward, G. H., R. J. Moffett, S. Quegan, and T. J. Fuller-Rowell, A coupled thermosphere-ionosphere-plasmasphere model (CTIP), in *STEP: Handbook of Ionospheric Models*, edited by R. W. Schunk, pp. 239–279, Cent. for Atmos. and Space Sci., Logan, Utah, 1996.

Min, Q.-L., D. Lummerzheim, M. H. Rees, and K. Stamnes, Effects of a parallel electric field and the geomagnetic field in the topside ionosphere on auroral and photoelectron energy distributions, *J. Geophys. Res.*, *98*, 19,223, 1993.

Mitra, A. P., A review of D-region processes in non-polar latitudes, *J. Atmos. Terr. Phys.*, *30*, 1065, 1968.

Mitra, S. K., *The Upper Atmosphere*, 2nd ed., The Asiatic Society, Calcutta, India, 1952.

Moddeman, W. E., T. A. Carlson, M. O. Krause, B. P. Pullen, W. E. Bull, and G. K. Schweitzer, Determination of the $K - LL$ Auger spectra of N_2, O_2, CO, H_2O, and CO_2, *J. Chem. Phys.*, *55*, 1971.

Nagy, A. F., and P. M. Banks, Photoelectron fluxes in the ionosphere, *J. Geophys. Res.*, *75*, 6260, 1970.

Nicolls, M. J., R. H. Varney, S. L. Vadas, M. C. Kelley, P. Stamus, and C. J. Heinselman, Influence of an inertia-gravity wave on mesospheric dynamics: A case study with the Poker Flat Incoherent Scatter Radar, *J. Geophys. Res.*, *115*, D00N02, 2010.

Nisbet, J. S., Photoelectron escape from the ionosphere, *J. Atmos. Terr. Phys.*, *30*, 1257, 1968.

Nygrén, T., *Introduction to incoherent scatter measurements*, Invers Oy, Sondakylä, Finland, 1996.

Onda, K., M. Hayaski, and K. Takayanagi, Monte Carlo calculaitons of ionization and excitation rates in electron aurora, *Rep. 645*, Inst. of Space and Astron. Sci., Kanagawa, Japan, 1992.

Otsuka, Y., S. Kawamura, N. Balan, S. Fukao, and G. J. Bailey, Plasma temperature variations in the ionosphere over the middle and upper atmosphere radar, *J. Geophys. Res.*, *103*, 20,705, 1998.

Pedatella, N. M., J. M. Forbes, A. Maute, A. D. Richmond, T.-W. Fang, K. M. Larson, and G. Millward, Longitudinal variations in the F region ionosphere and topside ionosphere-plasmasphere: Observations and model simulations, *J. Geophys. Res.*, *116*, A12,309, 2011.

Perkins, F., Motion of a test particle in a plasma, *Phys. Fluids*, *8*, 1361, 1965.

Perkins, F., and E. E. Salpeter, Enhancement of plasma density fluctuations by nonthermal electrons, *Phys. Rev.*, *139*, 55, 1965.

Peterson, W. K., T. N. Woods, P. C. Chamberlin, and P. G. Richards, Photoelectron flux variations observed from the FAST satellite, *Adv. Space Res.*, *42*, 947, 2008.

Picone, J. M., A. E. Hedin, D. P. Drob, and A. C. Aikin, NRLMSISE-00 empirical model of the atmosphere: Statistical comparisons and scientific issues, *J. Geophys. Res.*, *107*, 1468, 2002.

Pingree, J. E., Incoherent scatter measurements and inferred energy fluxes in the equatorial F-region ionosphere, Ph.D. thesis, Cornell University, Ithaca, NY, 1990.

Polyakov, V. M., G. V. Khazanov, and M. A. Koen, The ionosphere-plasmasphere photoelectron transport, *Phys. Solariterr.*, *10*, 93, 1979.

Porter, H. S., and A. E. S. Green, Comparison of Monte Carlo and continuous slowing-down approximaitons treatments of 1-keV proton energy deposition in N_2, *J. Appl. Phys.*, *46*, 5030, 1975.

Press, W. H., S. A. Teukolsky, W. T. Vetterling, and B. P. Flannery, *Numerical Recipes: The Art of Scientific Computing*, 3$^{\text{rd}}$ ed., Cambridge University Press, 2007.

Raizada, S., M. P. Sulzer, C. A. Tepley, S. A. González, and M. J. Nicolls, Inferring D region parameters using improved incoherent scatter radar techniques at Arecibo, *J. Geophys. Res.*, *113*, A12,302, 2008.

Rawer, K., *The Ionosphere*, Frederick Ungar, New York, 1957.

Rees, M. H., *Physics and Chemistry of the Upper Atmosphere*, Cambridge Univsersity Press, 1989.

Rees, M. H., and D. Lummerzheim, Characteristics of auroral electron precipitation derived from optical spectroscopy, *J. Geophys. Res.*, *94*, 6799, 1989.

Reifman, A., and W. G. Dow, Dynamics probe measurements in the ionosphere, *Phys. Rev.*, *76*, 987, 1949.

Retterer, J. M., Physics-based forecasts of equatorial radio scintillation for the Communication and Navigation Outage Forecasting System (C/NOFS), *Space Weather*, *3*, S12C03, 2005.

Richards, P. G., Theremal electron quenching of N(^{2}D): Consequences for the ionospheric photoelectron flux and the thermal electron temperature, *Planet. Space Sci.*, *34*, 689, 1986.

Richards, P. G., An improved algorithm for determining neutral winds from the height of the F_2 peak electron density, *J. Geophys. Res.*, *96*, 17,839, 1991.

Richards, P. G., and G. V. Khazanov, On the thermal electron energy balance in the ionosphere in January 1993 and June 1990, *J. Geophys. Res.*, *102*, 7369, 1997.

Richards, P. G., and W. K. Peterson, Measured and modeled backscatter of ionospheric photoelectron fluxes, *J. Geophys. Res.*, *113*, A08,321, 2008.

Richards, P. G., and D. G. Torr, A simple theoretical model for calculating and parameterizing the ionospheric photoelectron flux, *J. Geophys. Res.*, *88*, 2155, 1983.

Richards, P. G., and D. G. Torr, Ratios of photoelectron to EUV ionizations rates for aeronomic studies, *J. Geophys. Res.*, *93*, 4060, 1988.

Richards, P. G., and D. G. Torr, Auroral modeling of the 3371 Å emission rate: Dependence on characteristic electron energy, *J. Geophys. Res.*, *95*, 10,337, 1990.

Richards, P. G., and P. G. Torr, The field line interhemispheric plasma model, in *STEP: Handbook of Ionospheric Models*, edited by R. W. Schunk, pp. 207–216, Cent. for Atmos. Space Sci., Logan, Utah, 1996.

Richards, P. G., J. A. Fennelly, and D. G. Torr, EUVAC: A solar EUV flux model for aeronomic calculations, *J. Geophys. Res.*, *99*, 8981, 1994.

Richards, P. G., T. N. Woods, and W. K. Peterson, HEUVAC: A new high resolution solar EUV proxy model, *Adv. Space Res.*, *37*, 315, 2006.

Ridley, A. J., Y. Deng, and G. Tóth, The global ionosphere-thermosphere model, *J. Atmos. Solar-Terr. Phys.*, *68*, 839, 2006.

Roble, R. G., The NCAR therosphere-ionosphere-mesosphere-electrodynamics general circulation model, in *STEP: Handbook of Ionospheric Models*, edited by R. W. Schunk, pp. 281–288, Cent. for Atmos. and Space Sci., Logan, Utah, 1996.

Roble, R. G., and J. T. Hastings, Thermal response properties of the Earth's ionospheric plasma, *Planet. Space Sci.*, *25*, 217–231, 1977.

Roble, R. G., E. C. Ridley, and R. E. Dickinson, On the global mean structure of the thermosphere, *J. Geophys. Res.*, *92*, 8745, 1987.

Roble, R. G., E. C. Ridley, A. D. Richmond, and R. E. Dickinson, A coupled

thermosphere/ionosphere general circulation model, *Geophys. Res. Lett.*, *15*, 1325, 1988.

Roederer, J. G., *Dynamics of Geomagnetically Trapped Radiation*, Springer-Verlag, New York, 1970.

Rosenbluth, M. N., and N. Rostoker, Scattering of electromagnetic waves by a nonequilibrium plasma, *Phys. Fluids*, *5*, 776, 1962.

Rosenbluth, M. N., W. M. MacDonald, and D. L. Judd, Fokker-Planck equation for and inverse-square force, *Phys. Rev.*, *107*, 1–6, 1957.

Salpeter, E. E., Electron density fluctuations in a plasma, *Phys. Rev.*, *120*, 1528–1535, 1960.

Salpeter, E. E., Plasma density fluctuations in a magnetic field, *Phys. Rev.*, *122*, 1663–1674, 1961.

Scherliess, L., and B. G. Fejer, Radar and satellite global equatorial F region vertical drift model, *J. Geophys. Res.*, *104*, 6829, 1999.

Schunk, R. W., An ionosphere-plasmasphere model (IPM), *Tech. rep.*, Space Environ. Corp., Logan, UT, 2002.

Schunk, R. W., and P. B. Hays, Photoelectron energy losses to thermal electrons, *Planet. Space Sci.*, *19*, 113, 1971.

Schunk, R. W., and A. F. Nagy, Electron temperatures in the F region of the ionosphere: Theory and observations, *Rev. Geophys. Space Phys.*, *16*, 355, 1978.

Schunk, R. W., and A. F. Nagy, *Ionospheres: Physics, Plasma Physics, and Chemistry*, 2nd ed., Cambridge University Press, 2009.

Smith, F. L., III, and C. Smith, Numerical evaluation of Chapman's grazing incidence integral ch(X, χ), *J. Geophys. Res.*, *77*, 3592, 1972.

Smithtro, C. G., and J. J. Sojka, A new global average model of the coupled thermosphere and ionosphere, *J. Geophys. Res.*, *110*, A08,305, 2005.

Smithtro, C. G., and S. C. Solomon, An improved parameterization of thermal electron heating by photoelectrons, with application to an X17 flare, *J. Geophys. Res.*, *113*, A08,307, 2008.

Solomon, S. C., Auroral electron transport using the Monte Carlo method, *Geophys. Res. Lett.*, *20*, 185, 1993.

Solomon, S. C., Auroral particle transport using Monte Carlo and hybrid methods, *J. Geophys. Res.*, *106*, 107, 2001.

Solomon, S. C., and V. J. Abreu, The 630 nm dayglow, *J. Geophys. Res.*, *94*, 6817, 1989.

Solomon, S. C., and L. Qian, Solar extreme-ultraviolet irradiance for general circulation models, *J. Geophys. Res.*, *110*, A10,306, 2005.

Solomon, S. C., P. B. Hays, and V. J. Abreu, The auroral 6300 Å emission: Observations and modeling, *J. Geophys. Res.*, *93*, 9867, 1988.

Solomon, S. C., S. M. Bailey, and T. N. Woods, Effect of solar soft X-rays on the lower ionosphere, *Geophys. Res. Lett.*, *28*, 2149, 2001.

Solomon, S. C., T. N. Woods, L. V. Didkovsky, J. T. Emmert, and L. Qian, Anomalously low solar extreme-ultraviolet irradiance and thermospheric density during solar minimum, *Geophys. Res. Lett.*, *37*, L16,103, 2010.

Solomon, S. C., L. Qian, L. V. Didkovsky, R. A. Viereck, and T. N. Woods, Causes of low thermospheric density during the 2007-2009 solar minimum, *J. Geophys. Res.*, *116*, A00H07, 2011.

Spencer, L. V., Theory of electron penetration, *Phys. Rev.*, *98*, 1597, 1955.

Stamnes, K., Analytic approach to photoelectron transport: Extensions to Stolarski's (1972) work, *J. Geophys. Res.*, *82*, 2391, 1977.

Stamnes, K., Analytic approach to auroral electron transport and energy degradation, *Planet. Space Sci.*, *28*, 427, 1980.

Stamnes, K., On the two-stream approach to electron transport and thermalization, *J. Geophys. Res.*, *86*, 2405, 1981.

Stamnes, K., and P. Conklin, A new multi-layer discrete ordinate approach to radiative transfer in vertically inhomogeneous atmospheres, *J. Quant. Spectrosc. Radiat. Trans.*, *31*, 273, 1984.

Stamnes, K., S. C. Tsay, W. J. Wiscombe, and K. Jayaweera, Numerically stable algorithm for disrete-ordinate-method radiative transfer in multiple scattering and emitting layered media, *Appl. Optics*, *27*, 2502, 1988.

Stolarski, R. S., Analytic approach to photoelectron transport, *J. Geophys. Res.*, *77*, 2862, 1972.

Strickland, D. J., D. L. Book, T. P. Coffey, and J. A. Fedder, Transport equation techniques for the deposition of auroral electrons, *J. Geophys. Res.*, *81*, 1976.

Strobel, D. F., T. R. Young, R. R. Meier, T. P. Coffey, and A. W. Ali, The nighttime ionosphere: E region and lower F region, *J. Geophys. Res.*, *79*, 3171, 1974.

Sulzer, M. P., A radar technique for high range resolution incoherent scatter autocorrelation function measurements utilizing the full average power of klystron radars, *Radio Sci.*, *21*, 1033–1040, 1986.

Sulzer, M. P., and S. Gonzalez, The effect of electron Coulomb collisions on the incoherent scatter spectrum in the F region at Jicamarca, *J. Geophys. Res.*, *104*, 22,535, 1999.

Swartz, W. E., Electron production, recombination, and heating in the F-region of the ionosphere, Ph.D. thesis, The Pennsylvania State University, University Park, PA, 1972.

Swartz, W. E., Thermalization and transport of photoelectrons: A comparison of theoretical approaches, 2, Transport details for isotropic scattering, *J. Geophys. Res.*, *81*, 183, 1976.

Swartz, W. E., Optimization of energetic electron energy degradation calculations, *J. Geophys. Res.*, *90*, 6587, 1985.

Swartz, W. E., and D. T. Farley, A theory of incoherent scattering of radiowaves by a plasma, 5, The use of the Nyquist theorem in general quasi-equilibrium situations, *J. Geophys. Res.*, *84*, 1930–1932, 1979.

Swartz, W. E., and J. S. Nisbet, Revised calculations of F region ambient electron heating by photoelectrons, *J. Geophys. Res.*, *77*, 6259, 1972.

Swartz, W. E., and J. S. Nisbet, Incompatibility of solar EUV fluxes and incoherent scatter measurements at Arecibo, *J. Geophys. Res.*, *78*, 5640, 1973.

Swartz, W. E., J. S. Nisbet, and A. E. S. Green, Analytic expression for the energy-transfer rate from photoelectrons to thermal-electrons, *J. Geophys. Res.*, *76*, 8425, 1971.

Swartz, W. E., G. J. Bailey, and R. J. Moffett, Electron heating resulting from interhemispherical transport of photoelectrons, *Planet. Space Sci.*, *23*, 589, 1975.

Synnes, S. A., F. Søraas, and J. P. Hansen, Monte-Carlo simulations of proton aurora, *J. Atmos. Solar-Terr. Phys.*, *60*, 1695, 1998.

Tam, S. W. Y., F. Yasseen, T. Chang, and S. B. Ganguli, Self-consistent kinetic photoelectron effects on the polar wind, *Geophys. Res. Lett.*, *22*, 2107, 1995.

Tam, S. W. Y., F. Yasseen, and T. Chang, Further development in theory/data closure of the photoelectron-driven polar wind day-night transition of the outflow, *Ann. Geophys.*, *16*, 948, 1998.

Tanenbaum, B. S., Continuum theory of Thomson scattering, *Phys. Rev.*, *171*, 215, 1968.

Tatarski, V. I., *Wave Propagation in a Turbulent Medium*, McGraw-Hill Book Company, Inc., 1961.

Titheridge, J. E., Temperatures in the upper ionosphere and plasmasphere, *J. Geophys. Res.*, *103*, 2261, 1998.

Torr, M. R., D. G. Torr, P. G. Richards, and S. P. Yung, Mid- and low-latitude model of thermospheric emissions: 1. $O^+(^2P)$ 7320 Å and $N_2(2P)$ 3371 Å, *J. Geophys. Res.*, *95*, 21,147, 1990.

Trac, H., and U.-L. Pen, A primer on eulerian computational fluid dynamics for astrophysics, *Publ. Astron. Soc. Pac.*, *115*, 303, 2003.

van Leer, B., Towards the ultimate conservative difference scheme II. Monotonicity and conservation combined in a second-order scheme, *J. Comp. Phys.*, *14*, 361, 1974.

Venkatraman, S., and R. Heelis, Longitudinal and seasonalvariations in nighttime plasma temperatures in the equatorial topside ionosphere during solar maximum, *J. Geophys. Res.*, *104*, 2603, 1999a.

Venkatraman, S., and R. Heelis, Effects of solar activity variations on adiabatic heating and cooling effects in the nighttime equatorial topside ionosphere, *J. Geophys. Res.*, *104*, 17,117, 1999b.

Vlasov, M. N., M. C. Kelley, and E. Gerken, Impact of vibrational excitation on ionospheric parameters and artificial airglow during HF heating in the F region, *J. Geophys. Res.*, *109*, A09,304, 2004.

Walt, M., W. M. MacDonald, and W. E. Francis, Penetration of auroral electrons into the atmosphere, in *Physics of the Magnetosphere*, edited by R. L. Carovillano, J. F. McClay, and H. R. Radoski, pp. 534–562, D. Redidel Publising Company, Dordrecht, Holland, 1967.

Winningham, J. D., D. T. Decker, J. U. Kozyra, J. R. Jasperse, and A. F. Nagy, Energetic ($>$ 60 eV) atmospheric photoelectrons, *J. Geophys. Res.*, *94*, 15,335, 1989.

Woodman, R. F., Incoherent scattering of electromagnetic waves by a plasma, Ph.D. thesis, Harvard University, 1967.

Woodman, R. F., On a proper electron collision frequency for a Fokker-Planck collision model with Jicamarca applications, *J. Atmos. Solar-Terr. Phys.*, *66*, 1521, 2004.

Woodman, R. F., and T. Hagfors, Methods for the measurement of vertical ionospheric motions near the magnetic equator by incoherent scattering, *J. Geophys. Res.*, *74*, 1205–1212, 1969.

Woodman, R. F., and C. La Hoz, Radar observations of F region equatorial irregularities, *J. Geophys. Res.*, *81*, 5447–5466, 1976.

Yngvesson, K. O., and F. W. Perkins, Radar Thomson scatter studies of photoelectrons in the ionosphere and Landau damping, *J. Geophys. Res.*, *73*, 97, 1968.

Young, E. R., D. G. Torr, P. G. Richards, and A. F. Nagy, A computer simulation of the midlatitude plasmasphere and ionosphere, *Planet. Space Sci.*, *28*, 881, 1980.